Lanthanide-Based Probes for Oxidative Stress

A Dissertation
SUBMITTED TO THE FACULTY OF
UNIVERSITY OF MINNESOTA
BY

Katie Louise Peterson

IN PARTIAL FULFILLMENT OF THE REQUIREMENTS
FOR THE DEGREE OF
DOCTOR OF PHILOSOPHY

Valérie C. Pierre, Advisor

June 2014

DEDICATION

To my husband, Nathan,

Who continually supported me and sacrificed so much for me.

My Ph.D is, in many ways, as much his as mine.

To my parents, Tom and Lori,

Who reinforced my interest in science

and taught me that hard work and dedication go a long way.

Their love for life, attention to detail, and creativity are traits

I am thankful for inheriting.

To my in-laws, David and Joan,

Who showed me that enjoying life is more important than working

so hard that you might miss it.

Their compassion and encouragement are unyielding.

To my entire family,

Who taught me that a sense of humor is critical to happiness.

Because of them, I know how to laugh

and make anything – even chemistry – fun.

ACKNOWLEDGEMENTS

I sincerely thank all those who contributed
– directly or indirectly –
to the work presented in this dissertation.

First, I thank my advisor, Dr. Valérie Pierre. Her innovative ideas inspired me, while her guidance, understanding and ability to break large projects into manageable tasks kept me going. Valérie taught me the importance of careful experimental design and how to always find the positive, especially with unexpected results. ("Well, now we know that doesn't work. What can we try next?") Her thoughtful mentoring has shaped my future research ideas, teaching philosophy, and values.

The members of the Pierre group, both past and present, have helped and supported me. Over five years, we have become an evolving family with a shared love for lanthanide metals. Evan Weitz introduced me to the joys and trials of synthetic chemistry. His skilled hands produced complexes that I further studied in cellular systems. Jonathan Dang, Cutler Lewandowski, and Brian Hanson maintained positive attitudes as they optimized reaction conditions and purified synthetic intermediates. Despite their busy schedules, they were devoted to the successes of our shared projects and were a pleasure to mentor. Maximilian Margherio, Phi Doan, and Kyle Wilke spent many hours collecting data on the spectrofluorometer and pioneered the lanthanide-based hydroxyl radical probe project. Thakshila Wickramaratne modeled for me how to persist through research struggles while keeping a smile on your face and happiness in your heart. As we disused research ideas and life, her insightful comments developed me not only as a researcher and teacher, but as a person. I must also thank her for creating graphics for this dissertation. Sarah Harris and Jen Koezly, as friends and co-workers, shared with me the difficulties ("This reaction/purification/experiment is not working!") and delights ("I finished the synthesis of my compound libraries!") of research. Dr. Eric Smolensky and Dr. Kriti Srivastava challenged me to fully understand my

research projects and communicate them clearly. Also, I thankfully acknowledge Dr. Kriti Srivastava for performing DFT geometry optimization calculations. I especially thank the members of the Pierre group that assisted in the revising and editing of this dissertation.

The work described here was a result of fruitful collaborations with talented researchers at the University of Minnesota. Dr. Edgar Arriaga, and his group members Michelle Henderson, Dr. Greg Wolken, and Dr. Chad Satori, coached me through cellular studies and graciously shared their time, equipment, and instruments. Michelle deserves special recognition for teaching me *everything* I know about culturing mammalian cells and sharing her personal research space with me (two organized people get along quite well). Dr. Małgorzata (Gosia) Marjańska and Dr. Gregor Adriany at the Center of Magnetic Resonance Research acquired the fluorine MRI images and constructed the resonance frequency coil.

Lastly, I thank my undergraduate research advisor, Dr. Jason Halfen. He, through teaching chemistry and involving me in undergraduate research, fostered and encouraged my development as a scientist. When offering me a summer research position (I thought I would just go home and waitress for 3 months), he told me, “This is not just a summer job; it is the start of a career.” He was right.

ABSTRACT

Oxidative stress, or the imbalance of reactive oxidative species and antioxidants, is implicated in a wide variety of physiological functions and diseases. Currently, little is known about the biological concentrations and the exact roles of individual species. In particular, the cellular concentrations of hydroxyl radical and the etiology of this reactive oxygen species in disease states are unclear. The photophysical properties of luminescent lanthanide-based imaging agents and the magnetic properties of fluorinated contrast agents make them favorable candidates to monitor oxidative species in biological environments.

Luminescent lanthanide-based probes for hydroxyl radical are presented. These probes utilize aromatic acid pre-antennas that sensitize terbium emission upon hydroxylation. The ability of hydroxylated and non-hydroxylated aromatic acids including benzoate, benzamide, isophthalate, isophthalamide, trimesate, and trimesamide to sensitize Tb-DO3A was evaluated by time-delayed luminescence spectroscopy. The formation of a weak ternary complex between hydroxytrimeasamide and Tb-DO3A was confirmed by temperature-dependent titrations. The luminescence response of the bimolecular Tb-DO3A and trimesamide probe to hydroxyl radical generated by the photolysis of hydrogen peroxide was investigated. The system exhibits excellent selectivity for hydroxyl radical over other biologically relevant reactive oxygen and nitrogen species.

Next, fluorinated magnetic resonance imaging contrast agents responsive to hydroxyl radical are described. The 3,5-difluorobenzoic acid probe is water soluble and ratiometrically responds to hydroxyl radical. Upon hydroxylation, a fluoride ion is released. The relative signal intensity of the product and that of the unreacted contrast agent can then be used to monitor the analyte in a ratiometric manner by ^{19}F NMR and ^{19}F MRI. The selectivity of the system towards hydroxyl radical compared to other

reactive oxygen and nitrogen species is also measured. Paramagnetic, lanthanide-based contrast agents incorporating the sensing moiety are also evaluated for increased sensitivity of detection compared to the diamagnetic analogs.

Additionally, a family of lanthanide-based luminescent complexes based on a macrocyclic core featuring different sensitizing antennas and variable pendant arms are investigated in terms of their biological compatibility. The cellular uptake of Tb-DOTA complexes containing hydroxyisophthalamide (IAM), methoxyisophthalamide (IAM(OMe)), or phenathridine (Phen) antenna were comparable despite their differences in hydrophobicity. The luminescence quenching of Tb-DOTA-IAM(OMe) was also investigated in cell lysate by time-delayed spectroscopy. Pendant arms varying in hydrophobicity and charge were used to evaluate the effect of structural and electronic properties on cellular viability and cell association as measured by a MTT assay and ICP-MS, respectively. Regardless of the amide substituents, complexes based on Tb-DOTAm-IAM(OMe) core exhibited low cytotoxicity and low cellular association. Thus, complexes based on this platform are well-suited for the detection of extracellular analytes.

TABLE OF CONTENTS

CHAPTER 1

CHAPTER 2

CHAPTER 3

CHAPTER 4

List of Tables

Chapter 1
An Introduction to Imaging Oxidative Stress

Chapter 2
Time-Delayed Luminescence Detection of Hydroxyl Radical

Chapter 3
Fluorine Magnetic Resonance Detection of Hydroxyl Radical

Chapter 4
Cellular Compatibility of Lanthanide Complexes

LIST OF FIGURES

CHAPTER 1
AN INTRODUCTION TO IMAGING OXIDATIVE STRESS

CHAPTER 2
TIME-DELAYED LUMINESCENCE DETECTION OF HYDROXYL RADICAL

CHAPTER 3
FLUORINE MAGNETIC RESONANCE DETECTION OF HYDROXYL RADICAL

CHAPTER 4
CELLULAR COMPATIBILITY OF LANTHANIDE COMPLEXES

List of Schemes

Chapter 3
Fluorine Magnetic Resonance Detection of Hydroxyl Radical

Chapter 4
Cellular Compatibility of Lanthanide Complexes

LIST OF ABBREVIATIONS

8-OH-G	8-hydroxyguainine
^{19}FLIS	fluorine lanthanide induced shift
ATP	adenosine triphosphate
BA	benzoic acid
BET	back energy transfer
BOC	*tert*-butoxycarbonyl
BODIPY	boron-dipyrromethene
BRW	Bloch-Redfield-Wangsness
CA	contrast agent
CCA	coumarin-3-carboxylic acid
cGMP	cyclic guanosine monophosphate
$\bullet CH_3$	methyl radical
$CO_3\bullet^-$	carbonate radical
Cy	cyanine dye
$DCFH_2$	dihydrodichlorofluorescein

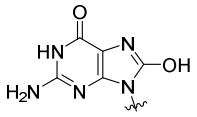
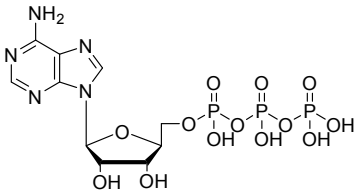
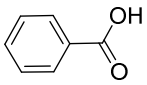
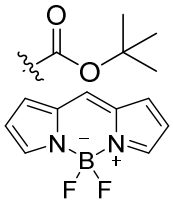
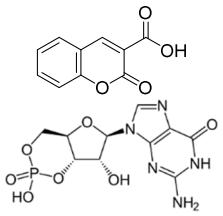
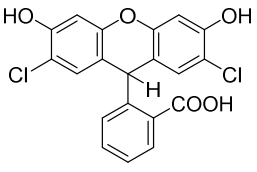

DIPEA	*N*,*N*-diisopropylethylamine	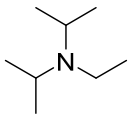
DMEM	Dulbecoo's modified eagle medium	
DMF	dimethylformamide	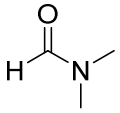
DMSO	dimethyl sulfoxide	
DNA	deoxyribonucleic acid	
DO3A	1,4,7,10-tetraazacyclododecane-1,4,7-tris(acetic acid)	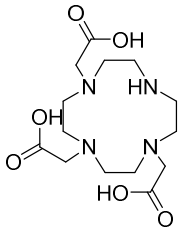
DO2A	1,4,7,10-tetraazacyclododecane-1,7-bis(acetic acid)	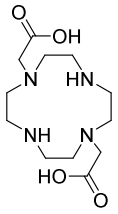
DOTA	1,4,7,10-tetraazacyclododecane-1,4,7,10-tetraacetic acid	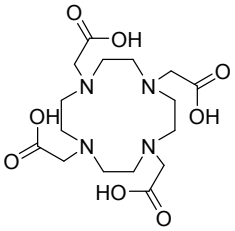
DOTAm	1,4,7,10-tetrakis(carbamoylmethyl)-1,4,7,10-tetraazacyclododecane	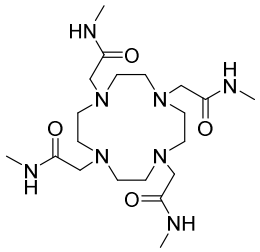
DTPA	diethylene triamine pentaacetic acid	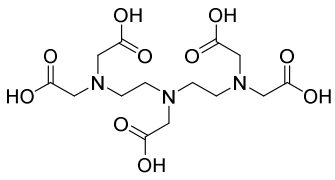

DTPA-BMA	5,8-Bis(carboxymethyl)-11-[2-(methylamino)-2-oxoethyl]-3-oxo-2,5,8,11-tetraazatridecan-13-oic acid
E°'	standard reduction potential
EDTA	ethylenediaminetetraacetic acid
EC_{50}	half maximal effective concentration
EPR	electron paramagnetic resonance
ER	endoplasmic reticulum
ESI-MS	electrospray ionization mass spectrometry
ESR	electron spin resonance
ET	energy transfer
FOV	field of view
GPx	glutathione peroxidase
GSH	gluathione
GSSH	oxidized glutathione
HATU	1-[Bis(dimethylamino)methylene]-1H-1,2,3-triazolo[4,5-b]pyridinium 3-oxid hexafluorophosphate
HEPES	4-(2-hydroxyethyl)-1-piperazineethanesulfonic acid
H_2O_2	hydrogen peroxide
HO•	hydroxyl radical

HPLC	high performance liquid chromatography
hROS	highly reactive oxygen species
IAM	2-hydroxyisothalamide
IAM(OMe)	2-methoxyisophthalamide
ICP-MS	inductively coupled plasma mass spectrometry
LIS	lanthanide induced shift
Ln	lanthanide
MOPS	4-morpholinepropanesulfonic acid
MPO	myeloperoxidase
MR	magnetic resonance
MRI	magnetic resonance imaging
MRS	magnetic resonance spectroscopy
MTT	3-(4, 5-dimethylthiazolyl-2)-2,5-diphenyltetrazolium bromide
NADPH	nicotinamide adenine dinucleotide phosphate
NI	naphthalimide
NIR	near infrared
NMR	nuclear magnetic resonance

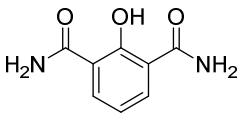

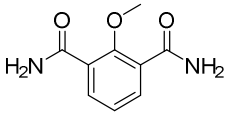

$\Delta\delta = \delta_{paramagnetic} - \delta_{diamagnetic}$

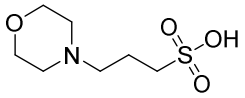

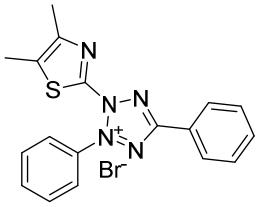

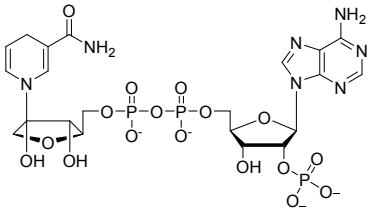

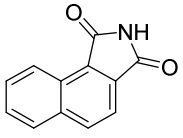

NO	nitric oxide
NO_2•	nitrogen dioxide
NOS	nitric oxide synthase
nNOS	neuronal nitric oxide synthase
eNOS	endothelial nitric oxide synthase
iNOS	inducible nitric oxide synthase
NOX2	NADPH (nicotinamide adenine dinucleotide phosphate) oxidase
NP	1,8-naphthyridine
oAA	orthoaminoanilide
OCl^-	hypochlorite
O_2	molecular oxygen
O_2^-	superoxide
$^1O_2$	singlet oxygen
$ONOO^-$	peroxynitrite
PARACEST	paramagnetic chemical exchange saturation transfer
PBS	phosphate buffered saline
PIPES	1,4-piperazinediethanesulfonic acid
PCC	pyridinium chlorochromate
Phen	6-methylphenanthridine

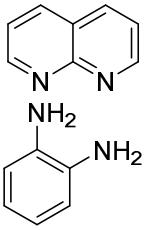

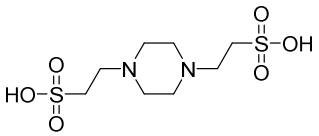

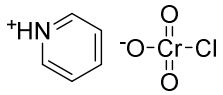

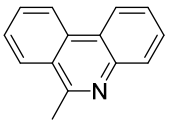

PMA	phorbol myristate acetate	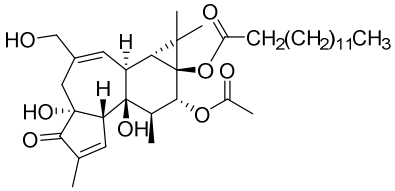
PMT	photomultiplier tube	
PRE	paramagnetic relaxation enhancement	
PSC	pseudo contact shift	
R_1	longitudinal relaxation rate	Equal to $1/T_1$
R_2	transverse relaxation rate	Equal to $1/T_2$
R	rhodamine	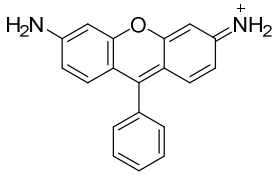
R•	carbon centered radical	
RNA	ribonucleic acid	
RNS	reactive nitrogen species	
RO•	alkoxyl radical	
ROO•	alkyl peroxyl radical	
ROOH	lipid hydroperoxide	
ROS	reactive oxygen species	
SA	salicylic acid	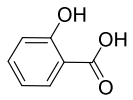
SHE	standard hydrogen electrode	
SNR	signal-to-noise ratio	
SOD	superoxide dismutase	
T_1	longitudinal relaxation time	Equal to $1/R_1$
T_2	transverse relaxation time	Equal to $1/R_2$

TBHP	*tert*-butyl hydroperoxide 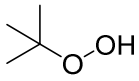
^{t}BuO•	*tert*-butoxy radical
TEMPO	(2,2,6,6-tetramethylpiperidin-1-yl)oxy 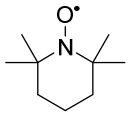
TFA	trifluoroacetic acid 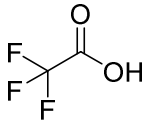
TPA	terephthalic acid 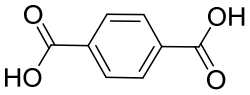
UV	ultraviolet light

CHAPTER 1
AN INTRODUCTION TO IMAGING OXIDATIVE STRESS

I. OXIDATIVE STRESS AND HUMAN HEALTH

A. Cellular redox state

Oxidative stress refers to a state where oxidative or redox active species overwhelm the antioxidant mechanisms in a cell. This results in damage to cellular proteins, DNA, and lipids that can ultimately lead to inflammation, pain, and cell death. Within a cell, pro-oxidant and antioxidant molecules are balanced to control the cellular redox state; deviations from the normal redox potential can result in oxidative damage to biomolecules and toxic effects. Common classes of oxidative molecules include the families of reactive oxygen species (ROS) and reactive nitrogen species (RNS), along with reactive thiols and carbon radicals. These species are produced during normal cellular functions such as mitochondrial respiration, metabolism of xenobiotics, and ionizing radiation.[1-2] Currently, it is known that ROS play critical roles in normal physiological functions including protein folding, signaling, and immune responses.[3]

Prevalent antioxidants in enzymatic and non-enzymatic forms control the amount of oxidative species present. Small molecule antioxidants such as glutathione (GSH), ascorbic acid (vitamin C), α-tocopherol (vitamin E), carotenoids, and flavonoids are efficient scavengers of cellular oxidants. Additionally, enzymes like superoxide dismutase (SOD), peroxidases, and catalase convert reactive oxygen species to less reactive forms. Redox homeostasis describes the maintenance of the cellular redox state within a narrow range. Slight disturbances in the equilibrium of pro-oxidants and antioxidants can greatly influence the cellular redox environment. For example, a 30 mV change in redox potential inside a cell correlates to a 10-fold change in reducing *versus* oxidizing species. The amount of oxidative species are thus carefully managed through these opposing routes of production and inactivation.

Accumulation of ROS at the cellular level has both beneficial and detrimental consequences. At low concentrations, ROS have beneficial roles including their ability to

act as vasodilators to improve cardiovascular circulation and fight infections during inflammatory responses.[2] However, bursts of ROS produced, for example by neutrophils and macrophages during inflammation, can overwhelm antioxidant defense mechanisms. To facilitate advantageous redox signaling and simultaneously control oxidative damage, cells spatially and temporally regulate ROS production.[4] The local redox buffer capacity of a cell plays a critical role in controlling the flux of ROS. Glutathione (GSH), present at millimolar concentrations within cells, reacts rapidly with some ROS like hypochlorite, yet has limited reactivity with hydrogen peroxide. Therefore, oxidants generated at a specific subcellular location must overwhelm the redox capacity within that local region before exerting deleterious effects throughout the entire cell. Additionally, cells colocalize the production of ROS and their targets, placing the signaling molecules in close proximity to the substrate. An excellent example includes NADPH oxidases that are located in the plasma membrane along with target phosphatases that respond to the product ROS. These cellular mechanisms modulate and "buffer" the redox events in a biological environment.

Over production of these reactive species, and the resulting oxidative stress, is linked to three main classes of pathological conditions.[3, 5] The first class of disorders include cancers and diabetes that are linked to the altered redox state or mitochondrial oxidative stress. The second class is comprised of inflammatory and oxidative conditions like arthritis, chronic inflammation, or reperfusion injury that are associated with altered NADPH oxidases or xanthine oxidase activity and an immune response directed at the host.[3] Last is the category of oxidative damage to biomolecules including proteins (carbonylation or nitrosylation), lipids (peroxidation) and DNA (adducts and breaks) that accumulate overtime and contribute to aging and aging-associated degenerative diseases.[6] Thus, oxidative stress is currently implicated in the etiology of a wide variety of conditions throughout the body (Figure 1.1). Presently, the exact role of each oxidant in these altered redox processes and the concentrations required to elicit protective or damaging effects are unclear.

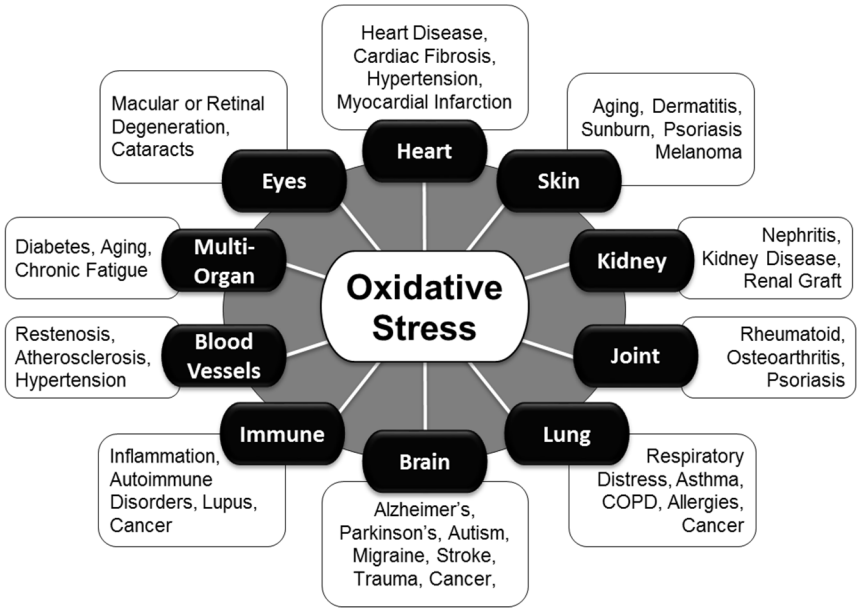

Figure 1.1. Oxidative stress is implicated in a wide variety of human diseases.[7]

B. Reactive oxygen and nitrogen species

Physiologically relevant ROS and RNS include superoxide (O_2^-), singlet oxygen ($^1O_2$), hydrogen peroxide (H_2O_2), hypochlorite (OCl^-), hydroxyl radical (OH•), alkoxyl radical (RO•), alkyl peroxyl radical (ROO•), nitric oxide (NO), peroxynitrite ($ONOO^-$), and nitrogen dioxide (NO_2•). Although the terms ROS and RNS are used to refer to the collective group of oxygen or nitrogen species, each oxidant is generated by different mechanisms and has a unique reactivity profile. The species are produced in response to similar physiological stimuli, react with each other, and have shared biological targets. Detection systems exploit the distinctive characteristics of each oxidant, attempting to respond specifically to only one species. This is a complicated process as multiple oxidants are produced at the same time, and the species interact with each other, antioxidants, and other biomolecules (Figure 1.2).

ROS and RNS are divided into one electron (radical) and two electron (non-radical) oxidants, and within each category there is a range of reactivity and oxidizing strength (Table 1.1). The standard reduction potential ($E°'$) indicates the relative strength of the oxidant, but cannot alone describe reactivity, as kinetic considerations are also a dominant factor.[3] The best example is H_2O_2 that exhibits a moderately low reactivity and slow reaction rates (with GSH) due to the high activation energy required, despite its high reduction potential. The remaining portion of this section will discuss the formation, reactivity, biological implications, and interactions between members of the ROS and RNS families.

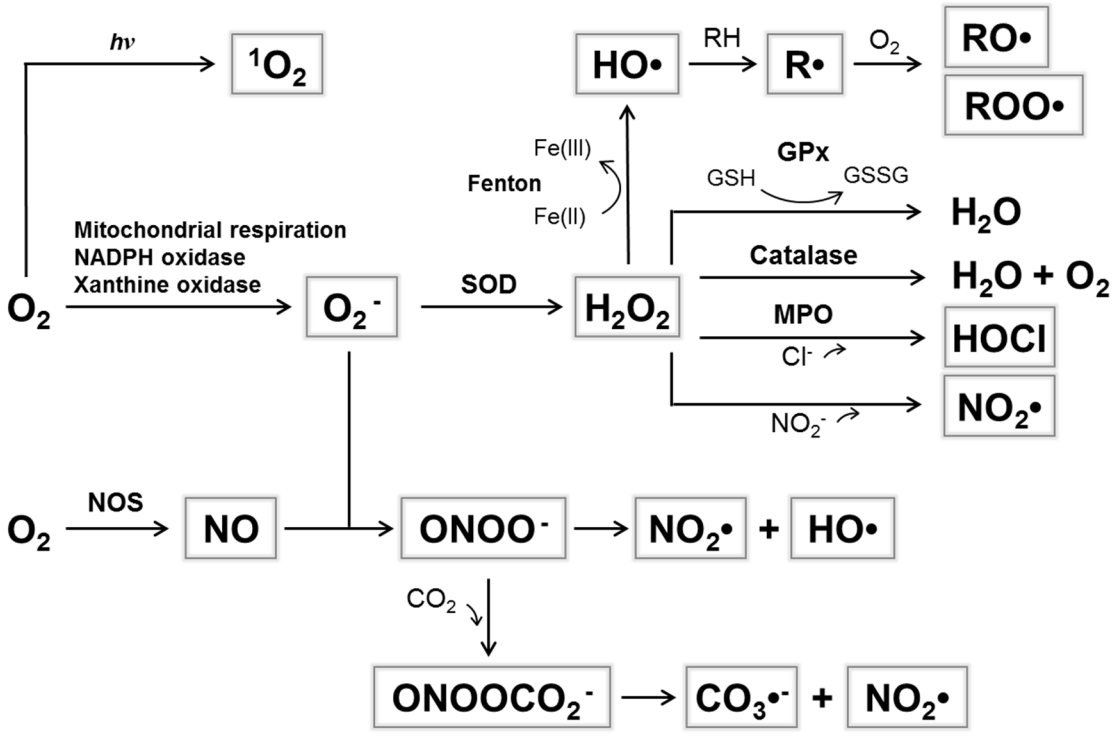

Figure 1.2. Formation, degradation, and interactions between physiologically relevant ROS and RNS. SOD, superoxide dismutase; GPx, glutathione peroxidase; MPO, myeloperoxidase; NOS, nitric oxide synthase.

Table 1.1. Reactivity of ROS and RNS.[a]

		Half life[b]	Estimated *in vivo* concentration[c]	Rate Constant (M^{-1} s^{-1}) with GSH[d]	Reduction Potential (V)[e]	pK_a[g]
One electron oxidants, radicals						
Hydroxyl radical	HO•	1 ns	fM range	1.6×10^{10}	2.31 (HO•, H^+/H_2O)	-
Carbonate radical	$CO_3^{\bullet-}$			2.3×10^{10}	1.78 ($CO_3^{\bullet-}$, H^+/HCO_3) [e]	< 0
Alkoxyl radical	RO•			5.3×10^6	1.60 (RO•, H^+/ROH)	-
Nitrogen dioxide	NO_2•	10 – 100 μs		~2×10^7	0.6 (NO_2/NO_2^-) [f]	-
Superoxide	O_2^-	~1 μs	0.1 nM	2×10^2	0.94 (O_2^-, $2H^+/H_2O_2$) -0.16 (O_2/O_2^-)	4.8
Alkyl peroxyl	ROO•			1.1×10^3	0.77-1.44 (ROO•, H^+/ROOH)	-
Nitric oxide	NO	0.05 – 5 s	< 1 μM	8.0×10^{-2}	-0.80 (NO/NO^-) -0.1 ($2NO/ONNO^-$) [f]	-
Two electron oxidants, non-radicals						
Hypochlorite	OCl^-	< 400 μs	< 150 μM	3×10^7	1.48 (HOCl, H^+/Cl^-, H_2O)	7.5
Peroxynitrite	$ONOO^-$	~ 10 ms	~ 1 nM	1.4 × 10^3	0.6 (NO_2/NO_2^-) [f]	6.8
Nitroxyl	HNO				0.6 (HNO, H^+/H_2NO) [f] -0.7 (NHO/HNO^-) [f]	11.5
Hydrogen peroxide	H_2O_2	~ 10 μs	0.1 μM	0.87	1.1 (HOO•, H^+/H_2O_2)	11.6
Singlet oxygen	$^1O_2$	~ 200 ns		9.4×10^8	0.65 ($^1O_2/O_2^-$)	-

[a] Missing entries reflect currently unknown values. [b] Ref. HO•,[6] NO_2•,[8] O_2^-,[6] NO,[5, 9] OCl^-,[10] $ONOO^-$,[11] H_2O_2,[6] $^1O_2$.[12-13]
[c] Ref. HO•,[6] O_2^-,[6] NO,[8] OCl^- (upper level),[14] $ONOO^-$ varies with O_2 concentration, [5, 11] H_2O_2 ranges from 0.001 – 0.7 μM. [6, 15]
[d] Ref. HO•,[16] $CO_3^{\bullet-}$,[17] RO•,[17] NO_2•,[8] O_2^-,[18] ROO•,[16] NO,[19] OCl^-,[3] $ONOO^-$,[11] H_2O_2,[3] $^1O_2$.[16]
[e] Standard reduction potentials ($E°'$) are relative to the SHE electrode and at pH 7. Ref. HO•,[3] $CO_3^{\bullet-}$,[3, 20-21] RO•,[3] NO_2•,[3] O_2^-,[3, 22] ROO•,[3] NO,[3, 22] OCl^-,[23] HNO,[24] H_2O_2,[25] $^1O_2$.[25] [f] Theoretical predictions, ± 0.3 V.[26]
[g] Ref. $CO_3^{\bullet-}$,[20-21] O_2^-,[5] OCl^-,[27] $ONOO^-$,[23] HNO,[5] H_2O_2.[23]

Superoxide is considered the primary ROS, as its reaction with other molecules generates secondary ROS and RNS. The process of oxidative phosphorylation in the electron transport chain of mitochondrial respiration converts from 0.5 - 3 % of molecular oxygen (O_2) to O_2^-.[5-6] Additionally O_2^- is formed by enzymes involved in the immune response, such as NADPH oxidases, and xanthine oxidases that catabolize purine bases.[3, 5] With a pK_a of 4.8, O_2^- exists primarily in the deprotonated form at physiological pH.[5] Few biomolecules react directly with O_2^- despite its ability to act as either an oxidant or reductant; however, it commonly interacts with other radical species to form two electron, non-radical oxidants.[3] The low reactivity of O_2^- is offset by its near diffusion-controlled reaction with NO (k = 7.0 x 10^9 M^{-1} s^{-1}) to generate the oxidatively active peroxynitrite ($ONOO^-$)[1, 5] and its depletion by superoxide dismutase (SOD) that forms the slightly more reactive H_2O_2 as a by-product. The high enzymatic efficiency of SOD (k = ~1 x 10^9 M^{-1} s^{-1}) results in a low intracellular biological concentration of O_2^- on the order of 10^{-10} M.[6, 28]

The primary source of biological H_2O_2 is from the antioxidant enzyme SOD, but it is also formed in peroxisomes. The high activation energy of this strong two electron oxidant, results in few direct reactions with biomolecules. Further, the high pK_a of 11.6 allows only 1 in 10,000 molecules of H_2O_2 to exist in the more nucleophilic, deprotonated state (HOO^-) at physiological pH.[23] Its low reactivity and membrane permeability complement its ability to modulate energy metabolism, stress, and growth signaling pathways. In particular, H_2O_2 oxidation of cysteine residues can reversibly modify proteins, including phosphatases involved in the attenuation of growth-factor signaling cascades.[4, 6] Antioxidant enzymes including catalases and peroxidases modulate the biological concentration of H_2O_2 using heme, thiolate, or seleocystine containing active sites that lower the activation energy, allowing them to efficiently scavenge H_2O_2 with reaction rates of 10^7 M^{-1} s^{-1}.[29] Peroxidases, such as glutathione peroxidases (GPx), reduce H_2O_2 to H_2O using glutathione as the oxidizing agent (GHS → GSSH), while catalases convert H_2O_2 into O_2 and H_2O. The resulting intracellular concentration of H_2O_2 can fluctuate from a low steady state of 0.001 μM to up to 0.7 μM during periods of severe oxidative stress,[6, 15] and the extracellular concentration can be increased by an order of magnitude. The cellular effects of H_2O_2 vary with its concentration; at the low

micromolar level it is correlated with cell proliferation, while above 0.5 μM it arrests cell growth and induces apoptosis.[6] The main detrimental biological effects of H_2O_2 ensue from the more reactive downstream products (OCl^- and HO•).

Hypochlorite (OCl^-) is produced from H_2O_2 and chloride anion (Cl^-) by myeloperoxidase (MPO) enzymes in neutrophils to defend against pathogens.[23] This species is involved in the inflammatory response and the associated chronic conditions. It is a highly reactive two electron oxidant ($E°'$ = 1.48 V) that reacts rapidly (k = 3.0 x 10^7 M^{-1} s^{-1}) with thiols, such as GSH, in a non-radical mechanism (Table 1.1).[3-4] The electrophilic character of OCl^- makes is susceptible to nucleophilic attack by cysteine thiols, generating oxidized sulfenic acid intermediates that yield mixed disulfides and other downstream products.[4] Additionally, OCl^- can react with tyrosine protein residues forming chlorotyrosines that impair protein function and are associated with the pathology of atherosclerosis and cystic fiborosis.[4] Cognate species include chloramines (RNHCl), generated from OCl^- and amines, and the bromine analogs hypobromous acid and bromamines.

The interaction of H_2O_2 with reduced metals such as Fe^{2+} promotes the formation of hydroxyl radical (HO•) in a process commonly called Fenton chemistry (*vide infra*).[30-31] With a lifetime in the nanosecond range and a reduction potential of 2.13 V, HO• is the most reactive member of the ROS family.[3] It reacts close to its site of generation with a wide variety of biomolecules. However, its primary pathological consequences result from its ability to damage both the DNA bases and the deoxyribose backbone ultimately causing permanent alterations in the genetic material of the cell.[1, 5] The most extensively studied hydroxylation product is 8-hydroxyguanine (8-OH-G), a biomarker of oxidative stress (Figure 1.3). DNA damage of this type induces further mutagenesis and has an established role in the etiology of breast cancer.[28]

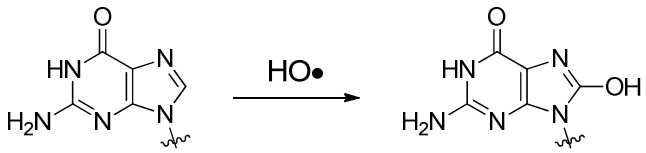

Figure 1.3. Hydroxylation of the DNA base quanine by HO• forms 8-hydroxyguanine.

Additional radical species are formed as a consequence of the high reactivity of HO•. Carbon-centered radicals (R•) are generated upon H-atom abstraction by HO• from polyunsaturated fatty acids, and further reaction with O_2 yields alkoxyl (RO•) and peroxyl (ROO•) radicals.[5, 28] Additionally, both of these species can be generated through the interaction of a lipid hydroperoxide (ROOH) with Fe^{2+} or Fe^{3+}, respectively. The ultimate downstream consequences are lipid oxidation and cyclization reactions that can generate reactive aldehydes, such as malondialdehyde, through endoperoxide intermediates.[5, 28] Malondialdehyde, a mutagen, reacts with nucleophilic amines on DNA to form adducts that lead to mutations or permanent DNA lesions if not repaired.

RNS are a family of nitrogen-containing oxidants derived from nitric oxide (NO). *In vivo*, NO is produced by Fe-containing nitric oxide synthase (NOS) enzymes that metabolize arginine to citrulline using NADPH as a reducing agent. Three primary isoforms mediate NO production: neuronal (nNOS) and endothelial (eNOS) are constitutively active and produce nanomolar levels of NO for regulatory functions, while the inducible (iNOS) isoform in macrophages generates micromolar NO during inflammatory responses.[1] NO is a surprisingly poor oxidant ($E°'$ = -0.80 V) for a radical species with half-life of a few seconds in an aqueous environment.[5] These features, coupled with its ability to diffuse through lipid membranes, make it an ideal intracellular messenger involved in neuronal and systemic signal transmission. NO initiates signaling cascades that involve the prominent second messenger cyclic guanosine monophosphate (cGMP) that modulates activity of ion channels, phosphodiesterases, and protein kinases. Physiological consequences of NO signaling are quite diverse and involve neurotransmission, blood pressure regulation, and immune system modulation.

The deleterious effects of NO are related to its diffusion limited reaction with O_2^- that generates peroxynitrite ($ONOO^-$). During oxidative bursts, immune cells facilitate the formation of $ONOO^-$ to fight pathogens by simultaneously generating both NO and O_2^-.[5] At physiological pH, $ONOO^-$ is mostly protonated (pK = 6.8),[1, 23] and it reacts slower, but more selectively than HO•. Its complex chemistry includes nitration of biomolecules that can fragment DNA, oxidize lipids, and damage proteins. The primary fates of $ONOO^-$ are isomerization to nitrite (NO_3^-) and reaction with carbon dioxide (CO_2) that produces nitrosoperoxycarbonate ($ONOOCO_2^-$). Subsequent decomposition of this

species generates mainly NO_3^- and CO_2 along with 35 % carbonate radical ($CO_3^{\bullet-}$) and nitrogen dioxide ($NO_2\bullet$) (Figure 1.2). The radicals generated in the latter reaction facilitate most of the biological damage connected with $ONOO^-$. Additional reactive radicals are produced during the homolysis of ONOOH to $NO_2\bullet$ and HO•, but this reaction accounts for only *ca.* 5 % of biological reactivity.[1] Finally, the antioxidant GSH is an important sink for $ONOO^-$, reacting with a rate constant near 600 M^{-1} s^{-1}.

Lastly, the interactions between ROS or RNS and redox active metals are of biological importance. Fe (and Cu) metal centers can redox cycle (*i.e.*, $Fe^{3+} \leftrightarrow Fe^{2+}$) and facilitate electron transfers under biological conditions. The Fenton reaction involves Fe^{2+} (or Cu^+) and H_2O_2 and results in the formation of HO•:[31]

$$Fe^{2+} + H_2O_2 + H^+ \rightarrow Fe^{3+} + H_2O + HO\bullet \quad (1)$$

Reduced Fe^{2+} is regenerated in the following reaction:

$$Fe^{3+} + \frac{1}{2}H_2O_2 \rightarrow Fe^{2+} + \frac{1}{2}O_2 + H^+ \quad (2)$$

The combination of the above two reactions, where Fe^{2+} is the catalyst describes the conversion of hydrogen peroxide to hydroxyl radical:

$$\frac{3}{2}H_2O_2 \rightarrow H_2O + \frac{1}{2}O_2 + HO\bullet \quad (3)$$

Fenton chemistry is cited as the main source of HO• production *in vivo*, but the physiological conditions and iron homeostatic mechanisms involved are not well understood.[5, 28, 30] The sequestration of Fe by metal binding proteins and small molecule ligands creates a negligible concentration of free Fe and a pool of labile Fe atoms estimated at 50-100 μM.[28] It is important to note that even Fe^{2+} atoms chelated by biological ligands (proteins, chaperones, transporters) participate in the above redox reactions. In fact, chelated Fe^{2+} (Fe^{2+}-EDTA) can be even more reactive than the free Fe^{2+} ion. Thus, this chemistry represents the primary source of highly reactive radical species.

The cellular redox state is a multifaceted function of ROS production and the metabolism of redox active metals (primarily Fe^{2+} and Cu^+) that is synchronized through interactions between the species. Regulation of cellular iron homeostasis by NO and $ONOO^-$ that modulate the binding affinity of iron-regulatory proteins to DNA response elements provides evidence of the complex interplay.[1] Another connection between

ROS and Fe homeostasis is the O_2^- mediated release of Fe from protein Fe-S clusters, which increases labile Fe that can produce ROS or assists in the carbonylation of amine containing amino acid residues (lysine, arginine, proline, and histidine).[4] As a result, ROS, RNS, and metal dyshomeostasis are dual contributors to the development of oxidative stress and related health conditions.

Clearly, the production, function, and decomposition of ROS and RNS are interrelated (Figure 1.2). The complexity of biological oxidants and their interactions make it challenging to determine which species is responsible for a particular process. To fully understand the biological impact of ROS, the identity of each particular species produced under defined conditions must be linked to the associated physiological processes. Interrogating the role of each individual ROS relies on the development of molecular probes capable of selectively detecting each ROS. Below, is a discussion of the design considerations of probes for ROS and RNS that harness the unique selectivity, kinetic, and localization profiles of each species to unravel the complex redox processes in biological systems.

II. Design Considerations for Responsive Imaging Agents

Ultimately, the goal is to design imaging agents that can be routinely used in biomedical research. As such, several strict requirements must be fulfilled by probes in order to generate reliable results regarding the concentration of *in vivo* analytes. Probes must be water soluble, exhibit low toxicity, function under biological conditions, and permeate membranes for the detection of intracellular species.[32-33] Physical considerations such as thermodynamic and kinetic stability in addition to parameters that determine sensitivity of detection must be also be optimized. Probes for biological analytes thus require careful design and testing in order to accurately report on an analyte *in vivo* for biomedical research or diagnostic purposes.

A. Physical considerations

With respect to lanthanide-based imaging agents, the toxicity is primarily a function of the metal-ligand complex stability, as free lanthanide ions are responsible for adverse side effects and cell death. The field of gadolinium-based contrast agents has illustrated the direct correlation between toxicity with kinetic lability and thermodynamic stability.[34] Kinetically inert complexes, including macrocyclic derivatives of Ln-DOTA and Ln-DOTAm (Figure 1.4), are advantageous as transmetallation with biological metals does not readily occur at physiological temperature in the time-frame of days.[34] In comparison, linear ligands such as Ln-DTPA or Ln-EDTA (Figure 1.4) are kinetically labile with the ability to release the metal, often within minutes. As such, complexes based on linear ligand frameworks pose a greater risk of being toxic if they are not sufficiently stable.

The stability of a lanthanide complex is governed primarily by the ligand denticity and the hardness of the donor atoms. For a same donor type and ligand architecture, the smaller the denticity, the less stable the complex. The linear octadentate ligand DTPA forms sufficiently stable complexes with lanthanides for *in vivo* applications (Log $K_{Gd\text{-}DTPA}$ = 22) whereas the smaller, heptadentate ligand EDTA does not (Log $K_{Gd\text{-}EDTA}$ = 17).[35] Similarly, the octadentate macrocyclic ligand DOTA (Log $K_{Gd\text{-}DOTA}$ = 24) yields substantially more stable – and inert – complexes than the heptadentate DO3A (Log $K_{Gd\text{-}DO3A}$ = 21), which is in turn more stable than the hexadentate DO2A (Log $K_{Gd\text{-}DO2A}$ = 13).[34, 36-37] Next, the hardness of the donor atom should be considered. Lanthanides favor harder ligands such as carboxylates over amides; therefore, they form more stable complexes with the DTPA ligand compared to the bis-methylamide derivative, DTPA-BMA (Log $K_{Gd\text{-}DTPA\text{-}BMA}$ = 17). [36] It is important to note that linear chelates (DTPA and EDTA) are also more susceptible to enzymatic degradation than macrocylic polyaminocarboxylate ligands.[38] In terms of design, lanthanide-based probes featuring a macrocylic polyaminocarboxylate core are preferred over less thermodynamically stable linear chelates.

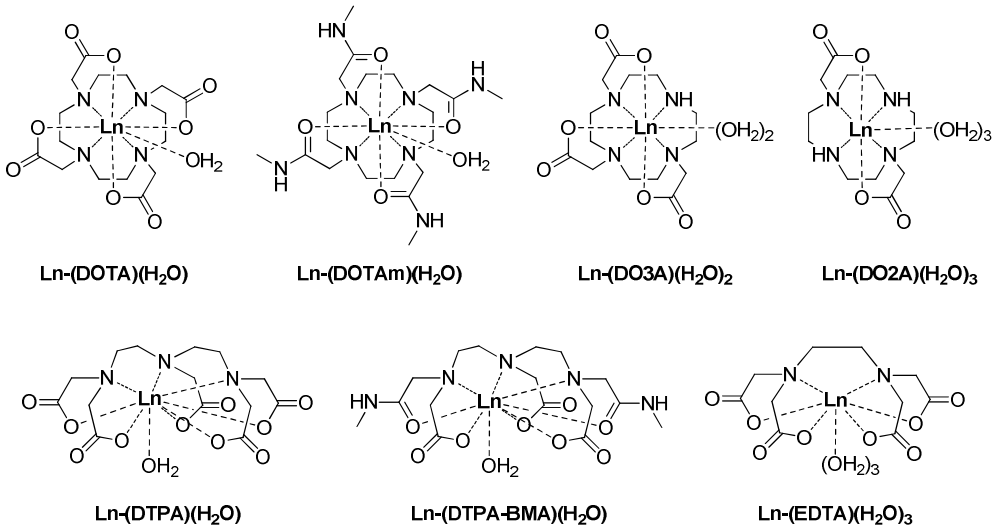

Figure 1.4. Chemical structures of lanthanide complexes of common polyaminocarboxylate ligands.

Another consideration in the design of luminescent probes is the photophysical properties of the imaging agent that facilitate a change in signal in the presence of the analyte. It is important to remember that responsive probes must be very reactive towards their analyte. For luminescent probes, the brightness, and thus sensitivity is related to its ability to absorb and emit light, and its mechanism of fluorescent response. The extinction co-efficient (ε) of a fluorescent or phosphorescent reporter measures how strongly they absorb light at a defined wavelength, and the quantum yield (ϕ) describes the efficiency of emitting the absorbed light. Sensitive luminescent reporters thus display large extinction coefficients (ε) and quantum yields (ϕ) in order to maximize signal intensities. Ideally, the excitation wavelength (λ_{ex}) and emission wavelength (λ_{em}) will be in the visible light or near infrared ranges to reduce background fluorescence and biological damage. A fluorescence response that increases emission intensity in the presence of the analyte is easier to detect than a decrease in signal. "Turn-on" probes are thus favored over a turn-off emission-quenching response.[32] Lastly, the photostability of the fluorophore must be considered to minimize photobleaching or destruction of the emitter by overexposure to light.

The physical properties of responsive magnetic resonance probes are also selected to maximize probe response in the presence of an analyte. Two main

mechanisms of detection are employed: alteration of relaxation rates or modulation of chemical shift. The magnetic properties of the nuclei detected (for example, ^{1}H, ^{19}F, or ^{13}C) including their spin state (*i.e.* $I = ½$), natural abundance, relative sensitivity, and gyromagnetic ratio (γ) influence the sensitivity of the probe at a particular magnetic field strength. Nuclear relaxation rates in an applied magnetic field and the chemical shift range of the resonance frequencies also impact probe design. Further, nuclear relaxation rates and chemical shift can be modulated by introducing a paramagnetic metal center into the probe structure.

B. Biological considerations

To use a probe in a biological system, several additional requirements must be met. Along with being water soluble, probes must exhibit high selectively for their target analytes over others present in biological systems, including those present at higher concentrations. Selectivity is achieved by harnessing the unique reactivity of the analyte or, in the case of metals, their coordinating ability. Generating a unique response to one particular ROS, in the presence of other related species, is a major challenge in developing probes to monitor oxidative stress.

Probe function and detection also requires responding to target analytes in a biological environment while in the presence of physiological ions and small molecules capable of interfering with signal turn-on mechanisms. For example, luminescence probes that rely on excited state energy transfer mechanisms can be quenched by reducing agents such as ascorbate, urate, and gluthathione.[39-40] Probe-protein interaction inside cells, as well as extracellularly with serum albumin are also reported to reduce luminescence intensity.[41] For MRI contrast agents it is equally important to consider the biological matrix. Human serum contains millimolar concentrations of anions such as bicarbonate (HCO_3^-, 24.5 mM), hydrogen phosphate (HPO_4^{2-}, 0.38 mM), and citrate (0.11 mM) along with acetate, lactate, oxalate, malonate, and acidic amino acids. Thus, depending on the mechanism of analyte detection, these anions could interfere with a probe's response by coordinating the lanthanide center. This interference has been observed, in particular, with responsive Gd-based contrast agents that rely on changes in the lanthanide coordination sphere.[42-46] Relating to the stability

of lanthanide complexes as discussed above, coordinating anions like phosphates can compete with ligand groups for lanthanide coordination and affect complex stability. Therefore, it is important to consider what alternative biological species could react with the probe, the relative reaction rates, and how products of these reactions can affect the response.[47] Evaluating probe function in complex biological media is thus a crucial step in the process of probe development

Biological imaging agents, ideally, will be reversible in nature and elicit a ratiometric response. Reversible sensors can monitor changes in analyte concentration over time and are less likely to disrupt homeostatic cellular mechanisms. Probes are ratiometric if they experience a change in one signal in response to an analyte while another signal remains unchanged. This type of probe is particularly valuable because the quantity of the analyte can be determined by the ratio of two different signal intensities, even if the exact concentration of the probe is unknown. As the biodistribution of probes is difficult to predict, this feature is a requirement for analyte quantitation.

A primary goal in imaging biological species is to determine the cellular location of analyte generation or accumulation. Thus, for detection in intracellular analytes, probes must be able to enter cells. Passage through cellular membranes can be achieved either *via* passive, diffusion-based mechanisms or by endocytotic uptake processes such as macropinocytosis, clathrin or caveolae dependent internalization.[48] Current research has correlated structural parameters, including lipophilicity, of metal-centered imaging agents to subcellular localization profiles.[48-57]

Within a cell, there are several regions relevant to ROS production: mitochondria, endoplasmic reticulum (ER), phagosomes, peroxisomes, and the plasma membranes (Figure 1.5).[4] Cellular respiration occurs in the mitochondria; in particular, the electron transport chain that reduces O_2 to H_2O and forms O_2^- in the process is located in the inner mitochondrial membrane. The ER is the location of protein folding and processing where the oxidative process of disulfide bond formation occurs. Oxidative metabolism within peroxisome organelles produces ROS like O_2^- and NO during the catabolism of long chain fatty acids or biosynthesis of phospholipids and plasminogen. Immunogenic phagosomes contain NADPH oxidases, of which the most studied is NOX2, that defend

against invading pathogens.[3] Microorganisms stimulate the production of O_2^- inside the phagosome that can be subsequently converted to H_2O_2 and then into OCl^- or other reactive oxidants. Lastly, NADPH oxidases in the plasma membrane are a relevant site of ROS production. Classically, these enzymes were thought to only be involved in the immune response, but since they are present among all cell types, they are now suspected to have a more general role.[4] As membrane bound enzymes, they are perfectly positioned to communicate with cell surface receptors through the transfer of electrons from NADPH to extracellular O_2 creating O_2^-, which is likely involved in signaling though H_2O_2 formed by SOD. The variety of cellular ROS generation sites dictates the need for probes that can be directed to a specific organelles or remain in the extracellular space to detect analytes in defined regions.

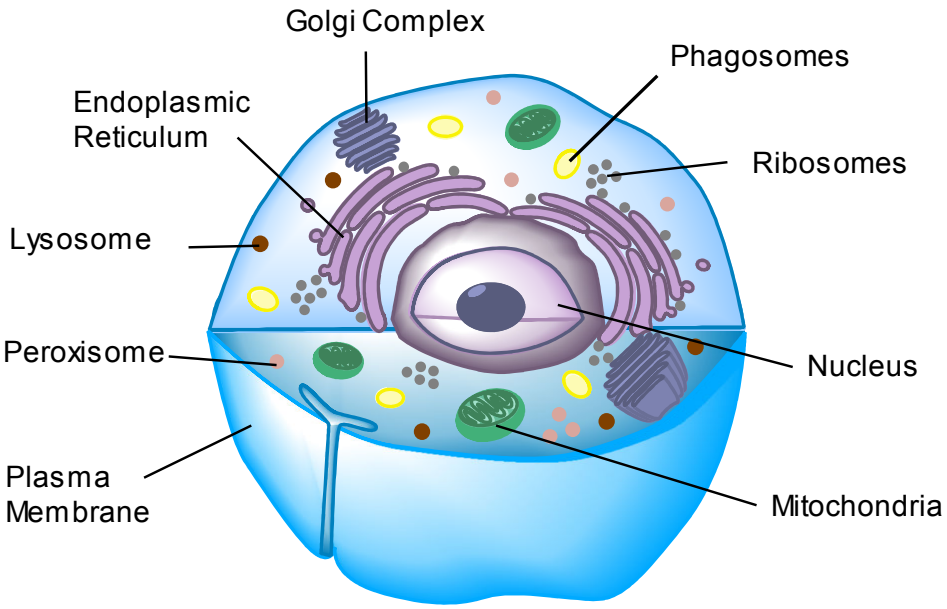

Figure 1.5. Structure and subcellular compartmentalization of eukaryotic cells.

C. Goals of biological imaging agents

Imaging agents that respond to ROS aim to meet the following goals, in order of increasing difficulty. First generation probes report on cellular redox state, and an excellent example of the progress towards this goal is illustrated by the non-selective oxidation of dihydrodichlorofluorescein ($DCFH_2$) to a fluorescent product. The next goal is development of imaging agents that respond to a specific oxidant, which mandates rigorous protocols to test selectivity. Ideally, probes will be reversible in nature and be capable of detecting fluxes in ROS concentrations related to the formation and destruction of a particular oxidant. Currently, there are limited examples of molecular probes that can reversibly monitor ROS production,[58-59] O_2^-,[60-61] OCl^-,[62-63] $ONOO^-$,[64] and NO.[65]

Another equally important aim is to design probes that identify the site of production or location of a specific oxidant. These probes must be localized or targeted to areas of ROS production and accumulation and demonstrate a selective response. Progress towards this goal includes mitochondrial targeted molecular probes for highly reactive ROS,[66] H_2O_2,[67] O_2^-,[68] and NO,[69] as well as a H_2O_2 probe that accumulates in lysosomes.[70]

Lastly, quantitative, or ratiometric, probes that can report on the exact concentration of an oxidant are desired. Such detection systems can differentiate the absence of probe from the absence of analyte circumventing inconsistencies in probe biodistribution throughout cells. An increasing number of ratiometric probes for individual ROS are being developed. To date, most ratiometric probes for HO• utilize nanostructures;[71-73] however, several examples of ratiometric molecular probes for HO• are discussed in the following section.

Probes that simultaneously fulfill all of these goals are highly sought after; however, the current focus of the field is on independently developing selective, reversible, localized, or quantitative probes. For ROS, a few example probes are emerging that simultaneously meet multiple of these objectives, which highlights the inherent challenges in designing selective and sensitive probes for use in biological systems.

III. IMAGING TECHNIQUES

Luminescence spectroscopy (or microscopy) and magnetic resonance imaging (MRI) are two common molecular imaging techniques. The advantages and disadvantages of these methods in terms of resolution, sensitivity, and tissue penetration are complementary. For example, luminescence microscopy is ideal for imaging cellular events in culture or tissue slices and promoting advances in fundamental biomedical research. MRI, on the other hand, is used for clinical diagnostic purposes on entire organisms (*i.e*. the human body). Understanding the complex roles of biological analytes, such as ROS, first requires investigation on the cellular level that study the amount, location, causes, and consequences of analyte production. Interrogation of the roles of a biomarker in cellular systems precedes detection in full organisms. Ultimately, MRI contrast agents monitoring the analyte *in vivo* will provide diagnostic insights to guide treatment of conditions associated with oxidative stress.

A. Luminescence spectroscopy

1. Advantages and limitations

For cellular imaging, luminescence microscopy is widely used due to its high resolution and sensitivity. Luminescence probes compatible with confocal fluorescence microscopy can achieve nanometer spatial resolution, thus distinguishing the subcellular location (cytosol, organelles, or nucleus). Detection limits for luminescent complexes are dependent on the photophysical properties, mainly the extinction coefficient (ε) and quantum yield (ϕ), of the dye, but they typically fall in the nanomolar range.[74] Certain ROS present at sub-nanomolar concentrations require the accumulation of signal intensity of irreversible probes for detection. As this technique is dependent on the absorption and emission of light, its use is restricted to cell or tissue slices with maximum imaging depths < 0.1 mm.[75]

A notable advantage of luminescence spectroscopy is the ability to image multiple analytes simultaneously. The concurrent use of two probes, for different analytes, is possible when the emission wavelengths are non-overlapping allowing the signal intensity of each to be independently measured. With regards to ROS, multiplex imaging

is a valuable feature because, in theory, this technique can differentiate the production and downstream effects of closely related ROS. Luminescence probes for ROS and RNS have recently been reviewed,[47, 76] and the progress in the field of HO• detection is discussed below.

2. Current luminescent probes for hydroxyl radical

The role of HO• in disease states has prompted the development of HO• probes for cellular imaging and biomedical research applications. Reported luminescent probes for HO• can be divided into three categories: i) those that respond to highly reactive oxygen species, but lack selectively for HO•; ii) probes that respond to HO• *via* an indirect detection method; and iii) aromatic probes that become fluorescent upon hydroxylation. The successes of these probes illustrate that oxidative stress, and in particular HO•, can be monitored in cellular systems. However, future probes must overcome low selectivity of current probes for HO•, especially in the presence of biologically relevant concentrations of competing oxidants. Biocompatibility must also be improved for widespread use.

a. Probes for hydroxyl radical and other highly reactive oxygen species

Probes that are not selective for one oxidant, but respond to multiple members of the ROS family are only useful as general indicators of oxidative stress. Typically, a response is observed in the presence of the highly reactive oxygen species (hROS) such as O_2^-, OCl^-, and HO•. In 2009, Kundu *et. al*. reported a class of hydrocyanine dyes, including Hydro-Cy3, that belong to this category (Figure 1.6).[77] These probes are generated by $NaBH_4$-mediated reduction of members of the cyanine dye family and include probes with range of excitation and emission wavelengths extending into the near infrared (NIR) region. Oxidation by O_2^- or HO• linearly increases fluorescence intensity and converts the probe from a membrane permeable form to a cationic species that accumulates inside cells. Hydro-Cy3 can monitor ROS production in rat aortic muscle during angiotensin II mediated signaling (a pathway implicated in atherosclerosis and hypertension) and in explanted mouse aortas. Thus, this research demonstrates the capability of fluorescent probes to monitor ROS production in cells and tissues.

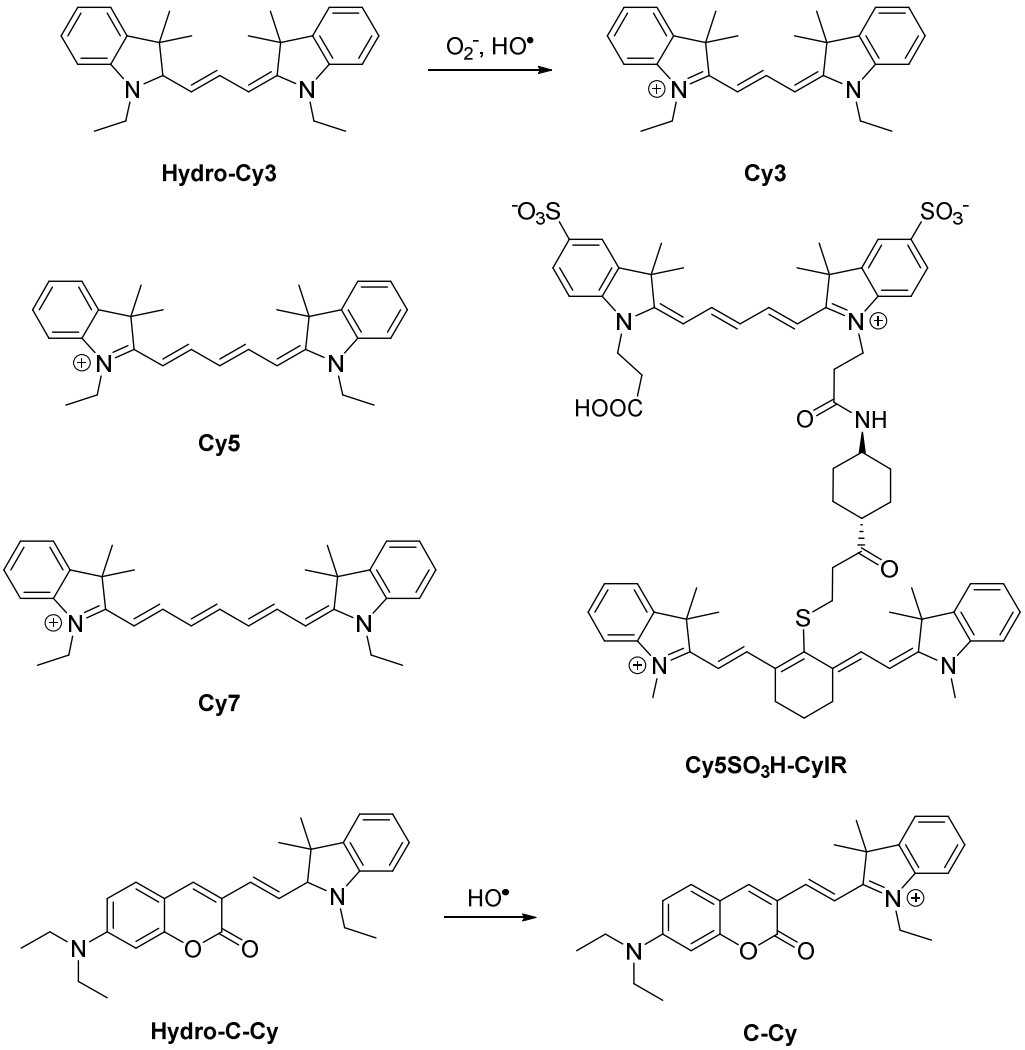

Figure 1.6. Chemical structures of non-selective fluorescent ROS probes based on cyanine dyes.[77-79]

Concurrently, the Nagano lab developed a related system for the detection of hROS based on cyanine dyes.[78] These fluorophores absorb and emit light in the NIR and have lower phototoxicity, reduced background fluorescence, and better tissue penetration than dyes that emit in the visible range. Preliminary work identified that cyanine dyes with lower oxidation potentials were more susceptible to oxidation. For example, Cy7 is responsive to HO•, $ONOO^-$, OCl^-, O_2^-, and high concentrations of H_2O_2, while Cy5, with a higher oxidation potential is less sensitive to these ROS (Figure 1.6). Further, the electron-withdrawing sulfonate groups in $Cy5SO_3H$ increased the oxidation

potential and suppressed reactivity with ROS. This knowledge was then used to develop a novel NIR emitting probe for ROS utilizing two link cyanine dyes ($Cy5SO_3H$-CyIR, Figure 1.6). A relatively non-responsive dye ($Cy5SO_3H$) serves as the fluorophore, and an oxidant sensitive dye (CyIR) modulates the response by quenching fluorescence in the absence of ROS. The preferential oxidation of CyIR by ROS relieves quenching and restores the fluorescence of $Cy5SO_3H$. Indeed, $Cy5SO_3H$-CyIR experienced a near 10-fold emission enhancement in upon treatment with HO•, $ONOO^-$, and OCl^-, but also responded to O_2^- (6-fold) and $^1O_2$ (4-fold).[78] Lastly, this probe was applied to ROS imaging in HL60 cells expressing membrane-bound and cytoplasmic forms of NADPH oxidase, neutrophils, and a mouse model of peritonitis. An increase in fluorescence intensity was observed in cells stimulated to release O_2^- followed by a decrease upon treatment with SOD. Thus, $Cy5SO_3H$-CyIR can detect physiologically important ROS in biological systems with an emission in NIR region, but it lacks selectivity for one oxidant.

Using a similar strategy in 2010, Yuan *et. al.* designed a hybrid coumarin-cyanine probe, Hydro-C-Cy, for the intracellular detection of HO• (Figure 1.6).[79] The reduced form Hydro-C-Cy emits at 495 nm, while the oxidized system, C-Cy, is fully conjugated and emits in the NIR. A ratiometric response is observed; the fluorescence intensity ratio (I_{651}/I_{495}) increases 210-fold in the presence of HO•. Such a large ratiometric response is uncommon; fluorescence enhancements of 10 to 20-fold are suitable. The observed pseudo-first order rate constant for HO• mediated oxidation was 5.1×10^{-4} s^{-1}.[79] However, it is important to note that the rate constants for HO• and aromatic systems is diffusion limited (10^9 M^{-1} s^{-1}).[80-81] Surprisingly, this probe reports high selectivity for HO• over other ROS including O_2, which contradicts the work of Kundu (discussed above) on a related cyanine-based system.[77] Despite its poor water solubility (analyses were performed in 1:1 mixtures of water and acetonitrile), this probe was applied to cellular imaging of HO• in HeLa cells stimulated to produce ROS.

Another NIR emitting probe developed by the Nagano group in 2012 utilizes the redox properties of a bis-dimethyl tellurium-containing rhodamine dye (TeR) to respond to ROS in a semi-reversible manner (Figure 1.7).[58] Oxidation of TeR to TeOR is accompanied by a large increase in fluorescence intensity (*ca.* 200-fold) and red shifted absorbance maximum (600 nm to 667 nm). This probe responds to HO•, $ONOO^-$, and

OCl^-, and a negligible increase in fluorescence is observed after treatment with O_2^-, H_2O_2, and NO.[58] The primary advantage of this probe is its reversibility; excess gluthathione (GSH) reduced the oxidized probe back to the original form. An application to cellular imaging confirmed the reversible nature. HL60 cells incubated with TeR and H_2O_2, experienced an increase in fluorescence intensity corresponding to the intracellular production of OCl^- by MPO enzymes followed by a decrease in intensity as the cellular redox environment was restored to the resting state. Note that within a cell, GSH is present at a relatively constant concentration and also competes with the probe for reaction with the ROS, limiting the overall response.

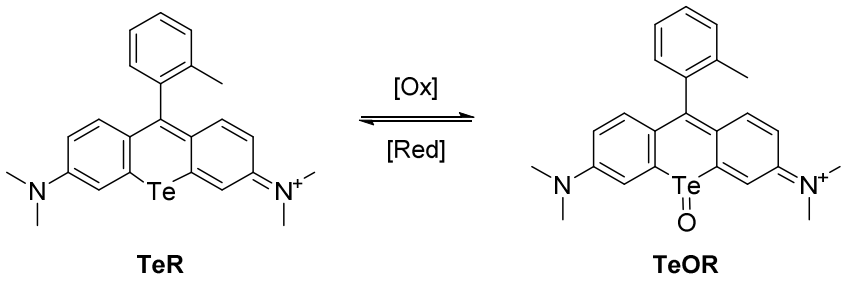

Figure 1.7. Chemical structure of a reversible fluorescent ROS probe featuring a redox active tellurium atom.[58]

An alternative strategy to detect hROS was developed by Cui *et. al.* in 2011. They modulated Tb-luminescence with an ROS responsive sensitizing antenna. The probe, Tb-BMPTA, contains a novel chelate that doubles as a sensitizer and a *para*-aminophenoxy group that quenches Tb-emission (Figure 1.8).[82] ROS, including HO• and OCl^-, cleave the ether linkage causing a 10 or 5-fold increase in luminescence intensity, respectively. A year later, the same group reported a second generation, ratiometric probe comprised of a 1:1 mixture of Tb and Eu-AMTTA (Figure 1.8).[83] Each complex responds to HO• and OCl^-, but to a different extent allowing the ratio of Tb to Eu-emission (I_{540}/I_{610}) to ratiometrically report on the ROS concentration. In the presence of micromolar concentrations of HO•, the fluorescence intensity ratio (I_{540}/I_{610}) increases 7.8-fold.[83] Compared to other fluorescent ROS probes, this system has the advantages of long-lived luminescence emission and a large difference between the

excitation and emission wavelengths that avoid self-absorption issues. However, these probes respond to both HO• and OCl^-, and lack the selectivity needed for cell studies.

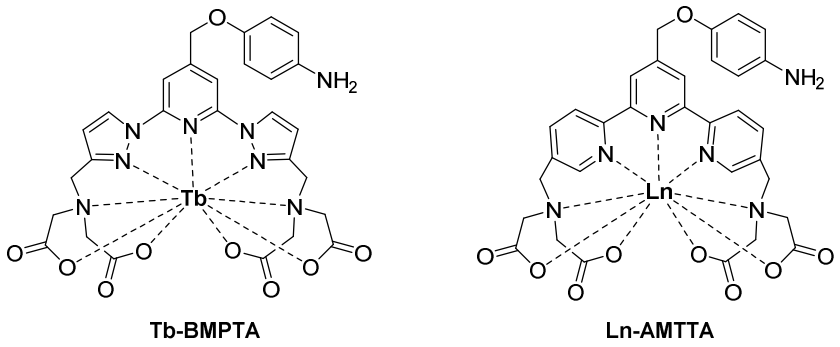

Figure 1.8. Chemical structures of luminescent probes for HO• and OCl^-.[82-83]

b. Indirect detection methods for hydroxyl radical

Probes in the next class do not report directly the on concentration of HO•, but respond to methyl radicals ($•CH_3$) formed form the reaction of HO• and DMSO. In the absence of HO•, a paramagnetic nitroxide radical TEMPO moiety linked to the fluorophore quenches emission and a turn-on response is generated upon the reaction with $•CH_3$ that forms a stable *O*-methoxy group (Figure 1.9). Thus, probes based on this mechanism have excellent selectivity for HO•, but require the presence of DMSO that is toxic to cells at high concentrations and influences membrane permeability of probes. The *in vivo* and *in vitro* toxicity of DMSO was recently evaluated by Galbao, *et. al*. Their findings indicate that cell viability is effected by low concentrations of DMSO (2-4% *v*/*v*), and in some cell lines apoptotic pathways are increased in the presence of as low as 0.1% DMSO.[84] Detection of radicals *via* spin trapping with electron spin resonance (ESR) has been applied to spin-labeled fluorophores[85-86] including anthracene[87] and naphthalene,[88-89] and the most recent progress in the field is discussed below.

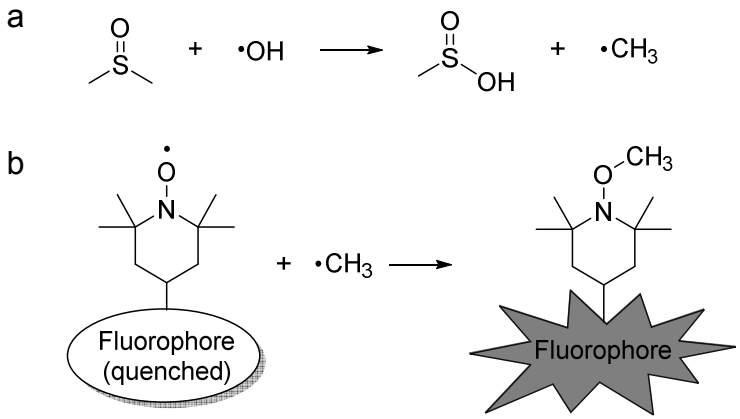

Figure 1.9. Indirect fluorescence detection of HO• by nitroxide-containing TEMPO probes. (a) Reaction of DMSO with HO• generates methyl radicals (•CH_3) that (b) are trapped by the nitroxide producing a fluorescent response.

In 2012, Yapici and coworkers applied the concept of nitroxide-linked probes to rhodamine dyes.[90] Click chemistry was employed in the synthesis of molecular probes TEMPO-R and $(TEMPO)_2$-R to generate rhodamine dyes conjugated to either one or two nitroxide moieties, respectively (Figure 1.10). For $(TEMPO)_2$-R, a 400-fold fluorescence increase was observed upon treatment with DMSO and HO• with a detection limit in the micromolar range.[90] As anticipated, a higher fluorescent response is achieved with the binitroxide containing $(TEMPO)_2$-R *versus* TEMPO-R. The analyses were performed at pH 4.0 to optimize HO• formation by Cu(I) mediated Fenton chemistry and to facilitate cleavage of the lactam ring that results in enhanced fluorescent properties. The lactam ring precursor is very weakly fluorescent and allows for a high signal-to-noise ratio in the presence of the analyte; however, this requires acidic reaction conditions outside the physiological pH range. A high selectivity (1000-fold) for HO• was observed with both probes when treated with approximately 20 μM of each oxidant. Thus, further selectivity studies that examine the response of the probe to biologically relevant concentrations of each species are needed. Cellular studies in human retinal pigment epithelial (ARPE-19) cells confirmed that phorbol myristate acetate (PMA) stimulated cells exhibit fluorescence enhancement compared to control cells. Additionally, counterstaining experiments in cancer cells (HepG2) detected reacted probe in the mitochondria.

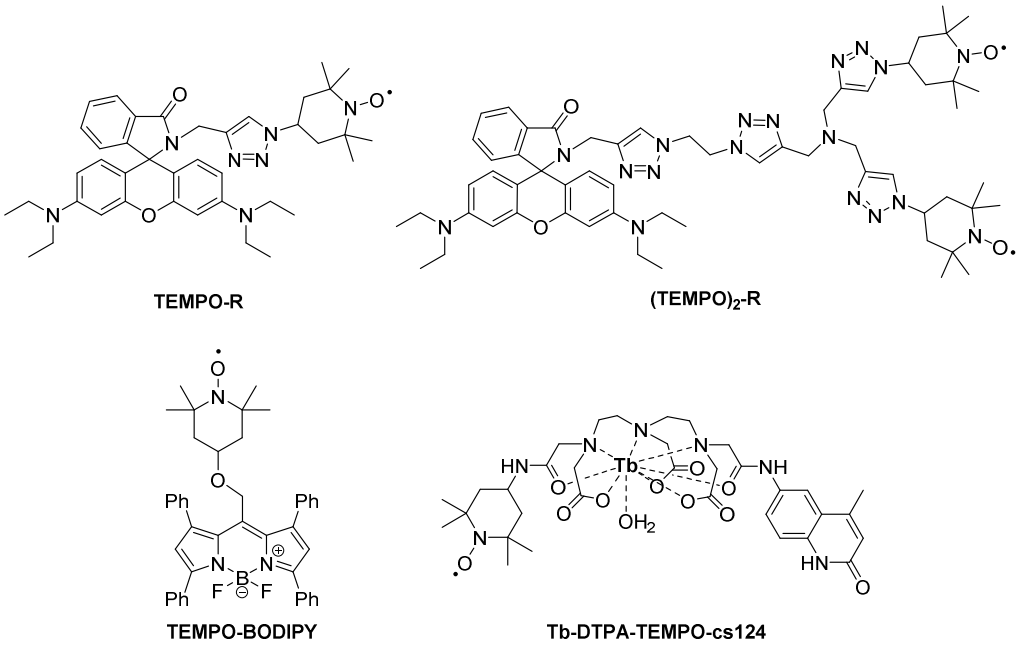

Figure 1.10. Chemical structures of luminescent probes that utilize a nitroxide moiety to indirectly monitor HO•.[90-91]

Earlier in 2010, a nitroxide-containing boron dipyrromethane (BODIPY) probe, TEMPO-BODIPY, was designed by Li *et. al.* (Figure 1.10).[91] TEMPO-BODIPY experiences an increase (*ca.* 10-fold) in fluorescence intensity at 600 nm upon treatment with HO• in the presence of DMSO. Sensitivity experiments determined an 18 pM detection limit of using 2.0 μM probe and 100 μM DMSO. Selectivity for HO• over biologically relevant ROS including O_2^-, OCl^- and $ONOO^-$ is observed. However, in these studies each oxidant was administered to the probe at the same concentration which is not representative of the relative concentrations of ROS in biological systems. Cell viability studies, performed in the absence of DMSO, with macrophages (RAW264.7) determined an ED_{50} of 69 μM, which is well above the probe concentration (1.0 μM) used in subsequent cellular applications.[91] Confocal microscopy studies verified that TEMPO-BODIPY fluorescence is increased in macrophages stimulated with PMA to increase ROS production compared to control cells. Note that all cellular studies were performed in the presence of 100 μM DMSO. Lastly, the fluorescence intensity of TEMPO-BODIPY was enhanced in human hepatoma cells compared to normal human liver cells supporting the role of ROS in tumor physiology.

A final example in the class is a luminescent complex, Tb-DTPA-TEMPO-cs124, whose chelate is substituted with a fluorophore and nitroxide moiety that modulates the Tb-centered emission (Figure 1.10).[92] The mechanism of probe response was thoroughly evaluated with both luminescence and electron paramagnetic resonance (EPR) spectroscopy. Reduction of the nitroxide with ascorbate revealed a direct correlation between the disappearance of the EPR signal and increase in luminescence intensity, thus confirming that the nitroxide quenches Tb-emission. Applications to ROS detection were performed with HO• generated *via* the photolysis of nitrate ions (NO_3^-). Tb-luminescence (546 nm) increased linearly with irradiation time using 2 μM Tb-DTPA-TEMPO-cs124, 1.0 M DMSO, and 0.02 – 0.5 M KNO_3 in 10 mM Tris buffer at pH 7.4. The estimated detection limit for this system is in the low nanomolar range. In addition to being the first example of a spin-labelled lanthanide complex, Tb-DTPA-TEMPO-cs124 has the advantages of water solubility and compatibility with time-delayed luminescence techniques.

c. Probes based on hydroxylation of aromatic substrates

The final class of HO• probes are aromatic substrates that become fluorescent upon hydroxylation. These probes often contain aromatic acid moieties and typically are highly selective for HO•. In the 1990s, coumarin-based probes, such as coumarin-3-carboxylic acid (3-CCA), were evaluated as HO• detectors in aqueous solutions due to the formation of the highly fluorescent 7-hydroxycourmain-3-carboxylic acid (7-hCCA) upon hydroxylation (Figure 1.11).[93] A detailed kinetic study by Manevich, *et. al*. in 1997 determined he rate of hydroxylation was diffusion limited (k = 5.0 x 10^9 M^{-1} s^{-1}), agreeing with published rate constants for aromatic hydroxylation.[80] The multiple chemically inequivalent hydroxylation sites on 3-CCA leads to the production of primarily 7-hCCA and four additional products, as determined by HPLC. The fluorescence properties of hydroxycoumarin are highly dependent on the site of hydroxylation. Thus, the authors validated their method for detection of HO• by demonstrating the similar linear decay rate of 3-CCA and linear increase of 7-hCCA, establishing that the fluorescence of response is proportional to the amount of HO• produced. They also demonstrated that HEPES, MOPS, and PIPES buffers scavenge HO• and interfere with probe response.[93]

Over the past decade, coumarin-based probes that exhibit a change in the excitation and emission profiles upon hydroxylation have been applied to variety of other biological applications. In particular, the succinimidyl ester derivative of 3-CCA was coupled to protein albumin,[15] histones,[94] oligonucleotides,[95] poly-arginine,[96] and phospholipids[97] to study the effects of HO• in the vicinity of biomolecules.

Similar to the coumarin probes discussed above, a ratiometric probe was recently published in 2014 in which hydroxylation of an aromatic dye alters the fluorescence properties. The hybrid naphthyridine-naphthalimide probe, NP-NI, capitalizes on the electronic modulation of both dyes at the 4- and 2-positions, respectively, by linking them together (Figure 1.11).[98] Upon hydroxylation, the fluorescence intensity of the NP chromaphore at 418 nm increases, and the response of the NI dye at 552 nm stays relatively constant. Thus, a liner ratiometric response (I_{418}/I_{552}) with respect to HO• concentration was observed with a detection limit of 700 nM. Characterization of the product points to hydroxylated naphthyridine that dissociates from a non-fluorescent naphthalimide. High selectivity for HO• was observed over ROS, but alkoxyl radicals (RO•) and nitric oxide (NO) were not included in the study. Cellular applications with PMA stimulated macrophages (RAW264.7) revealed that NP-NI can detect physiologically produced HO• and has a minimal effect on cell viability up to 20 μM. However, the main drawback of this probe is its poor water solubility.

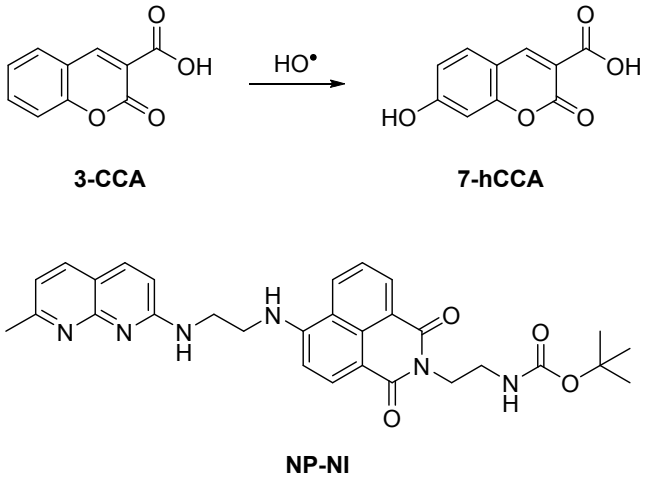

Figure 1.11. Chemical structures of aromatic HO• probes that exhibit changes in fluorescence upon hydroxylation.[93]

Structurally less complex aromatic acids, such as benzoic acid (BA), salicylic acid (SA), 4-hydroxybenzoic acid (4-hBA), and terephthalic acid (TPA) have also been used to selectively detect HO• (Figure 1.12).[99-103] This work was pioneered in the early 2000's and also has more recent applications. Hydroxylation of these probes produces fluorescent products such as 3,4-dihydroxybenzonic acid (3,4-dhBA) from 4-hBA and hydroxyterephthalic acid (hTPA) from TPA. For monitoring HO•, TPA is preferred over BA, SA, and 4-hBA because, as a result of the symmetrical structure, monohydroxylation yields one product.[102, 104] In addition, fluorescence increase upon hydroxylation of TPA is three times that of BA.[102] Regardless of the probe, a complex and time consuming HPLC-based detection method is utilized to quantitate hydroxylated products in both *in vitro* and *in vivo* samples. Thus, even though a 4 nM detection limit can be achieved with TPA,[100] these methods are hindered by destructive sample preparation procedures prior to HPLC analysis and inability to monitor HO• in real time.

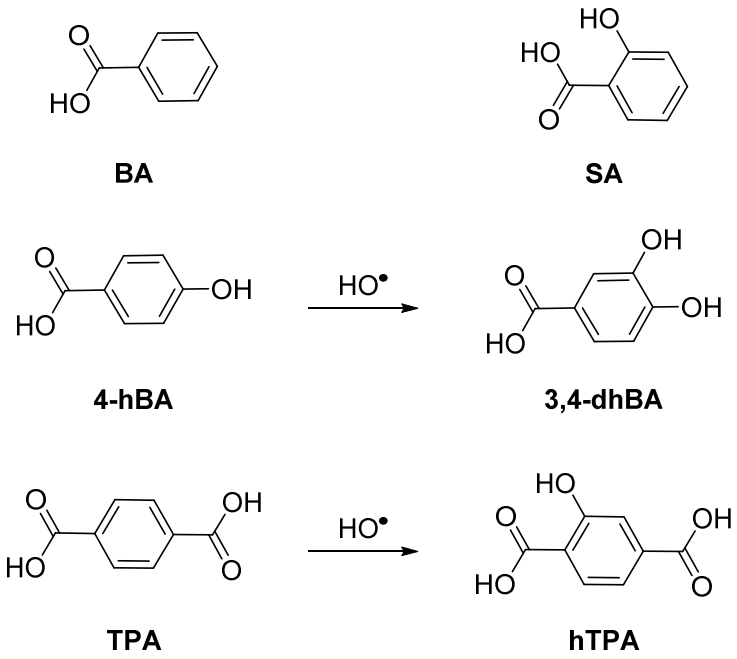

Figure 1.12. Chemical structures of aromatic acid-containing probes for the detection of HO•.

Despite their drawbacks, these probes have been widely used to monitor HO• production in complex biological systems. For example, Liu *et. al.* verified that *in vivo* microdialysis of 4-hBA can reliably detect HO• produced during cerebral ischemia and reperfusion in rats,[99] and Yan and coworkers used the same technique to measure radical production in fetal sheep brain with TPA.[105] Additional studies using TPA include monitoring HO• production by liver microsomal enzymes[106] and the photoreactions of melanin.[107] The more recent expansion of this technique to environmental systems, where TPA was used to monitor photochemical produced HO• in natural water systems,[103] highlights the selectivity and rapid kinetics of aromatic acid systems.

3. Summary of luminescent probes for hydroxyl radical

The probes discussed above are examples of a progressing field in ROS detection. However, there is room for improvement particularly in terms of the selectivity of probes for HO• over other hROS (O_2^- and OCl^-). For practical *in vitro* applications, probes must selectively respond to HO• while in the presence of a large excess of other ROS (H_2O_2 and NO) that have much longer cellular half-lives and exist at orders of magnitude higher concentrations. Experimentally, this means performing selectivity studies with biologically relevant concentrations of analytes. Faster reaction kinetics are also required to accumulate appreciable signal intensity and thus improve sensitivity to monitor the low physiological concentration of HO•. Ideally, next generation probes will respond selectively to HO• using a direct detection method and interrogate the sites of HO• production with a ratiometric response capable of quantification. Ratiometric and reversible probes to monitor HO• are also required to elucidate the roles of the oxidant in physiological processes and disease states.

B. Magnetic resonance spectroscopy and imaging

1. Advantages and limitations

MRI is a non-invasive, *in vivo* detection method that measures changes in chemical shift or relaxation rates of nuclei in a magnetic field. The primary advantage of magnetic resonance detection is the capability of generating three dimensional images of entire organisms. Therefore, this technique has wide clinical and diagnostic applications. Disadvantages include poor spatial resolution and low sensitivity. Modern high field (> 4 T) scanners are capable of achieving *ca.* 100 μm resolution over several hours of imaging, while many clinical scanners can distinguish objects separated by millimeters.

Compared to luminescence-based methods, MRI has a low sensitivity and requires millimolar concentrations of contrast agent for detection. Traditional gadolinium-based MRI agents rely on altering the relaxation rates of ^{1}H nuclei of water molecules. As water is highly abundant within the body (~ 55 M), sensitivity is not a limiting issue in the presence of contrast agents. However, MRI contrast agents that detect alternative nuclear magnetic resonance active nuclei (^{13}C, ^{15}N, ^{19}F) typically employ strategies (*vide infra*) to increase sensitivity, such as increasing relation rates with a paramagnetic lanthanide metal.

2. Current magnetic resonance probes for oxidative stress

Recent work in the detection of oxidative stress has produced three contrast agents for ROS: a ^{13}C probe for H_2O_2, a paramagnetic chemical exchange saturation transfer (PARACEST) agent for NO, and a ^{19}F probe for HO•. These contrast agents generate a change in signal, not by altering the relaxation rate, but through a change in chemical shift upon reaction with the analyte. The limited number of examples not only indicates the challenges in developing responsive contrast agents with the required selectivity and sensitivity for detection, but also highlights the potential growth for this area of research.

The most recently published (in 2011) contrast agent for oxidative stress is a ^{13}C MRI probe for H_2O_2 developed by the Chang laboratory.[108] The H_2O_2 mediated oxidation of a ^{13}C labeled benzoylformic acid (^{13}C-BFA) to benzoic acid (^{13}C-BA)

proceeds with in minutes (Figure 1.13). High micromolar (200-1000 μM) levels of H_2O_2 can be detected by monitoring the ratio of the ^{13}C signal of the labeled carboxylate in the product (δ_C = 176 ppm) *versus* the unlabeled carboxylate in the unreacted ^{13}C-BFA (δ_C = 173.5 ppm).[108] Note that these concentrations of H_2O_2 are well above the physiologically relevant upper level of 1 μM.[6, 15] Additionally, this probe exhibits a *ca*. 8 fold selectivity for H_2O_2 over other ROS. Phantom images were collected at 14.1 T using hyperpolarized samples of ^{13}C-BFA (20 mM) to enhance the MRI signal intensity in the presence of 0-200 mM H_2O_2. Results indicate that reaction based detection coupled with a hyperpolarized ^{13}C MRI probe lacks the sensitivity to monitor H_2O_2 *in vivo*.

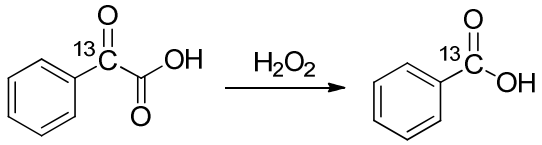

^{13}C-BFA **^{13}C-BA**

Figure 1.13. Chemical structure of the ^{13}C MRI contrast agent responsive to H_2O_2.[108]

The second example of an MRI agent for oxidative stress is an irreversible paramagnetic chemical exchange saturation transfer (PARACEST) agent responsive to NO in the presence of O_2. Contrast agents of this type possess one or more protons that exchange with bulk water. Upon saturation of the resonance frequency of an exchangeable proton, chemical exchange reduces the single intensity of the bulk water. A paramagnetic lanthanide ion shifts the resonance of the exchangeable ^1H, allowing it to be detected at a unique chemical shift. The NO responsive PARACEST agent, Yb-DO3A-oAA, contains an orthoaminoanilide moiety that is oxidized by NO in the presence of O_2 to a nitroso intermediate that results in the formation of the dimeric triazene product (Figure 1.14).[9] *In vitro* studies revealed that a complete deactivation of the PARACEST effects for the exchangeable amide and amine are observed upon reaction of Yb-DO3A-oAA (40 mM) with NO for 1 h. This system demonstrates that responsive MRI agents can be developed using PARACEST, but also illustrates that positioning probes at the sites of oxidant production is needed for *in vivo* applications.

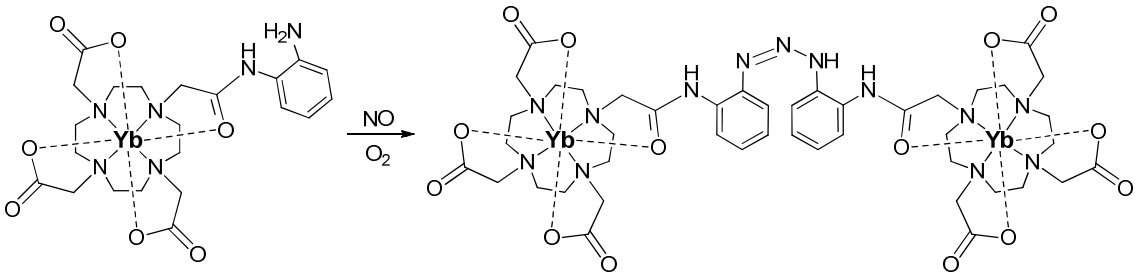

Yb-DO3A-oAA

Figure 1.14. Chemical structure of an NO responsive PARACEST agent.[109]

The only published magnetic resonance detection method for HO• is a fluorinated contrast agent developed by Aime *et. al*. in 1999. Hydroxylation of the hydroxyphenyl-trifluoroacetanilide (CF_3PAF, δ_F = -76.16 ppm) releases trifluoroacetamide (TFAM, δ_F = -76.79 ppm) or trifluoroacetic acid (TFA, δ_F = -76.14 ppm) in a reaction followed by ^{19}F NMR (Figure 1.15).[110] Using a *ca.* 5 mM solution of CF_3PAF, the relative signal intensity of the TFAM product increased with respect to the concentration of HO• (which is proportional to the concentration of Fenton regent in the presence of H_2O_2). This probe was further applied to measure the antioxidant capacity of biomolecules and biofluids *via* ^{19}F NMR spectroscopy. Due to the small change in fluorine resonance frequency ($\Delta\delta_F$) of < 1 ppm upon hydroxylation, these studies were limited to ^{19}F NMR, as the individual resonances could not be resolved by MRI. Future fluorine contrast agents should capitalize on the large chemical shift range of the ^{19}F nuclei to design probes with resonances of the reacted and unreacted forms that are separated by *ca.* 10 ppm and, thus, are compatible with MRI.

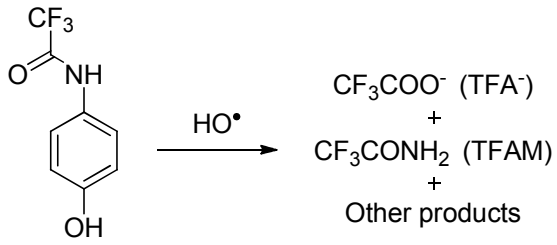

CF_3PAF

Figure 1.15. Chemical structure of CF_3PAF a ^{19}F NMR contrast agent for HO•.[110]

3. Summary of magnetic resonance detection for oxidative stress

The limited examples of MR probes for oxidative stress illustrates that this field is at its infancy. Interestingly, the three published examples utilize different techniques – hyperpolarized ^{13}C MRI, PARACEST, and ^{19}F NMR – to generate responsive contrast agents, and they monitor different analytes. The obstacle shared by the MR probes discussed above is low sensitivity. Currently, the detection limits of MRI probes and the concentration of the oxidative species are separated by orders of magnitude. Future generation ROS or RNS probes must have sufficient sensitivity to detect their analytes within the physiological concentration ranges, while still maintaining high selectivity. Fundamental research in the development of responsive contrast agents and the application of these techniques to other biological analytes will strongly impact the promulgation of HO• MR probes.

IV. Focus of the Current Study

The primary focus of this work is to develop responsive imaging agents for HO• that are selective, sensitive, and function in a biological environment. This goal is addressed through the development of aromatic acid containing luminescent and fluorine magnetic resonance probes. In addition to high selectivity, these probes monitor HO• directly, unlike some recently developed probes.

Initial work, described in chapter two, focuses on developing time-delayed luminescence probes that directly detect HO• in aqueous solutions with high sensitivity and high selectivity. Components of the probe include a sensitizing antenna that is formed upon hydroxylation and a Tb-complex with open coordination sites to bind the antenna. The increase in luminescence intensity of Tb-DO3A in the presence of hydroxylated aromatic acid and aromatic amide containing antennas is measured with respect to the non-hydroxylated, pre-antenna derivative of each. Formation of a weak ternary complex between the lanthanide complex and the hydroxylated antenna is examined by varying the Tb-chelate, measuring the hydration number (q) of the metal center, and temperature dependent titrations. Further, the selectivity for the optimized

probes over other ROS is investigated, and the increase in Tb-emission upon hydroxylation of the pre-antenna is used to monitor the *in vitro* production of HO•.

In chapter three, a water soluble ^{19}F MRI contrast agent for HO• is presented. First, the ratiometric response of a diamagnetic fluorinated benzoic acid probe is evaluated using ^{19}F NMR by monitoring the appearance of a reaction product relative to the disappearance of the probe. *In vitro* production of HO• is followed by ^{19}F MRI, and the selectivity for the probe for HO• over other ROS is also assessed. Next, the synthesis and evaluation of second generation probes, which feature a paramagnetic lanthanide to increase sensitivity, are discussed.

Finally, in chapter four, the cellular compatibility of luminescent lanthanide probes based on a macrocyclic polyaminocarboxylate (DOTA) ligand framework is evaluated. A library of complexes is synthesized that systematically and independently varies either the sensitizing antenna or the hydrophobicity of substituents. *In vitro* analysis of the complexes includes spectrophotometric characterization, quantum yield determination, and assessment of luminescence quenching in cell lysate. Then, the effect of each complex on cell viability is evaluated, and the cellular association is measured by ICP-MS and fluorescence spectroscopy.

CHAPTER 2
TIME-DELAYED LUMINESCENCE DETECTION OF HYDROXYL RADICAL

I. SYNOPSIS

Molecular probes for the detection of hydroxyl radical (HO•) by time-delayed luminescence spectroscopy directly in water at neutral pH with high sensitivity and selectivity are presented. The bimolecular probes consist of a lanthanide complex with open coordination sites and a reactive pre-antenna composed of an aromatic acid or amide; the latter binds to and sensitizes terbium emission upon hydroxylation by HO•. These probes exhibit long luminescence lifetimes compatible with time-delayed measurements that remove interfering background fluorescence from the sample. Six different reactive pre-antenna (benzoate, benzamide, isophthalate, isophthalamide, trimesate, and trimesamide) and two different terbium complexes (Tb-DO3A and Tb-DO2A) were evaluated. Of these the trimesamide/Tb-DO3A system enables the most sensitive detection of HO• with a *ca.* 1000-fold increase in metal-centered time-delayed emission upon hydroxylation of the pre-antenna to 2-hydroxytrimesamide. Excellent selectivity for both the trimesamide/Tb-DO3A and trimesate/Tb-DO3A systems over other reactive oxygen and nitrogen species are observed. Notably, the increase in metal-centered luminescence intensity is not associated with a decrease in the hydration number (*q*) of Tb-DO3A, suggesting that the antenna is interacting with the lanthanide *via* a second sphere coordination environment or that coordination by the antenna occurs by displacement of one or more of the carboxylate arms of DO3A. Formation of a weak ternary complex Tb-DO3A•hydroxytrimesamide was confirmed by temperature-dependent titrations that illustrated a decrease in K_{app} with increasing temperature.

II. INTRODUCTION

A. Detecting hydroxyl radical by luminescence

Previous luminescent probes for HO•, as discussed in Chapter 1 (Section III.A.2), suffer from low selectivity over other ROS or detect HO• using an indirect method. Since ROS and RNS react with each other and share downstream biological targets, probes that selectively – and directly – detect one species are required. Additionally, probes compatible with multiplex imaging could simultaneously monitor two (or more) species and dissect their interrelated nature. Current probes also lack the rapid kinetics required to improve the sensitivity of detection, which is particularly important for monitoring ROS that are present at low concentrations. Enhanced biological compatibly is also desired. Not all current probes are water soluble, and additional techniques to mitigate the interference of background fluorescence would greatly impact biomedical research.

In this chapter, the design, evaluation, and mechanism of action of molecular probes for the detection of HO• by time-delayed luminescence spectroscopy are described. The probes function in water at neutral pH with high sensitivity and are highly selective for HO• over other competing ROS and RNS. The bimolecular probes consist of an aromatic acid that reacts with HO• to produce hydroxylated chromophores that interact with the Tb-DO3A center and sensitize lanthanide-centered emission. Further, this method of detection is non-destructive, selective, and can directly measure HO•.

B. Advantages of lanthanide-based luminescent probes

The probes discussed in this chapter utilize a luminescent lanthanide metal to elicit an analyte-induced response. Several distinct advantages over traditional fluorescent probes are gained with luminescent lanthanide probes. The large Stokes shift – or difference in the absorption wavelength of the antenna and emission wavelength of the lanthanide – reduces self-absorption issues and provides the advantage of a linear relationship between the probe response and the concentration of complex.[33] Typical Stokes shifts for terbium (Tb) and europium (Eu) are greater than 200 nm, compared to approximately 20 nm for common fluorescent dyes.[33] Secondly, lanthanides have narrow emission bands (~20 nm) and emission spectra that do not overlap, allowing for

simultaneous detection of multiple analytes (Figure 2.1a).[33] A third advantage of lanthanide-based probes is a long luminescence lifetime, on the order of milliseconds, that arises from the Laporte forbidden energy transition from the ^5D to ^7F states of the lanthanide.[33, 111] Organic dyes and traditional chemsensors or probes have nanosecond fluorescent lifetimes, while components in biological media are in the sub-microsecond range.[33] The long-lived luminescence eliminates the interference of background fluorescence with measurements, making these probes particularly useful for time-delayed assays in complex biological samples.[33, 112-113] In time-delayed detection methods, a pulse of excitation light is followed by a time delay, which allows signal intensity from background fluorescence to decay prior to detection of the luminescence. The resulting signal is a function solely of the lanthanide-complex bound to analyte, without interfering background fluorescence or scattered light (Figure 2.1b).[33, 111] So strictly from theory alone, lanthanide-based probes are able to overcome the significant limitations of their organic counterparts. With large Stokes shifts, narrow emission bands, and long luminescent lifetimes, lanthanide-based molecular probes are intrinsically well suited use in biological systems.

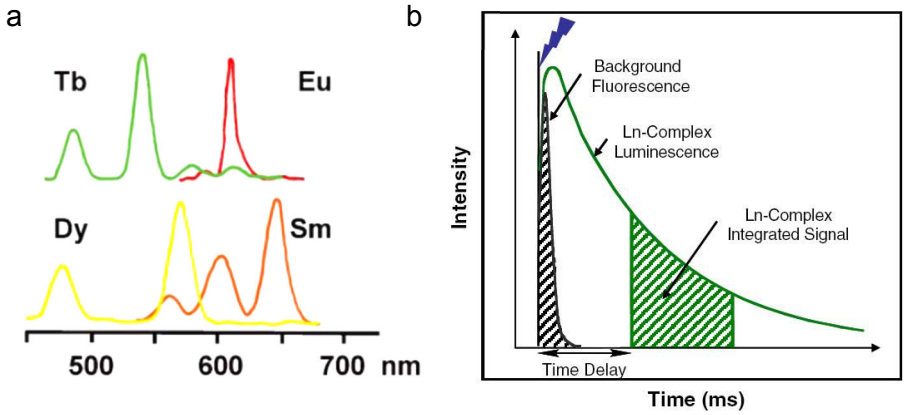

Figure 2.1. Spectral features of lanthanide metals that facilitate their use in biological applications. (a) Characteristic emission spectra of lanthanide complexes illustrating their narrow, non-overlapping emission bands.[111] (b) Time-delayed detection methods allow background fluorescence from the sample to decay prior to measuring the lanthanide emission intensity.[33]

C. Design principles of lanthanide-based probes

Lanthanide sensor design is based on four principles that increase luminescence quantum yield: efficiency of exciting the triplet state of the antenna, the energy level difference between the excited antenna and the lanthanide metal, the physical distance between the antenna and lanthanide, and the number of water molecules bound to the lanthanide metal center. The probe described in this chapter uses each of these mechanisms to respond to HO• with a high sensitivity of detection. Forbidden 4f - 4f transitions of lanthanides causes low molar absorption coefficients (< 3 M^{-1} s^{-1}) and, for practical biological imaging, the lanthanide cannot be directly excited.[111] Therefore, an antenna is incorporated that absorbs energy and transfers it to the lanthanide (Figure 2.2a). The energy transfer process is outlined by the Jablonski diagram in Figure 2.2b. In the first step, the antenna is excited to the singlet state (S_1) upon absorbing excitation light. Subsequent intersystem crossing (ISC) populates the lowest lying triplet excited state (T_1), which must be slightly higher in energy than the lanthanide ^5D state. When in close proximity, intramolecular energy transfer (ET) occurs from the antenna triplet state (T_1) causing the metal to be excited into the emitting state (^5D). The lanthanide metal ion then emits visible light upon relaxation to the ^7F states; the energy level differences correspond to characteristic values for each lanthanide (545 nm for Tb and ~ 614 nm for Eu).[33]

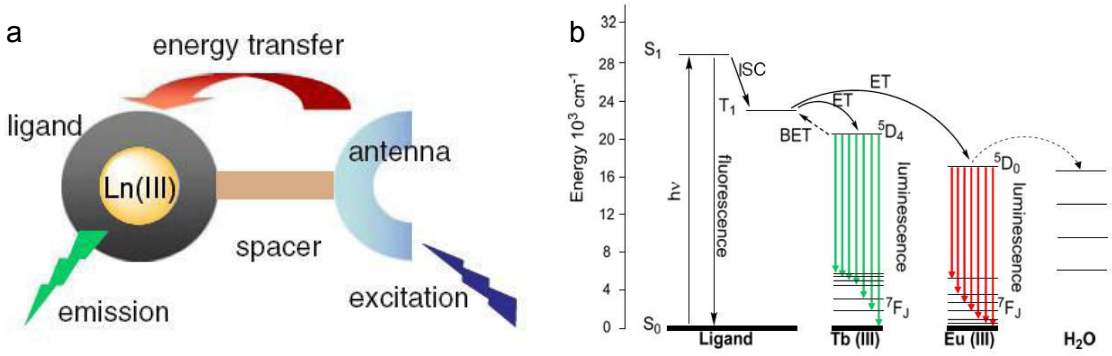

Figure 2.2. Design and energy transfer of lanthanide-based luminescent probes:[33] (a) Lanthanides are sensitized indirectly through an antenna, and (b) the energy transfer pathway from the antenna to the emitting lanthanide metal. Deactivation of the lanthanide metal to the ground state is characterized by the production of green (Tb) or red (Eu) light.

Efficient energy transfer from the antenna to the lanthanide metal center relies on the energy levels of the two components and the distance that separates them. The excited triplet state of the antenna must be higher in energy than the ^5D energy level of the lanthanide for the energy transfer to occur. A triplet state lower in energy than the ^5D lanthanide cannot populate the higher energy state, while an energy level that is too high results in direct fluorescence of the antenna.[33] However, if the lanthanide ^5D is too close in energy to the T_1 back energy transfer (BET) to the excited antenna can occur. A shorter distance, *d*, between the antenna and lanthanide metal ion facilitates the Förster energy transfer, according to an d^6 dependence. Lastly, the number of water molecules coordinated to the lanthanide center affects the quantum yield. Fewer bound water molecules reduces the likelihood of a non-radiative decay processes occurring through the vibration of high-energy O-H bonds.[111] Therefore, ligand design should minimize the number of coordination sites around the lanthanide available for interactions with water molecule in the analyte-responsive state.[33, 111]

D. First generation time-delayed luminescent HO• probe

Given the unmet need to detect HO•, a luminescent lanthanide-based probe for the sensitive and selective detection of HO• in water was reported.[81] An effective strategy involves modulating the ability of an antenna to sensitize the lanthanide luminescence. Altering the efficiency of energy transfer of an antenna to an emissive lanthanide can in turn be achieved by changing either the excited triplet state energy level of the antenna, and/or the antenna-lanthanide distance.[33, 111] A first generation probe was designed to make use of both of these parameters. This probe consists of a Tb-DO3A complex and 10 equivalents of trimesate (Figure 2.3a). In the absence of HO•, the trimesate does not interact with the Tb-center and, therefore, does not sensitize the lanthanide emission. Initially it was thought the hydroxylated antenna, formed by the reaction of the pre-antenna with HO•, would coordinate to the terbium and displace two water molecules. The coordinated antenna, with a triplet excited state energy level more amenable to terbium emission causes an 11-fold increase in the time-delayed luminescence intensity upon reaction with a steady-state concentration of 0.75 fM HO• over at time of one hour (Figure 2.3b) with excellent selectivity (Figure 2.3c).[81]

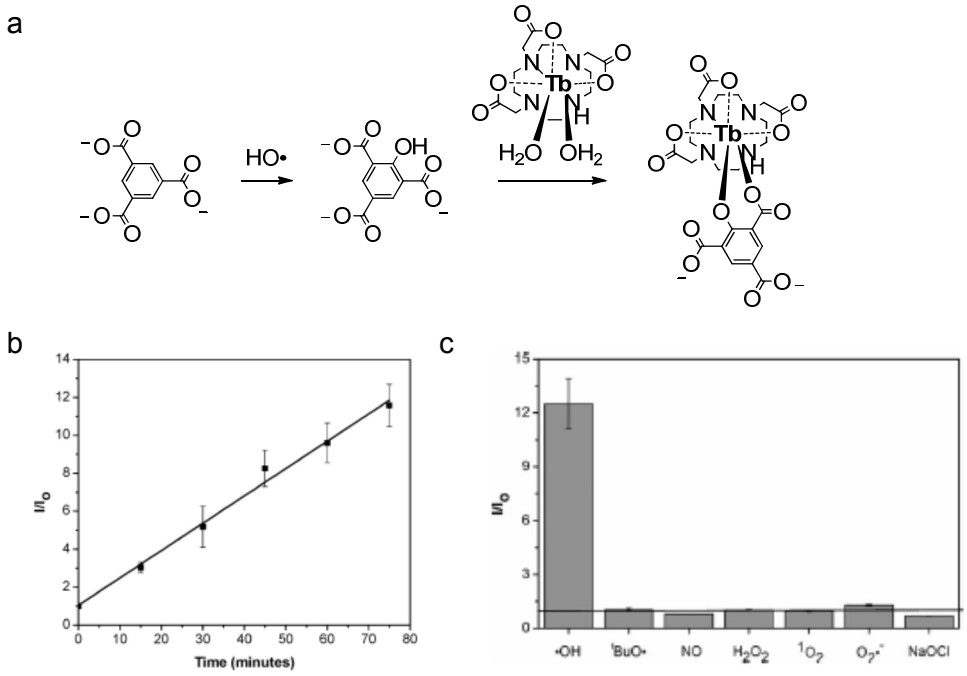

Figure 2.3. Hydroxyl radical sensing *via* reaction with trimesate and Tb-DO3A.[81] (a) The hydroxylated trimesate antenna interacts with the Tb-DO3A causing an increasing in metal-centered emission. (b) The relative time-delayed luminescence of Tb-DO3A-trimeasate as a function of time with $[HO•]_{ss}$ = 0.37 fM. (c) Selectivity of Tb-DO3A-trimesate for HO• *versus* other ROS.

In this study, the mechanism of the turn-on luminescence of lanthanide probes for HO• is investigated enabling the design of a new system with improved sensitivity and selectivity. The nature and coordinating ability of the antenna are evaluated *via* luminescence lifetime measurements and temperature dependent titrations. The sensitivity of the antennas with the highest turn-on potentials is determined by monitoring HO• produced by the photolysis of H_2O_2. Two antennas, trimesate and trimesamide, are demonstrated to selectively respond to HO• over other ROS and RNS.

II. RESULTS AND DISCUSSION

A. Probe design

The probe consists of two parts: a lanthanide complex with at least two open coordination sites initially occupied by solvent molecules and a pre-antenna that coordinates to and sensitizes terbium only after reaction with HO•. The first step in optimizing its design so as to achieve maximum sensitivity for HO• detection, focuses on the nature of the pre-antenna. Six different pre-antenna/antenna pairs are investigated: salicylicate, salicylamide, isophthalate, isopthalamide, trimesate and trimesamide (Figure 2.4). The acids were selected because of their previous incorporation into HO• detection systems,[81, 100-102, 114] while the amides were chosen due to reports by Raymond and co-workers that demonstrated the isophthalamide and trimesamide based ligands are efficient sensitizers of lanthanide (Sm^{3+}, Eu^{3+}, Tb^{3+}, Dy^{3+}, Ho^{3+}) emission.[115] The trimesate and trimesamide antennas have the additional benefit of three equivalent primary reaction sites for HO•; reaction at either site results in the same product. Thus, the investigated antennas were selected to maximize both HO• response and relative time-delayed luminescence intensity.

B. Effect of the antenna

The probe further relies on a substantial difference in sensitizing ability between the antenna and the pre-antenna. For example, trimesamide (**2**.**6a**) does not sensitize Tb effectively, but upon reaction with HO• it yields the powerful hydroxytrimesamide (**2.6b**) antenna (Figure 2.5). This same turn-on of luminescence intensity is experienced in the presence of the other hydroxylated antennas investigated with respect to the corresponding pre-antenna. In each case, the time-delayed excitation, time-delayed emission, and fluorescence intensity of Tb-DO3A is substantially higher for the hydroxylated antenna than for its corresponding non-hydroxylated analog (Figure 2.6).

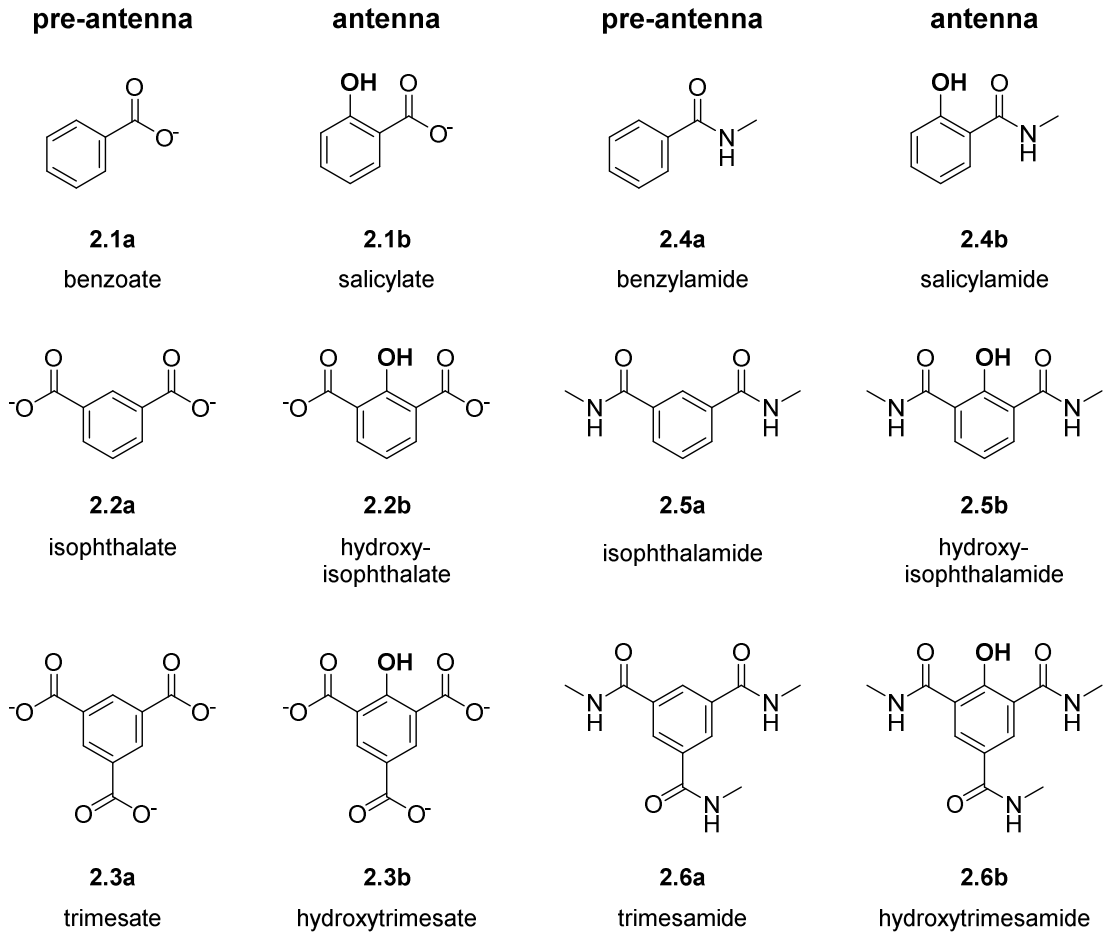

Figure 2.4. Chemical structures of pre-antennas and hydroxylated antennas.

To evaluate which pre-antenna/antenna pair yielded the highest response, ability of each aromatic compound to sensitize terbium emission under identical conditions was determined. Note that each pre-antenna/antenna pair requires a different excitation wavelength in order to maximize the luminescence intensity in the presence of the hydroxylated antenna. In each case, this wavelength was selected from the time-delayed excitation profiles of the hydroxylated antenna/Tb-DO3A mixture (Figures 2.7 – 2.12).

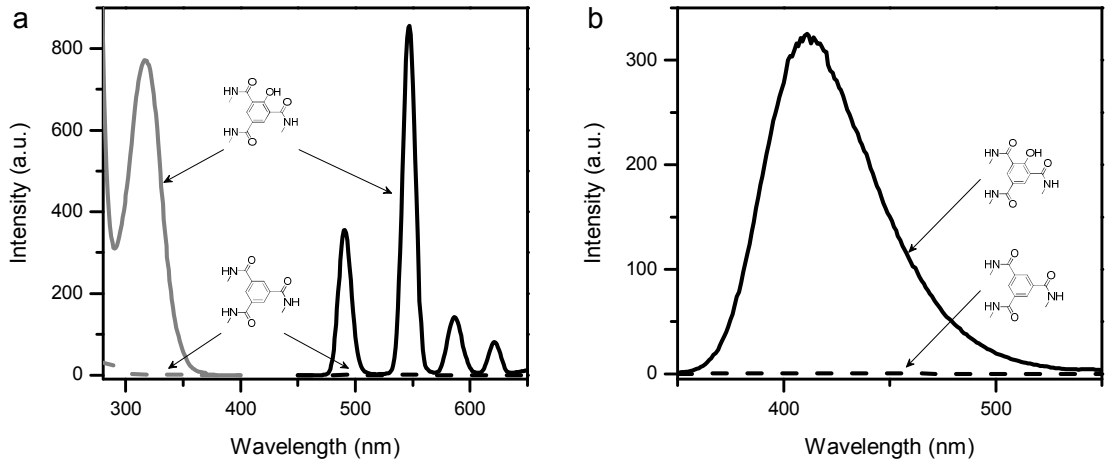

Figure 2.5. (a) Time-delayed excitation (grey), time-delayed emission (black) and (b) fluorescence profiles of Tb-DO3A in the presence of pre-antenna **2.6a** (dashed) or hydroxylated antenna **2.6b** (solid). Conditions: [Tb-DO3A] = 10 μM, [(pre)antenna, **2.6a** or **2.6b**] = 100 μM, [Tris] = 10 mM, pH 7.2, slit widths (excitation and emission) = 10 nm, *T* = 20 °C. Phosphorescence parameters for (a): λ_{em} = 545 nm, λ_{ex} = 328 nm, time delay = 0.1 ms. Fluorescence parameters for (b): λ_{ex} = 314 nm.

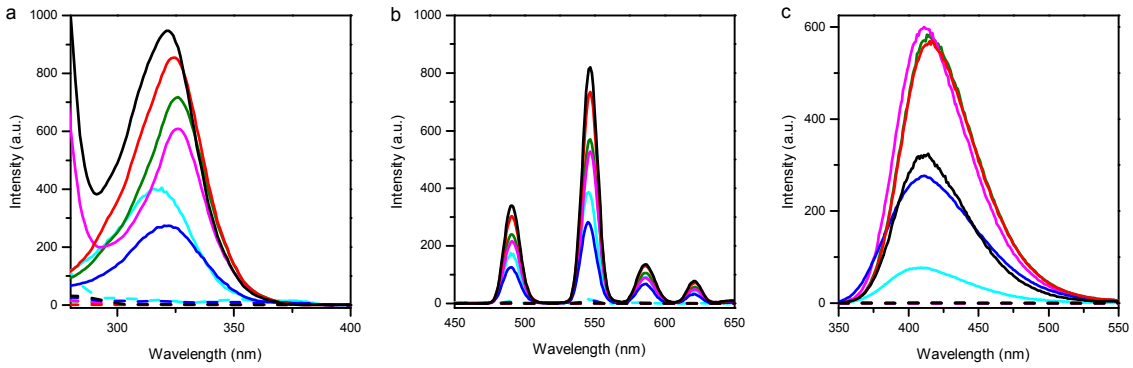

Figure 2.6. (a) Time-delayed excitation, (b) time-delayed emission, and (c) fluorescence profiles of Tb-DO3A in the presence of **2.1a** (dashed cyan), **2.1b** (solid cyan), **2.2a** (dashed green), **2.2b** (solid green), **2.3a** (dashed magenta), **2.3b** (solid magenta), **2.4a** (dashed blue), **2.4b** (solid blue), **2.5a** (dashed red), **2.5b** (solid red), **2.6a** (dashed black), or **2.6b** (solid black). Conditions: [Tb-DO3A] = 10 μM, [(pre)antenna] = 100 μM, [Tris] = 10 mM, pH 7.2, slit widths (excitation and emission) = 10 nm, *T* = 20 °C. Excitation wavelengths: **2.1a/b**, λ_{ex} = 321 nm; **2.2a/b**, λ_{ex} = 333 nm; **2.3a/b**, λ_{ex} = 333 nm; **2.4a/b**, λ_{ex} = 324 nm; **2.5a/b**, λ_{ex} = 331 nm; **2.6a/b**, λ_{ex} = 328 nm. Phosphorescence parameters: delay = 0.1 ms, gate time = 5.0 ms, decay time = 0.02 s.

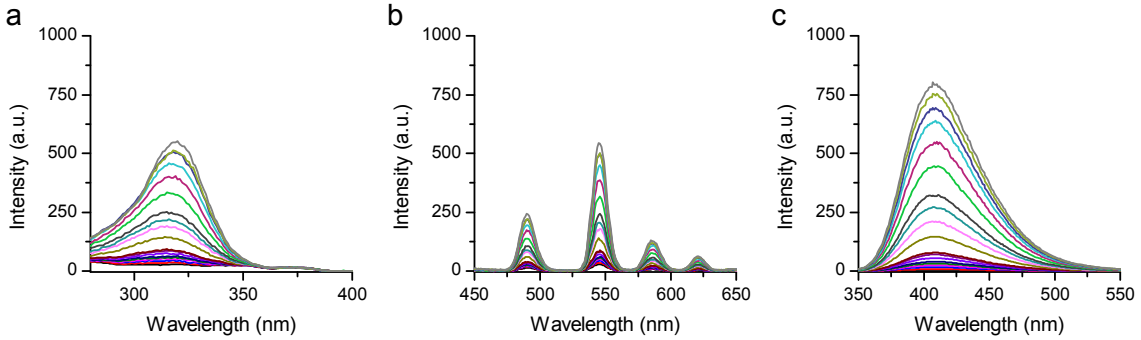

Figure 2.7. Titration of Tb-DO3A with salicylate (**2.1b**): (a) time-delayed excitation spectra, (b) time-delayed emission spectra, and (c) fluorescence spectra. Conditions: [Tb-DO3A] = 10 μM, [(pre)antenna] = 0-200 μM, [Tris] = 10 mM, pH 7.2, slit widths = 10 nm, *T* = 20 °C. Phosphorescence parameters: λ_{em} = 545 nm, λ_{ex} = 321 nm, time delay = 0.1 ms, gate time = 5.0 ms, decay time = 0.02 s. Fluorescence parameters: λ_{ex} = 306 nm.

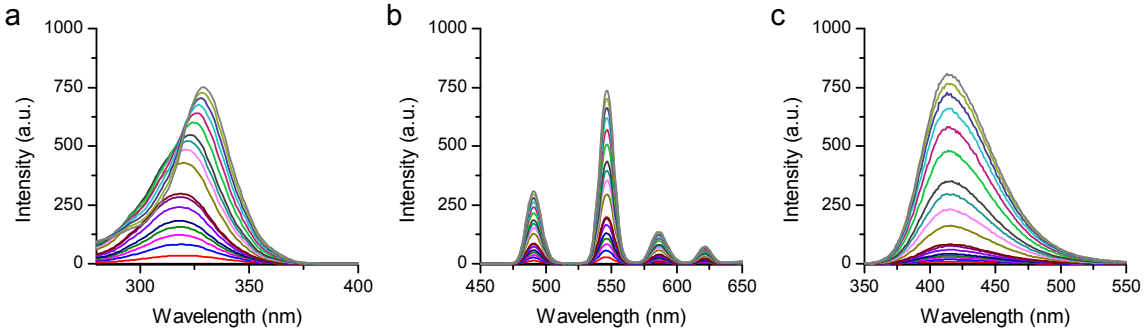

Figure 2.8. Titration of Tb-DO3A with hydroxyisophthalate (**2.2b**): (a) time-delayed excitation spectra, (b) time-delayed emission spectra, and (c) fluorescence spectra. Conditions: [Tb-DO3A] = 10 μM, [(pre)antenna] = 0-200 μM, [Tris] = 10 mM, pH 7.2, slit widths = 10 nm, *T* = 20 °C. Phosphorescence parameters: λ_{em} = 545 nm, λ_{ex} = 333 nm, time delay = 0.1 ms, gate time = 5.0 ms, decay time = 0.02 s. Fluorescence parameters: λ_{ex} = 324 nm.

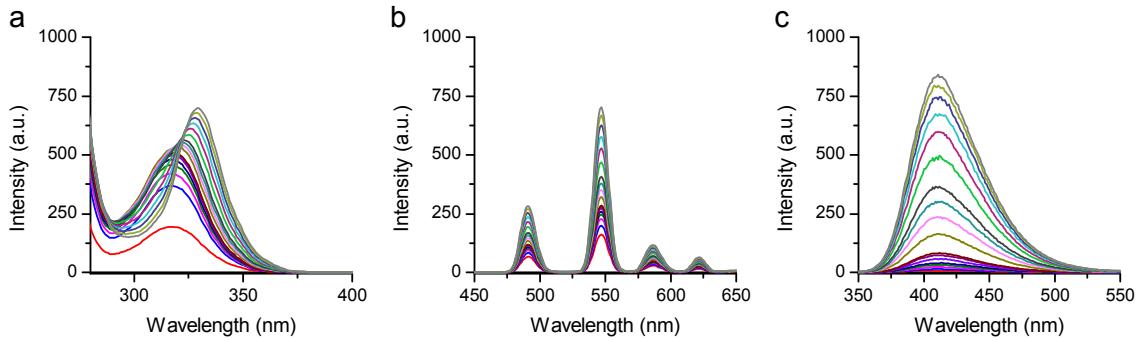

Figure 2.9. Titration of Tb-DO3A with hydroxytrimeasate (**2.3b**): (a) time-delayed excitation spectra, (b) time-delayed emission spectra, and (c) fluorescence spectra. Conditions: [Tb-DO3A] = 10 μM, [(pre)antenna] = 0-200 μM, [Tris] = 10 mM, pH 7.2, slit widths = 10 nm, *T* = 20 °C. Phosphorescence parameters: λ_{em} = 545 nm, λ_{ex} = 333 nm, time delay = 0.1 ms, gate time = 5.0 ms, decay time = 0.02 s. Fluorescence parameters λ_{ex} = 327 nm.

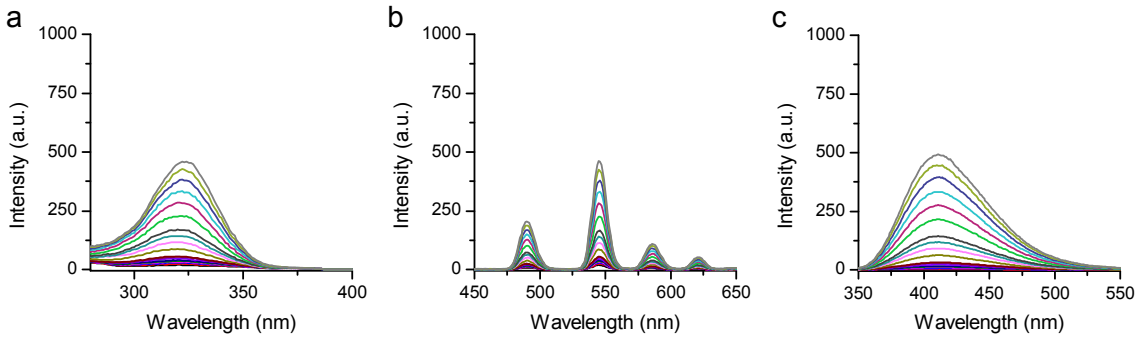

Figure 2.10. Titration of Tb-DO3A with salicylamide (**2.4b**): (a) time-delayed excitation spectra, (b) time-delayed emission spectra, and (c) fluorescence spectra. Conditions: [Tb-DO3A] = 10 μM, [(pre)antenna] = 0-200 μM, [Tris] = 10 mM, pH 7.2, slit widths = 10 nm, *T* = 20 °C. Phosphorescence parameters: λ_{em} = 545 nm, λ_{ex} = 324 nm, time delay = 0.1 ms, gate time = 5.0 ms, decay time = 0.02 s. Fluorescence parameters: λ_{ex} = 328 nm.

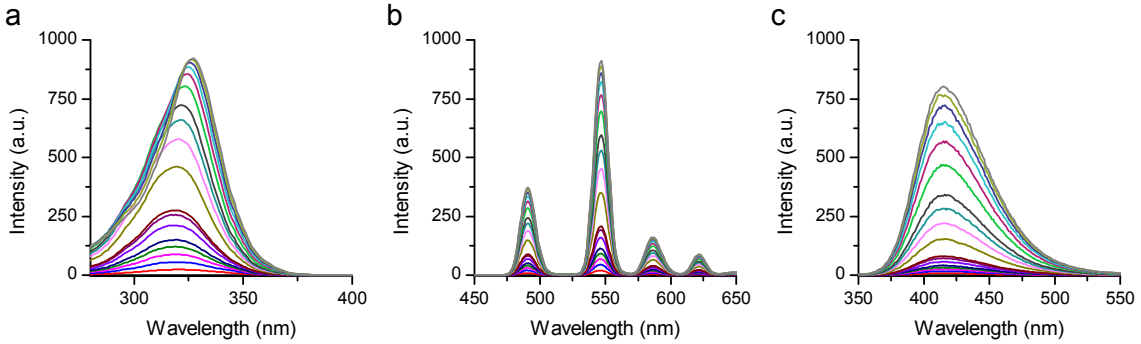

Figure 2.11. Titration of Tb-DO3A with hydroxyisophthalamide (**2.5b**): (a) time-delayed excitation spectra, (b) time-delayed emission spectra, and (c) fluorescence spectra. Conditions: [Tb-DO3A] = 10 μM, [(pre)antenna] = 0-200 μM, [Tris] = 10 mM, pH 7.2, slit widths = 10 nm, *T* = 20 °C. Phosphorescence parameters: λ_{em} = 545 nm, λ_{ex} = 331 nm, time delay = 0.1 ms, gate time = 5.0 ms, decay time = 0.02 s. Fluorescence parameters: λ_{ex} = 320 nm.

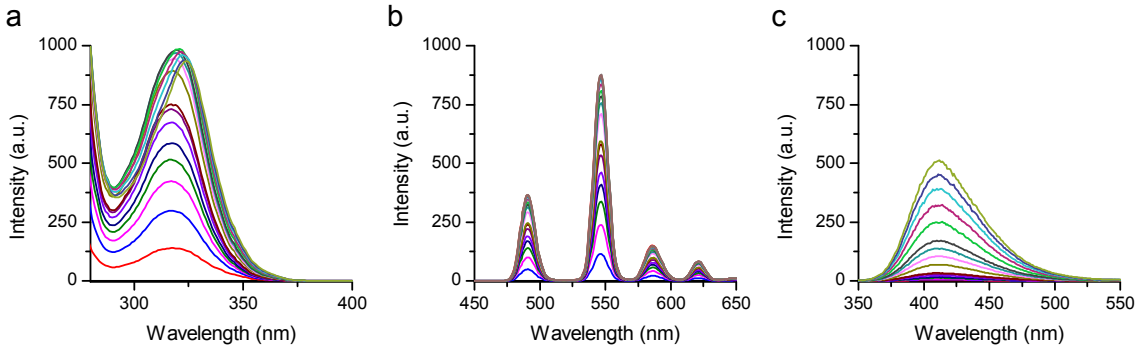

Figure 2.12. Titration of Tb-DO3A with hydroxytrimesamide (**2.6b**): (a) time-delayed excitation spectra, (b) time-delayed emission spectra, and (c) fluorescence spectra. Conditions: [Tb-DO3A] = 10 μM, [(pre)antenna] = 0-200 μM, [Tris] = 10 mM, pH 7.2, slit widths = 10 nm, *T* = 20 °C. Phosphorescence parameters: λ_{em} = 545 nm, λ_{ex} = 328 nm, time delay = 0.1 ms, gate time = 5.0 ms, decay time = 0.02 s. Fluorescence parameters: λ_{ex} = 314 nm.

Keeping all other experimental conditions constant, the ability of each hydroxylated antenna to modulate Tb-DO3A luminescence can be directly compared (Figure 2.13). Alternatively, this turn-on ability can also be expressed by the change in relative integrated emission intensity ($\Delta I/I_0 = I/I_{0\ Tb\bullet antenna} - I/I_{0\ Tb\bullet pre\text{-}antenna}$) as calculated with 10 equivalents of the antenna per Tb-DO3A (Table 2.2). Note that these comparisons are possible because the same excitation wavelength and photomultiplier tube (PMT) voltage was used for the pre-antenna and antenna in each pair; all other experimental parameters were kept constant for all pre-antenna/antenna pairs. The high $\Delta I/I_0$ values, ca. 1000-fold increase for pre-antenna/antenna pairs **2.2**, **2.3**, **2.5**, and **2.6** indicate that the hydroxyisophthalate (**2.2b**), hydroxytrimesate (**2.3b**), hydroxyisophthalamide (**2.5b**), and hydroxytrimesamide (**2.6b**) antennas are significantly more efficient antennas for Tb-DO3A than the salicylate (**2.1b**) and salicylamide (**2.4b**).

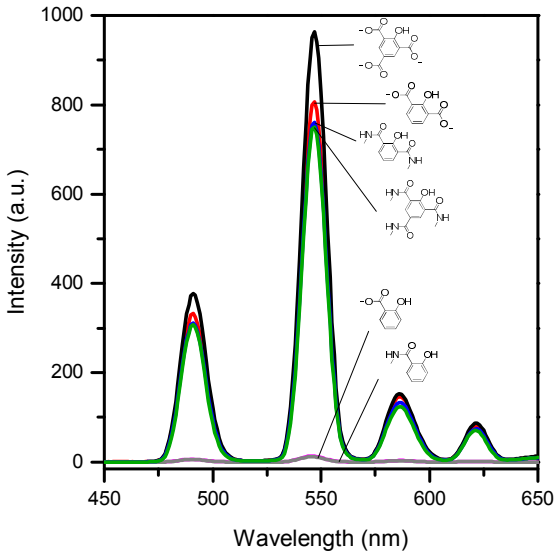

Figure 2.13. Time-delayed emission of Tb-DO3A in the presence of hydroxylated antennas: **2.1b** (magenta), **2.2b** (red), **2.3b** (black), **2.4b** (grey), **2.5b** (blue), and **2.6b** (green). Conditions: [Tb-DO3A] = 10 μM, [antenna] = 100 μM, [Tris] = 10 mM, pH 7.2, time delay = 0.1 ms, slit widths (excitation and emission) = 10 nm, *T* = 20 °C. Excitation wavelengths (λ_{ex}): **2.1b**, 321 nm; **2.2b**, 333 nm; **2.3b**, 333 nm; **2.4b**, 324 nm; **2.5b**, 331 nm; **2.6b**, 328 nm.

Table 2.1. Relative integrated emission intensity (I/I_0) for each pre-antenna and antenna pair representing the turn-on ability of each pre-antenna.

Pre-Antenna				**Antenna**				
		λ_{ex} (nm)	**I/I_0**			**λ_{ex} (nm)**	**I/I_0**	**$\Delta I/I_0$**
2.1a	benzoate	321	1.2	**2.1b**	Salicylate	321	23	**22**
2.2a	isophthalate	333	1.1	**2.2b**	Hydroxyisophthalate	333	1141	**1140**
2.3a	trimesate	333	1.4	**2.3b**	Hydroxytrimesate	333	1131	**1130**
2.4a	benzylamide	324	1.8	**2.4b**	Salicylamide	324	25	**23**
2.5a	isophthalamide	331	1.0	**2.5a**	hydroxyisophthalamide	331	1104	**1103**
2.6a	trimesamide	328	3.9	**2.6a**	hydroxytrimesamide	328	992	**988**

Conditions: [Tb-DO3A] = 10 μM, [(pre)antenna] = 100 μM, [Tris] = 10 mM, pH 7.2, time delay = 0.1 ms, slit widths (excitation and emission) = 10 nm, *T* = 20 °C. I = integrated emission intensity from 470 – 635 nm. $\Delta I/I_0$ = I/I_0 Tb•antenna - I/I_0 Tb•pre-antenna. Each value represents the average of 3 replicates (*n* = 3).

In addition to a high luminescence intensity, the ideal antenna for HO• detection is able to respond to the analyte when it is present in low concentrations (Figure 2.14). With concentrations in the micromolar range, the hydroxytrimesate (**2.3b**) and hydroxytrimesamide (**2.6b**) cause the largest increases in the luminescence of Tb-DO3A (Figure 2.15). The 500-fold luminescence increase of **2.3b** and **2.6b** when present at 0.5 equivalents to Tb-DO3A, make these antennas the most promising candidates for the detection of HO• at biologically relevant concentrations. Interestingly, for some systems (hydroxyisophthalate, **2.2b**, hydroxytrimesate, **2.3b**, hydroxyisophthalamide, **2.5b**, hydroxytrimesamide, **2.6b**), the maximum excitation wavelength is red shifted at higher concentration of antenna (Figures 2.7- 2.12). These observations suggest that at higher concentrations, the antenna is not fully solvated but is likely aggregated, resulting in multiple different luminescing states.

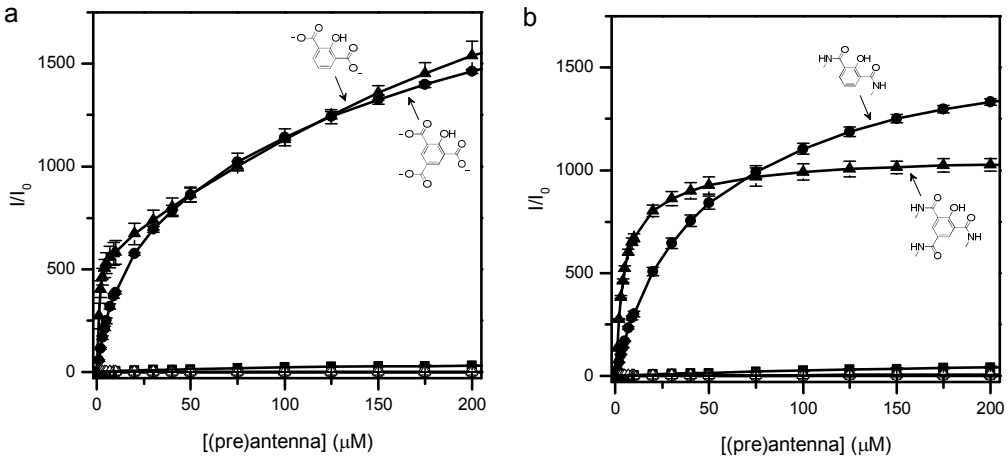

Figure 2.14. Relative time-delayed luminescence (I/I_0) of Tb-DO3A as a function of increasing concentrations of (a) acid (pre)antennas: **2.1a** (open square), **2.1b** (filled square), **2.2a** (open circle), **2.2b** (filled circle), **2.3a** (open triangle), **2.3b** (filled triangle), and (b) amide (pre)antennas: **2.4a** (open square), **2.4b** (filled square), **2.5a** (open circle), **2.5b** (filled circle), **2.6a** (open triangle), **2.6b** (filled triangle). Conditions: [Tb-DO3A] = 10 μM, [(pre)antenna] = 0 - 200 μM, [Tris] = 10 mM, pH 7.2, time delay = 0.1 ms, slit widths (excitation and emission) = 10 nm, *T* = 20 °C. Excitation wavelengths: **2.1a/b**, λ_{ex} = 321 nm; **2.2a/b**, λ_{ex} = 333 nm; **2.3a/b**, λ_{ex} = 333 nm; **2.4a/b**, λ_{ex} = 324 nm; **2.5a/b**, λ_{ex} = 331 nm; **2.6a/b**, λ_{ex} = 328 nm. I = integrated emission intensity from 470 – 635 nm. Results are mean ± SD (*n* = 3).

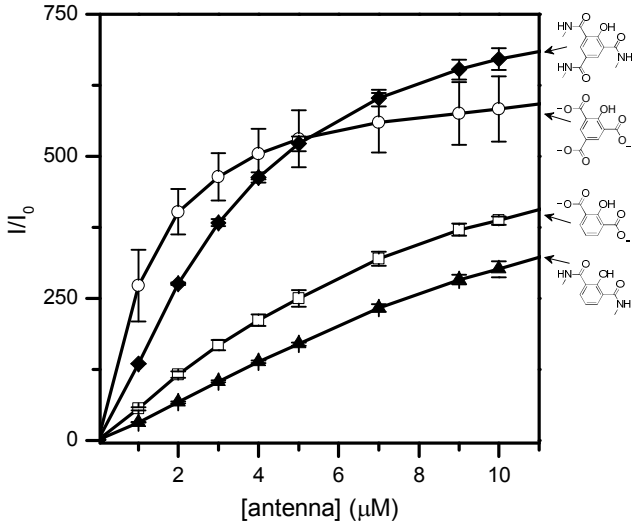

Figure 2.15. Relative time-delayed luminescence (I/I_0) of Tb-DO3A as a function of increasing concentrations of antennas: **2.2b** (open square), **2.3b** (open circle), **2.5b** (filled triangle), and **2.6b** (filled diamond). Conditions: [Tb-DO3A] = 10 μM, [antenna] = 0 - 10 μM, [Tris] = 10 mM, pH 7.2, time delay = 0.1 ms, slit widths (excitation and emission) = 10 nm, *T* = 20 °C. Excitation wavelengths: **2.2b**, λ_{ex} = 333 nm; **2.3b**, λ_{ex} = 333 nm; **2.5b**, λ_{ex} = 331 nm, **2.6b**, λ_{ex} = 328 nm. I = integrated emission intensity from 470 – 635 nm. Results are mean ± SD (*n* = 3).

C. Formation of a ternary complex

The substantial increase in time-delayed luminescence of the terbium center up to 700-fold for a 1:1 mixture of 2-hydroxytimesamide and Tb-DO3A in the μM range strongly implies a simple equilibrium and the formation of ternary complex between the hydroxylated antenna and the lanthanide complex. These results are consistent with prior observations by Gunnlaugsson and co-workers with similar systems.[114, 116] With this in mind, the initial hypothesis was that the substantial increase in metal-centered emission was due to direct coordination of the hydroxylated antenna to the terbium ion. One should note, however, that the data do not necessarily prove that the antenna is directly coordinated to the metal.

To establish the presence of this ternary complex, the effect of temperature on the binding curve was evaluated. Energy transfer from the antenna to the lanthanide can in theory occur either *via* a static or a dynamic mechanism. The first step involves equilibrium and formation of a ternary complex, Tb-DO3A•antenna, which is entropically disfavored.

$$Tb - DO3A + antenna \rightleftharpoons Tb - DO3A \bullet antenna$$

Assuming that energy transfer from the triplet excited state of the antenna to the ^5D state of the lanthanide is relatively constant in the temperature range considered, an increase in the temperature would shift the equilibrium to the left, resulting in a decrease in K_{app}. On the other hand, if no ternary complex is formed, sensitization of the lanthanide ion would occur in a purely dynamic or collisional mechanism that would be favored at high temperature. In this case, K_{app}, would increase as temperature increases. It is apparent from the temperature-dependence titration of Tb-DO3A with 2-hydroxytrimesamide (**2.6b**) that K_{app} decreases as the temperature increases from 5 °C to 80 °C (Figure 2.16). This decrease confirms the formation of a ternary complex between Tb-DO3A and the hydroxylated antenna, which is the basis of the substantial turn-on for this probe.

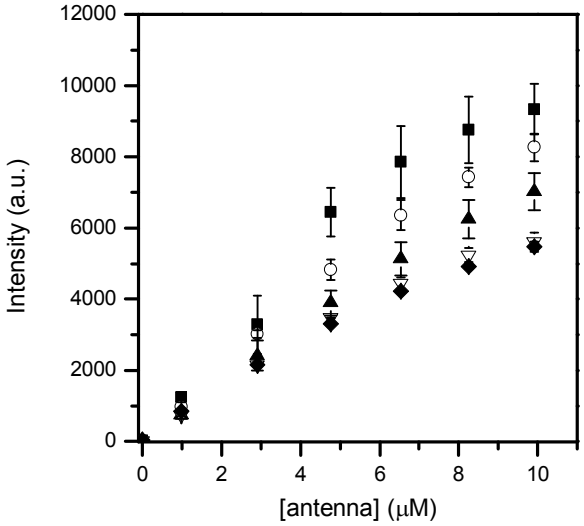

Figure 2.16. Relative time-delayed luminescence (I/I_0) of Tb-DO3A as a function of increasing concentrations of hydroxytrimesate antenna **2.6b** at different temperatures: 5 °C (filled square), 20 °C (open circle), 40 °C (filled upright triangle), 60 °C (open downward triangle) and 80 °C (filled diamond). Conditions: [Tb-DO3A] = 10 μM, [antenna] = 0 - 10 μM, [Tris] = 10 mM, pH 7.2, time delay = 0.1 ms, λ_{ex} = 328 nm, slit widths (excitation and emission) = 10 nm. I = integrated emission intensity from 470 – 635 nm. Results are mean ± SD (*n* = 3).

One possibility to evaluate the binding mode of the hydroxylated antenna and the structure of the ternary complex is to determine the number of inner-sphere water molecules directly coordinated on the lanthanide ion. This was achieved by measuring the luminescence lifetimes (τ) for the terbium centered emission in H_2O and D_2O according to the method of Horrocks.[117] The number of Tb-bound water molecules (*q*) can then be calculated as follows:

$$q = 4.2[(1/\tau_{H_2O}) - (1/\tau_{D_2O})]$$

Of the nine coordination sites available for terbium, the heptadentate ligand DO3A leaves two sites open for water molecule coordination, while the hexadentate DO2A leaves three (Figure 2.17). Assuming a salicylate binding mode as observed by Raymond in lanthanide hydroxyisophthalamide complexes,[118] in each case coordination of the hydroxylated antenna on the terbium was expected to reduce the *q* value by two (Figure 2.3).

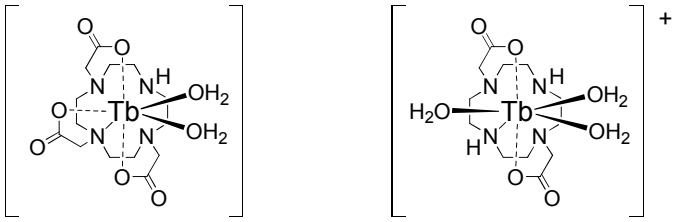

Tb-DO3A **Tb-DO2A**

Figure 2.17. Chemical structures of lanthanide complexes Tb-DO3A and Tb-DO2A.

The surprising results of this experiment are given in Table 2.2. For the parent Tb-DO3A complex, there is no noticeable change of the hydration number regardless of the hydroxylated antenna considered; $\Delta q = q_{\text{Tb-DO3A}} - q_{\text{Tb-DO3A•antenna}} = 0 \pm 0.5$ in the presence of 10 equivalents of hydroxylated antenna. These results thus suggest that, in contradiction with the initial theory, none of the efficient antennas (**2.2b**, **2.3b**, **2.5b**, **2.6b**) replace the two inner-sphere water molecules in Tb-DO3A. One could postulate that this lack of binding is due to steric hindrance around the two open coordination sites on the terbium ion.

Table 2.2. Luminescence lifetimes and corresponding hydration numbers (q) for Tb-DO3A and Tb-DO2A in the presence of hydroxylated antennas.

		Tb-DO3A				**Tb-DO2A**			
		τ_{H_2O} (ms)	τ_{D_2O} (ms)	q	Δq [a]	τ_{H_2O} (ms)	τ_{D_2O} (ms)	q	Δq [b]
2.1b	salicylate	1.04	1.76	**1.6**	**0.4**	1.08	2.38	**2.1**	**0.9**
2.2b	hydroxyisophthalate	1.14	2.19	**1.8**	**0.2**	1.05	2.33	**2.2**	**0.8**
2.3b	hydroxytrimesate	0.91	1.82	**2.3**	**-0.3**	1.05	2.24	**2.1**	**0.9**
2.4b	salicylamide	1.01	1.80	**1.8**	**0.2**	1.08	2.20	**2.0**	**1.0**
2.5a	hydroxyisophthalamide	0.99	2.22	**2.3**	**-0.3**	1.04	2.40	**2.3**	**0.7**
2.6a	hydroxytrimesamide	0.86	2.14	**2.9**	**-0.9**	1.02	2.12	**2.1**	**0.9**

Conditions: [Tb-DO3A or Tb-DO3A] = 50 µM and [antenna] = 500 µM, [Tris] = 10 mM for Tb-DO3A and 100 mM for Tb-DO2A, pH 7.2, λ_{em} = 545 nm, time delay = 0.1 ms, slit widths (excitation and emission) = 10 nm, T = 20 °C. Each value represents the average of 3 replicates (n = 3). [a] $\Delta q = q$Tb-DO3A - qTb-DO3A•antenna [b] $\Delta q = q$Tb-DO2A - qTb-DO2A•antenna

In the hope of favoring direct coordination of the hydroxylated antenna by replacing the two inner sphere water molecules, the less stable but less sterically hindered Tb-DO2A was selected. Coordination of the antenna using two of the three open coordination sites would .increase the luminescence of the ternary complex and the sensitivity of the probe. Opening one more coordination site does enable every hydroxylated antenna to coordinate the terbium, $\Delta q = 1 \pm 0.5$; however, in each case, two inner-sphere water molecules still remain (Table 2.2). Note that this does not necessarily indicate that the hydroxylated antennas do not coordinate the terbium ion in the case of Tb-DO3A. This experiment alone cannot distinguish between complete lack of ligation by the aromatic antenna (in which case the terbium would be solely complexed by the polyaminocarboxylate ligand) and coordination of the antenna in a salicylate (or other) binding mode concomitant with release of two carboxylate arms from the DO3A or DO2A ligand. Both cases results in a lanthanide complex with two inner-sphere water molecules. Also note that the conclusions from this system may not apply to other polyaminorcarboxylate lanthanide complexes. While investigating the ability of salicylate-based antenna to coordinate and sensitize a terbium complex with a tridimethylacetamide cyclen chelate; Gunnlaugsson and co-workers determined that the cationic complex does interact with negatively charged aromatic acid antenna through either a bidentate binding mode utilizing both oxygen of the carboxylic acids, a salicylate binding mode involving both the carboxylate and the phenolate, or in a monodentate version solely *via* the phenolate.[114, 119]

D. Monitoring production of hydroxyl radical

The purpose of these previous studies was to optimize the two component system for the detection of HO• by time-delayed luminescence with higher sensitivity. The ability of the isophthalate (**2.2a**), trimesate (**2.3a**), isophthalamide (**2.5a**), and trimesamide (**2.6a**) pre-antennas to detect a low steady-state concentration of HO• in the femtomolar range in the presence of Tb-DO3A is given in Figure 2.18. In each of the presented studies, HO• was generated by photolysis of H_2O_2 (irradiation $\lambda = 254$ nm). The near diffusion limited rate constant of HO• with aromatics systems (10^9 M^{-1} s^{-1})[80] results in the formation of hydroxylated antenna and ternary complex in the μM concentration range.

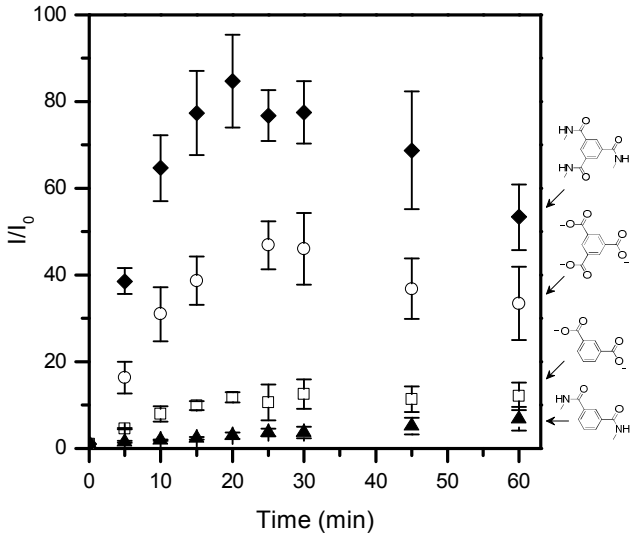

Figure 2.18. Relative time-delayed luminescence response (I/I_0) of Tb-DO3A in the presence of pre-antennas **2.2a** (open square), **2.3a** (open circle), **2.5a** (filled triangle), and **2.6a** (filled diamond) to HO• generated by photolysis of H_2O_2. Experimental conditions: [pre-antenna] = 103 μM, [H_2O_2] = 50 μM, photolysis wavelength = 254 nm. Phosphorescence conditions: [Tb-DO3A] = 12 μM, [pre-antenna] = 97 μM, [Tris] = 12 mM, pH 7.2, time delay = 0.1 ms, slit widths (excitation and emission) = 10 nm, T = 20 °C. Excitation wavelengths: **2.2a**, λ_{ex} = 333 nm; **2.3a**, λ_{ex} = 333 nm; **2.5a**, λ_{ex} = 331 nm; **2.6a**, λ_{ex} = 328 nm. I = integrated emission intensity from 470 – 635 nm. Results are mean ± SD (n = 3).

Given the brightness of the ternary complex and the dullness of the unreacted probe, this causes a substantial increase in luminescent intensity even with reaction times under 1 hour. Moreover, the initial linear response to HO• is indicative of the pseudo-zeroth order kinetics of the system, as is expected given the flooding conditions of antenna and the low, steady-state concentration of HO•. After 30 min, the relative time-delayed luminescence intensity increased by 77-fold in the presence of trimesamide (**2.6a**) and 46-fold with the trimesate (**2.3a**) pre-antenna. The isophthalate (**2.2a**) and isophthalamide (**2.5a**) pre-antennas yielded much lower increase in metal-centered emissions in the presence of HO•, 12-fold for **2.2a** and 4-fold **2.5a**. The increased sensitivity of the trimesate (**2.3a**) and especially the trimesamide (**2.6a**) pre-antennas over the isophthalate (**2.2a**) and isophthalamide (**2.5a**) are partly attributed to the symmetry of the 3a and 6a. For these pre-antennas, only one product can be formed upon reaction with HO•. Hydroxylation of isophthalate and isophthalamide, on the other hand, can occur at three different ring positions, only two of which favor lanthanide

coordination and sensitization. Moreover, the luminescence increase with the trimesamide system (**2.6a**) is significantly greater than with the trimesate (**2.3a**). The 77-fold increase in terbium luminescence with the use of trimesamide illustrate a distinct advantage of this second generation probe over the initial trimesate and Tb-DO3A detection system.[81] The decrease in luminescence intensity in the presence of the trimesamide (**2.6a**) antenna after 30 minutes of treatment with HO• is likely due to hydroxylation of the antenna at multiple sites, which further alters the excited state energy level of the antenna and reduces lanthanide sensitization. Importantly, the trimesamide (**2.6a**)/Tb-DO3A system is able to respond to HO• produced from the photolysis of biologically relevant concentrations of H_2O_2, as the biological concentration of H_2O_2 during periods of oxidative stress in an inflammatory environment is reported to reach *ca.* 100 μM.[5-6]

In comparison, the earlier detection system based on the fluorescence of hydroxylated terephthalate has an estimated detection limit of 50 nM,[102] although more recent systems can monitor HO• in the fM range.[103] A probe designed by Sho and co-workers has the advantage of monitoring HO• generated by Fenton chemistry with millimolar concentrations of H_2O_2 ratiometrically, although it is characterized by a limited turn-on of less than 4-fold.[120] Unfortunately, comparison of the sensitivity of this probe with other fluorescence-based HO• detection methods is problematic given the varying procedures used for the generation of HO•, such as Fenton chemistry or photolysis of H_2O_2 or $NaNO_3$. Moreover, the concentrations of the reagents or irradiation source power impact the amount of HO• produced, and the concentration of HO• are seldom measured or reported. Keeping this in mind, the sensitivity of the TbDO3A/trimesamide system remains comparable to or better than other luminescent probes reported.

E. Selectivity for hydroxyl radical over other ROS and RNS

Given the very low concentration of HO• in biological and environmental systems compared to other ROS and RNS, the selectivity of the probe *versus* these other reactive species is as crucial as the sensitivity of the probe. The ability of the trimesate (**2.3a**) and trimesamide (**2.6a**) pre-antennas to selectively respond to HO• over other ROS was investigated (Figure 2.19). In both cases, excellent selectivity was observed;

a greater than 180-fold or 75-fold selectivity for HO• over other ROS was observed for the trimesamide (**2.6a**) and trimesate (**2.3a**) pre-antennas, respectively, although substantially higher concentrations of the competing ROS/RNS were used. Importantly, the response to H_2O_2 and NO that are present at orders of magnitude higher concentrations and have longer life times *in vivo* is negligible.[3-4] This excellent selectivity was anticipated given the nature of the detection system. Hydroxylation of the antenna is key to adjusting the energy level of its triplet excited state so as to allow maximum energy transfer to the lanthanide ion. Since this hydroxylation is not possible with other ROS and RNS, these other species were postulated not to turn on the luminescence, hence the observed selectivity.

Comparison with other reported systems is limited since the selectivity of most probes for HO• over other ROS and RNS is seldom reported. Moreover, in most selectivity studies published, the concentration of HO• is typically irrelevant to biological or environmental conditions. In some of the most studied systems, selectivity for HO• toward other highly reactive species such as O_2^-, OCl^-, ^{t}ButO• limits the utility of the systems.[58, 77, 82] Since they respond to multiple oxidative species, these detection systems serve as general indicators of oxidative stress and not as probes for hydroxyl radical.[58, 77] Aside from our probe, the nitroxide radical based detection systems demonstrate the highest selectivity for HO•, but are unfortunately limited in that they detect not hydroxyl radical itself, but the products of the reaction of HO• with DMSO.[91] In comparison, the metal-centered luminescence intensity of the trimesamide (**2.6a**)/Tb-DO3A system showed excellent selectivity for a steady state concentration of HO• in the fM range, compared H_2O_2, O_2^- and NO in the mM range.

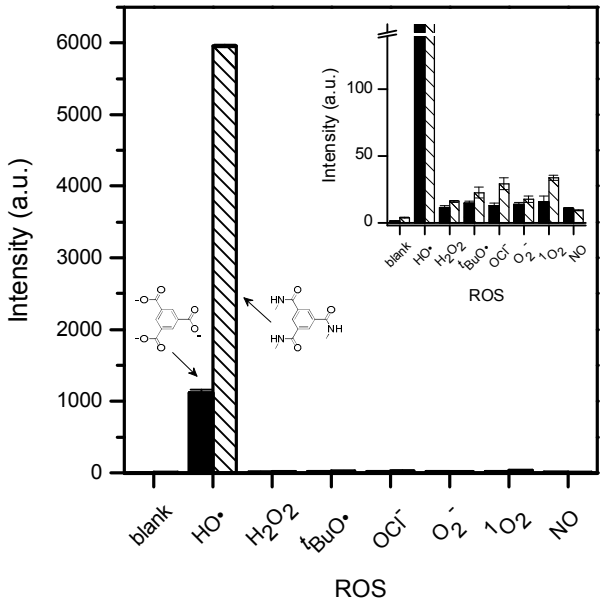

Figure 2.19. Selectivity of Tb-DO3A and **2.3a** (filled bars) or **2.6a** (striped bars) for HO• versus other reactive oxygen species. Experimental conditions: [**2.3a** or **2.6a**] = 103 μM, [HO•] = fM range, [H_2O_2] = 16.4 mM, [^{t}ButO•] = 2.0 μM, [OCl^-] = 103 μM, [O_2^-] = 3.9 mM, [$^1O_2$] = μM range, [NO] = 1.0 mM, reaction time = 30 min, photolysis wavelength = 254 nm, room temperature. Phosphorescence conditions: [Tb-DO3A] = 12 μM, [pre-antenna] = 97 μM, [Tris] = 12 mM, pH 7.2, time delay = 0.1 ms, slit widths (excitation and emission) = 10 nm, *T* = 20 °C. Excitation wavelengths: **3a**, λ_{ex} = 333 nm; **6a**, λ_{ex} = 328 nm. Blank = 100 μM **3a** or **6a**, 10 μM Tb-DO3A, 10 Mm Tris buffer. I = integrated emission intensity from 470 – 635 nm. Results are mean ± SD (*n* = 3).

III. CONCLUSIONS AND FUTURE WORK

Molecular probes for the time-delayed luminescence detection of HO• are discussed. The bimolecular probes consist of an aromatic acid that reacts with HO• to produce hydroxylated chromophores that readily interacts with Tb-DO3A and sensitizes lanthanide-centered emission. Of the six antenna investigated (benzoate, benzamide, isophthalate, isophthalamide, trimesate, and trimesamide), the trimesamide (**2.6a**) demonstrates the highest sensitivity with 77-fold increase in time-delayed luminescence upon reaction with steady state fM concentration of HO• after 30 min. In addition, the system displays excellent selectivity, greater than 180-fold, over other ROS and RNS species. The increase in luminescence intensity does not correlate with a decrease in the hydration number (*q*) of the terbium center for TbDO3A. Nonetheless, temperature-

dependent titrations confirmed the formation of a ternary complex, in which the antenna binds the terbium either by displacing two carboxylate arms or *via* a second sphere coordination environment. The turn-on mechanism, selectivity, and sensitivity of this system express significant gains over the first generation probe based on the reactivity of trimesate and Tb-DO3A time-delayed luminescence.[81]

The bimolecular nature of this probe is its primary disadvantage and hinders its use in cellular systems. For intracellular detection, a membrane permeable probe is required. Thus, the aim of future work is the synthesis of monomolecular probe in which the isothphalamide (or isophthalate) pre-antenna is conjugated to the polyaminocarboxylate ligand (Figure 2.20). The luminescence turn-on mechanism, which relies on altering the excited state energy level of the antenna upon hydroxylation is identical to the bimolecular systems. The selectivity of this probe for HO• is expected to be retained, due to the use of an aromatic pre-antenna as discussed above. However, an increase in sensitivity will likely result as the formation of a ternary complex between Tb-DO3A and the hydroxylated antenna will not rely on diffusion.

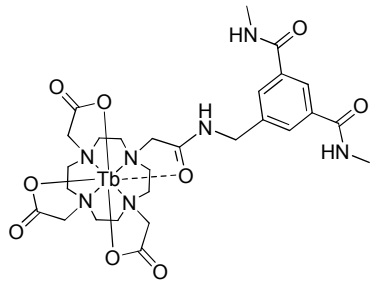

Figure 2.20. Chemical structure of the proposed monomolecular luminescent hydroxyl radical probe for cellular imaging.

Ideally, the probe could be targeted to the mitochondria where HO• are generated during cellular respiration. The high reactivity and small diffusion distance of this ROS necessitates targeting probes to the subcellular locations where the analyte is produced. This can be accomplished by conjugating the Tb-complex to a triphenylphosphonium ion, known to facilitate uptake of metal complexes into mitochondria based on differences in electric potential across the inner mitochondrial membrane.[121] These future probes will capitalize on the selective response of isophthalamide-based antennas to HO• and their ability to sensitize lanthanide luminescence.

IV. EXPERIMENTAL

General considerations. Chemicals were obtained from commercial suppliers and used without further purification, unless otherwise indicated. All solutions were prepared with deionized water further purified by a Millipore Simplicity cartridge system (18 MΩ). Experiments were conducted in air at ambient temperature, unless otherwise noted. pH measurements were taken using a Thermo Orion 3 Benchtop pH meter. Fluorescence and phosphorescent measurements were acquired on a Varian Cary Eclipse Fluorescence Spectrophotometer using a quartz cell with a path length of 1 cm, excitation and emission slit widths of 10 nm. Solutions were not degassed prior to measurement of their luminescence spectra and lifetimes.

The following pre-antennas and antennas are commercially available (Sigma-Aldrich) and were used without further purification: **2.1a**, **2.1b**, **2.2a**, **2.3a**, **2.4a**, and **2.4b**. The remaining pre-antennas and antennas, **2.2b**, **2.3b**, **2.5a**, **2.5b**, **2.6a**, and **2.6b** were synthesized according to published literature procedures.[92, 118, 122-124] Successful synthesis was established by ^{1}H NMR and ESI-MS. Tb-DO3A (1,4,7,10-tetra- azacyclododecane-1,4,7-tris(acetic acid)) and Tb-DO2A (1,4,7,10-tetra-azacyclododecane-1,7-bis(acetic acid)) were synthesized according to literature precedent for lanthanide carboxylate complexes.[118, 125-128] The *tert*-butyl protected DO3A and DO2A are commercially available (Macrocyclics).

Time-delayed luminescence intensity of Tb-DO3A with (pre)antennas (2.1a-2.6b). An aqueous solution of (pre)antenna (**2.1a**-**2.6b**) (400 μM) and Tb-DO3A (10.0 μM) in Tris buffer (10 mM, pH 7.2) was titrated into an aqueous solution of Tb-DO3A (10.0 μM) in Tris buffer (10 mM, pH 7.2). The time-delayed emission profile was recorded in the presence of 0 - 200 μM of (pre)antenna (**2.1a**-**2.6b**). Measurements were recorded with a time delay of 0.1 ms, excitation and emission slit widths of 10 nm, and at a temperature of 20 °C. The following excitation wavelengths were used: **2.1a/b**, λ_{ex} = 321 nm; **2.2a/b**, λ_{ex} = 333 nm; **2.3a/b**, λ_{ex} = 333 nm; **2.4a/b**, λ_{ex} = 324 nm; **2.5a/b**, λ_{ex} = 331 nm; **6a/b**, λ_{ex} = 328 nm. The luminescence response was reported as the integrated emission intensity from 470 – 635 nm. The experiment was repeated in triplicate (n = 3).

Luminescence lifetimes and hydration number (q). The luminescence decay of an aqueous solution of hydroxylated antenna, **2.1a**-**2.6b**, (500 μM), Tb-DO3A or Tb-DO3A (50 μM), and Tris (10 mM for Tb-DO3A and 100 mM for Tb-DO2A, pH 7.2) was measured. For measurements in D_2O, the samples were lyophilized and re-dissolved in D_2O three times prior to analysis. All decay measurements monitored the emission at 545 nm, using an initial time delay of 0.01 ms, delay increments of 0.1 ms or 0.2 ms, total decay time of 10 ms, and excitation and emission slit widths of 10 nm at a temperature of 20 °C. Luminescence lifetimes (τ) were determined by fitting the data to an exponential decay. The hydration number was calculated according to the following equation developed by Horrocks:[117] $q = 4.2[(1/\tau_{H_2O}) - (1/\tau_{D_2O})]$. Data was collected in triplicate (n = 3).

Effect of temperature on formation of the Tb-DO3A•hydroxytrimesamide ternary complex. An aqueous solution of antenna (**2.6b**) (100 μM) and Tb-DO3A (10.0 μM) in Tris buffer (10 mM, pH 7.2) was titrated into an aqueous solution of Tb-DO3A (10.0 μM) in Tris buffer (10 mM, pH 7.2). The time-delayed emission profile was recorded in the presence of 0 - 10 μM of antenna (**2.6b**). Measurements were recorded with a time delay of 0.1 ms, excitation wavelength of 328 nm, excitation and emission slit widths of 10 nm, and at temperatures of 10, 20, 40, 60, and 80 °C. The luminescence response was reported as the integrated emission intensity from 470 – 635 nm. At each temperature, the experiment was repeated in triplicate (n = 3).

Monitoring HO• produced by photolysis of H_2O_2. An aqueous solution of H_2O_2 (50 μM) and pre-antenna (**2.2a**, **2.3a**, **2.5a**, or **2.6a)** (103 μM) were added to a quartz cuvette. The solution (3 × 4 mL total volume) was then irradiated in the quartz cell for 1 h at 254 nm with a Spectroline hand-held UV lamp. An aliquot (1.00 mL) was removed from the irradiated cell at 0, 5, 10, 15, 20, 25, 30, 45, and 60 minutes. Tris buffer (12 mM, pH 7.2), and Tb-DO3A (12 μM) were added to the aliquot. The luminescence intensity was measured with a time delay of 0.1 ms, excitation and emission slit widths of 10 nm, and at a temperature of 20 °C. The following excitation wavelengths were used for luminescence measurements: **2.2a**, λ_{ex} = 333 nm; **2.3a**, λ_{ex} = 333 nm; **2.5a**, λ_{ex} =

331 nm; **2.6a**, λ_{ex} = 328 nm. The luminescence response is reported as the integrated emission intensity from 470 – 635 nm. The experiment was repeated in triplicate (*n* = 3).

Selectivity versus reactive oxygen species and reactive nitrogen species. ROS and RNS were administered to aqueous solutions of the pre-antennas (**2.3a** or **2.6a**) as described below. After stirring the reaction mixtures at room temperature for 30 min, Tris buffer, and Tb-DO3A were added to a 1000 µL aliquot of the reaction mixture resulting in the following final concentrations: Tris buffer (12 mM, pH = 7.2), Tb-DO3A (12 µM), pre-antenna (**2.3a** or **2.6a**) (97 µM). The luminescence intensity was measured with a time delay of 0.1 ms, excitation and emission slit widths of 10 nm, and at a temperature of 20 °C. The following excitation wavelengths were used for luminescence measurements: **2.3a**, λ_{ex} = 333 nm; **2.6a**, λ_{ex} = 328 nm. The luminescence response was reported as the integrated emission intensity from 470 – 635 nm. Each experiment was repeated in triplicate (*n* = 3).

Hydroxyl radical (HO•): An aqueous solution of H_2O_2 (50 µM) and pre-antenna (**2.3a** or **2.6a**) (103 µM) was irradiated in a quartz cuvette for 30 min at 254 nm using a Spectroline hand-held UV lamp.

Hydrogen peroxide (H_2O_2): An aqueous solution of H_2O_2 (16.4 mM) and pre-antenna (**2.3a** or **2.6a**) (103 µM) was stirred for 30 min at room temperature.

Tert-butoxy radical (^{t}BuO•): ^{t}BuO• was generated *in situ* according to the procedure of Winston.[129] Briefly, an aqueous solution of *tert*-butyl hydrogen peroxide (2.0 µM), $[Fe(bpy)_3(ClO_4)_2]$ = 0.52 µM, and pre-antenna (**2.3a** or **2.6a**) (103 µM) was stirred for 30 min at room temperature ***Caution:*** The iron perchlorate salt is potentially explosive and should be handled with care.

Hypochlorite (OCl^-): An aqueous solution of hypochlorite (103 µM) and pre-antenna (**2.3a** or **2.6a**) (103 µM) was stirred for 30 min at room temperature.

Superoxide (O_2^-): Solid KO_2 (1.1 mg, 0.015 mmol, 3.9 mM final concentration) was added to an aqueous solution of pre-antenna (**2.3a** or **2.6a**) (103 μM), and the reaction mixture was stirred for 30 min at room temperature. Note that the solid KO_2 was added directly to the solution of pre-antenna and not administered from a stock solution since the lifetime of O_2^- is insufficient to make stock solutions.

Singlet oxygen ($^1O_2$): An aqueous solution of Rose Bengal (0.52 μM) and pre-antenna (**2.3a** or **2.6a**) (103 μM) was purged three times with O_2 and stirred under irradiation with UV light using a 90 W Halogen Flood lamp for 30 min.

Nitric Oxide (NO): An aqueous solution of spermine NONOate (520 μM final concentration, delivered from a stock solution in 0.01 M NaOH) and pre-antenna (**2.3a** or **2.6a**) (103 μM) was adjusted to pH 5 with HCl and stirred for 30 min at room temperature. The reaction mixture was readjusted to pH 7.0 with NaOH prior to analysis

CHAPTER 3
FLUORINE MAGNETIC RESONANCE DETECTION OF HYDROXYL RADICAL

I. SYNOPSIS

Responsive fluorine contrast agents for the selective imaging of hydroxyl radical in water by ^{19}F MRI are evaluated. The ability to detect hydroxyl radical *in vivo* both sensitively and selectively is a yet unmet need, crucial to understanding the impact of this transient species and to developing therapeutic to reduce oxidative stress. Using the reactivity of HO• with aromatic acids, a fluorinated benzoic acid probe, CA-F_2, was developed. CA-F_2 reacts with HO• and enables sensitive and ratiometric detection of the reactive oxygen species with both ^{19}F NMR and MRI by monitoring the appearance of its reaction products relative to the disappearance of the reacting probe. Upon hydroxylation, two different products are formed with distinct chemical shifts +12 and +14 ppm upfield from the probe. The signal for the unreacted probe and those of the products can readily and independently be visualized by MRI allowing for ratiometric monitoring of HO•. The detection method is highly selective for HO• over other ROS and RNS. Next, the fluorinated aromatic acid was incorporated into paramagnetic, lanthanide-based fluorine contrast agents to increase sensitivity. As described by Bloch-Redfield-Wangsness theory, a proximal paramagnetic center increases sensitivity by enhancing relaxation rates of ^{19}F nuclei allowing more data to be collected per unit time. Unfortunately, these second generation contrast agents were hindered by either low water solubility or instability in the presence of HO•.

II. INTRODUCTION

A. Detecting hydroxyl radical by fluorine magnetic resonance

Direct *in vivo* detection of ROS presents an unmet need. The non-destructive, three-dimensional imaging capabilities of MRI make it the technique of choice for such experiments. However, only three responsive contrast agents for ROS (H_2O_2, NO, and HO•) have been reported (see Chapter 1, section III.B.2).[9, 108, 110] A hyperpolarized ^{13}C labeled benzoylformic acid is responsive to H_2O_2 (Figure 1.13), but requires exposure to high concentrations (200 – 1000 μM) of H_2O_2 for reactivity.[108] Phantom images were collected using 20 mM of the contrast agent, demonstrating the limited sensitivity of this system. For detection of NO, a water soluble PARACEST agent, Yb-DO3A-oAA, has been described that consists of a polyaminocarboxylate ligand with a pendant orthoaminoanilide (Figure 1.14)[9] Upon oxidation by NO, a nitroso intermediate initiates dimerization and eliminates the PARACEST signals of the exchangeable amide and amine protons. For this system, the detection threshold of unreacted Yb-DO3A-oAA is in the low millimolar range (3-6 mM). Complications in detecting the PARACEST response were encountered and demonstrate the need for methods to selectively saturate resonances with small offset frequencies. Additionally, the biomolecular nature of this detection system is not compatible with *in vivo* imaging.

The previously reported fluorinated probe for HO•, CF_3PAF, is a diamagnetic hydroxyphenyltrifluoroacetanilide (Figure 1.15). After 24 h incubation with 10 mM H_2O_2 and 50 μM Fe(II)DTPA, the reaction product (TFAM) was detected in the low micromolar range (20 μM).[110] However, this contrast agent is only capable of monitoring the reactive species by ^{19}F NMR. Further application of this probe to ^{19}F MRI is limited by the small differences (< 1 ppm) in resonance frequencies between the probe and the reaction products. Additionally, techniques to increase the sensitivity are needed to enable the detection of physiological concentrations of low abundance analytes.

Herein, a ^{19}F responsive MRI contrast agent for the ratiometric and selective imaging of hydroxyl radical by MRI is presented. The fluorinated contrast agent, CA-F_2, selectively responds to HO• forming characteristic products with substantially different fluorine chemical shifts (δ_F) such that each of them can be readily differentiated and

imaged not only by NMR but also by MRI. Further, the ^{19}F MR signals can be applied to the ratiometric MR imaging of HO•.

B. Advantages of fluorine magnetic resonance

Fluorine MRI and fluorinated contrast agents present multiple advantages over standard ^{1}H MRI for three-dimensional *in vivo* imaging. The fluorine nuclei (^{19}F, I = ½) is attractive due to its 100% abundance and high receptivity (83% of ^{1}H), which provide a sensitivity of detection comparable to that of ^{1}H nuclei. The similar gyromagnetic ratios (γ) of ^{19}F and ^{1}H allow images to be collected on standard ^{1}H MRI scanners after retuning the radiofrequency coils.[130] In addition, ^{19}F MRI has the primary advantage of avoiding interference with background signals as biological fluorine is negligible. Current ^{1}H gadolinium-based and magnetic iron oxide nanoparticle contrast agents detect differences in the relaxation rate of the water molecules associating with the contrast agent and ambiguity due to the high background of bulk water can arise.

In addition, ^{19}F nuclei are more sensitive to electronic and molecular changes, which produces a large chemical shift range (> 300 ppm). This facilitates the design of ratiometric fluorine contrast agents featuring two distinct resonances that can be independently imaged. The importance of ratiometric responses is paramount given that it is not possible to predict the distribution of a contrast agent *in vivo*. The observed signal is proportional to the concentration of the contrast agent and that of the biomarker, which can introduce uncertainty based on the non-uniform biodistribution of the imaging agent. False positives and false negatives due to higher and lower concentrations of contrast agents, respectively, can be observed with gadolinium-based responsive contrast agents because they are not ratiometric. For example, the same level of contrast can be generated by either a low local concentration of contrast agent and high levels of a biomarker or by a high concentration of contrast agent and low biomarker levels. Fluorine nuclei have a large chemical shift range, which allows ^{19}F MRI contrast agents to employ ratiometric detection methods to circumvent this problem. The ratio of these signals can then be used to determine the concentration of an analyte even if the concentration of the contrast agent is unknown.

Despite the advantages of ^{19}F MRS/ MRI, the primary limitation is the need for a high concentration of ^{19}F contrast agent (10-50 mM) for detection compared to ^{1}H MRI agents that affect the relaxation rate of bulk water molecules (~ 55 M).[131-132] The collection of images with high SNR is also hindered by the long longitudinal relaxation times, T_1, (0.5 - 3 s) of diamagnetic fluorine contrast agents that necessitate longer image acquisition times. Lastly, diamagnetic contrast agents typically experience small changes in chemical shifts ($\Delta\delta_F$ ~ 5 ppm) upon chemical perturbation.[132-133] Fluorinated contrast agents evade ambiguity from interfering background signals, require higher loading of contrast agent, and are applicable to the design of ratiometric responsive imaging agents for MRI. To meet the current objective of ratiometrically monitoring HO• in three dimensions, ^{19}F MRI is a suitable technique.

III. Results and Discussion

A. Responsive diamagnetic fluorine contrast agent for HO•

1. Contrast agent design and reactivity

The design of this fluorinated responsive contrast agent, CA-F_2, is based on the reactivity of HO• with aromatic acids[81, 134] and aryl fluorine (Figure 3.1).[135] It was hypothesized that upon hydroxylation of the aromatic ring, a change in ^{19}F chemical shift would be observed. At physiological pH, 3,5-difluorobenzoic acid, CA-F_2, is highly soluble in water and is characterized by a single ^{19}F singlet at δ_F = -110.6 ppm (Figure 3.2a). Reaction with HO• yields primarily two products: F^- anion and 5-fluoro-2,3-dihydroxybenzoic acid, CA-F$(OH)_2$. F^- is a common product of the reaction of aryl fluorides with hydroxyl radical.[135] The identity of the major aromatic product, CA-F$(OH)_2$, was confirmed through comparison with literature values of fluorinated aromatic acid products and mass-spectrometry.[136-139] Each of these two products has a distinct ^{19}F signal: F^- appears at δ_F = -122.5 ppm whereas CA-F$(OH)_2$ is characterized by a singlet at δ_F = -124.2 ppm (Figure 3.2b), allowing the abundance of either to be independently measured by ^{19}F MRI. Further, a ratiometric response can be obtained from signal intensity of the F^- product over that of the unreacted CA-F_2 contrast agent.

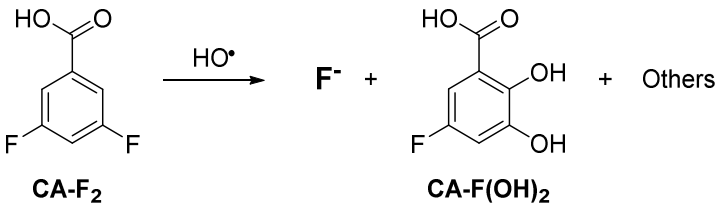

Figure 3.1. Chemical structure of the HO• responsive contrast agent, CA-F_2. Reaction with HO• generates primarily F^- and CA-$F(OH)_2$.

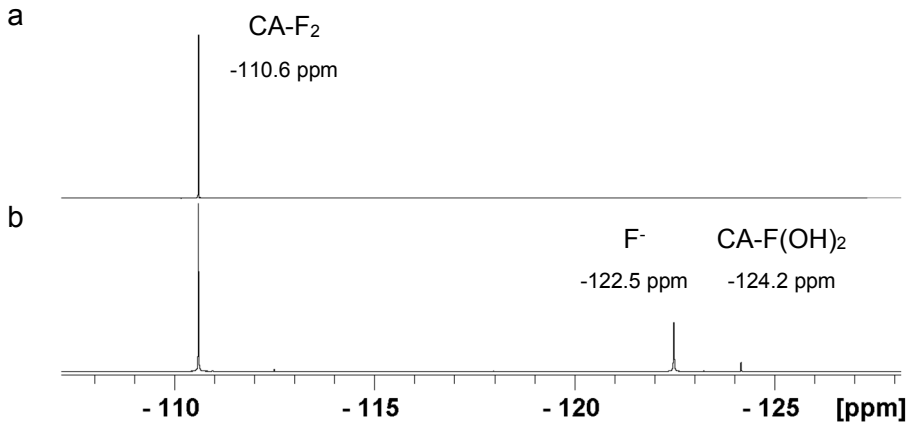

Figure 3.2. ^{19}F NMR spectra of CA-F_2 (a) before reaction and (b) after reaction with HO• generated from the photolysis of H_2O_2.

2. Monitoring the production of hydroxyl radical by ^{19}F NMR

The response of CA-F_2 to HO• is monitored by the unique ^{19}F resonances of the products formed: F^- and CA-$F(OH)_2$. Note that in the reaction of the contrast agent with HO•, CA-$F(OH)_2$ is not the only organic compound produced. Other side reactions allow for the formation of different aromatic compounds with different NMR spectra, although in most cases F^- is a by-product. Consequently, the F^- peak grows significantly more than that of CA-$F(OH)_2$, and the corresponding signal at δ_F = -122.5 ppm is more sensitive for monitoring the presence of HO• (Figure 3.3).

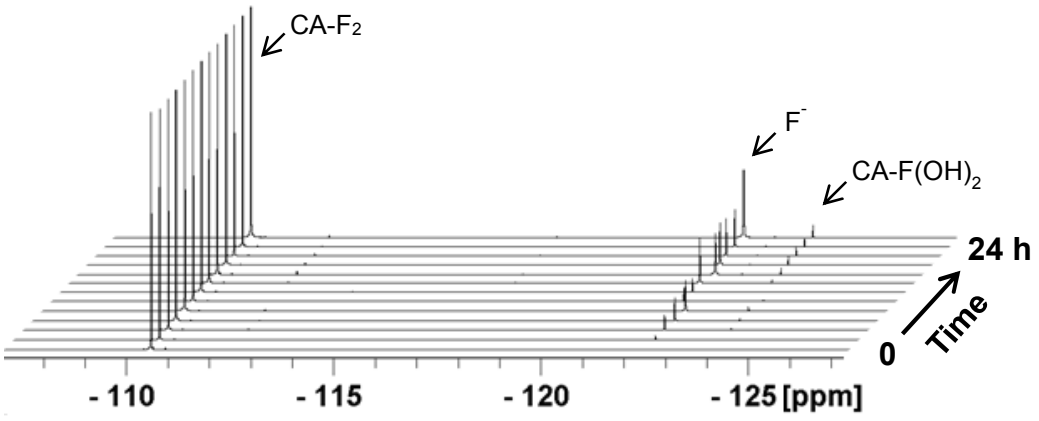

Figure 3.3. ^{19}F NMR spectra of aqueous solutions of CA-F_2 upon reaction with HO• generated by photolysis of H_2O_2. ^{19}F spectra are normalized to the δ_F = -110.6 ppm peak. Reaction time: 0, 2, 4, 6, 8, 10, 12, 14, 16, 18, 20, 22, and 24 h. Experimental conditions: [CA-F_2] = 50.0 mM, [H_2O_2] = 5.0 M, reaction time = 0 – 24 h, irradiation wavelength = 254 nm, *T* = 22 ˚C. NMR samples in D_2O, [DPO_4^{2-}] = 10.0 mM, pD = 7.4.

Importantly, the ability for CA-F_2 to detect HO• is independent of the method by which the ROS is generated; comparable responses were observed regardless of whether HO• was generated by photolysis of aqueous H_2O_2 (Figure 3.4) or by Fenton chemistry with Fe(II)EDTA (Figure 3.5). The reactivity of the contrast agent is key to achieving sufficient sensitivity to image low concentrations of HO• closer to biomedical relevance that are produced both at a steady state level during normal physiological functions and at elevated concentrations during periods of oxidative stress. As a result of the flooding conditions of the probe which is in large excess *versus* HO•, the steady-state generation of HO• by photolysis of H_2O_2 (*aq*) results in pseudo-zeroth order kinetics for the formation of the two products F^- and CA-F$(OH)_2$. Consequently, under these conditions, the concentrations of both products increase linearly with time (Figure 3.4). The combination of the near diffusion-limited rate constants of aromatic hydroxylation (10^9 M^{-1} sec^{-1})[80] with a sufficient reaction period (hours) allows the formation of both products in the micromolar range, a concentration sufficient for detection both by NMR and MRI (at > 11 T). However, it is important to note that for *in vivo* applications it is not feasible to flood the system with a large excess of contrast agent.

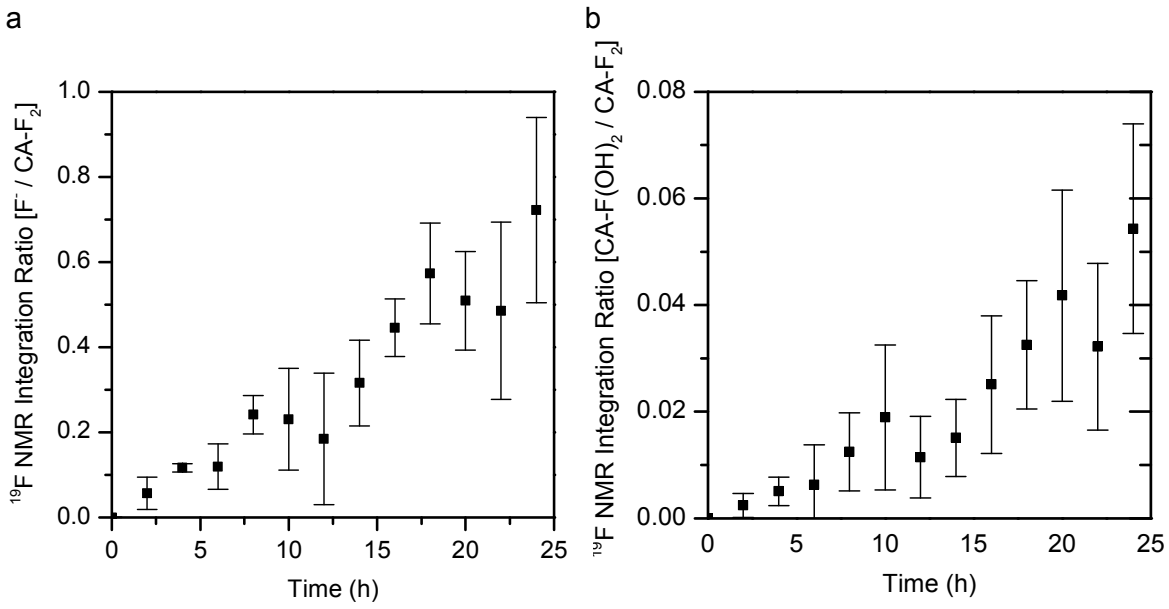

Figure 3.4. Turn on response of CA-F_2 as a function of HO• generated from photolysis of H_2O_2 with respect to reaction time measured by the ratio of (a) F^- (δ_F = -122.5 ppm) over CA-F_2 (δ_F = -110.6 ppm) or (b) CA-F$(OH)_2$ (δ_F = -124.2 ppm) over the starting material CA-F_2 (δ_F = -110.6 ppm). Experimental conditions: [CA-F_2] = 50.0 mM, [H_2O_2] = 5.0 M, reaction time = 0 – 24 h, irradiation wavelength = 254 nm, *T* = 22 ˚C. NMR samples in D_2O, [DPO_4^{2-}] = 10.0 mM, pD = 7.4. Results are mean ± SD (n = 4).

The limiting parameter is thus not the rate constant of the reaction between CA-F_2 and HO• but the concentration of HO•, which dictates how quickly the two products F^- and CA-F$(OH)_2$ can accumulate. Hydroxyl radical is primarily generated *in vivo* through the Fenton reaction between iron(II) complexes and hydrogen peroxide.[30] In this case, the concentration of HO• produced is proportional to the available H_2O_2 in the presence of a constant concentration of Fe^{2+} catalyst and higher concentrations of HO• are generated rapidly. Thus, the concentration of HO• is not at a steady state in the femtomolar range. This situation is analogous to the production of high local concentrations of HO• during inflammatory or host-defense responses. Consequently, during *in vitro* simulations the reaction does not need to be carried out for long periods of time and sufficient product signal can be observed by ^{19}F NMR in one hour (Figure 3.5).

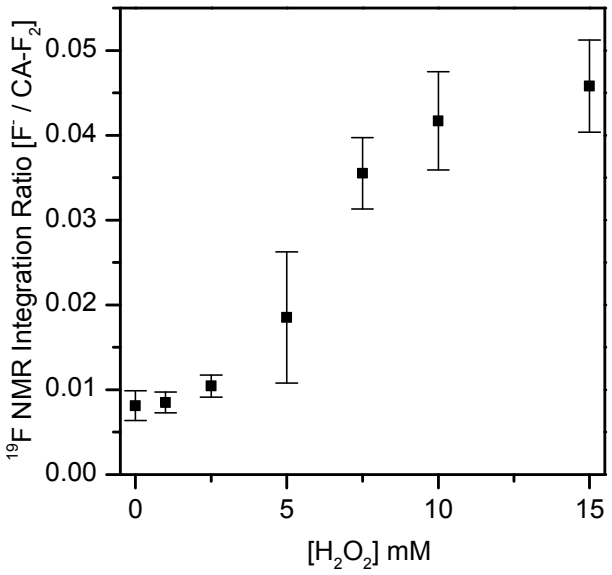

Figure 3.5. Turn on response of CA-F_2 as a function of HO• generated from Fenton chemistry. Ratio of F^- (δ_F = -122.5 ppm) over the starting material CA-F_2 (δ_F = -110.6 ppm). Experimental conditions: [CA-F_2] = 30.0 mM, [Fe(II)EDTA] = 3.00 mM, [H_2O_2] = 0 - 15 mM, reaction time = 1 h, *T* = 22 ˚C. NMR samples in D_2O, [DPO_4^{2-}] = 10.0 mM, pD = 7.4. Results are mean ± SD (*n* = 3).

3. Detecting hydroxyl radical production with ^{19}F MRI

The significant difference in the ^{19}F chemical shift of the starting probe and that of the two products allows the species to be independently monitored not only by NMR but also by MRI. The previously described ^{19}F MR agent for HO•, CF_3PF (Figure 1.15), generated products with small changes in chemical shift ($\Delta\delta_F$) of < 1 ppm that could not be resolved by MRI.[140] However, the products of CA-F_2 have resonances that are shifted by -12 and -14 ppm for F^- and CA-$F(OH)_2$, respectively. This allows the unreacted contrast agent and the products to be imaged separately.

Gradient echo ^{19}F phantom images monitoring the production of F^- and the disappearance of the starting contrast agent CA-F_2 after 0, 6, 12, and 24 h of H_2O_2 photolysis mirror the data collected by ^{19}F NMR spectroscopy (Figure 3.6). The signal intensity of the products, F^- (δ_F = -122.5 ppm) and CA-$F(OH)_2$ (δ_F = -124.2 ppm) increases with increasing reaction time, resulting in a brighter image (Figure 3.6). Simultaneously, the intensity of CA-F_2 image (δ_F = -110.6 ppm) decreases as the reaction proceeds. The primary advantage of the responsive contrast agent CA-F_2 is its application to MR imaging, a technique suitable for 3-dimensional *in vivo* detection.

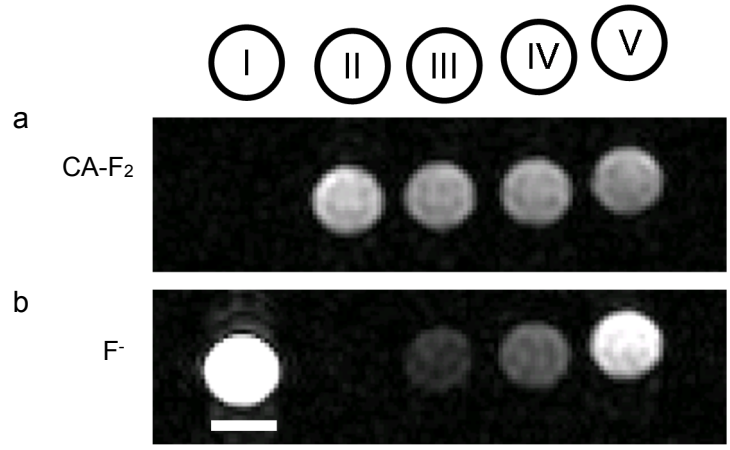

Figure 3.6. Gradient echo ^{19}F MR images obtained at 16.4 T of CA-F_2 upon reaction with HO• at (a) δ_F = -110.6 ppm, CA-F_2, (b) δ_F = -122.5 ppm, F^-. I. KF, and II. 0 h, III. 6 h, IV. 12 h, V. 24 h of photolysis at 254 nm. Experimental conditions: [CA-F_2] = 50.0 mM, [H_2O_2] = 5.0 M, pH = 7. Acquisition parameters: T_R = 400 ms, T_E = 3.23 ms, FOV = 2.0 cm × 2.0 cm, matrix = 64 × 64, slice thickness = 5 mm, flip angle = (a) 36°, (b) 42°, ns = (a) 64, (b) 256. Scale bar = 3 mm.

4. Selectivity for hydroxyl radical over other ROS and RNS

Importantly, CA-F_2 responds selectively to HO• over other biologically relevant reactive oxygen and nitrogen species. CA-F_2 has a limited response to reactive oxygen and nitrogen species, such as H_2O_2, O_2^- , $ONOO^-$, and NO, that are present at either higher concentrations or have greater diffusion distances and cellular lifetimes.[4] ^{19}F NMR analysis of solutions of CA-F_2 indicate that neither the F^- peak at δ_F = -122.5 ppm nor the CA-F$(OH)_2$ peak at δ_F = -124.2 ppm increase substantially in the presence of a large excess of each ROS and RNS after 2 hours of reaction (Figure 3.7). Notably, a higher selectivity is obtained by monitoring the weaker, less sensitive CA-F$(OH)_2$ signal (Figure 3.7b). Note that for all ROS and RNS except HO•, no CA-F$(OH)_2$ product could be detected upon addition of the competing ROS and RNS. Overall, when monitoring either product this system exhibits excellent selectivity for HO• over biologically-relevant ROS and RNS that are present at higher concentrations *in vivo*.

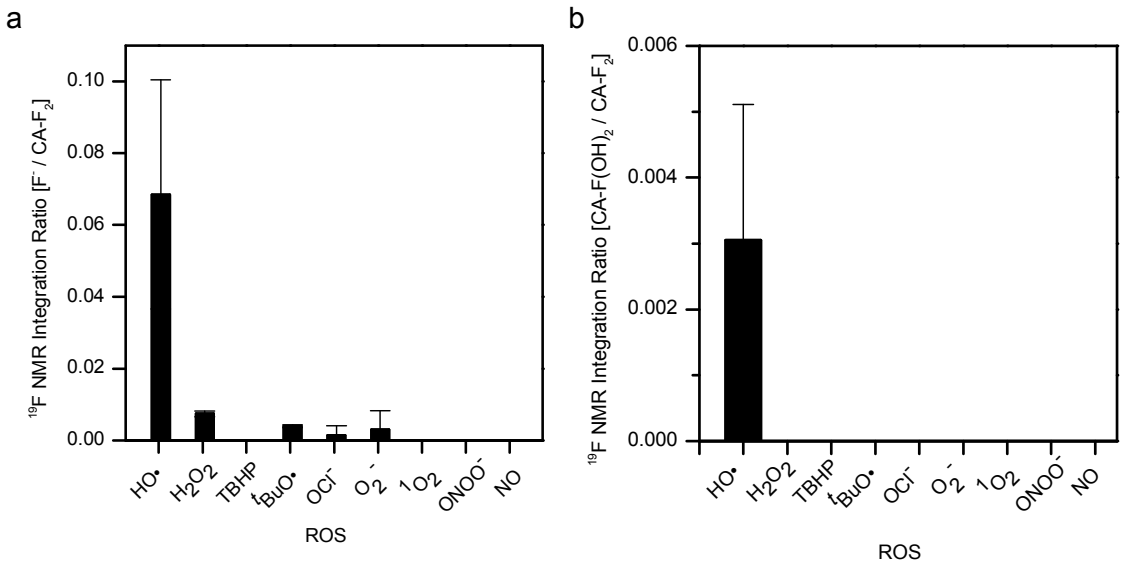

Figure 3.7. Selectivity of CA-F_2 responsive contrast agent for HO•. (a) Integration ratio of F^- over CA-F_2 and (b) integration ratio of CA-$F(OH)_2$ over CA-F_2 upon addition of competing reactive oxygen and nitrogen species. Experimental conditions: [CA-F_2] = 50.0 mM, [HO•] = fM range, [H_2O_2] = 5.0 M, [TBHP] = 2.5 M, [^{t}ButO·] = 250 mM, [OCl$^-$] = 250 mM, [O_2^-] = 250 mM, [$^1O_2$] = μM range, [NO] = 250 mM, [ONOO$^-$] = 50 mM, reaction time = 120 min, irradiation wavelength = 254 nm, T = 22 ˚C. NMR samples in D_2O, [DPO_4^{2-}] = 10.0 mM, pD = 7.4. Results are mean ± SD (n = 3).

5. Progress with diamagnetic fluorine contrast agents for HO•

In conclusion, the first responsive contrast agent for the ratiometric magnetic resonance imaging of hydroxyl radical is described. CA-F_2 reacts rapidly with HO• to generate two characteristic products, F^- and CA-$F(OH)_2$. The ratio of the ^{19}F signals directly enables ratiometric fluorine MR imaging of HO• even in conditions where the concentration of the contrast agent is unknown. The probe is selective for HO• over other biologically relevant ROS or RNS. Monitoring HO• with a method capable of three-dimensional *in vivo* detection represents a major advancement of this imaging agent over those previously described. Other detection methods based on the fluorescence properties of organic dyes,[58] lanthanide-based probes,[81-82] or nanoprobes,[72] are all limited to *in vitro* imaging of cells or tissue slices. However, CA-F_2 is limited by low sensitivity and the necessity for high (*i.e.* flooding) concentrations of contrast agent. Future fluorine probes must enhance sensitivity to be capable of unambiguous and direct imaging of HO• by MRI.

B. Increasing sensitivity with a paramagnetic lanthanide

Fluorine magnetic resonance imaging, particularly with organic compounds, suffers from low sensitivity. Signal intensity and signal-to-noise ratios (SNR) can be augmented when multiple chemically equivalent fluorine nuclei are incorporated into the imaging agent. This is one technique to marginally enhance the sensitivity of next generation ^{19}F MR probes for HO•. However, multiple ^{19}F resonances may be observed due to stereoisomers and the increased hydrophobicity can limit water solubility. Thus, an alternative approach to improve the sensitivity of ^{19}F probes relies on the relaxation enhancement induced by paramagnetic lanthanide metals.

Incorporating a lanthanide, or other paramagnetic metal, into a ^{19}F responsive contrast agent augments the relaxation rates of proximal fluorine nuclei and increases the sensitivity of detection. The T_1 of most diamagnetic ^{19}F reporters, like CA-F_2, are in the range of 0.5 - 4 s, which limits the amount of data that can be collected per unit time. Paramagnetic relaxation enhancement (PRE) has been shown to decrease T_1 by two orders of magnitude (from 1 s to 10 ms) offering increased sensitivity and higher SNR with a reduction in acquisition time.[131] The enhanced relaxation mechanisms at high magnetic fields are described by the Bloch-Redfield-Wangsness (BRW) Theory in terms of the electron-nucleus dipole-dipole and Curie relaxation processes.[131, 141-144] As a result, the longitudinal (R_1) and transverse (R_2) relaxation rates are defined by the following relationships (Equations 1-5):[141]

$$R_1 = \frac{2}{15}\left(\frac{\mu_0}{4\pi}\right)^2 \frac{\gamma_F^2 \mu_{\text{eff}}^2}{d^6}\left(\frac{7\tau_{R+e}}{1+\omega_e^2\tau_{R+e}^2} + \frac{3\tau_{R+e}}{1+\omega_F^2\tau_{R+e}^2}\right) + \frac{2}{5}\left(\frac{\mu_0}{4\pi}\right)^2 \frac{\omega_F^2 \mu_{\text{eff}}^4}{(3kT)^2 d^6}\ \frac{3\tau_R}{1+\omega_F^2\tau_R^2} \quad (1)$$

$$R_2 = \frac{1}{15}\left(\frac{\mu_0}{4\pi}\right)^2 \frac{\gamma_F^2 \mu_{\text{eff}}^2}{d^6}\left(4\tau_{R+e} + \frac{3\tau_{R+e}}{1+\omega_e^2\tau_{R+e}^2} + \frac{13\tau_{R+e}}{1+\omega_F^2\tau_{R+e}^2}\right) + \frac{1}{5}\left(\frac{\mu_0}{4\pi}\right)^2 \frac{\omega_F^2 \mu_{\text{eff}}^4}{(3kT)^2 d^6}\ \left(4\tau_R + \frac{3\tau_R}{1+\omega_F^2\tau_R^2}\right) \quad (2)$$

$$\mu_{\text{eff}}^2 = g_J^2\, \mu_B^2\, J(J+1) \quad (3)$$

$$\omega_e = \left(\frac{g_J \mu_B}{\hbar}\right) B_0 \quad (4)$$

$$\tau_{R+e} = (\tau_R^{-1} + T_{1e}^{-1}) \quad (5)$$

where d is the ^{19}F – Ln^{3+} distance, μ_0 is the vacuum permeability, γ_F is the gyromagnetic ratio of ^{19}F nuclei, T is the absolute temperature, and k is the Boltzmann constant. The

effective magnetic moment, μ_{eff}, is proportional to the effective electron g-factor (g_J), the Bohr magneton (μ_B), and the electron angular momentum, J(J+1) (Equation 3). The Zeeman frequency of fluorine is represented by ω_f, and the electron frequency (ω_e) is a function of the magnetic field strength (B_0) (Equation 4). The τ_{R+e} term is dependent on the rotational correlation time (τ_R) and the electron spin longitudinal relaxation time (T_{1e}) (Equation 5). Together these equations define the relationship of R_1 and R_2 to the effective magnetic moment (μ_{eff}) of the Ln^{3+} metal, the $^{19}F - Ln^{3+}$ distance (d), rotational correlation time (τ_R), field strength (B_0), and temperature (T). Thus, optimizing the sensitivity of ^{19}F MRS/ MRI agents requires understanding each of these relationships.

In terms of designing the next fluorinated contrast agent for HO•, the two most important parameters that impact relaxation are the effective magnetic moment (μ_{eff}) of the lanthanide metal and the $^{19}F - Ln^{3+}$ distance (d). Each lanthanide metal has a characteristic μ_{eff}/μ_B value (Table 3.1), and the highest values (μ_{eff} of ~ 10) for Tb^{3+}, Dy^{3+}, Ho^{3+}, and Er^{3+} allow them to more drastically enhance relaxation.[131] Indeed, a steeper increase in R_1 for Dy^{3+} and Ho^{3+} *versus* Tm^{3+}, Tb^{3+}, and Eu^{3+} with respect to field strength is observed,[131, 141] and the latter metals are likely better suited to application at higher field strengths (> 10 T). Additionally, both R_1 and R_2 relaxation rates have a steep d^{-6} dependence on distance. Therefore, controlling the $^{19}F - Ln^{3+}$ distance of probes is required to improve sensitivity. Harvey *et. al.* suggests an optimal distance of 5.5 – 7.5 Å.[131] If the ^{19}F nuclei is positioned too far from the Ln^{3+} center the relaxation is not affected; however, a $^{19}F - Ln^{3+}$ distance less than 5 Å causes a drastic enhancement in relaxation that contributes to signal reduction as a consequence of line broadening. The inequivalent coefficients for R_1 and R_2 (Equation 1 and 2) result in differential effects on the corresponding relaxation rates. Thus, the $^{19}F - Ln^{3+}$ distance can be adjusted to balance the positive and negative consequences of relaxation enhancement and achieve a T_2/T_1 ratio near unity.

Table 3.1. Magnetic and relaxation properties of lanthanide(III) ions.[131]

Lanthanide Ion	Ground state term	μ_{eff}/μ_B [a]	μ_{eff}/μ_B (exp) [b]	Electron relaxation time (T_{1e}) / 10^{-13} s [c]	Relative PCS strength [e]
Ce^{3+}	$^2F_{5/2}$	2.56	2.55	0.90	-6.5
Pr^{3+}	$^3H_4$	3.62	3.47	0.57	-11.4
Nd^{3+}	$^4I_{9/2}$	3.68	3.69	1.15	-4.5
Pm^{3+}	$^5I_4$	2.68	2.41	Unknown	2.4
Sm^{3+}	$^6H_{5/2}$	1.55-1.65	1.58	0.45	-0.5
Eu^{3+}	$^7F_0$	3.40-3.51	3.4	0.09	4.0
Gd^{3+}	$^8S_{7/2}$	7.94	7.63	10^4-10^5 [d]	0
Tb^{3+}	$^2F_6$	9.7	9.8	2.03	-87
Dy^{3+}	$^6H1_{5/2}$	10.6	10.3	2.99	-100
Ho^{3+}	$^5I_8$	10.6	10.4	1.94	-39
Er^{3+}	$^4H_{15/2}$	9.6	9.4	2.38	32
Tm^{3+}	$^3H_6$	7.6	7.6	3.69	53
Yb^{3+}	$^2F_{7/2}$	4.5	4.3	1.37	22

[a] Ref. [145] ; [b] Ref.[141-143, 146-147]; [c] aqua ion, 2.1 T, Ref. [148]; [d] Ref. [142]; [e] Ref.[149]

BRW theory correctly predicts that the identity of the Ln metal affects the relaxation rates of ^{19}F nuclei in studies with non-responsive complexes featuring polyamine macrocyclic ligands substituted with acetamide arms containing aryl or alkyl trifluoromethyl groups. When the lanthanide metal is varied, the observed fluorine relaxation rates correlate with the μ_{eff}/μ_B of the Ln metal.[31, 42-44] The strong relaxing metals (Tb^{3+}, Dy^{3+}, Ho^{3+}, and Er^{3+}) cause the greatest reduction in R_1 and R_2, and Eu^{3+}, Tb^{3+}, Dy^{3+}, and in the extreme case of Gd^{3+}, have a substantial effect on R_2 compared to R_1. The fast R_2 leads to highly broadened resonances that reduce the SNR. Due to the dependence of relaxation rates on field strength (B_0), strong relaxing ions are preferred at higher magnetic fields, while Tm^{3+} and Er^{3+} provide adequate relaxation enhancement above 7 T.[131, 141]

The increased relaxation rates, and corresponding decreased relaxation times, allow for the collection of more data per unit time. Thus, PRE increases spectral sensitivity and SNR in comparison to diamagnetic analogues. Chalmers *et. al.* demonstrated that the Dy^{3+} and Ho^{3+} complexes increased image SNR 10 to 15-fold compared to the diamagnetic Y^{3+} analogue.[150] The improved SNR correlates with a

T_2/T_1 ratio closer to 1, where the benefit of longitudinal relaxation is not diminished by signal broadening as a consequence of rapid transverse relaxation. Sensitivity gains of 15-20 times that of diamagnetic complexes can be achieved with fluorinated lanthanide-based contrast agents from 1.5 to 9.4 T.[131] This represents a major advancement in the field of ^{19}F MRI as sub-millimolar concentrations of contrast agent can be imaged in under 15 min with adequate SNR.[150] Utilizing paramagnetic relaxation enhancement in the design and function of responsive probes is thus a growing area of research.

C. Paramagnetic fluorine contrast agent for hydroxyl radical

1. Design and synthesis

The PRE effect described above is the basis for the improved sensitivity on a per ^{19}F basis of lanthanide-based probes as compared to their organic counterparts. Particularly effective are the lanthanide ions, such as Dy^{3+}, Ho^{3+}, and Tm^{3+} that substantially reduce T_1 and have a more limited influence on T_2. Second generation ^{19}F contrast agents, $[Dy\text{-}F_8]^{3+}$ and $[Tm\text{-}F_2]$ for HO• were envisioned that rely on PRE to improve sensitivity (Figure 3.8). Here, the lanthanides Dy^{3+} and Tm^{3+} are selected. Dy^{3+}, with a μ_{eff} of 10.3 (Table 3.1), strongly influences relaxation of ^{19}F nuclei and is reported by Chalmers, *et. al*. to have optimal T_2/T_1 ratios (~ 0.65) with macrocylic complexes containing aryl trifluromethyl groups appended to the amide arms.[150-151] Alternatively, Tm^{3+} (μ_{eff} = 7.6, Table 3.1) is a slightly weaker modulator of ^{19}F relaxation that is better suited for measurements at high magnetic fields. Also, non-responsive ^{19}F contrast agents that incorporated Tm^{3+} exhibited preferential T_2/T_1 ratios (~ 0.60).[150, 152]

Due to the high selectivity of CA-F_2 for HO•, a related fluorinated benzyl amide moiety was incorporated into $[Dy\text{-}F_8]^{3+}$ and $[Tm\text{-}F_2]$ for analyte response. The number of chemically equivalent difluorobenzyl groups was varied; the symmetrical $[Dy\text{-}F_8]^{3+}$ contains four analyte sensitive groups to further increase sensitivity over the mono-functionalized $[Tm\text{-}F_2]$. Calculation of the lowest energy geometry determined the Ln-^{19}F distances of $[Tm\text{-}F_2]$ to be 7.5 and 9.1 Å (Figure 3.9), which are slightly longer than the 5 - 7 Å range suggested by Parker.[131]

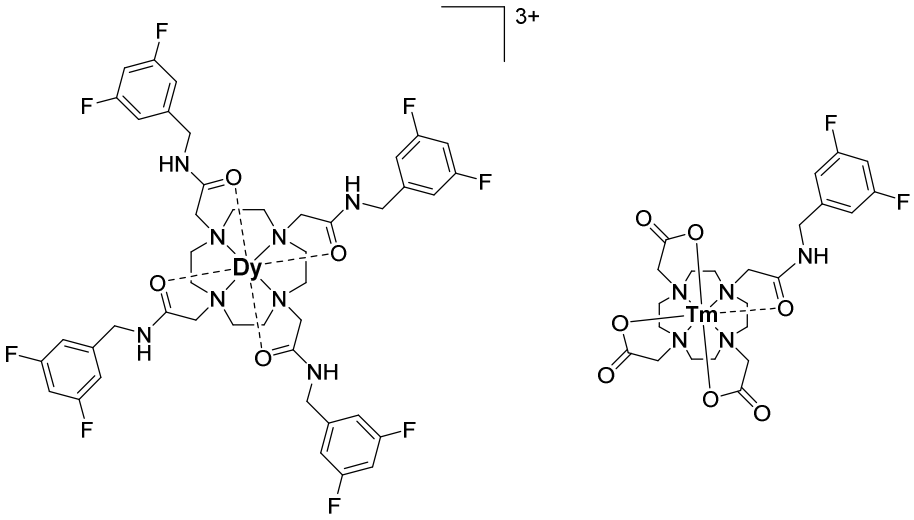

[Dy-F$_8$]$^{3+}$ **[Tm-F$_2$]**

Figure 3.8. Chemical structures of paramagnetic fluorine contrast agents [Dy-F$_8$]$^{3+}$ and [Tm-F$_2$] for the detection of HO•.

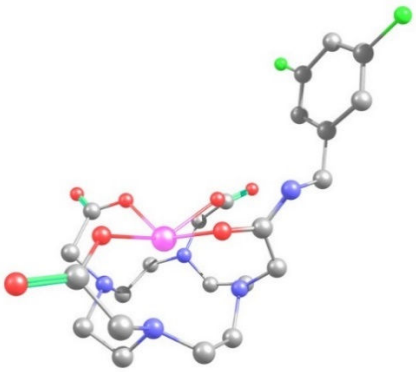

Figure 3.9. Optimized geometry of [Tm-F$_2$] determined ^{19}F-Ln distances of 7.5 and 9.1 Å. Tm (magenta), F (green), O (red), N (blue), carbon (grey),

A three step synthesis was employed to generate [Dy-F$_8$]$^{3+}$ (Scheme 3.1). First, 3,5-difluorobenzylamine was converted to the corresponding difluorobenzyl-bromoacetamide (**3.1**). Next, cyclen was fully substituted to afford the F$_8$ ligand (**3.2**) in a low yielding reaction. An alternative synthetic approach of coupling 3,5-difluoro-benzylamine to the four carboxylic acids on the macrocycle DOTA was unsuccessfully mediated by several activating agents (HATU and PyBOP). Heating the ligand with DyI$_3$

in a mixture of methanol and water at neutral pH for 20 h afforded the final complex, [Dy-F_8]$^{3+}$. Similarly, [Tm-F_2] was synthesized *via* mono-alkylation of cyclen with the fluorobenzyl pendant arm (**3.1**, Scheme 3.2). This reaction proceeded with moderate to good yields (*ca.* 60%) at room temperature, while the tetra-substitution in the synthesis of [Dy-F_8]$^{3+}$ required mild heating to functionalize the fourth nitrogen of the macrocyclic ring. Subsequent addition of *tert*-butylbromoacetate followed by deprotection under acidic conditions yielded the final ligand F_2 (**3.5**). The complex, [Tm-F_2], was obtained by heating with $TmCl_3$ in an aqueous solution at pH 7 for 3 d. Formation of both complexes, [Dy-F_8]$^{3+}$ and [Tm-F_2], was verified by ESI-MS, and their corresponding ^{1}H NMR spectra illustrated paramagnetism.

Scheme 3.1. Synthesis of [Dy-F_8]$^{3+}$.[a]

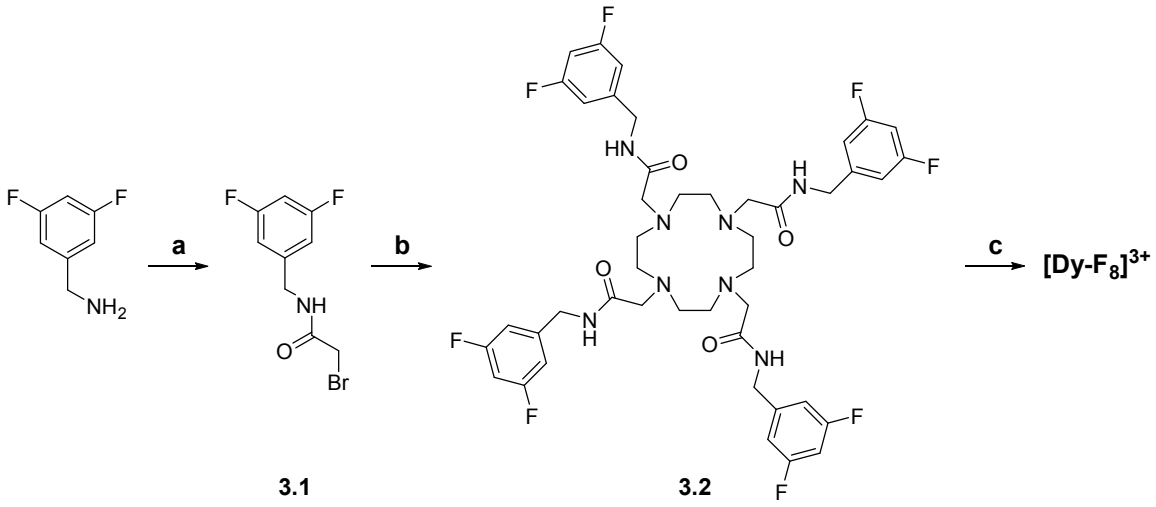

[a] Reagents and conditions: (a) K_2CO_3, CH_2Cl_2/H_2O (1:1), 22 °C, 2 h; (b) cyclen, K_2CO_3, CH_3CN, 50 °C, 48 h; (c) DyI_3, H_2O/CH_3OH, pH 7, 65 °C, 20 h.

Scheme 3.2. Synthesis of [Tm-F_2].[a]

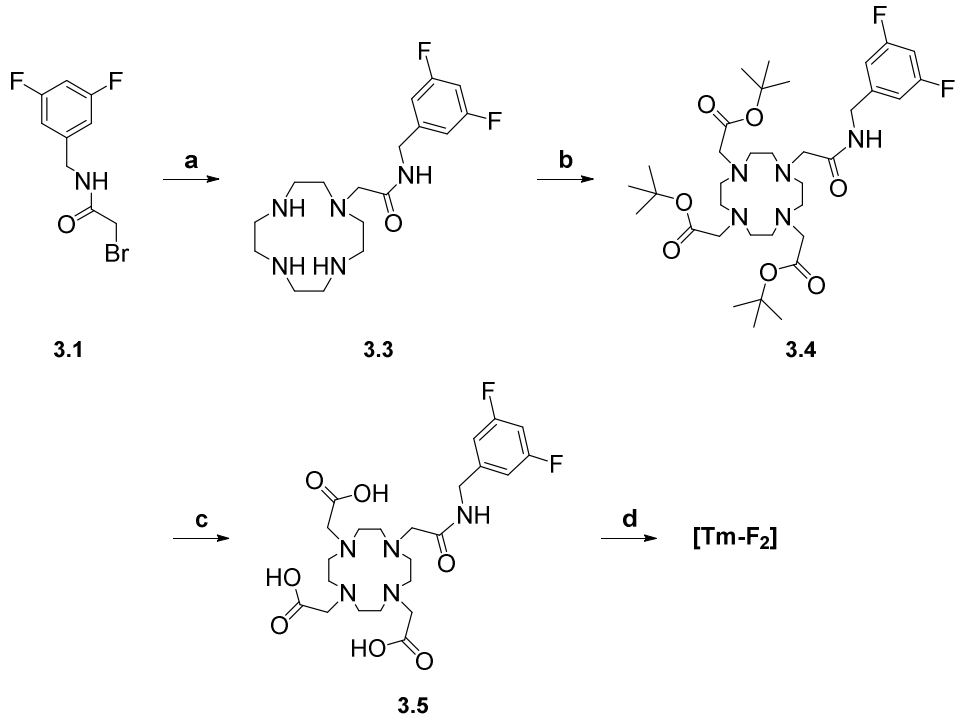

[a] Reagents and conditions: (a) cyclen, Cs_2CO_3, CH_3CN, 22 °C, 18 h; (b) *tert*-butyl bromoacetate, Cs_2CO_3, CH_3CN/DMF, 40°C, 18 h; (c) HCl, CH_3OH, 22 °C, 24 h; (d) $TmCl_3$, H_2O, pH 7, 45 °C, 3 d.

A lanthanide induced shift (LIS) of the fluorine resonances was observed for each complex. LIS is defined as the difference in chemical shift, Δδ, between a paramagnetic complex and its diamagnetic analog (*i.e.* the ligand): ($\Delta\delta = \delta_{para} - \delta_{dia}$). In terms of lanthanide-based fluorine probes, the observed shift is defined as the ^{19}FLIS. If the ^{19}F nuclei is at least 5 Å away from the Ln^{3+}, the pseudocontact shift (PCS) is a function of the lanthanide, its coordination environment, and the geometric relationship between the ^{19}F nuclei and the principal dipolar magnetic axis of the Ln^{3+} ion (Figure 3.10).

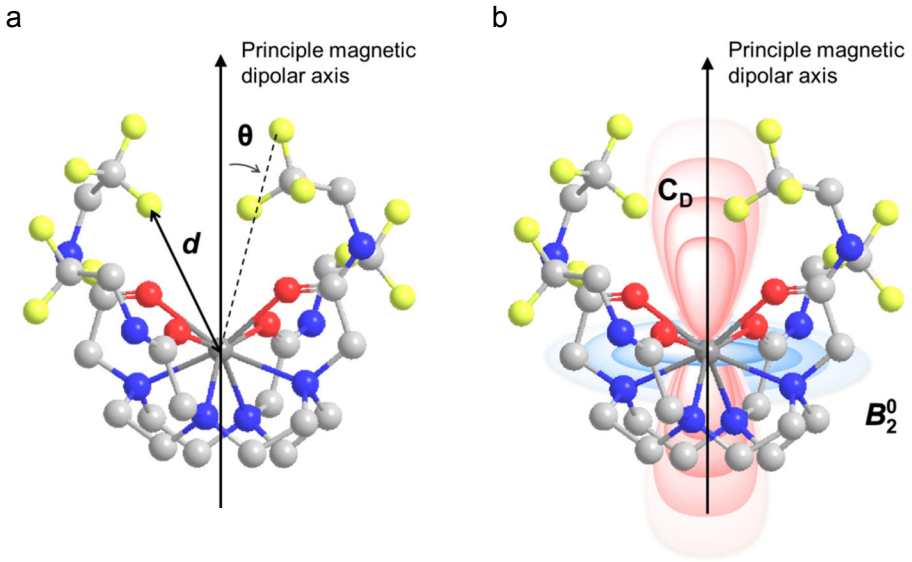

Figure 3.10. Model of a Ln-DOTAm complex with trifluoroethylacetamide substituents illustrating (a) the distance, *d*, between the Ln^{3+} ion and the ^{19}F nuclei and the angle, *θ*, between the Ln^{3+}-^{19}F vector and the principle magnetic dipolar axis of the lanthanide ion; and (b) the positive (red) and negative (blue) regions of the pseudocontact shift field around the Ln^{3+} ion.

This relationship is defined by the McConnell-Robertson equation (Equation 6):[131]

$$^{19}\mathrm{FLIS} = C_{\mathrm{D}} \frac{\beta^2}{60(\mathrm{kT})^2} \frac{(3\cos^2\theta - 1)}{d^3} B_2^0 \qquad (6)$$

where *d* is the Ln – ^{19}F distance, *θ* is the angle between the principal magnetic dipolar axis of the Ln^{3+} ion and ^{19}F nuclei, B_2^0 is the second order crystal field coefficient that is dependent on Ln^{3+} coordination environment, and C_D is the Bleaney constant for the specific lanthanide. Both the direction and magnitude of the shift are dependent on the identity of the lanthanide ion, allowing lanthanides to be ranked by their relative PCS strength (Table 3.1).

In the present study, the observed ^{19}FLIS of $[Dy\text{-}F_8]^{3+}$ (δ_F = -104.9 ppm) with respect to the F_8 ligand (**3.2**, δ_F = -111.4 ppm) is +6.5 ppm, while the fluorine resonance of $[Tm\text{-}F_2]$ (δ_F = -125.5 ppm) was shifted -14.5 ppm from the F_2 ligand (**3.5**, δ_F = -111.0 ppm). Each system displays opposing directions of $\Delta\delta_F$, mirroring the opposite signs of the Bleaney constants and PCS strengths of the respective Ln^{3+} ions. The $\Delta\delta_F$ induced by the Dy^{3+} complex is greater in magnitude than that of the Tm^{3+} complex, congruent with the -100 and +53 relative PCS strengths of the ions, respectively (Table 3.1). Additionally, the ^{19}FLIS value of the $[Tm\text{-}F_2]$ system agrees with

reported $\Delta\delta_F$ values of -12 to -28 ppm for non-responsive Tm^{3+} complexes.[150-152] ^{19}F NMR spectra of [Tm-F_2] were collected in deuterium oxide, while [Dy-F_8]$^{3+}$ was characterized in deuterated methanol (CD_3OD). In both cases, the ^{19}F NMR spectra were referenced to trifluoroethylamine (δ_F = -77.28 ppm). Unfortunately, [Dy-F_8]$^{3+}$ exhibited low water solubility. Comparison with structurally related complexes revealed that tetra-trifluoromethylbenzylacetamide substituted DOTAm complexes were also not soluble in fully aqueous solutions (NMR characterization was performed in mixture of 80% CD_3OD and 20% D_2O).[141] To meet the objective of a water soluble contrast agent for HO•, further studies were pursued with [Tm-F_2] complex.

The ^{19}F PRE induced by the Tm^{3+} was also investigated. As described by BRW theory, a lanthanide metal can increase the relaxation rates (and decrease the relaxation times) of nearby fluorine nuclei. Using the inversion recovery method, the T_1 of the diamagnetic CA-F_2 was determined as 4.1 s at 282 MHz. This agrees with reported T_1 values of aryl ^{19}F nuclei in the 3 - 4 s range at 376 MHz.[153] Note that T_1 is dependent on the field strength, and T_1 values of 1 - 2 s for aryl ^{19}F nuclei are typical at 470 MHz.[154] Incorporation of the paramagnetic Tm^{3+} metal in [Tm-F_2] was expected to substantially decrease T_1 in comparison with CA-F_2. Indeed, the T_1 of [Tm-F_2] was reduced to 49 ms at 470 MHz. These preliminary studies demonstrate the influence of Tm^{3+} on the relaxation rates of proximal ^{19}F nuclei in the current system.

2. Response to hydroxyl radical

Based on the results with CA-F_2, it was expected that hydroxylation of [Tm-F_2] would release F^- and form a hydroxylated product, and each would have a unique δ_F. However, when [Tm-F_2] is treated with HO• generated *via* the photolysis of H_2O_2, two resonances are observed by ^{19}F NMR. A resonance is present at either δ_F =-124.1 ppm or δ_F = -121.5 ppm for 2 h or 24 h reaction time, respectively, and an impurity is evident at -76.3 ppm (Figure 3.11). Further analysis of the reaction mixtures by ^{1}H NMR revealed the absence of paramagnetic character (Figure 3.12). ESI-MS confirmed the absence of [Tm-F_2] or other high molecular weight species (> 600 *m/z*) in the reaction mixture. To verify the stability of [Tm-F_2] with respect to H_2O_2, an aqueous solution of the complex was combined with 100 equivalents of H_2O_2 in the absence of UV light. After 2 h, the existence of [Tm-F_2] was confirmed by ^{1}H NMR, ^{19}F NMR, and ESI-MS.

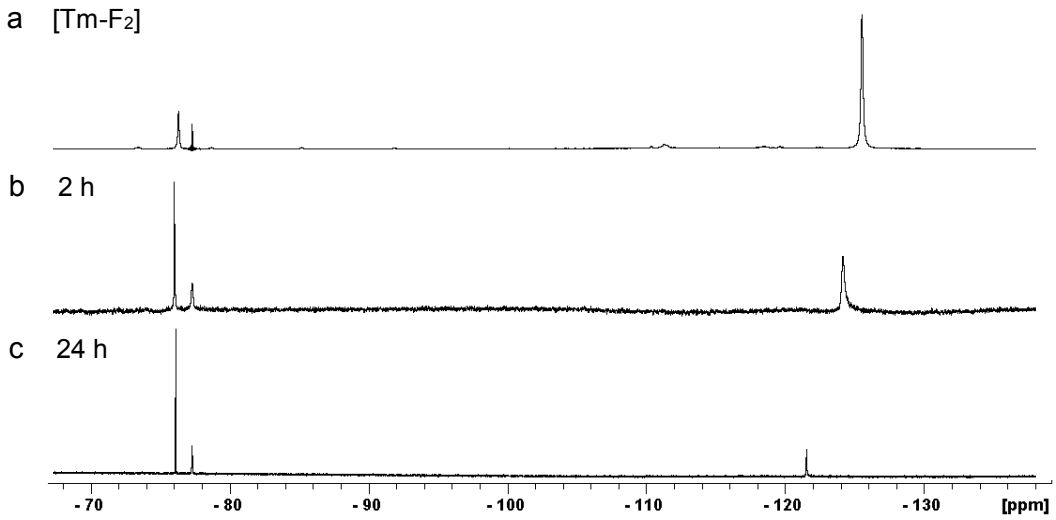

Figure 3.11. ^{19}F NMR spectra of (a) unreacted [Tm-F_2], the [Tm-F_2] reaction mixture after (b) 2 h or (c) 24 h of photolysis in the presence of H_2O_2. Experimental conditions: [Tm-F_2] = 5.0 mM, [H_2O_2] = 0.5 mM, photolysis wavelength = 254 nm. NMR samples in D_2O, [DPO_4^{2-}] = 10.0 mM, pD = 7.4, referenced to trifluoroethylamine (δ_F = -77.28 ppm). The peak at δ_F =-76.3 ppm corresponds to an unknown impurity.

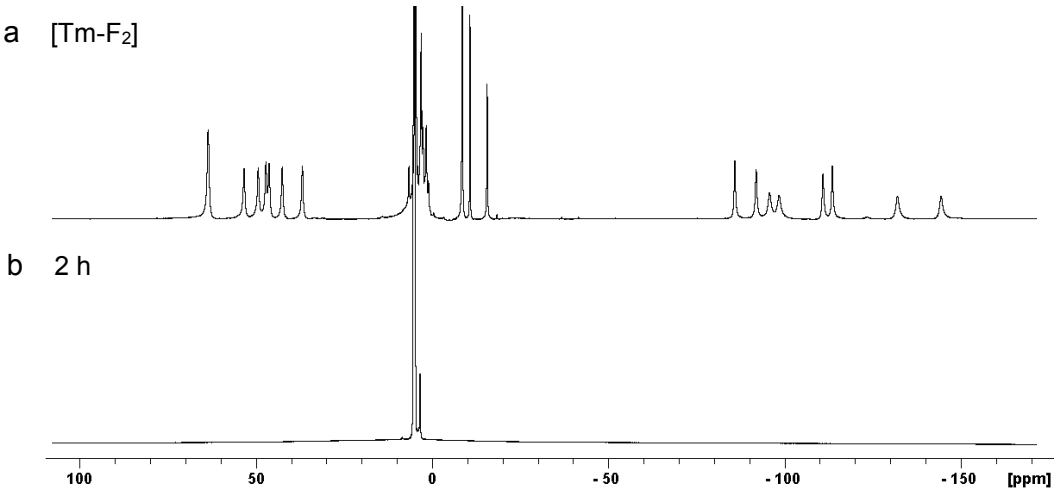

Figure 3.12. ^{1}H NMR spectra of (a) [Tm-F_2], and (b) [Tm-F_2] reaction mixture after 2 h of photolysis in the presence of H_2O_2. Experimental conditions: [Tm-F_2] = 5.0 mM, [H_2O_2] = 0.5 M. NMR samples in D_2O, [DPO_4^{2-}] = 10.0 mM, pD = 7.4.

This study indicates that [Tm-F_2] is stable with respect to H_2O_2 and is degraded in the presence of HO• generated from the photolysis of H_2O_2. It is hypothesized that HO• reacts with the polyaminocarboxylate ligand and degrades the complex, releasing the Tm^{3+} metal. A white precipitated formed upon dissolving the reaction mixture in phosphate buffer (10 mM, DPO_4^{2-}, pD 7.4) prior to NMR characterization. This is in concert with the insolubility of lanthanide phosphate salts. Degradation of metal-EDTA complexes by H_2O_2/UV processes are reported in the literature,[155] and the reaction of HO• with Ln-DPTA complexes occurs with fast rate constants ($k \sim 4 \times 10^9$ M^{-1} s^{-1}).[156]

The reactivity of [Tm-F_2] with HO• is surprising, especially when considering the reported lanthanide-based probes Tb-BMPTA,[82] Ln-AMTTA,[83] and trimesate/Tb-DO3A[81] for its detection (Figures 1.8 and 2.3). In the case of the bimolecular (pre)antenna and Tb-DO3A probes discussed in Chapter 2, the photolysis of H_2O_2 to generate HO• was performed only in the presence of the pre-antenna. The luminescence intensity was subsequently measured after the addition of Tb-DO3A to the reaction mixture. Using this protocol, degradation of the lanthanide complex by HO• would not be observed. As for Tb-BMPTA and Ln-AMTTA, they contain non-macrocylic polyaminocarboxylate ligands with coordinating aromatic amines. Sensitivity studies with these complexes were performed with HO• generated *via* Fenton chemistry, which does not involve UV light.[82-83] Therefore, the response of [Tm-F_2] to HO• generated by Fenton chemistry should be evaluated. Further instability of [Tm-F_2] to its analyte, HO•, will prevent its use as an imaging agent. As such, alternative strategies and contrast agent architectures must be employed to increase the sensitivity of HO• responsive ^{19}F MRI contrast agents.

IV. Conclusions and Future Work

Novel contrast agents for the magnetic resonance imaging of HO• are described. Hydroxylation of the diamagnetic probe CA-F_2 forms two products, F^- and CA-F$(OH)_2$, that can be monitored independently by ^{19}F NMR. Further the ratio of the ^{19}F signals of the products compared to that of the unreacted probe can ratiometrically monitor HO• by ^{19}F MRI. The ratiometric response and compatibility with ^{19}F MRI present major advantages of CA-F_2 over the previously reported ^{19}F NMR probe for HO•. In addition,

CA-F_2 exhibits excellent selectivity for HO• when treated with other ROS and RNS, including those existing at much higher concentrations *in vivo*. Despite the rapid reaction of HO• with CA-F_2, the probe suffers from low sensitivity and requires high concentrations of contrast agent.

To increase the SNR ratio, the paramagnetic ^{19}F contrast agents [Dy-F_8]$^{3+}$ and [Tm-F_2] were designed for the detection of HO•. Enhanced sensitivity and SNR was expected as a result of the PRE induced by the lanthanide metal. The complexes were synthesized over facile three or four step syntheses, respectively. Characterization of the complexes by ^{19}F NMR reported ^{19}FLIS in the direction predicted by the relative Bleaney co-efficient and relativity PCS strength of the lanthanide (Dy^{3+} or Tm^{3+}). PRE was also observed. The longitudinal relaxation time of [Tm-F_2] was reduced by *ca.* two orders of magnitude compared to the diamagnetic CA-F_2. Regrettably, the low aqueous solubility of [Dy-F_8]$^{3+}$ impeded further studies. On the other hand, [Tm-F_2] was water soluble, but decomposed upon treatment with HO• generated by the photolysis of H_2O_2.

Future studies include designing ^{19}F contrast agents for HO• with increased sensitivity that employ alternative approaches to PRE. BRW theory (Equations 1 and 2) demonstrates that the relaxation rates of fluorine atoms are affected by proximal paramagnetic metals and by the rotational correlation time (τ_R) of the imaging agent. Increasing τ_R of the probe with a macromolecular structure will cause a reduction in both R_1 and R_2. For the detection of HO•, difluorobenzyl moieties can be displayed on the surface of gold nanoparticles or incorporated into a hyperbranched polymer. There are limited examples of responsive macromolecular fluorinated contrast agents in the literature of despite the theoretical advantages of this approach.[157] A non-responsive example is a Dy^{3+} chitosan conjugate that amplifies the relaxation rates of the ^{19}F nuclei by both PRE and increasing τ_R.[158] However, diamagnetic macromolecular structures based on hyperbranched polymers, or dendrimers that incorporate a high number of ^{19}F nuclei have been designed as ^{19}F MRI contrast agents.[157, 159-166] These fluorinated structures have the benefit of decreasing T_1 as a result of the increased τ_R along with improving water solubility and *in vivo* retention. As such, application of this technique to ^{19}F MRI contrast agents can utilize the selectivity of the difluorobenzyl moiety for HO• and simultaneously improve sensitivity of detection.

V. EXPERIMENTAL

General considerations. Chemicals were obtained from commercial suppliers and used without further purification, including 3,5-difluorobenzoic acid which can be purchased from TCI or Sigma Aldrich. All aqueous solutions were prepared with distilled water purified by a Millipore Simplicity cartridge system (18 MΩ). Reactions and analyses were conducted in non-aerated solutions at ambient temperature, unless otherwise noted. NMR and mass spectrometry were performed in the LeClaire-Dow Instrumentation Facility and the Waters Center of Innovation for Mass Spectrometry, respectively, at the Department of Chemistry at the University of Minnesota–Twin Cities. NMR spectra were collected on a Bruker Biospin AG 500 Ascend Spectrometer at 500 MHz for ^{1}H and 470 MHz for ^{19}F. All ^{19}F spectra are ^{1}H decoupled. The residual solvent peak was used as an internal reference for ^{1}H NMR. Electrospray ionization mass spectra (ESI-MS) were measured on a Bruker BioTOF II. pH measurements were taken using a Thermo Orion 3 Benchtop pH meter.

A. Synthesis and Characterization

2-bromo-N-(3,5-difluorobenzyl)acetamide (3.1). Using an upright 3-neck flask, aqueous Cs_2CO_3 (5.60 g, 17.1 mmol) in water (15 mL) and bromoacetylbromide (557 µL, 6.40 mmol) in CH_2Cl_2 (15 mL) were added drop wise simultaneously over 10 min to 3,5-difluorobenzylamine (500 µL, 4.26 mmol) in CH_2Cl_2 (10 mL) at 0 ºC. Following the addition, the reaction mixture was stirred at room temperature for 2 h. The organic layer was washed with MQ water until the pH was approximately neutral (6 x 15 mL), brine (15 mL) and then dried over $MgSO_4$ and filtered. Removal of the solvent *in vacuo* yielded the product as a white powder (1.02 g, 3.89 mmol, 91% yield). ^{1}H NMR (500 MHz, $CDCl_3$, δ): 3.94 (s, 2H), 4.45 (d, J = 6.2 Hz, 2H), 6.73 (m, 1H), 6.80 (d, J = 5.8 Hz, 2H), 6.91 (s, 1H). ^{19}F NMR (470 MHz, $CDCl_3$, δ): -110.5 (s, 2F). ^{13}C NMR (125 MHz, $CDCl_3$, δ): 29.1, 43.5, 103.4 (t, J_{CF} = 25 Hz), 110.5 (dd, J_{CF} = 20, 6.0 Hz), 141.5 (t, J_{CF} = 9.0 Hz), 162.4 (d, J_{CF} = 13 Hz), 164.4 (d, J_{CF} = 13 Hz), 165.8 (s). HR-ESI-MS (*m/z*): $[M+H]^+$ calcd for $C_9H_8BrF_2NO$, 263.9830.; found, 263.9830.

2,2',2'',2'''-(1,4,7,10-tetraazacyclododecane-1,4,7,10-tetrayl)tetrakis(N-(3,5-difluorobenzyl)acetamide) (3.2). Under N_2, 2-bromo-N-(3,5-difluorobenzyl)acetamide (**3.1**, 280 mg,1.06 mmol) in anhydrous CH_3CN (15 mL) was added drop wise to cyclen (45.6 mg, 0.265 mmol) and K_2CO_3 (586 mg, 4.24 mmol) in anhydrous CH_3CN (15 mL) at 0°C. After stirring the reaction mixture at 50 °C for 48 h, the solid was removed by filtration, and the volatiles were removed under reduced pressure. The crude mixture was deposited onto silica and purified by flash chromatography (eluent: 0 – 10% MeOH in CH_2Cl_2) to yield the product as a wild solid (35 mg, 0.039 mmol, 7% yield). ^{1}H NMR (500 MHz, $(CD_3)_2O$, δ): 2.11 (m, 6H), 2.84 (m, 6H), 3.26 (m, 8H), 4.41 (s, 8H), 6.79 (t, J = 9.2 Hz, 4H), 6.98 (d, J = 6.5 Hz, 8H), 8.69 (bs, 4H). ^{19}F NMR (470 MHz, $CDCl_3$, δ): -111.4 (s, 8F). ^{13}C (125 MHz, CD_3OD, δ): 55.5, 56.4, 101.7 (t, J_{CF} = 25 Hz), 105.5 (dd, J_{CF} = 6.0, 20 Hz), 142.8 (app m), 143.7 (dd, J_{CF} = 12, 120 Hz), 172.0. ESI-MS (*m/z*): $[M+Na]^+$ calcd for $C_{44}H_{48}F_8O_4N_8$, 927.4; found, 927.5.

[Dy-F$_8$]$^{3+}$. In methanol (1 mL), the F_8 ligand (**3.2**, 14 mg, 0.016 mmol) and DyI_3 (8.4 mg, 0.016 mmol, 386 µL of an 40.2 mM aqueous solution) were combined. The pH was adjusted to 7 with dilute NaOH and the reaction mixture was heated at 65 °C for 20 h. The solvent was removed under reduced pressure to yield the product as a light yellow powder (16 mg, 0.015 mmol, quant. yield). ^{1}H NMR (500 MHz, CD_3OD, δ): selected peaks at -88.8, -47.5, 9.8, 12.6, 14.0, 19.0, 34.3, 36.7, 40.9, 46.1, 82.5, 130.4. ^{19}F NMR (470 MHz, CD_3OD, δ): -109.0 (s, minor conformer), -104.9 (s, major conformer). ESI-MS (*m/z*): $[M]^{3+}$ calcd for $C_{44}H_{48}F_8O_4N_8Dy$, 356.1; found, 356.1.

N-(3,5-difluorobenzyl)-2-(1,4,7,10-tetraazacyclododecan-1-yl)acetamide (3.3). Under N_2, the fluorinated bromoacetamide arm (**3.1**, 757 mg, 2.88 mmol) in anhydrous CH_3CN (15 mL) was added dropwise at room temperature to a solution of cyclen (1.98 g, 11.5 mmol) and Cs_2CO_3 (1.39 g, 4.27 mmol) in CH_3CN (30 mL) over 1 minute. The reaction mixture was stirred at ambient temperature for 18 h. The CH_3CN was removed under reduced pressure and the resulting oil was dissolved in $CHCl_3$ (20 mL). The organic layer was washed with 1 M NaOH (8 x 20 mL), distilled water (3 x 20 mL), and brine (1 x 20 mL), and then dried with $MgSO_4$ and filtered. The volatiles were removed

under reduced pressure to yield the product as a colorless oil (609 mg, 1.71 mmol, 60% yield). ^{1}H NMR (500 MHz, $CDCl_3$, δ): 2.79 (m, 18H), 4.45 (s, 2H), 6.68 (s, 1H), 6.92 (s, 1H). ^{19}F NMR (470 MHz, $CDCl_3$, δ): -111.1 (s, 2F). ^{13}C NMR (125 MHz, $CDCl_3$, δ): 43.6, 44.0, 45.7, 51.1, 56.7, 103.4 (t, J_{CF} = 25 Hz), 110.1 (dd, J_{CF} = 6.0, 19 Hz), 143.8 (t, J_{CF} = 8.0 Hz), 164.7 (dd, J_{CF} = 12, 250 Hz), 174.2. HR-ESI-MS (*m/z*): $[M+H]^+$ calcd for $C_{17}H_{27}N_5OF_2$, 356.2256; found, 356.2242.

(1,4,7,10-Tris-tert-butoxycaronylmethyl-1,4,7,10-tetraazacyclododecan-1-yl) difluorobenzylamide (3.4). Under N_2, *tert*-butylbromoacetate (156 µL, 1.06 mmol) in anhydrous CH_3CN (10 mL) was added drop wise to cyclen-F_2 conjugate (**3.3**, 160 mg, 0.344 mmol) and Cs_2CO_3 (1.19 g, 3.65 mmol) in a mixture of anhydrous CH_3CN (10 mL) and DMF (2 mL). Following the addition, the reaction mixture was stirred at 40 ºC for 18 h. The solid was removed by filtration, and the solvent removed under reduced pressure. The crude product was deposited onto silica and purified by flash chromatography (eluent: 0 – 10% MeOH in CH_2Cl_2) to yield the product as a yellow oil (140 mg, 0.20 mmol, 58% yield). ^{1}H NMR (500 MHz, $CDCl_3$, δ): 1.42 (m, 27H), 1.99-3.70 (bm, 24H), 4.43 (m, 2H), 6.63 (m, 1H), 6.89 (m, 2H), 9.69 (s, 1H). ^{19}F NMR (470 MHz, $CDCl_3$, δ): -112.5 (s, 2F, major conformer), -112.6 (s, 2F, minor conformer). ^{13}C NMR (125 MHz, $CDCl_3$, δ): 28.0, 28.3, 42.2, 52.7, 53.5, 55.7, 56.1, 82.1, 102.1 (app m), 110.3 (app d, J_{CF} = 19 Hz), 110.6 (app d, J_{CF} = 19 Hz), 144.4 (t, J_{CF} = 10 Hz), 163.1 (dd, J_{CF} = 11, 240 Hz), 170.6, 172.4. HR-ESI-MS (*m/z*): $[M+Na]^+$ calcd for $C_{35}H_{57}F_2N_5O_7$, 720.4118; found, 720.4103.

2,2',2''-(10-(2-((3,5-difluorobenzyl)amino)-2-oxoethyl)-1,4,7,10-tetraazacyclododecane-1,4,7-triyl)triacetic acid (3.5). A solution of HCl in MeOH (15 mL, 1.25 M) was added drop wise to the tris-*tert*-butyl-DO3A-F_2 (**3.4**, 103 mg, 0.148 mmol) in MeOH (2 mL). The reaction was stirred 24 h at room temperature. The solvent was removed under reduced pressure to yielding a light tan solid (78 mg, 0.14 mmol, quant. yield). ^{1}H NMR (500 MHz, D_2O, δ): 1.86-3.29. (bm, 24H), 4.18 (s, 2H), 6.55 (t, *J* = 9.1 Hz, 1H), 6.74 (d, *J* = 6.6 Hz, 2H). ^{19}F NMR (470 MHz, D_2O, δ): -111.0 (s, 2F). ^{13}C NMR (125 MHz, D_2O, δ): 42.0, 50.4, 51.0, 56.6, 58.5, 59.1, 102.2 (t, *J* = 18 Hz),

110.2 (app d, J_{CF} = 17 Hz), 143.4 (app m), 162.6 (dd, J_{CF} = 12, 240 Hz), 172.9, 179.7, 179.9. HR-ESI-MS (*m/z*): [M-3H+2Na]$^-$ calcd for $C_{23}H_{33}F_2O_7N_5$, 572.1914; found, 572.1864.

Tm-F$_2$. Aqueous $TmCl_3$ (464 µL of a 40.0 mM solution, 19.0 µmol) was added the DO3A-F_2 ligand (**3.5**, 10 mg, 19 µmol) in water (320 µL). The pH was adjusted to 7 with dilute NaOH, and the reaction mixture was incubated at 45 °C for 3 days. The solvent was removed under vacuum generating the complex as a white powder (13 mg, 19 µmol, quant yield). ^{1}H NMR (500 MHz, D_2O, δ): illustrates paramagnetism, selected peaks at -144.5, -132.2, -113.6, -111.0, -98.5, -95.8, -92.0, -86.0, -15.7, -10.8, -8.6, 1.6, 2.6, 2.9, 3.0, 6.5, 36.7, 42.4, 46.1, 47.0, 49.2, 53.3, 63.5. ^{19}F NMR (470 MHz, D_2O, δ): -125.5 (minor conformer), -76.3 (impurity). HR-ESI-MS (*m/z*): [M+Na]$^+$ calcd for $TmC_{23}H_{30}O_7N_5F_2$, 718.1348; found, 718.1352.

B. Experimental Methods

Generation of HO• via photolysis of H_2O_2. An aqueous solution of H_2O_2 (1.45 mL, 30% wt., 0.015 mol, 5.00 M final concentration, 100 eq) and water (50.0 µL) were added to an aqueous solution of CA-F_2 (1.50 mL, 100 mM, 0.150 mmol, 50.0 mM final concentration). The solution was transferred to a quartz cuvette and irradiated at 22 °C for 0 - 24 h at 254 nm using a Spectroline hand-held UV lamp (power = 0.20 amps). Reaction mixtures were immediately lyophilized and redissolved in D_2O, DPO_4^{2-} (10.0 mM, pD = 7.4) for NMR characterization. Experiments were repeated in quadruplate (n = 4), and outlying data points were evaluated and removed according to the Q-test with 90% confidence interval.

Generation of HO• via Fenton chemistry. An aqueous solution of Fe(II)EDTA (60.0 µL, 50.0 mM, 3.00 µmol, 3.00 mM final concentration, 0.10 eq) was added to an aqueous solution of CA-F_2 (300 µL, 100 mM, 30.0 µmol, 30.0 mM final concentration, 1 eq), H_2O_2 (0 – 157 µL, 0.30% wt., 0 – 0.015 mmol, 0 – 15.0 mM final concentration, 0 – 0.5 eq) and MQ water (12.0 – 640 µL, 5.0 mL final volume). Reaction mixtures were stirred for 1 h at

room temperature. The reaction mixtures were immediately concentrated to dryness and redissolved in D_2O, DPO_4^{2-} (10.0 mM, pD = 7.4) for NMR characterization.

Selectivity versus reactive oxygen or nitrogen species. ROS and RNS were administered to CA-F_2 in aqueous solutions as follows. Reaction mixtures were stirred at room temperature for 2 h, then immediately lyophilized and redissolved in D_2O, DPO_4^{2-} (10.0 mM, pD = 7.4) for NMR characterization. Experiments were repeated in triplicate (n = 3).

Hydroxyl radical (HO•): An aqueous solution of H_2O_2 (1.45 mL, 30% wt., 0.015 mol, 5.00 M final concentration, 100 eq) and water (50.0 µL) were added to an aqueous solution of CA-F_2 (1.50 mL, 100 mM, 0.150 mmol, 50.0 mM final concentration). The solution was transferred to a quartz cuvette and irradiated for 2 h at 254 nm using a Spectroline hand-held UV lamp (power = 0.20 amps).

Hydrogen peroxide (H_2O_2): An aqueous solution of H_2O_2 (1.45 mL, 30% wt., 0.015 mol, 5.00 M final concentration, 100 eq) and water (50.0 µL) were added to an aqueous solution of CA-F_2 (1.50 mL, 100 mM, 0.150 mmol, 50.0 mM final concentration). ^{t}BuOOH (TBHP): An aqueous solution of *tert*-butyl hydrogen peroxide (347 µL, 70% wt., 7.20 M, 2.50 mmol, 2.50 mM final concentration, 50 eq) and water (153 µL) were added to an aqueous solution of CA-F_2 (500 µL, 100 mM, 0.050 mmol, 50.0 mM final concentration).

Hypochlorite (OCl^-): An aqueous solution of hypochlorite (179 µL, 4.5% wt., 1.40 M, 0.250 mmol, 0.25 mM final concentration, 5 eq) and water (321 µL) were added to an aqueous solution of CA-F_2 (500 µL, 100 mM, 0.050 mmol, 50.0 mM final concentration).

Superoxide (O_2^-): KO_2 (18.0 mg, 0.250 mmol, 250 mM final concentration, 5 eq) and water (500 µL) were added to an aqueous solution of CA-F_2 (500 µL, 100 mM, 0.050 mmol, 50.0 mM final concentration).

Tert-butoxy radical (^{t}BuO•): *Tert*-butoxy radical was generated according to previously published procedure [129]. $Fe(bpy)_3(O_4Cl)_2$ (9.0 mg, 0.013 mmol, 12.5 mM final concentration, 0.25 eq), an aqueous solution of TBHP (34.7 µL, 70% wt., 7.20 M, 0.250 mmol, 250 mM final concentration, 5 eq), and water (465 µL) were added to an aqueous solution of CA-F_2 (500 µL, 100 mM, 0.050 mmol, 50.0 mM final concentration).

Nitric Oxide (NO): Spermine NONOate (241 µL, 254 mM in 0.01 M NaOH, 0.0625 mmol, 125 mM final concentration, 2.5 eq) and water (9 µL) were added to an aqueous solution of CA-F_2 (250 µL, 100 mM, 0.025 mmol, 50.0 mM final concentration). The reaction mixture was adjusted to pH < 5 with concentrated HCl (12 M) and stirred at room temperature.

Peroxynitrite ($ONOO^-$): SIN-1 (260 µL, 121 mM, 0.025 mmol, 50.0 mM final concentration, 1 eq) and water (44.0 µL) were added to an aqueous solution of CA-F_2 (250 µL, 100 mM, 0.025 mmol, 50.0 mM final concentration).

Singlet oxygen ($^1O_2$): An aqueous solution of Rose Bengal (1.00 mL, 2.00 µM, 2.00 nmol, 1.00 µM final concentration) was added to an aqueous solution of CA-F_2 (1.00 mL, 100 mM, 0.100 mmol, 50.0 mM final concentration). The solution was purged three times with O_2 and stirred under irradiation with UV light using a 90 W Halogen Flood lamp for 2 h.

MRI. Magnetic resonance images of samples in 3 mm NMR tubes were acquired on a 16.4-T, 26-cm horizontal bore magnet (Magnex Scientific, Oxford, UK) interfaced with a Varian Direct Drive console (Varian, Palo Alto, CA, USA). The magnet was equipped with a gradient insert capable of reaching 1000 mT/m in 150 µs (Resonance Research, Inc., Billerica, MA). A linear surface coil (12 mm diameter) tunable to both ^{1}H (698.1 MHz) and ^{19}F (656.8 MHz) frequency was used to transmit and receive the signal. ^{1}H gradient echo images were acquired using following parameters: repetition time

(T_R) = 20 ms, echo time (T_E) = 2.98 ms, field of view (FOV) = 2 cm x 2 cm, matrix = 256 x 256, slice thickness = 5 mm, flip angle = 20°. ^{19}F gradient echo images were acquired using following parameters: T_R = 400 ms, T_E = 3.23 ms, FOV = 2 cm x 2 cm, matrix = 64 x 64, slice thickness = 5 mm, excitation pulse = 5 ms Gauss. Images at -120 ppm were acquired with flip angle = 36°, number of scans (ns) = 64, acquisition time = 27 min. Images at -110 ppm were acquired with flip angle = 42º, ns = 256, acquisition time = 1 h 50 min.

Geometry calculations of Tm-F_2. Geometry optimization was carried out using Gaussian09[167] with B3LYP functional by employing the 6-31G(d) basis set for the light elements (H, C, N, O and F) and the quasirelativistic effective core potential (RECP) of Dolg et al.[168-169] and the related [5s4p3d]-GTO valence basis set for the Tm. This RECP accommodates 46+4fn electrons in the core for the lanthanide and the outermost 11 electrons are treated explicitly. Such RECP has been earlier used in DFT studies to understand the structure and energetics of the lanthanide complexes.[170]

Response of Tm-F_2 to HO•. An aqueous solution of H_2O_2 (25.5 μL, 30 wt%, 0.250 mmol, 0.500 M final concentration, 100 eq) and MilliQ water (290.5 μL) were added to an aqueous solution of Tm-F_2 (184 μL, 13.6 mM, 2.50 μmol, 5.00 mM final concentration). The solution was transferred to a quartz cuvette and irradiated for 2-24 h at 254 nm using a Spectroline hand-held UV lamp (power = 0.20 amps). Reaction mixtures were immediately lyophilized and redissolved in D_2O, DPO_4^{2-} (10.0 mM, pD = 7.4) for NMR characterization.

CHAPTER 4
CELLULAR COMPATIBILITY OF LANTHANIDE COMPLEXES

I. SYNOPSIS

A systematic study of the effect of the hydrophobicity and charge on the cell viability and cell association of lanthanide metal complexes is presented. The terbium luminescent probes feature a macrocyclic polyaminocarboxylate ligand (DOTA) in which the hydrophobicity of the antenna and that of the carboxyamide pendant arms are independently varied. Three sensitizing antennas were investigated in terms of their function *in vitro*: 2-methoxyisophthalamide (IAM(OMe)), 2-hydroxyisothalamide (IAM), and 6-methylphenanthridine (Phen). Of these complexes, the Tb-DOTA-IAM exhibited the highest quantum yield, although the higher cell viability and more facile synthesis of the structurally related Tb-DOTA-IAM(OMe) platform renders it more attractive. Further modification of this latter core structure with carboxyamide arms featuring hydrophobic benzyl, hexyl, trifluoro groups as well as hydrophilic amino acid based moieties generated a family of complexes that exhibit high cell viability (EC_{50} > 300 μM) regardless of the lipophilicity or the overall complex charge. Only the hexyl substituted complex reduced cell viability to 60% in the presence of 100 μM complex. Additionally, cellular association was investigated by ICP-MS and fluorescence microscopy. Surprisingly, the hydrophobic moieties did not increase cell association in comparison to the hydrophilic amino acid derivatives. It is thus postulated that the hydrophilic nature of the 2-methoxyisophthalamide antenna (IAM(OMe)) disfavors the cellular association of these complexes. As such, responsive luminescent probes based on this scaffold are appropriate for the detection of extracellular species.

II. INTRODUCTION

A. Luminescent lanthanide probes for biological imaging

Luminescent metal complexes are increasingly employed as biomolecular and cellular probes due to their unique photophysical properties that make them particularly well suited to monitor biological processes.[171-174] Examples include not only complexes of transition metals such as Pt, Ir, and Ru, but also those that incorporate lanthanides, most commonly Eu and Tb.[33, 111, 174] In particular, the long luminescence lifetimes of the emitting metal mitigates the interference of background fluorescence originating from the biological sample. Moreover, since the large energy difference between the absorbing and emissive states of lanthanide complexes removes self-absorption issues, their luminescence signal intensity is proportional to their concentration over a wide range of values. With this in mind, lanthanide-based molecular probes have been applied to the detection of reactive oxygen species (ROS),[82-83, 175-176] redox active metals,[116, 177] pH,[178-179] and intracellular analytes, such as ATP.[180] The continued applications of such metal-based luminescent probes, however, further rely on the ability to limit their cellular association altogether for certain tissue imaging experiments or, alternatively, to direct them to specific cellular regions. Prior studies indicate that structural and chemical properties of metal complexes, such as their size and hydrophobicity, influence their cell viability and cellular association, including their membrane permeability.[49-52, 54] Although cell-penetrating peptides have been applied to increase the cell uptake of lanthanide complexes,[181-182] the goal of this project is to modify the intrinsic properties of the metal complex to control cellular association. Presented here is a systematic study to evaluate the effects of structural variations on a core structure common to most luminescent lanthanide probes and an investigation of the practicality of such probes for cellular and tissue applications requiring extracellular imaging agents.

The most common platform of luminescent lanthanide complexes features a chelating polyamino carboxylate ligand substituted with one or more carboxamide pendant arms from which additional moieties are attached, notably the probe's antenna. The Laporte-forbidden nature of the f-f transition dictates that for practical applications in

biologically relevant settings, the probe must incorporate a sensitizing antenna. In terms of the design of a responsive probe, the luminescence intensity of the lanthanide complex can then be modulated by altering, among other parameters, the excited triplet state energy level of the antenna and the antenna-lanthanide distance.[33, 112] For biological applications, it is thus important to select an antenna with suitable energetic properties for lanthanide sensitization that is also resistant to quenching by the medium. Work by Parker and coworkers identified that the nature of the antenna, specifically its point of attachment to the cyclen backbone of the ligand, affects the subcellular localization of the complexes.[52] This work focused primarily on azaxanthone and other extended aromatic antenna.[51-52, 54, 183-185] Given the increasing use of phenanthridine and isophthalamide antenna for the design of luminescent lanthanide probes,[115, 118, 180, 186-187] a deeper understanding of the structural parameters influencing their effect on cellular viability and cell association is necessary to further optimize their structures for biological application both extra- and intracellularly.

B. Complex architecture for systematic study

Herein, two parameters were evaluated for their effect on cell viability and association: the nature of the antenna and that of the pendant amide arms. Each complex features a luminescent Tb^{3+} ion chelated by a DOTA(m)-type ligand. The macrocyclic polyaminocarboxylate ligand provides kinetic inertness, and thus predicted lower toxicity on cell viability.[34] Furthermore, the overall positive charged lanthanide complexes of DOTA tetraamide (DOTAm) ligands are kinetically more inert than DOTA analogues as a result of the decreased basicity of the nitrogen atoms.[35] Moreover, the macrocyclic framework are less susceptible to enzymatic degradation.[38] The high kinetic inertness of macrocyclic lanthanide complexes and their ability to resist degradation is critical for their use *in vivo*. Three different antenna were investigated: the hydrophilic 2-hydroxyisophthalamide, IAM, a reported sensitizer of both Tb and Eu;[115, 118] the closely related and synthetically more facile 2-methoxyisophthalamide, IAM(OMe); and the extended aromatic 6-methylphenanthridine, Phen (Figure 4.1). For each complex, the quantum yield, cellular viability, and cell association were evaluated. The effect of charge

and hydrophobicity on cell viability and association was subsequently evaluated with complexes comprising the IAM(OMe) antenna functionalized with varying carboxamide arms (Figure 4.2).

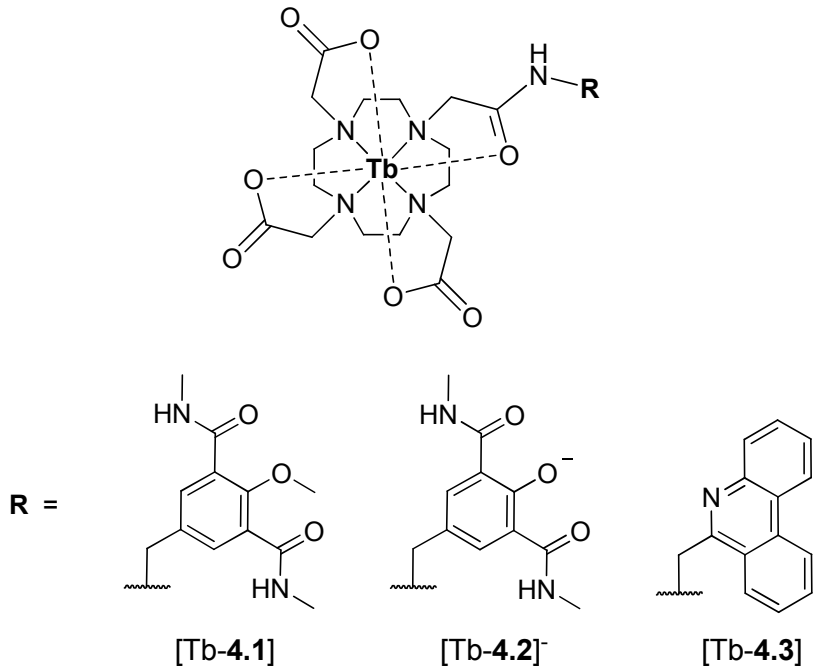

Figure 4.1. Chemical structures of Tb-DOTA-IAM(OMe) ([Tb-**4.1**]), Tb-DOTA-IAM ([Tb-**4.2**]$^-$), and Tb-DOTA-Phen ([Tb-**4.3**]).

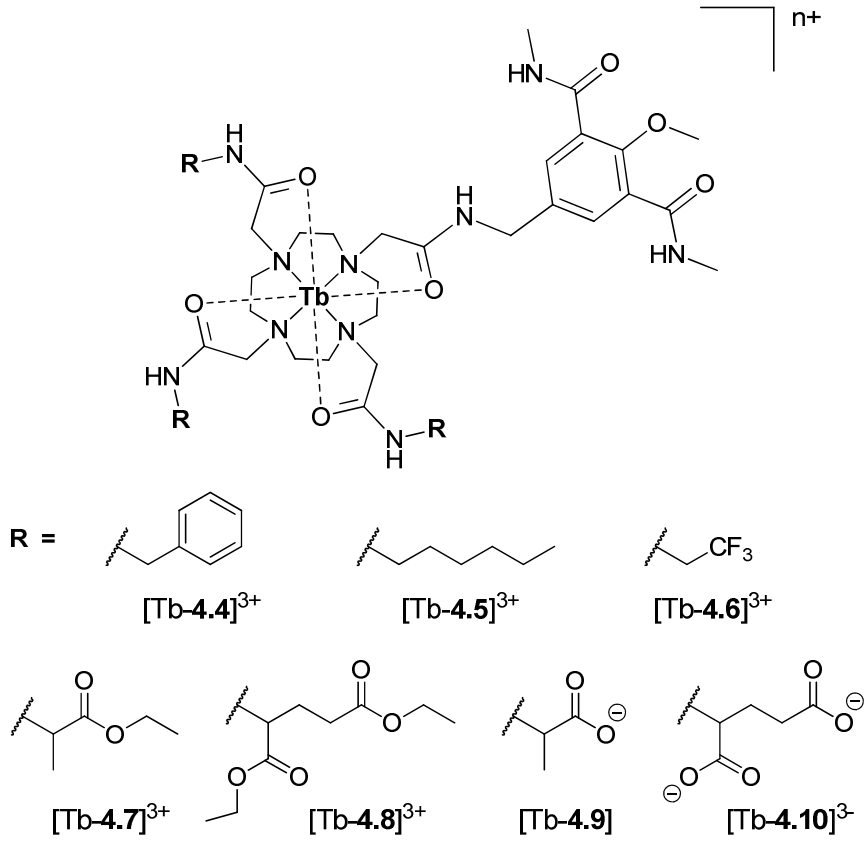

Figure 4.2. Chemical structures of derivatives of [Tb-**4.1**] with varying charge and hydrophobicity. All modifications were performed on the pendant arm.

III. RESULTS AND DISCUSSION

A. Synthesis of lanthanide complexes

The isophthalamide complexes Tb-DOTA-IAM(OMe) ([Tb-**4.1**]) and Tb-DOTA-IAM ([Tb-**4.2**]$^-$) were synthesized according to Scheme 4.1. Briefly, the oxidation of bis(hydroxymethyl)-*p*-cresol with MnO_2 and KOH generated the diacid **4.11**. Subsequent treatment with methyl iodide generated the methoxy protected diester **4.12**, which was then converted to the diamide **4.13** with methyl amine. The aldehyde **4.14** was generated *via* a Riley oxidation of the aryl methyl group in naphthalene at 215 °C. Periodinane oxidation methods (Dess-Martin and 2-iodoxybenzoic acid),

permananganates, and chromates (Jones' reagent and PCC) were unsuccessful mediators of this transformation. Reaction of the aldehyde **4.14** with hydroxylamine hydrochloride generated the oxime **4.15**, which was crystalized by addition of diethyl ether to an acidic solution of the crude reaction mixture in ethyl acetate and methanol, and then reduced to the amine form of the IAM antenna **4.16**. The tris-BOC protected cyclen **4.17** was synthesized as reported,[188-189] and further coupled to the amine **4.16** using HATU as the activating agent. BOC deprotection in a mixture of hydrochloric acid/methanol afforded the IAM(OMe) cyclen conjugate **4.19**, which served as a common intermediate in the synthesis of [Tb-**4.1**], [Tb-**4.2**]$^{-}$, and [Tb-**4.4**]$^{3+}$ – [Tb-**4.10**]$^{3-}$.

Alkylation of the cyclen derivative **4.19** with *tert*-butyl bromoacetate yielded the protected ligand, **4.20** (Scheme 4.1). Deprotection in a mixture of hydrochloric acid/methanol yielded the free ligand DOTA-IAM(OMe), **4.1**. Harsher deprotection conditions with boron tribromide removed both the *tert*-butyl groups and the aryl methyl ether to yield DOTA-IAM, **4.1**. The final complexes [Tb-**4.1**] and [Tb-**4.2**]$^{-}$ were obtained from their respective ligands, **4.1** and **4.2**, by heating with $TbCl_3$ in aqueous solutions at neutral to slightly basic pH for two or more days.[190-191] The phenathridine complex, [Tb-**4.3**], was synthesized according to the published procedure.[180, 186]

In order to evaluate the role of charge and hydrophobicity of the lanthanide complex on its cellular compatibility, seven derivatives of Tb-DOTA-IAM(OMe) ([Tb-**4.1**]) were synthesized (Figure 4.2 and Scheme 4.1). The synthesis was designed to take advantage of the common intermediate **4.19**, described above. Each bromoacetamide arm was synthesized using a biphasic method in which bromoacetylbromide in dichloromethane and aqueous potassium carbonate were simultaneously added dropwise to a solution of the corresponding amine in dichloromethane at 0 °C. This method resulted in moderate to high yields (65 – 85%) of the desired products in high purity. The ligands were obtained upon reaction of the bromoacetamide arms with the intermediate **4.19**. Metallation with $TbCl_3$ at neutral pH yielded [Tb-**4.4**]$^{3+}$ – [Tb-**4.8**]$^{3+}$. The carboxylic acid derivatives [Tb-**4.9**] and [Tb-**4.10**]$^{3-}$, were obtained by saponification of their corresponding esters, [Tb-**4.7**]$^{3+}$ and [Tb-**4.8**]$^{3+}$, respectively.

Scheme 4.1. Synthesis of Tb-DOTA-IAM(OMe) ([Tb-**4.1**), Tb-DOTA-IAM ([Tb-**4.2**]$^{-}$), complexes with varying charge and hydrophobicity ([Tb-**4.4**]$^{3+}$ – [Tb-**4.10**]$^{3-}$).[a]

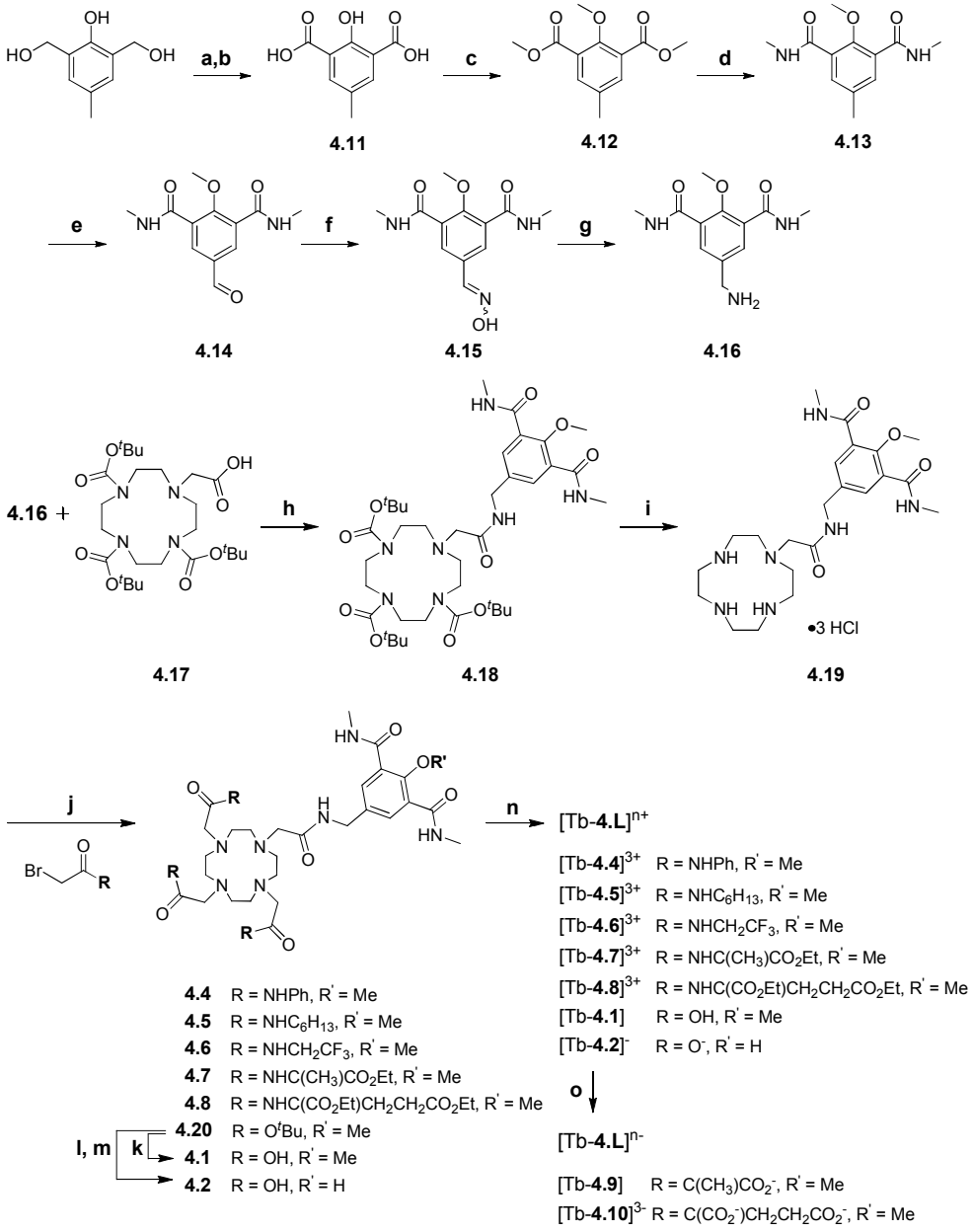

[a] Reagents and conditions: (a) MnO_2, CH_3Cl, 60 °C, 20 h; (b) KOH (s), 230 °C, 1 h; (c) CH_3I, K_2CO_3, acetone, 56 °C, 16 h; (d) NH_2CH_3, CH_3OH, 65 °C, 18 h; (e) SeO_2, naphthalene, 215 °C, 2.5 h; (f) hydroxylamine hydrochloride, pyridine, 22 °C, 24 h; (g) Pd/C (10%), HCl, ethanol/H_2O, 5 bar, 16 h; (h) HATU, DIPEA, DMF, 22 °C, 40 h; (i) HCl, CH_3OH, 22 °C, 18 h; (j) Cs_2CO_3, CH_3CN, 40 °C, 18 h; (k) HCl, CH_3OH, 22 °C, 18 h; (l) BBr_3, CH_2Cl_2, 25 °C, 18 h; (m) CH_3OH, 65 °C, 16 h; (n) $TbCl_3$, H_2O/CH_3OH, pH 7, 45 °C, 48 h; (o) 0.2 M KOH, H_2O, 22 °C, 20 h.

B. Quantum yield and quenching in cell lysate

The nature of the sensitizing antenna of a lanthanide complex can impact its function in a biological environment. Here, three complexes, [Tb-**4.1**], [Tb-**4.2**]$^-$, and [Tb-**4.3**], are compared that feature either an isophthalamide or a phenanthridine based antenna for sensitizing the lanthanide emissions (Figure 4.1). Note that each complex has the same acetate pendant arms. All three complexes luminesce in the green region of the visible spectrum, with maximum emission at 545 nm when excited at 345 nm (Figure 4.3). These three antenna platforms have different properties in terms of hydrophobicity and interactions with biomolecules, including nucleic acids, reducing agents and proteins. The hydrophilic isophthalamide and methoxy isophthalamide are comprised of a single aromatic ring and have no known interactions with biomolecules, while the phenanthridine is an extended aromatic system capable of base stacking with nucleotides and DNA intercalation.[180, 186]

The quantum yield, Φ, of the three Tb-complexes in PBS was investigated by comparing the luminescence intensity of each complex to that of a quinine sulfate standard in 0.1 M sulfuric acid (Φ_r = 0.577)[192] according to the optically dilute method.[118] At pH 7.8 and 22 °C, the quantum yields of [Tb-**4.1**] and [Tb-**4.3**] are statistically identical (4.6 ± 1.2% *vs*. 4.7 ± 2.2%, respectively). The quantum yield of the phenathridine derivative [Tb-**4.3**] is comparable that of similar lanthanide complexes featuring either triamide or triphosphinate substituted DOTA ligands.[193] However, [Tb-**4.2**]$^-$ is a more efficient emitter with an average quantum yield of 9.8 ± 1.5%, indicating that substituting the methoxy for the hydroxyl group on the isophthalamide antenna substantially affects the quantum yield of the complex. Note that quantum yields of *ca.* 50% have been reported by Raymond and coworkers for Tb-complexes with tetra-IAM substituted ligands.[118] The substantial difference between these complexes results from their structures. As opposed to [Tb-**4.2**]$^-$, in the tetra-IAM complex H(2,2)-IAM, the isophthalamide directly coordinates the lanthanide, thereby enabling a much more efficient Dexter-type energy transfer from the antenna to the Tb than the Förster-type, through-space mechanism likely taking place in [Tb-**4.2**]$^-$. On the other hand, [Tb-**4.2**]$^-$

has substantially higher water solubility (M range) than the cryptand H(2,2)-IAM (μM range) and enables the design of responsive probes.

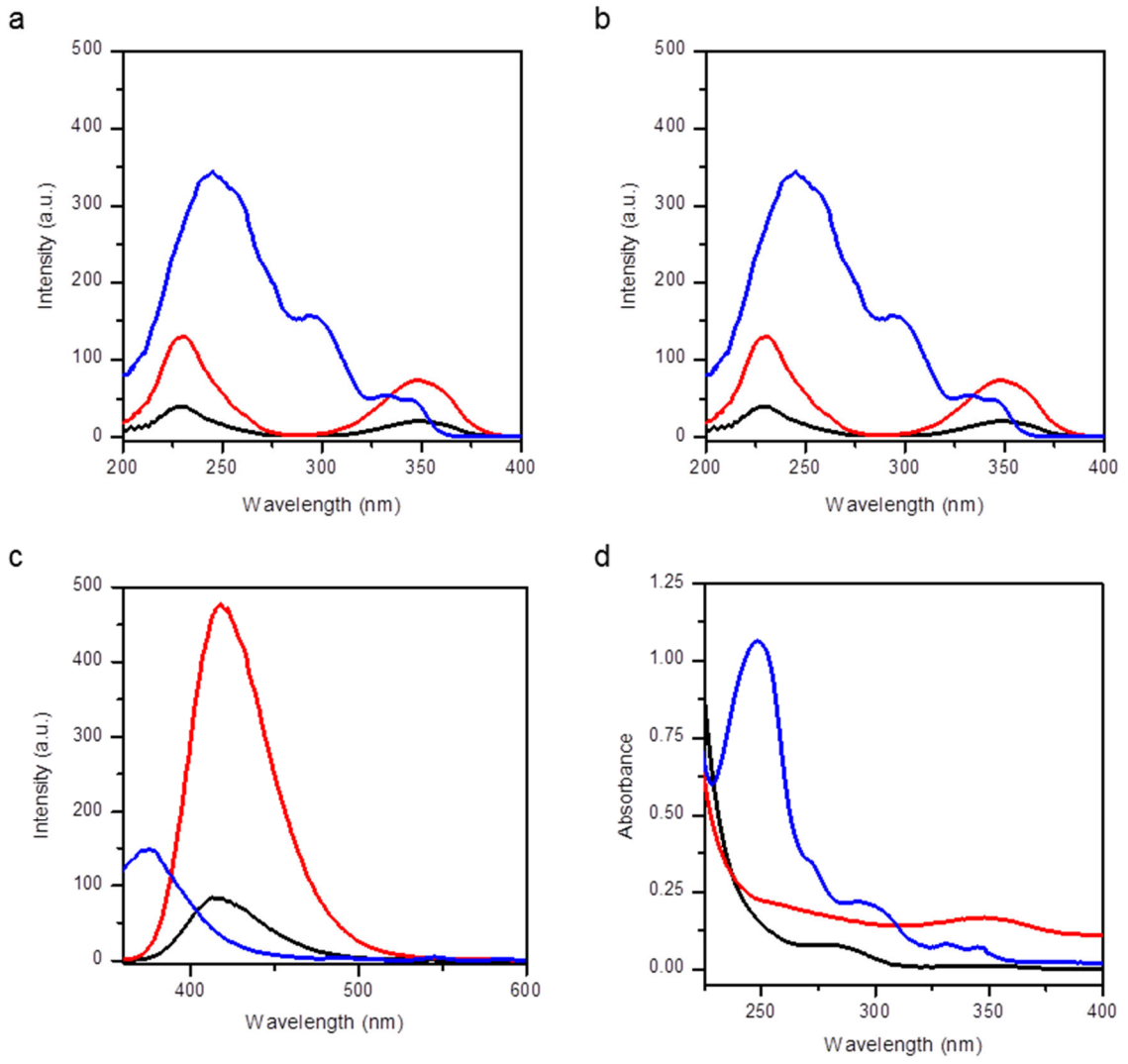

Figure 4.3. (a) Time-delayed excitation, (b) time-delayed emission, (c) fluorescence, and (d) absorbance profiles of [Tb-**4.1**] (black), [Tb-**4.2**]$^-$ (red), [Tb-**4.3**] (blue). Experimental conditions: [Tb-complex] = 50 μM, PBS (pH 7.8), slit widths (excitation and emission) = 10 nm, *T* = 22 °C. Luminescence parameters: λ_{em} = 545 nm, λ_{ex} = 345 nm, time delay = 0.1 ms, gate time = 5.0 ms, decay time = 0.02 s.

Nonetheless, the quantum yields of [Tb-**4.1**], [Tb-**4.2**]$^-$, and [Tb-**4.3**] are comparable to luminescent d-block compounds used for cellular imaging. For example, the quantum yields of Ir-complexes featuring 2-phenyl pyridine ligands are between 4 - 8% in PBS buffer.[194] Not surprisingly, the quantum yields of Tb-centered luminescence is lower than commonly used fluorescence dyes such as Cy3 (4% in PBS), Cy5 (30% in PBS), Alexa750 (12% in phosphate buffer), and Texas Red (30% in water).[195] However, in comparison with phosphorescent metal complexes, organic dyes suffer from short fluorescence lifetimes and small Stokes shifts.[196]

The brightness of a luminescent probe is determined by both the quantum yield and the molar absorption extinction co-efficient (ε) at the excitation wavelength. For [Tb-**4.1**], [Tb-**4.2**]$^-$, and [Tb-**4.3**] the ε_{345} values are 200 M^{-1} cm^{-1}, 3,320 M^{-1} cm^{-1}, and 1,400 M^{-1} cm^{-1}, respectively. Thus, the Tb-DOTA-IAM ([Tb-**4.2**]$^-$) complex is the brightest of those studied here due to its high molar absorption extinction co-efficient and quantum yield.

As for any luminescent or fluorescent probe, emission is susceptible to quenching by reducing agents, proteins, and other components of biological media. In the case of luminescent Tb and Eu complexes, the quenching pathways can involve electron or charge transfer from the excited states to intracellular reducing agents such as urate, ascorbate, and glutathione that are present in mM concentrations in cells.[39-40] In addition, luminescence quenching by proteins, such as human serum albumin, has been reported.[41] The degree of luminescence quenching was evaluated by measuring the time-delayed luminescence intensity of [Tb-**4.1**] with respect to its concentration (0 - 15 μM) in PBS and whole cell lysate at two different protein concentrations. In whole cell lysate containing 0.25 mg/mL protein, the luminescence intensity of [Tb-**4.1**] is quenched by 22 ± 2.8%; at 0.5 mg/mL protein the luminescence intensity is reduced by 30 ± 2.4% (Table 4.1 and Figure 4.4). Advantageously, the isophthalamide antenna is less susceptible to quenching than complexes containing electron-poor sensitizing moieties. For instance, the metal centered emission of terbium azaxanthone complexes is quenched by 30-60 % in the presence of 0.2 mM human serum albumin.[41] This highlights the potential of the IAM(OMe) antenna for biological applications.

Table 4.1. Luminescence quenching of [Tb-**4.1**] by whole cell lysate.[a]

		Quenching (%) [b]
Whole Cell Lysate [c]	0.25 mg/mL protein	22 ± 2.8
	0.50 mg/mL protein	30 ± 2.4

[a] Experimental conditions: [Tb-**4.1**] = 0 - 15 μM, PBS, pH 7.8, time delay = 0.1 ms, excitation wavelength = 345 nm, slit widths (excitation and emission) = 5 nm, integrated emission intensity from 470 – 635 nm, *T* = 20 °C. Results are mean ± SD (*n* = 3). [b] Percent quenching was calculated using the percent change in the slope of the integrated luminescence intensity *versus* the [Tb-4.**1**] (μM) plots (Figure 4.4). [c] Generated from L6 myoblasts; protein concentration was determined by a BCA assay.

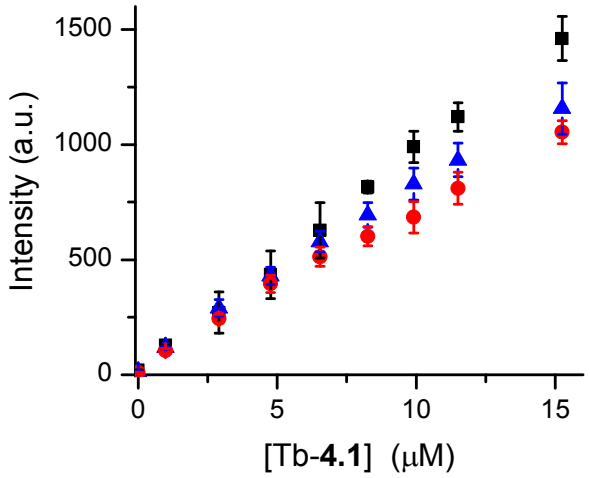

Figure 4.4. Time-delayed luminescence intensity of [Tb-**4.1**] as a function of increasing concentrations in PBS (black square; slope = 96 ± 1.5), whole cell lysate with 0.25 mg/mL protein (blue triangle; slope = 75 ± 2.2), and whole cell lysate with 0.50 mg protein/mL (red circle; slope = 67 ± 1.7). Experimental conditions: [Tb-**4.1**] = 0 - 15 μM, PBS pH 7.8, time delay = 0.1 ms, excitation wavelength = 345 nm, slit widths (excitation and emission) = 5 nm, integrated emission intensity from 470 – 635 nm, *T* = 20 °C. Results are mean ± SD (*n* = 3).

C. Influence of the nature of the antenna on cellular compatibility

The effect of [Tb-**4.1**], [Tb-**4.2**]$^-$, and [Tb-**4.3**] on the viability of L6 rat muscle myoblast cells was investigated using an MTT assay. It was hypothesized that the 2-methoxyisophthalamide would have a reduced effect on cell viability due to the protecting group on the phenol that could block non-specific interactions with the cell proteins and coordination of cellular metal, such as iron and copper. Additionally, the phenanthridine complex, [Tb-**4.3**], was expected to have a higher effect on cell viability due to its ability to intercalate DNA and RNA.[180, 186] Following a 24 h incubation with 0 - 300 μM Tb-complex, the phenanthridine derivative [Tb-**4.3**] decreases cell viability to 74% at 100 μM and to 63% at 300 μM. On the other hand, the cellular viability is maintained above 80% for both isophthalamide complexes, [Tb-**4.1**] and [Tb-**4.2**]$^-$ (Figure 4.5 and Table 4.2). The similar profiles indicate that the methoxy protecting group on the isophthalamide does not significantly improve cell viability at the doses studied here. This is contrary to a pair of Rh probes chelated by chrysenequinone diimine and *N*-functionalized dipyridyl amine ligands for which small structural changes were shown to have a substantial impact on cell viability. In that case, altering the ethoxy substituent to a propyl group reduces the viability of HCT116N and HCT116O cells from 80% to 60% after a 24 h incubation with 40 μM complex.[50]

Overall, the complexes in this study are slightly less toxic than lanthanide complexes containing tetraazatriphenylene or azaxanthone antennas with phenyl or ethylester substituted carboxamide arms, which have EC_{50} values in the 100 μM to > 240 μM range.[52-54] They also affect cell viability similarly to Ru(III) polypyridine complexes which also have EC_{50} (72 h) values ≥ 300 μM in MCF-7 and HT-29 cell lines.[56] It is interesting to note that [Eu-DOTA]$^-$, containing no antenna moiety, has a negligible effect on cell viability from 0 – 500 μM with a 72 h incubation.[57] Thus with respect to cell viability, [Tb-**4.1**] and [Tb-**4.2**]$^-$ are preferred for cellular imaging applications compared to [Tb-**4.3**].

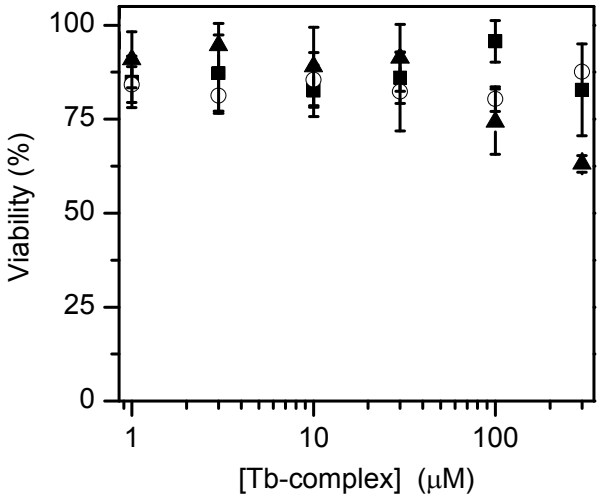

Figure 4.5. Viability (24 h) of L6 myoblasts treated with 0 - 300 μM [Tb-**4.1**] (solid square), [Tb-**4.2**]$^-$ (open circle), and [Tb-**4.3**] (solid triangle) as determined with an MTT assay. Results are expressed as mean ± SD (*n* = 3).

Table 4.2. Cellular viability and association of macrocyclic Tb-complexes.

	Cell viability [a] (%)	Cell association [b] (μmol Tb/g protein)
[Tb-**4.1**]	96 ± 6	6.0 ± 3
[Tb-**4.2**]$^-$	80 ± 3	12 ± 5
[Tb-**4.3**]	74 ± 9	5.3 ± 3
[Tb-**4.4**]$^{3+}$	81 ± 2	1.4 ± 0.6
[Tb-**4.5**]$^{3+}$	63 ± 4	22 ± 10
[Tb-**4.6**]$^{3+}$	90 ± 8	8.3 ± 3
[Tb-**4.7**]$^{3+}$	78 ± 8	2.2 ± 0.5
[Tb-**4.8**]$^{3+}$	90 ± 6	0.32 ± 0.07
[Tb-**4.9**]	81 ± 4	1.3 ± 0.4
[Tb-**4.10**]$^{3-}$	88 ± 10	0.47 ± 0.2
Control (no Tb-complex)	100 ± 6	0.07 ± 0.04

[a] Obtained by an MTT assay after a 24 h incubation with 100 μM Tb-complex. Results are mean ± SD (*n* = 3). [b] Determined by ICP-MS after a 4 h incubation with 50 μM Tb-complex. Results are mean ± SD (*n* = 3).

The nature of the antenna was also expected to impact the cellular association of the complexes. Following a 4 h incubation with 50 μM of Tb-complex, the cellular accumulation of the metal was determined by ICP-MS and expressed relative to the protein concentration as determined by a BCA assay. Importantly, it should be noted that the quantitative nature of measuring cellular association of metal complexes by ICP-MS is balanced by the inability of the technique to distinguish between internalized or membrane-bound complexes.[48] It was anticipated that the extended aromatic antenna of [Tb-**4.3**] would facilitate membrane permeability, as suggested by the increased cellular uptake of more lipophilic Ru-complexes and phenanthridine substituted *cis*-platin.[48-49, 55] However, cells exposed to the hydrophilic Tb-DOTA-IAM(OMe), [Tb-**4.1**], and the hydrophobic Tb-DOTA-Phen, [Tb-**4.3**], have similar cell association values, while the average value of the most hydrophilic Tb-DOTA-IAM, [Tb-**4.2**]$^-$, is nearly double (Table 4.2).

Small structural changes to the ligands of metal complexes have been reported to exert varied effects on the intracellular accumulation and distribution. Using a group of lanthanide complexes with tetraazatriphenylene or azaxanthone-based antennas, Parker identified that how the antenna was linked to the cyclen ring affected membrane permeability and localization more than small structural modifications on the antenna itself.[52] For the isophthalamide complexes, however, conversion from the methoxy group in [Tb-**4.1**] to the phenolate of [Tb-**4.2**]$^-$ does impact cellular association. This observation is more in concert with the findings of Barton, who measured substantial differences in cell association between an alkyl substituted dipyridyl Rh-complex (705 ng Rh / mg protein) compared to a complex that introduced a terminal alcohol on the alkyl group (165 ng Rh / mg protein).[50] The cellular association values measured for the hydroxyisophthalamide [Tb-**4.2**]$^-$ are comparable to the values reported for a Tb-complex with a tetraazatriphenylene antenna and phenyl substituted amide arms, which had a maximum accumulation of 10 μmol per g protein into NIH 3T3 cells after a 4 h incubation at 50 μM.[52] Unfortunately, further comparisons with cellular accumulation values reported in the literature are limited due to differences the method of data collection

(ICP-MS *vs.* flow cytometry[40, 49, 197-198]), and data presentation of metal in per amount protein or per cell.[53-56, 199-200]

Notable differences between the three metal complexes include the increased effect of [Tb-**4.3**] on cell viability above 100 μM in spite of its only modest cell association. The synthesis of [Tb-**4.2**]$^-$ requires a synthetically challenging boron tribromide deprotection to produce the 2-hydroxyisophthalamide antenna, and the resulting complex has a cellular association only slightly higher than its analog [Tb-**4.1**]. The more facile synthesis of the 2-methoxyisophthalamide of [Tb-**4.1**] compared to [Tb-**4.2**]$^-$ thus became a significant factor in selecting an antenna for further studies evaluating the effects of variable arms on the cellular compatibility of lanthanide complexes.

D. Effect of structural and electronic variations in pendant arms

The role of charge and hydrophobicity of the polyaminocarboxylate arms on the cell viability and association of the lanthanide probes was evaluated with a library of derivatives of [Tb-**4.1**]. Complexes [Tb-**4.4**]$^{3+}$ though [Tb-**4.10**]$^{3-}$ share a common cyclen backbone with a 2-methoxyisophthalamide antenna, but differ in the nature of the remaining substituents (Figure 4.2). The alkyl, benzyl, and trifluoro groups impart increasing hydrophobicity to the complexes, whereas alanine and glutamine amino-acid based substituents in either an ethylester or carboxylic acid form render greater hydrophilicity. The resulting complexes also differ in overall complex charge; neutral carboxamide arms generate the +3 charged complexes [Tb-**4.4**]$^{3+}$ - [Tb-**4.8**]$^{3+}$, the addition of monoanionic alanine-based arms forms the zwitterionic complex [Tb-**4.9**], and the di-anionic glutamate arm creates [Tb-**4.10**]$^{3-}$ bearing a net -3 charge.

As with the previous complexes that differ with respect to the antenna, the cell viability (24 h) was measured for the library of complexes featuring pendant arms with structural and electronic variations. Of the hydrophobic complexes, only [Tb-**4.5**]$^{3+}$ decreases cell viability significantly to 60%, while [Tb-**4.4**]$^{3+}$ and [Tb-**4.6**]$^{3+}$ are comparable to the parent complex [Tb-**4.1**], maintaining a viability above 80% in the concentration range measured (Figure 4.6a and Table 4.2). Each of the amino acid derivatives, [Tb-**4.7**]$^{3+}$, [Tb-**4.8**]$^{3+}$, [Tb-**4.9**], and [Tb-**4.10**]$^{3-}$ also sustain viability above

75% even in the presence of 300 μM Tb-complex (Figure 4.6b and Table 4.2). Interestingly, the notable reduction in cell viability upon addition of medium-length alkyl chains matches the results of a previous study comparing a family of Ir(III) cyclometallated probes. In that study, the Ir-complexes featuring the shortest (C_2) and longest (C_{18}) alkyl chains had comparable minimal effect on HeLa cell viability (EC_{50} ~15 μM), while the median length alky chain (C_{10}) was significantly more cytotoxic (EC_{50} = 2 μM).[198] The hexyl alkyl derivative, [Tb-**4.5**]$^{3+}$ excluded, the relatively low effect on cell viability (EC_{50} values > 300 μM) of this entire class of Tb-complexes suggests they have only limited interactions with cellular component and bodes well for their application.

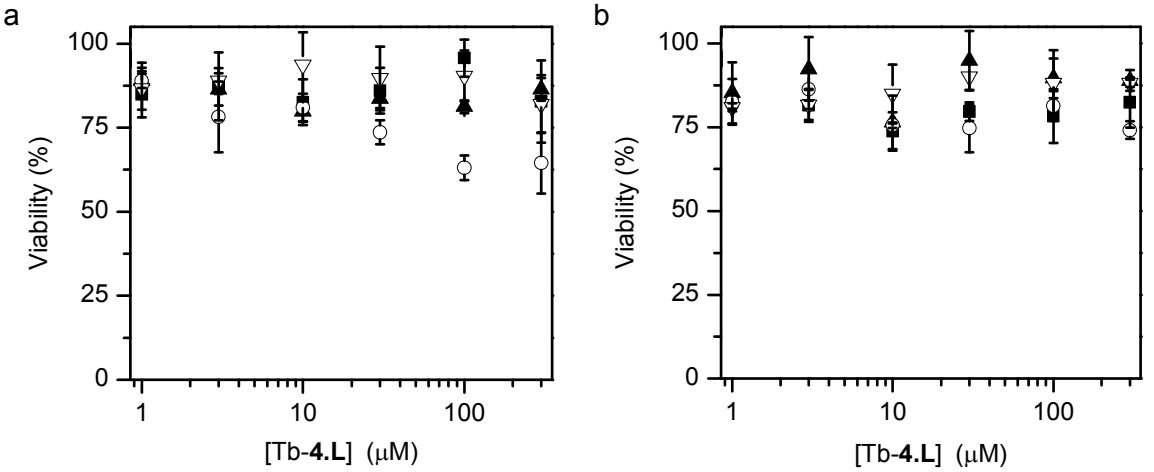

Figure 4.6. Viability (24 h) of L6 myoblasts treated with 0 - 300 μM Tb-complexes as determined with an MTT assay. (a) [Tb-**4.1**] (solid square), [Tb-**4.4**]$^{3+}$ (solid triangle), [Tb-**4.5**]$^{3+}$ (open circle), and [Tb-**4.6**]$^{3+}$ (open inverted triangle). (b) [Tb-**4.7**]$^{3+}$ (solid square), [Tb-**4.8**]$^{3+}$ (solid triangle), [Tb-**4.9**] (open circle), and [Tb-**4.10**]$^{3-}$ (open inverted triangle). Results are expressed as mean ± SD (n = 3).

The role of the pendent arms on the cellular association of the Tb-complexes was also investigated by ICP-MS. It was hypothesized, based on the results of Barton,[48-49] that [Tb-**4.4**]$^{3+}$, [Tb-**4.5**]$^{3+}$, and [Tb-**4.6**]$^{3+}$ would penetrate cells more efficiently due to their lipophilic substituents and cationic character that would assist transport across the plasma membrane.[201] Indeed, higher Tb accumulation is observed with the hydrophobic hexyl substituted [Tb-**4.5**]$^{3+}$ and trifluoro containing [Tb-**4.6**]$^{3+}$ than with the more

hydrophilic amino acid derivatives (Table 4.2). However, this conclusion cannot be universally applied to all hydrophobic arms, since the cellular association of the benzyl substituted [Tb-**4.4**]$^{3+}$ is less than that of the parent complex [Tb-**4.1**]. The alkyl substituted Ir-complexes discussed previously also do not illustrate a direct relationship between hydrophobicity and cellular association. In that study, each complex investigated displayed measurable cellular association by ICP-MS, but the C_{10} version afforded the greatest association followed by the C_2 and then the C_{18} derivative.[198] Thus, it is clear that the lipophilicity of the complex cannot alone be used to predict the cellular association of metal complexes.

Of the amino-acid derivatized complexes, the alanine-based [Tb-**4.7**]$^{3+}$ and [Tb-**4.9**] have higher cell association values than the glutamine-based compounds [Tb-**4.8**]$^{3+}$ and [Tb-**4.10**]$^{3-}$. Positively charged complexes containing esters are reported to have enhanced cell association compared to carboxylic acid derivatives,[49] and this is observed with the slightly higher cell association values of the ethylester complex of alanine [Tb-**4.7**]$^{3+}$ compared to the neutral acid complex [Tb-**4.9**]. This reflects the finding that the cell association of [Eu-DOTAm]$^{3+}$ is five times that of [Eu-DOTA]$^{-}$, which showed negligible cellular accumulation.[57] Interestingly, this trend is not repeated for the glutamine ethylester and acid complexes, [Tb-**4.8**]$^{3+}$ and [Tb-**4.10**]$^{3-}$, respectively, which both have low cell association values despite their large differences in overall complex charge. This is contrary to lanthanide complexes studied by Parker in which the intracellular concentration of a -3 charged glutamate functionalized DOTA with a tetraazatriphenylene antenna was approximately three times that of the neutral Ln-DOTA-tetraazatriphenylene.[40] An important conclusion is that the parameters influencing cellular association of lanthanide complexes are multifaceted and include both structural features (lipophilicity, nature of the antenna, terminal functional groups) and, to a lesser extent, overall complex charge.

E. Fluorescence microscopy

The cellular association of the Tb-complexes was also investigated with epifluorescence microscopy. According to previous reports, it was anticipated that punctuate staining would be observed if the complexes entered cells *via* endocytosis, and diffuse cytoplasmic fluorescence would be consistent with passive translocation through the cell membrane. L6 myoblasts were treated with Tb-complex (200 μM for 4 h), washed with PBS at room temperature, and fixed with formaldehyde prior to imaging. Results of representative cells indicate the presence of weak intracellular staining for the hydrophobic, trifluoro substituted [Tb-**4.6**]$^{3+}$, while the fluorescence intensity of phenanthridine containing [Tb-**4.3**] is comparable to the control cells (Figure 4.7). Likewise, the remaining Tb-complexes exhibit similar, weak internal fluorescence (Figure 4.7). Due to reports that different staining patterns can be observed in experiments that differ only in whether cells were imaged in a live or fixed state,[202] the intracellular fluorescence of [Tb-**4.6**]$^{3+}$ was also examined in live cells (Figure 4.8). In these images, an overall decrease in the intracellular fluorescence to levels comparable to the untreated control cells was observed.

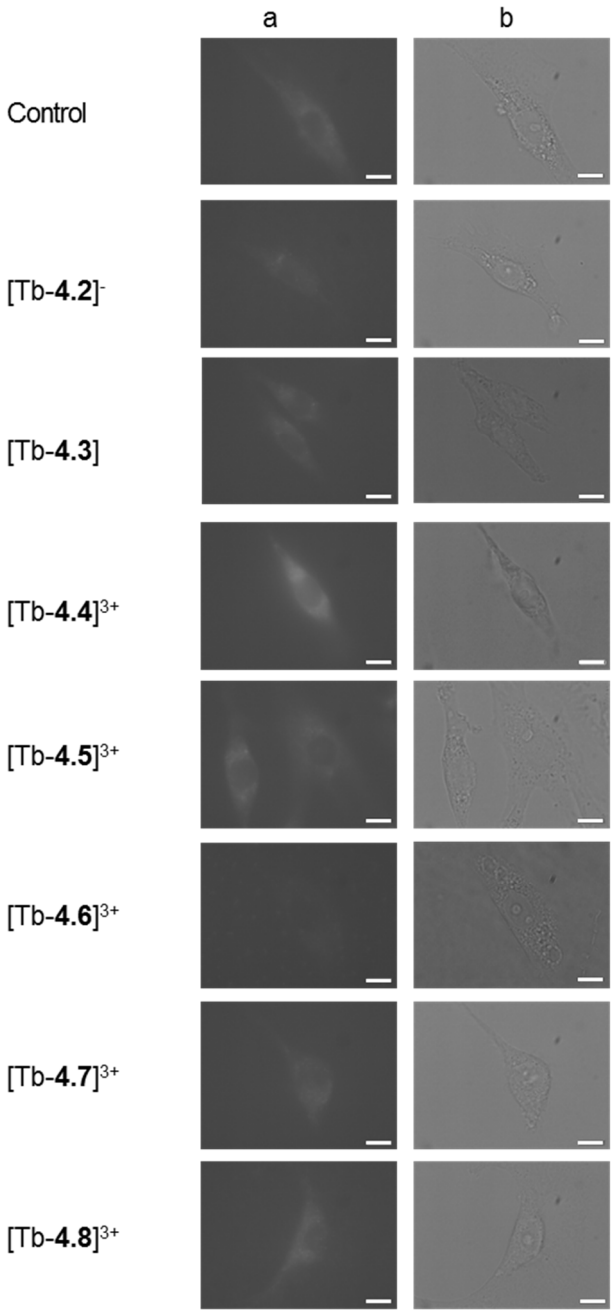

Figure 4.7. Fluorescence microscopy images of representative L6 myoblasts treated with 200 μM [Tb-**4.2**]- - [Tb-**4.8**]3+ for 4 h at 37 °C. Cells were rinsed with PBS and fixed with formaldehyde prior to imaging. (a) Fluorescence images: 60x objective, 325 – 375 nm excitation filter, 470 – 750 nm emission filter, 0.4 s exposure time. (b) Bright field images: 0.04 s exposure time. Scale bars represent 10 μm.

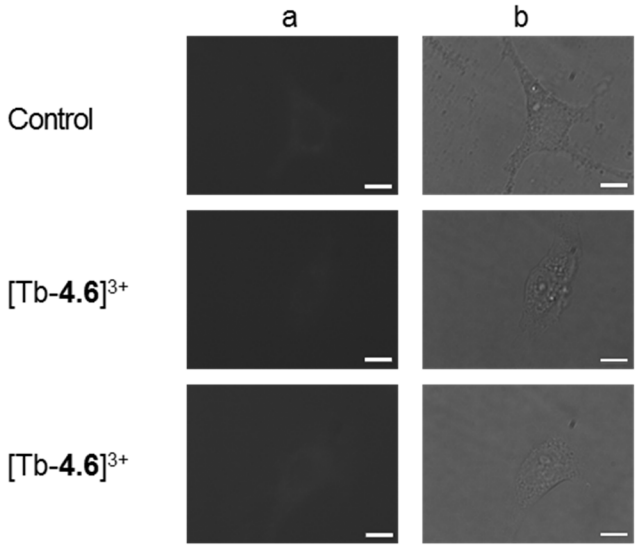

Figure 4.8. Fluorescence microscopy images of representative live L6 myoblasts treated with 200 μM [Tb-**4.6**]$^{3+}$ for 4 h at 37 °C. Cells imaged in phenol red-free media. (a) Fluorescence images: 60x objective, 325 – 375 nm excitation filter, 470 – 750 nm emission filter, 0.1 s exposure time. (b) Bright field images: 0.04 s exposure time. Scale bars represent 10 μm.

The reduced staining in cytoplasmic vesicles in live cells compared to fixed cells has also been observed by Belitsky.[202] However, unlike the 2-hydroxyisophthalamide complexes, lanthanide complexes featuring tetraazatriphenylene antennas containing phenyl, ester, or carboxylate substituents are taken up by CHO or NIH 3T3 cells and can be visualized with fluorescence microscopy regardless of the nature of their pendent arms.[52] Likewise, Bünzli observed lanthanide helicates ranging in overall charge from -6 to +6 localized to endosomes and lysosomes consistent with endocytotic uptake mechanisms irrespective of the polarity or overall charge of the complex.[51] Regardless of the reasons, the low cell associations exhibited by this entire class of complexes render them particularly useful for monitoring extracellular species.

IV. CONCLUSIONS AND FUTURE WORK

A family of luminescent lanthanide complexes featuring different sensitizing antennas varying in charge and hydrophobicity, and pendant arms of variable structural and electronic properties were synthesized. The cell viability and association of this family of complexes have been evaluated. With respect to the antenna, the 2-methoxyisophthalamide of [Tb-**4.1**] was selected as the ideal candidate for further studies due to its synthetic ease (compared to [Tb-**4.2**]$^-$), suitable quantum yield, little effect on cell viability, and modest cell association. Surprisingly, the addition of hydrophobic moieties (benzyl, hexyl, and trifluoro) did not increase cell association. All of the complexes investigated minimally effect cell viability and exhibit low cellular association, regardless of the overall complex charge or relative hydrophobicity; thus, it is presumed that it is the hydrophilic nature of the 2-methoxyisophthalamide antenna that confers the low membrane permeability of this class of compounds. In conclusion, the probes based on the structural framework presented here are well-suited for monitoring extracellular analytes such as group I ions, polysaccharides, hormones, or other signaling molecules.

This current study investigated the effect of structural modifications of the ligand on cell association in the absence of targeting moieties; however, conjugating Ln-complexes to cell penetrating peptides[203] or receptor targeting groups has successfully increased the cellular uptake. Additional studies are needed to identify structural features that promote membrane permeability of Ln-complexes based on the macrocyclic polyamine ligand with a 2-methoxylisophthalamide antenna. Future work includes appending a polyarginine peptide to Tb-DOTA-IAM(OMe) and evaluating the cellular association of this complex (Figure 4.9). Alternatively, the cell penetrating peptide could be linked to the complex *via* a disulfide bond that would be cleaved in reducing environment inside the cell. In terms of subcellular localization, cell penetrating peptides promote uptake *via* endocyotic pathways placing the “cargo” molecules in endosomes. Progress in the field of cell penetrating, lanthanide-based contrast agents has been reviewed[181-182, 204] and includes the use polyarginine[205-209] and Tat-based

peptides.[210] This technique is promising as it has previously been applied to luminescent metal complexes,[211-213] and dual imaging agents.[214]

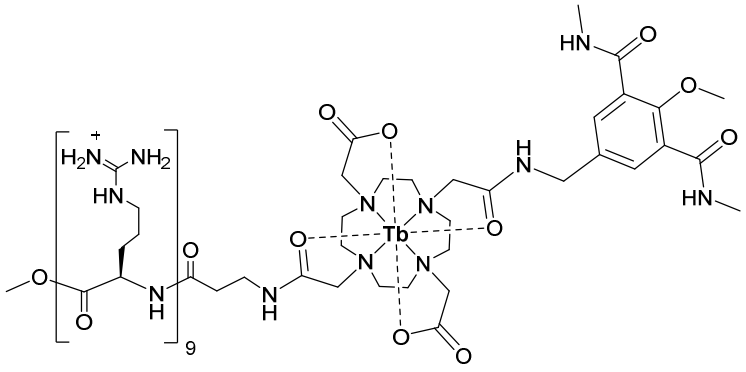

Figure 4.9. Chemical structure of a Tb-complex coupled to a polyarginine peptide designed for increased cellular uptake.

Additional approaches to increase cellular accumulation or target complexes to specific subcellular locations also warrant further investigation. Increased cell uptake can be pursued by coupling complexes to moieties that facilitate interactions with cellular membrane receptors,[215-219] transporters,[220] or special groups such as exofacial thiols.[221] The application of these approaches to the delivery luminescent macrocyclic polyaminocarboxylate complexes is likely to result in cytoplasmic delivery of the probes. However, some probes would benefit from an even finer control of distribution – being targeted to a specific subcellular region or organelles where the analyte is generated. For example, accumulation of HO• probes in the locations where the species is produced (mitochondria, ER, phagosomes, and peroxisomes) would not only improve the sensitivity of detection, but also increase the physiological relevance of the results. To target Ln-complexes to organelles, alternative methods are needed in addition to those that increase cellular accumulation. Previous localization studies with metal complexes has revealed that phosphonium ions targets complexes to the mitochondria[121] and fluorescein promotes nuclear localization (Figure 4.10).[222] Thus, a mitochondrial targeted probed responsive to HO• could be achieved by appending a phosphonium ion to the probes described in the previous chapters. This would be

particularly useful with the luminescent lanthanide-based probes as luminescence spectroscopy has a nanomolar resolution that can spatially distinguish organelles.

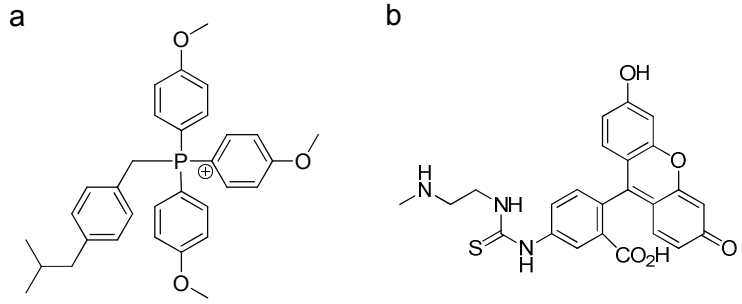

Figure 4.10. Targeting moieties used to direct metal complexes to subcellular locations. (a) Phosphonium ions facilitate mitochondria accumulation, and (b) fluorescein can redirect complexes to the nucleus.

Ultimately, future systematic studies will provide more insights into the complex relationship between cellular accumulation and probe structure. This knowledge can then be applied to target responsive imaging agents to extracellular or subcellular regions relevant to the analyte being detected. Work in this field is of growing interest, particularly in the development of probes for reactive oxygen or nitrogen species and redox active metals. Future generation biomedical imaging agents with defined cellular localizations will advance the understanding of these specie in normal physiological function and their roles in disease states.

V. EXPERIMENTAL

General considerations. Unless otherwise noted, starting materials were obtained from commercial suppliers and used without further purification. Water was distilled and further purified by a Millipore Simplicity cartridge system (resistivity 18 mΩ). ^{1}H NMR, ^{19}F NMR, and ^{13}C NMR spectra were recorded on a BrukerAvance III 500 at 500, 470 or 125 MHz or on a Varian Inova 300 at 300, 282, or 75 MHz at the LeClaire-Dow Characterization Facility of the Department of Chemistry at the University of Minnesota.

The solvent residual peak was used as the internal reference. Data for ^{1}H NMR as reported as follows: chemical shift (δ, ppm), multiplicity (s, singlet; d, doublet; t, triplet, m, multiplet, b, broad), integration, coupling constants (Hz). Data for ^{13}C NMR are reported as chemical shifts (δ, ppm). Mass spectra (HR = high resolution, ESI-MS = electrospray ionization mass spectrometry) were recorded on a Bruker BioTOF II at the Waters Center for Innovation in Mass Spectrometry of the Department of Chemistry at the University of Minnesota. Elemental analyses were performed by inductively coupled plasma mass spectrometry on a Thermo Scientific XSERIES 2 ICP-MS fitted with an ESI PC3 Peltier cooled spray chamber, SC-FAST injection loop, and SC-4 autosampler at the Department of Geology at the University of Minnesota. Samples were diluted appropriately and analyzed in the presence of a 20 ppb of In internal standard using the He/H2 collision-reaction mode. UV−Vis spectra were measured with a Varian Cary 100 Bio Spectrophotometer. Data was collected between 220 and 800 nm using a quartz cell with a path length of 10 mm. Luminescence data were recorded on a Varian Eclipse Fluorescence spectrophotometer using a quartz cell with a path length of 10 mm.

A. Synthesis and characterization

2-Hydroxy-5-methylisophthalic acid (4.11). In a round bottom flask, 2,6-bis(hydroxymethyl)-*p*-cresol (10.0 g, 59.8 mmol) was dissolved in chloroform (250 mL), and MnO_2 (36.0 g, 414 mmol) was added. The reaction mixture was stirred for at 60 °C for 20 h. The resulting mixture was filtered and concentrated under reduced pressure to yield a yellow solid which was treated with KOH powder (55.0 g, 980 mmol) and heated at 230 °C for 1 h. After cooling to ambient temperature, the solid mixture was dissolved in mQ water (150 mL), filtered, and acidified to pH = 1 with concentrated HCl. The product was collected by filtration, washed with mQ water, and dried overnight at 110 °C yielding a tan solid (9.36 g, 47.7 mmol, 80%). ^{1}H NMR (300 MHz, D_2O, NaOD, δ): 1.98 (s, 3H), 7.04 (s, 2H). ^{13}C NMR (125 MHz, D_2O, NaOD, δ): 19.4, 119.7, 129.3, 129.9, 160.1, 179.2. ESI-MS (*m/z*): $[M-H]^-$ calcd for $C_9H_8O_5$, 195.0; found, 195.1.

Dimethyl 2-methoxy-5-methylisophthalate (4.12). The diacid (**4.11**, 11.0 g, 56.3 mmol) and K_2CO_3 (50.5 g, 365 mmol) were added to anhydrous acetone (175 mL) and stirred for 5 minutes. Methyl iodide (70.5 mL, 1.12 mol) was added and the reaction was stirred at 56 °C for 16 h. After cooling to ambient temperature, the solid was filtered and the volatiles were removed under reduced pressure. The residue was taken up in ethylacetate and washed with 5% HCl (30 mL), 5% $NaHCO_3$ (30 mL), and brine (30 mL), then dried over $MgSO_4$ and concentrated on a rotary evaporator to yield a yellow oil (4.68 g, 19.6 mmol, 35%). ^{1}H NMR (300 MHz, $CDCl_3$, δ): 2.35 (s, 3H), 3.89 (s, 3H), 3.91 (s, 6H), 7.72 (s, 2H). ^{13}C NMR (125 MHz, $CDCl_3$ δ): 20.5, 52.4, 63.7, 126.3, 133.3, 135.4, 157.5, 166.3. ESI-MS (*m/z*): $[M+Na]^+$ calcd for $C_{12}H_{14}O_5$, 261.0; found, 260.9.

2-Methoxy-*N*^{1},*N*^{3},5-trimethylisophthalamide (4.13). The methoxy-protected diester (**4.12**, 3.65 g, 15.3 mmol) was dissolved in methanolic methylamine solution (2.0 M, 70 mL, 140 mmol), and the reaction was stirred at 65 °C for 18 h. The crude product was deposited onto silica and purified by flash chromatography over silica eluting with 30 to 100% ethyl aceteate in hexanes. The volatiles were removed on a rotary evaporator to yield a white powder (3.17 g, 13.4 mmol, 88% yield). ^{1}H NMR (500 MHz, $CDCl_3$, δ): 2.34 (s, 3H), 3.01 (d, *J* = 4.9 Hz, 6H), 3.80 (s, 3H), 7.34 (bs, 2H), 7.86 (s, 2H). ^{13}C NMR (125 MHz, $CDCl_3$, δ): 20.6, 26.8, 63.4, 127.3, 134.7, 135.1, 153.6, 165.9. ESI-MS (*m/z*): $[M+Na]^+$ calcd for $C_{12}H_{16}N_2O_3$, 259.1; found, 259.1.

5-Formyl-2-methoxy-*N*^{1},*N*^{3}-dimethylisophthalamide (4.14). In a mortar and pestle, the diamide (**4.13**, 3.57 g, 15.1 mmol), SeO_2 (2.01 g, 18.2 mmol) and naphthalene were ground to a powder. Under N_2, the mixture was heated to 215 °C for 1.5 h. The reaction was cooled to 85 °C, another aliquot of SeO_2 was added (1.00 g, 9.01 mmol, 0.6 eq), and the reaction was heated to 215 °C for an additional 1 h. After cooling to ambient temperature, the solid reaction components were dissolved in CH_2Cl_2 and the volatiles were removed under reduced pressure. The crude solids were suspended in hexanes (50 mL), filtered over celite, and washed with hexanes (200 mL). The product was eluted with CH_2Cl_2. Evaporation of the solvent under reduced pressure, followed by flash

chromatography over silica (0 – 8% CH_3OH in CH_2Cl_2) yielded the aldehyde (**14**), which was immediately used in the next step. ^{1}H NMR (300 MHz, $CDCl_3$, δ): 3.05 (d, *J* = 4.5 Hz, 6H), 3.96 (s, 3H), 7.22 (s, 2H), 8.47 (s, 2H), 9.99 (s, 1H).

5-((Hydroxyimino)methyl)-2-methoxy-*N*^{1},*N*^{3}-dimethylisophthalamide (4.15). The crude aldehyde (**4.14**, 2.54 g) and hydroxylamine hydrochloride (0.702 g, 10.0 mmol) were dissolved in pyridine (100 mL) and stirred at ambient temperature for 24 h. Pyridine was removed under reduced pressure generating a brown oil, which was precipitated by slow addition of diethyl ether to an acidic solution of the oil in ethyl acetate:CH_3OH (2:1). The white precipitate was isolated by vacuum filtration (827 mg, 3.12 mmol, 21% yield over 2 steps). ^{1}H NMR (500 MHz, D_2O, NaOD, δ): 2.79 (s, 6H), 3.62 (s, 3H), 7.60 (s, 2H), 7.94 (s, 1H). ^{13}C NMR (125 MHz, D_2O, NaOD, δ): 26.4, 62.6, 128.5, 128.7, 131.1, 147.9, 154.3, 168.9. ESI-MS (*m/z*): $[M+Na]^+$ calcd for $C_{12}H_{15}N_3O_4$, 288.1; found, 288.1.

5-(Aminomethyl)-2-methoxy-*N*^{1},*N*^{3}-dimethylisophthalamide hydrochloride (4.16•HCl). To a solution of the oxime (**4.15**, 0.722 g, 2.72 mmol) in ethanol (30 mL), water (2 mL) and concentrated HCl (2 mL) was added 10% Pd/C (0.14 g), and was reacted in a Parr hydrogenator at 5 bar H_2 for 16 h. The catalyst was removed by filtration, and the solvent was evaporated under reduced pressure then lyophilized to yield a pale yellow solid (0.663 g, 2.31 mmol, 85%). ^{1}H NMR (500 MHz, D_2O, δ): 2.87 (s, 6H), 3.73 (s, 3H), 4.13 (s, 2H), 7.68 (s, 2H). ^{13}C NMR (125 MHz, D_2O, δ): 26.4, 41.9, 62.7, 128.9, 129.2, 132.5, 155.4, 168.7. ESI-MS (*m/z*): $[M+H]^+$ calcd for $C_{12}H_{17}N_3O_3$, 252.1; found, 252.2.

5-(aminomethyl)-2-methoxy-*N*^{1},*N*^{3}-dimethylisophthalamide (4.16). The hydrochloride salt of the amine (**4.16•HCl**, 205 mg, 0.714 mmol) was deposited onto neutral silica (SiO_2 gel treated with 2% Et_3N in CH_2Cl_2 then 100% CH_2Cl_2) and isolated *via* flash chromatography, eluting with 0 – 10% CH_3OH and 0 – 1% NH_4OH in CH_2Cl_2 to yield the

free amine as a yellow oil (131 mg, 0.521 mmol, 73% yield). ^{1}H NMR (500 MHz, MeOD, δ): 2.98 (s, 6H), 3.85 (s, 3H), 3.98 (s, 2H), 7.82 (s, 2H).

2-(4,7,10-tris(*tert*-butoxycarbonyl)-1,4,7,10-tetraazacyclododecan-1-yl)acetic acid (4.17). The tris-BOC protected cyclen acid was synthesized as previously reported.[188-189] ^{1}H NMR (500 MHz, $CDCl_3$, δ): 1.44 (s, 18H), 1.46 (s, 9H), 2.88 (s, 4H), 3.42 (m, 14H). ^{13}C NMR (125 MHz, $CDCl_3$, δ): 28.5, 47.6, 49.9, 51.9, 54.2, 79.6, 80.0, 155.5, 156.1, 173.2. ESI-MS (*m/z*): $[M-H]^-$ calcd for $C_{25}H_{46}N_4O_8$, 529.3; found, 529.3.

Tri-*tert*-butyl 10-(2-((4-methoxy-3,5-bis(methylcarbamoyl)benzyl) amino)-2-oxoethyl)-1,4,7,10-tetraazacyclododecane-1,4,7-tricarboxylate (4.18). The isophthalamide amine (**4.16**, 235 mg, 0.934 mmol) and N-N,diisopropylethylamine (386 µL, 2.34 mmol) were dissolved in DMF (10 mL) and stirred at 0 °C for 15 min. Separately, the tris-BOC cyclen acid acid (**4.17**) (414 mg, 0.778 mmol) and HATU ((*O*-(7-azabenzotriazol-1-yl)-*N*,*N*,*N*′,*N*′-tetramethyluronium hexafluorophosphate) (359 mg, 0.934 mmol) were combined in DMF (10 mL) and stirred at 0 °C for 15 min. The solution containing HATU was added dropwise to the amine at 0 °C, and the reaction mixture was allowed to stir at ambient temperature for 40 h. The solvent was removed under reduced pressure, and the crude residue was deposited onto silica and purified by flash chromatography (eluent: 0 – 8% CH_3OH in CH_2Cl_2) to yield the product as a colorless oil (622 mg, 0.814 mmol, 87% yield). ^{1}H NMR (500 MHz, $CDCl_3$, δ): 1.37 (s, 18H), 1.46 (s, 9H), 3.00 (s, 6H), 3.44 (m, 14H), 3.85 (s, 3H), 4.40 (s, 2H), 5.30 (s, 2H), 7.43 (bs, 2H), 7.84 (s, 2H). ^{13}C NMR (125 MHz, $CDCl_3$, δ): 26.5, 26.7, 28.3, 28.5, 42.0, 47.5, 49.7, 63.06, 80.0, 120.4, 128.4, 128.7, 132.0, 134.8, 150.4, 154.9, 155.6, 162.8, 166.34, 166.45, 171.4. ESI-MS (*m/z*): $[M+H]^+$ calcd for $C_{37}H_{61}N_7O_{10}$, 764.4; found, 764.3.

5-((2-(1,4,7,10-tetraazacyclododecan-1-yl)acetamido)methyl)-2-methoxy-*N*^{1},*N*^{3}-dimethylisophthalamide trihydrochloride (4.19). The BOC protected cyclen (**4.18**, 678 mg, 0.888 mmol) was dissolved in 1.25 M HCl in CH_3OH (20 mL) at 0 °C. The reaction was brought to ambient temperature and stirred 18 h. The volatiles were

removed under reduced pressure to yield the product as a white solid (505 mg, 0.884 mmol, quant.). ^{1}H NMR (500 MHz, D_2O, δ): 2.89 (s, 6H), 3.00 (bs, 6H), 3.15 (m, 10H), 3.49 (s, 2H), 3.72 (s, 3H), 4.38 (s, 2H), 7.55 (s, 2H). ^{13}C NMR (125 MHz, D_2O, δ): 26.4, 42.2, 42.7, 44.20, 49.80, 62.77, 123.4, 128.6, 130.70, 134.1, 150.9, 154.1, 168.9, 173.3. ESI-MS (*m/z*): $[M+Na]^+$ calcd for $C_{22}H_{37}N_7O_4$, 464.3; found, 464.1.

Tri-*tert*-butyl 2,2',2''-(10-(2-((4-methoxy-3,5-bis(methylcarbamoyl) benzyl) amino)-2-oxoethyl)-1,4,7,10-tetraazacyclododecane-1,4,7-triyl)triacetate (4.20). Under N_2, *tert*-butylbromoacetate (19 µL, 0.13 mmol) in anhydrous CH_3CN (4 mL) was added dropwise to the cyclen methoxyisophthamide (**4.19**, 18 mg, 32 µmol) and Cs_2CO_3 (62 mg, 0.19 mmol) in anhydrous CH_3CN (10 mL) at 0 °C. Following the addition, the reaction mixture was stirred at 40 °C for 18 h. The solid was removed by filtration, and the solvent was removed under reduced pressure. The crude product was deposited onto silica and purified *via* flash chromatography (eluent: 0 – 8% CH_3OH in CH_2Cl_2) to yield the product as a light yellow oil (19 mg, 0.024 mmol, 76% yield). ^{1}H NMR (500 MHz, $CDCl_3$, δ): 1.46 (s, 18H), 1.48 (s, 9H), 2.25 (m, 18H), 3.00 (s, 6H), 3.49 (s, 6H), 3.91 (s, 3H), 4.45 (s, 2H), 7.99 (s, 2H), 8.25 (s, 2H), 8.63 (s, 1H). ^{13}C NMR (125 MHz, $CDCl_3$, δ): 26.5, 27.8, 40.9, 53.5, 55.6, 56.1, 62.9, 81.9, 128.4, 132.3, 133.2, 155.3, 166.6, 171.8, 172.3. ESI-MS (*m/z*): $[M+Na]^+$ calcd for $C_{40}H_{67}N_7O_{10}$, 828.5; found, 829.5.

2,2',2''-(10-(2-((4-methoxy-3,5-bis(methylcarbamoyl)benzyl)amino)-2-oxoethyl)-1,4,7,10-tetraazacyclododecane-1,4,7-triyl)triacetic acid (4.1). The protected cyclen (**4.20**, 18 mg, 23 µmol) was dissolved in 1.25 M HCl in CH_3OH (5 mL) at 0 °C. The reaction was stirred at ambient temperature 18 h. The volatiles were removed under reduced pressure to yield the product as a white solid (16 mg, 22 µmol, quant.). ^{1}H NMR (500 MHz, $(CD_3)_2SO$, δ): 2.78 (s, 6H), 3.51 (m, 20H), 3.74 (s, 3H), 4.33 (s, 2H), 7.52 (s, 2H). ESI-MS (*m/z*): $[M-H]^-$ calcd for $C_{28}H_{43}N_7O_{10}$, 636.3; found, 636.3.

Tb-DOTA-IAM-OMe ([Tb-4.1]). The cyclen methoxyisophthalate (**4.1**, 14 mg, 22 μmol) and $TbCl_3$ (8.2 mg, 22 μmol, 550 μL of a 40 mM aqueous solution) were combined in MQ water (1 mL). The pH was adjusted to 7.0 with dilute aqueous NaOH and the reaction mixture was heated at 45 °C for 48 h. The solvent was removed by lyophilization to yield the product as a white powder (17 mg, 22 μmol, quant.). ^{1}H NMR (500 MHz, D_2O, δ): selected peaks at -79.5, -76.1, -74.1, -68.9, -0.92, 2.87, 8.46, 18.3, 46.3. ESI-MS (*m/z*): $[M+Na]^+$ calcd for $C_{28}H_{40}O_{10}N_7Tb$, 816.2; found, 816.1.

2,2',2''-(10-(2-((4-hydroxy-3,5-bis(methylcarbamoyl)benzyl)amino)-2-oxoethyl)-1,4,7,10-tetraazacyclododecane-1,4,7-triyl)triacetic acid (4.2). The methoxy-protected IAM cyclen (**4.20**, 30.1 mg, 37.3 μmol) was dissolved in dry CH_2Cl_2 and magnetically stirred at -78 °C under argon in fully dried glassware. Boron tribromide (1 mL, 0.8 mmol) was added slowly, and the reaction mixture was allowed to warm to ambient temperature and was stirred for 18 h. The solvent was removed under reduced pressure and the reaction mixture dissolved in cold CH_3OH (10 mL) and refluxed for an additional 16 h. The solvent was removed under reduced pressure and CH_3OH/H_2O (1:1, 10 mL) was added, followed by concentrated HCl (0.5 mL) and this mixture was stirred at ambient temperature for 6 h. Solvents were removed under reduced pressure yielding a brown solid that was purified *via* reverse-phase HPLC, eluting with 0 – 60% acetonitrile in H_2O to yield a white solid (18.1 mg, 29.1 μmol, 78%). ^{1}H NMR (500 MHz, D_2O, δ): 7.89 (s, 2H), 4.37 (s, 2H), 3.87-3.57 (m, 6H), 3.51 (s, 2H), 3.32-3.22 (m, 16H), 2.92 (s, 6H). ^{13}C NMR (125 MHz, D_2O, δ): 171.1, 163.1, 160.1, 158.6, 137.8, 130.0, 120.4, 71.9, 71.4, 55.2, 54.8, 54.6, 52.3, 29.4.

[Tb-DOTA-IAM]$^-$ ([Tb-4.2]$^-$). The fully deprotected DOTA-IAM ligand (**4.2**, 6.0 mg, 9.6 μmol) was dissolved in mQ H_2O (10 mL) and magnetically stirred. To this, a stock solution of $TbCl_3$ (0.101 M, 95 μL) was added and the resultant solution was adjusted to pH 8 with aqueous NaOH. The reaction mixture was then heated at 80 °C for 86 h, after which it was allowed to cool to ambient temperature. The solvent was removed *via* lyophilizing to yield an off-white powder (7.4 mg, 9.6 μmol, quant.). ^{1}H NMR (500 MHz,

D_2O, δ): selected peaks at 1.3, 1.9, 2.9, 8.4, 11.4, 20.2, 22.6. HRMS (*m/z*): $[M+H]^+$ calcd for $C_{27}H_{38}N_7O_{10}Tb$, 780.2006; found, 780.2011.

2,2',2''-(10-(2-oxo-2-((phenanthridin-6-ylmethyl)amino)ethyl)-1,4,7,10-tetraazacyclododecane-1,4,7-triyl)triacetic acid (4.3). The DOTA-Phen ligand was synthesized as previously reported.[180, 186]

Tb-DOTA-Phen ([Tb-4.3]). The DOTA-Phen ligand (**4.3**, 14.1 mg, 23.7 μmol) was dissolved in mQ H_2O (15 mL) and magnetically stirred. To this, a stock solution of $TbCl_3$ (0.101 M, 235 μL) was added and the resultant solution was adjusted to pH 7 with aqueous NaOH. The reaction mixture was then heated at 80 ˚C for 114 h, after which it was allowed to cool to ambient temperature. The solvent was removed *via* lyophilization to yield an off-white powder (17.7 mg, 23.7 μmol, quant.). ^1H NMR (500 MHz, D_2O, δ): selected peaks at -11.9, -3.2, -1.7, 1.5, 10.5, 13.6, 16.0, 18.5, 22.2, 22.8, 27.0. HRMS (*m/z*): $[M+H]^+$ calcd for $C_{30}H_{35}N_6O_7Tb$, 751.1893; found, 751.1880.

***N*-Benzyl-2-bromoacetamide (4.21).** Aqueous K_2CO_3 (506 mg, 3.66 mmol) in water (3 mL) and bromoacetylbromide (120 μL, 1.38 mmol) in CH_2Cl_2 (3 mL) were added simultaneously dropwise over 15 min to benzylamine (100 μL, 0.915 mmol) in CH_2Cl_2 (3 mL) at 0 °C. Following the addition, the reaction mixture was stirred at ambient temperature for 2 h. The organic layer was washed with MQ water until the pH was approximately neutral (6 × 5 mL), brine (5 mL) and then dried over $MgSO_4$ and filtered. Removal of the solvent under reduced pressure yielded the product as a white powder (184 mg, 0.860 mmol, 88% yield). ^1H NMR (500 MHz, CD_2Cl_2 , δ): 3.91 (s, 2H), 4.45 (d, *J* = 6.0 Hz, 2H), 6.73 (s, 1H), 7.29 (m, 3H), 7.35 (m, 2H). ^{13}C NMR (125 MHz, CD_2Cl_2, δ): 29.3, 43.9, 127.6, 128.7, 137.8, 165.2. ESI-MS (*m/z*): $[M+Na]^+$ calcd for $C_9H_{10}BrNO$, 250.0; found, 250.0.

2-Methoxy-*N*¹,*N*³-dimethyl-5-((2-(4,7,10-tris(2-(benzylamino)-2-oxoethyl)-1,4,7,10-tetraazacyclododecan-1-yl)acetamido)methyl)isophthalamide (4.4). Under N_2, *N*-benzyl-2-bromoacetamide (**4.21**, 16 mg, 89 µmol) in anhydrous CH_3CN (2 mL) was added dropwise to the cyclen methoxyisophthalate (**4.19**, 13 mg, 24 µmol) and Cs_2CO_3 (75 mg, 0.23 mmol) in anhydrous CH_3CN (3 mL). Following the addition, the reaction mixture was stirred at 50 °C for 18 h. The solid was removed by filtration, and the solvent removed under reduced pressure. The crude product was deposited onto silica and purified by flash chromatography (eluent: 0 – 8% CH_3OH in CH_2Cl_2) to yield the product as a light yellow oil (8.0 mg, 8.8 µmol, 38% yield). ^{1}H NMR (500 MHz, CD_2Cl_2, δ): 2.01 – 2.85 (bm, 16H), 2.89 (m, 6H), 3.10 (m, 8H), 3.75 (s, 3H), 4.36 (m, 8H), 7.23 (m, 17H), 7.79 (s, 4H), 8.19 (bs, 2H). ^{13}C NMR (125 MHz, CD_2Cl_2, δ): 27.5, 43.2, 44.4, 51.5, 57.9, 58.8, 64.1, 128.2, 128.8, 129.2, 129.5, 134.1, 139.8, 167.1, 170.5, 172.4. HRMS (*m/z*): $[M+Na]^+$ calcd for $C_{49}H_{64}N_{10}O_7$, 927.4852; found, 927.4895.

[Tb-IAM-OMe-Benzyl]³⁺ ([Tb-4.4]³⁺). Aqueous $TbCl_3$ (200 µL of 40 mM solution, 7.9 µmol) was added to the benzyl isophthalamide ligand (**4.4**, 7.2 mg, 7.9 µmol) in CH_3OH (400 µL), for a final H_2O to CH_3OH ratio of 1:2. The pH was adjusted to 7 with dilute aqueous NaOH, and the reaction mixture was heated to 45 °C for 44 h. The solvent was removed by lyophilization generating the complex as a yellow oil (9.2 mg, 7.9 µmol, quant.). ^{1}H NMR (500 MHz, $(CD_3)_2SO$, δ): selected peaks at -78.40, -70.34, -66.79, -61.73, 0.46, 1.25, 1.94, 3.96, 5.19, 10.24, 13.12, 15.70, 21.58, 27.45, 32.64, 42.48, 50.40, 61.74. HRMS (*m/z*): $[M]^{3+}$ calcd for $C_{49}H_{64}N_{10}O_7Tb$, 354.4732; found, 354.4751.

2-Bromo-*N*-hexylacetamide (4.22). Synthesis was performed according to the procedure for compound (**4.21**) using hexyl amine. White powder (84% yield). ^{1}H NMR (500 MHz, $CDCl_3$, δ): 0.88 (t, *J* = 6.78 Hz, 3H), 1.32 (m, 6H), 1.52 (quin, *J* = 7.2 Hz, 2H), 3.27 (q, *J* = 6.7 Hz, 2H), 3.87 (s, 2H), 6.49 (s, 1H). ^{13}C NMR (125 MHz, $CDCl_3$, δ): 14.0, 22.5, 26.5, 29.2, 29.4, 31.4, 40.3,165.2. ESI-MS (*m/z*): $[M+Na]^+$ calcd for $C_8H_{16}BrNO$, 244.0; found, 244.1.

2-Methoxy-*N*¹,*N*³-dimethyl-5-((2-(4,7,10-tris(2-(hexylamino)-2-oxoethyl)-1,4,7,10-tetraazacyclododecan-1-yl)acetamido)methyl)isophthalamide (4.5). Synthesis was performed according to the procedure for compound (**4**) using 2-bromo-*N*-hexylacetamide (**4.22**). Light green oil (32% yield). ^{1}H NMR (500 MHz, $CDCl_3$, δ): 0.86 (m, 9H), 1.28 (m, 24H), 1.52 (m, 6H), 2.05-2.93 (bm, 16H), 2.98 (m, 6H), 3.23 (m, 10H), 3.89 (s, 3H), 7.76 (m, 1H), 7.92 (s, 2H), 8.08 (m, 3H), 8.70 (m, 1H). ^{13}C NMR (125 MHz, $CDCl_3$, δ): 14.0, 14.1, 22.6, 26.6, 29.3, 31.5, 39.8, 42.2, 51.0, 53.4, 56.8, 58.9, 62.7, 128.2, 133.5, 135.0, 155.7, 166.7, 170.5, 171.0. HRMS (*m/z*): $[M+Na]^+$ calcd for $C_{46}H_{82}N_{10}O_7$, 909.6260; found, 909.6264.

[Tb-IAM-OMe-Hexyl]³⁺ ([Tb-4.5]³⁺). Synthesis was performed according to the procedure for complex [Tb-**4.4**]$^{3+}$. Light green oil (quant.). ^{1}H NMR (500 MHz, $(CD_3)_2SO$, δ): selected peaks at -76.17, -66.40, -61.64, 1.25, 2.99, 4.86, 10.37, 15.79, 21.04, 27.31, 32.32, 37.08, 42.09, 50.36, 61.89. HRMS (*m/z*): $[M]^{3+}$ calcd for $C_{46}H_{82}N_{10}O_7Tb$, 348.5202; found, 348.5213.

2-Bromo-*N*-(2,2,2-trifluoroethyl)acetamide (4.23). Synthesis was performed according to the procedure for compound (**4.21**) using 2,2,2-trifluoroethanamine. White crystals (81%). ^{1}H NMR (500 MHz, $CDCl_3$, δ): 3.88-3.97 (m, 4H), 7.19 (br s, 1H). ^{19}F NMR (282 MHz, $CDCl_3$, δ): -72.9 (t, J = 8.7 Hz). ^{13}C NMR (75 MHz, $CDCl_3$, δ): 28.9, 41.9 (q, J = 34.8 Hz), 124.4, (q, J = 277 Hz), 167.4. HRMS (*m/z*): $[M+H]^+$ calcd for $C_4H_5BrF_3NO$, 219.9579; found, 219.9579.

2-Methoxy-*N*¹,*N*³-dimethyl-5-((2-(4,7,10-tris(2-oxo-2-((2,2,2-trifluoroethyl) amino)ethyl)-1,4,7,10-tetraazacyclododecan-1-yl)acetamido)methyl) isophthalamide (4.6). Synthesis was performed according to the procedure for compound (**4.4**) using 2-bromo-*N*-(2,2,2-trifluoroethyl)acetamide (**4.23**). Yellow oil (38% yield). ^{1}H NMR (500 MHz, CD_3OD, δ): 2.00-2.80 (bm, 18H), 2.94 (m, 6H), 3.03-3.29 (bm, 8H), 3.80 (s, 3H), 3.90 (m, 6H), 4.34 (s, 2H), 7.56 (s, 2H), 7.71 (s, 2H), 7.95 (s, 4H). ^{19}F NMR (470 MHz, CD_3OD, δ): -73.21 (s, 3F), -72.98 (s, 6F). ^{13}C NMR (76 MHz, CD_3OD, δ):

26.4, 26.8, 30.7, 40.7, 41.1, 42.7, 57.3, 57.6, 63.4, 123.9, 127.6, 130.1, 132.6, 136.8, 156.2, 168.6, 173.4, 174.1. HRMS (*m/z*): $[M+Na]^+$ calcd for $C_{34}H_{49}F_9N_{10}O_7$, 903.3534; found, 903.3523.

[Tb-IAM-OMe-CF$_3$]$^{3+}$ ([Tb-4.6]$^{3+}$). Synthesis was performed according to the procedure for complex [Tb-**4.4**]$^{3+}$. White powder (quant.). ^{1}H NMR (500 MHz, D_2O, δ): selected peaks at -88.14, -85.47, -74.79, -63.12, 1.55, 2.67, 12.51, 15.46, 19.25, 32.05, 36.13, 41.75, 46.10, 52.43, 56.51, 63.54. ^{19}F NMR (470 MHz, D_2O, δ): -72.4, -68.4, -59.7, -58.3, -54.5, -50.1, -48.4. HRMS (*m/z*): $[M-H]^{2+}$ calcd for $C_{34}H_{49}F_9N_{10}O_7Tb$, 519.1403; found, 519.1429.

Ethyl 2-(2-bromoacetamido)propanoate (4.24). Synthesis was performed according to the procedure for compound (**4.21**) using L-Alanine ethyl ester hydrochloride. White powder (68% yield). ^{1}H NMR (500 MHz, $CDCl_3$, δ): 1.27 (t, *J* = 7.2 Hz, 3H), 1.42 (d, *J* = 7.2 Hz, 3H), 3.86 (s, 2H), 4.20 (q, *J* = 7.2 Hz, 2H), 4.53 (quint, *J* = 7.2 Hz, 1H), 7.05 (s, 1H). ^{13}C NMR (125 MHz, $CDCl_3$, δ): 14.1, 18.2, 28.7, 48.8, 61.7, 165.1, 172.4. ESI-MS (*m/z*): $[M+Na]^+$ calcd for $C_7H_{12}BrNO_3$, 260.0; found, 260.0.

Triethyl-2,2',2''-((2,2',2''-(10-(2-((4-methoxy-3,5-bis(methylcarbamoyl)benzyl) amino)-2-oxoethyl)-1,4,7,10-tetraazacyclododecane-1,4,7-triyl)tris(acetyl)) tris(azanediyl)) tripropanoate (4.7). Synthesis was performed according to the procedure for compound (**4.4**) using ethyl 2-(2-bromoacetamido)propanoate (**4.24**). Light yellow oil (44% yield). ^{1}H NMR (500 MHz, $CDCl_3$, δ): 1.26 (m, 9H), 1.34 (d, *J* = 7.0 Hz, 3H), 1.40 (d, *J* = 7.1 Hz, 3H), 1.44 (d, *J* = 7.2 Hz, 3H), 2.13-2.81 (bm, 18H), 2.97 (m, 6H), 3.12-3.46 (bm, 8H), 3.87 (s, 3H), 4.16 (m, 6H), 4.34 (m, 1H), 4.44 (m, 1H), 4.54 (m, 1H), 7.90 (s, 2H), 8.02 (m, 4H), 8.64 (m, 2H). ^{13}C NMR (125 MHz, $CDCl_3$, δ): 14.1, 14.2, 17.2, 17.4, 17.6, 26.7, 42.2, 48.4, 48.6, 50.7, 53.4, 56.9, 61.2, 61.4, 61.6, 62.8, 128.3, 133.3, 134.9, 155.6, 166.6, 170.7 171.1, 171.4, 172.8, 173.0. HRMS (*m/z*): $[M+Na]^+$ calcd for $C_{43}H_{70}N_{10}O_{13}$, 957.5016; found, 957.5061.

[Tb-IAM-OMe-Ala-ester]$^{3+}$ ([Tb-4.7]$^{3+}$). Synthesis was performed according to the procedure for complex [Tb-**4.4**]$^{3+}$. Light yellow powder (quant.). ^{1}H NMR (500 MHz, D_2O, δ): selected peaks at -86.64, -74.70, -69.62, -17.12, -9.60, -6.71, 1.18, 3.24, 10.45, 17.70, 21.93, 24.80, 37.79, 45.09, 49.07, 60.34, 81.99. HRMS (*m/z*): $[M]^{3+}$ calcd for $C_{43}H_{70}N_{10}O_{13}Tb$, 364.4787; found, 364.4767.

Diethyl 2-(2-bromoacetamido)pentanedioate (4.25). Synthesis was performed according to the procedure for compound (**4.21**) using diethyl L-glutamate hydrochloride. White powder (66% yield). ^{1}H NMR (500 MHz, $CDCl_3$, δ): 1.24 (m, 6H), 2.05 (m, 1H) 2.20 (m, 1H), 2.24 (m, 2H), 3.86 (s, 2H), 4.11 (q, *J* = 7.0 Hz, 2H), 4.19 (q, *J* = 6.8 Hz, 2H), 4.56 (m, 1H), 7.13 (s, 1H). ^{13}C NMR (125 MHz, $CDCl_3$, δ): 14.1, 14.2, 27.1, 28.6, 30.1, 52.4, 60.8, 61.9, 165.7, 171.2, 172.6. ESI-MS (*m/z*): $[M+Na]^+$ calcd for $C_{11}H_{18}BrNO_5$, 346.0; found, 346.0.

Hexaethyl-2,2',2''-((2,2',2''-(10-(2-((4-methoxy-3,5-bis(methylcarbamoyl) benzyl)amino)-2-oxoethyl)-1,4,7,10-tetraazacyclododecane-1,4,7-triyl)tris (acetyl))tris (azanediyl)) tripentanedioate (4.8). Synthesis was performed according to the procedure for compound (**4.4**) using diethyl 2-(2-bromoacetamido)pentanedioate (**4.25**). Yellow oil (38% yield). ^{1}H NMR (500 MHz, $CDCl_3$, δ): 1.22 (m, 18H), 2.01-2.90 (bm, 28H), 2.97 (m, 6H), 2.80 – 3.00 (bm, 10H), 3.87 (s, 3H), 4.14 (m, 12H), 4.52 (m, 3H), 7.86 (s, 1H), 7.92 (m, 2H), 8.01 (s, 1H), 8.06 (m, 2H), 8.62 (m, 2H). ^{13}C NMR (125 MHz, $CDCl_3$, δ): 14.2, 26.4, 26.7, 29.7, 30.3, 30.5, 42.1, 51.9, 57.0, 60.7, 61.6, 62.7, 128.2, 133.3, 155.9, 166.7, 171.6, 171.8, 172.8. HRMS (*m/z*): $[M+Na]^+$ calcd for $C_{55}H_{88}N_{10}O_{19}$, 1215.6119; found, 1215.6148.

[Tb-IAM-OMe-Glu-ester]$^{3+}$ ([Tb-4.8]$^{3+}$). Synthesis was performed according to the procedure for complex [Tb-**4.4**]$^{3+}$. Light orange powder (quant.). ^{1}H NMR (500 MHz, D_2O, δ): selected peaks at -83.19, -79.33, -73.37, -69.19,-69.33, -65.33, -14.16, -7.58, -5.51, -4.51, -1.16, 1.13, 2.38, 9.62, 19.98, 24.79, 41.84, 50.36. HRMS (*m/z*): $[M]^{3+}$ calcd for $C_{55}H_{88}N_{10}O_{19}Tb$, 450.5155; found, 450.5159.

[Tb-IAM-OMe-Ala-acid]$^-$ ([Tb-4.9]$^-$). The Tb-complex of the alanine ester, [Tb-**4.7**]$^{3+}$, (6.1 mg, 5.1 μMol) was stirred with 0.2 M KOH (150 μL, 30.6 μMol) for 20 h at ambient temperature. The reaction was then neutralized with HCl and lypholized to yield a white powder (5.1 mg, 5.1 μMol, quant.). ^{1}H NMR (500 MHz, D_2O, δ): selected peaks at -85.69, -83.11, 1.38, 3.04, 8.11, 10.54, 15.33, 16.41, 17.69, 25.62, 33.80, 59.68, 100.02. ESI-MS (*m/z*): [M-H]$^-$ calcd for $C_{37}H_{55}N_{10}O_{13}Tb$, 1005.3; found, 1005.4.

[Tb-IAM-OMe-Glu-acid]$^{3-}$ ([Tb-4.10]$^{3-}$). The Tb-complex of the glutamine ester, [Tb-**4.8**]$^{3+}$, (9.0 mg, 6.2 μMol) was stirred with 0.2 M KOH (372 μL, 74.4 μMol, 12 eq) for 20 h at ambient temperature. The reaction was then neutralized with HCl and lypholized to yield a white powder (8.0 mg, 6.2 μMol, quant.). ^{1}H NMR (500 MHz, D_2O, δ): selected peaks at -85.05, -80.96, -77.73, 1.21, 2.10, 3.01, 4.40, 7.67, 9.26, 10.14, 11.48, 15.33, 18.74, 21.25, 24.77, 27.62, 34.21, 47.37, 58.13, 105.50. HRMS (*m/z*): [M+H]$^{2-}$ calcd for $C_{43}H_{58}N_{10}fO_{19}Tb$, 589.1650; found, 589.1665.

B. Experimental Methods

Determination of quantum yield (Φ). The absorbance and integrated luminescence intensity of [Tb-**4.1**] – [Tb-**4.3**] in PBS (pH 7.8, *n* = 1.3345) were compared to the reference fluorescence of quinine sulfate (Φ_r = 0.577)[192] in 0.1 M sulfuric acid (*n* = 1.333). Absorption spectra were collected on a Cary 100 Bio UV-Visible Spectrophotometer; emission spectra were recorded on a Cary Eclipse Fluorescence Spectrophotometer. Quantum yields (Φ) were calculated according to the optically dilute method using the equation

$$\Phi_x = \Phi_r \left(\frac{A_r}{A_x}\right)\left(\frac{n_x^2}{n_r^2}\right)\left(\frac{I_x}{I_r}\right)$$

Where *A* is the absorbance at the excitation wavelength (*λ*), *n* is the refractive index, and *I* is the integrated intensity.[115, 118] The subscripts *r* and *x* refer to the reference and samples, respectively. All data was collected using the same spectrophotometer on the same day, resulting in a constant intensity of the excitation light (λ_{ex} = 350 nm). Measurements were obtained at 22 °C in a quartz cell of 1 cm path length in degased

solutions using an excitation wavelength of 350 nm and excitation and emission slit widths of 10 nm for both complexes. The fluorescence response of quinine sulfate was reported as the integrated emission intensity from 365-665 nm; the Tb-luminescence of was collected with a time delay of 0.1 ms and reported as the integrated emission intensity from 470 – 688 nm. The experiment was performed in triplicate (n = 3).

Cell culture. Rat muscle L6 myoblast cell line was obtained from ATCC (Manassa, VA). Cells were cultured in 25-cm^2 or 75-cm^2 vented culture flasks in Dulbecco's modified eagle medium (DMEM) supplemented with 10% (v/v) bovine serum (BS) and 10 μg mL^{-1} gentamicin at 37 °C and 5% CO_2. The cells were maintained by splitting every 3-4 days before reaching confluence; cells were rinsed with PBS, lifted using 0.25 g L^{-1} typsin for 5 min, and diluted in fresh medium. All cells were propagated at low passage numbers (< 20) to maintain their myoblastic character.

Preparation of whole cell lysate. L6 cells were harvested from two 75 cm^2 culture flasks grown to 85% confluence and centrifuged at 400 *g* for 10 min at 4 °C. The resulting pellet was rinsed with ice-cold PBS (2 mL) and centrifuged. The cells were then suspended in PBS (1 mL) and transferred to a tight-fitting homogenizer (B-clearance 0.0008-0.0022 in). Approximately 90% of cells were ruptured after 120 strokes, as determined by cell counting with trypan blue and a hemocytometer. The total protein concentration of the whole cell lysate was determined with a bicinchoninic acid (BCA) assay (BCA Protein Assay Kit, ThermoScientific) using bovine serum albumin (BSA) protein standard solutions. The whole cell lysate was then diluted to a protein concentration of 1.0 mg/mL and aliquots (450 μL) were stored at -20 °C for later use.

Luminescence intensity in whole cell lysate. An aqueous suspension of [Tb-**4.1**] (100 μM) in whole cell lysate diluted in PBS (0.25 mg/mL protein or 0.5 mg/mL protein) was titrated into an aqueous solution of whole cell lysate in PBS (0.25 mg/mL or 0.5 mg/mL protein). The time-delayed emission profile was recorded in the presence of 0 - 15 μM of Tb-complex. The titration was repeated in pure PBS buffer (pH 7.8) without

cell lysate. Measurements were recorded with an excitation wavelength of 345 nm, time delay of 0.1 ms, excitation and emission slit widths of 5 nm, and at a temperature of 20 °C. The luminescence response was reported as the integrated emission intensity from 470 – 640 nm. Each experiment was repeated in triplicate (*n* = 3). The percent quenching of the luminescence was calculated from the slopes of the integrated luminescence intensity *versus* the concentration Tb-complex (μM) plots in PBS and whole cell lysate at the two protein concentrations.

Cell viability. L6 myoblasts (225 μL) were plated at ~ 4.0 x 10^4 cells mL^{-1} in a 48 well cell culture plate. Cells were allowed to recover 24 h, after which Tb-complexes in PBS (25 μL) were added to the culture media (final concentrations of 0, 1, 3, 10, 30, 100, and 300 μM). For the negative control, PBS (without Tb-complex) was used. The MTT assay was performed during the last 3 h of the compound exposure time as follows. MTT (3-(4, 5-dimethylthiazolyl-2)-2,5-diphenyltetrazolium bromide, 25 μL of 5 mg/mL stock solution, 0.5 mg/mL final concentration) was added to the media, and the plate was returned to the cell culture incubator for 3 h. When a purple precipitate was clearly visible, 250 μL of 0.04 M HCl in isopropanol was added to each well. After an incubation of 4 h at room temperature in the dark, the samples were centrifuged at 10,000 *g* for 5 min to pellet cellular debris. For each sample, a portion of the supernatant (200 μL) was transferred to a corresponding well of a 96 well plate, and the absorbance at 570 and 690 nm was recorded using a microtiter plate reader. The cell viability was calculated according to the following equation using the adjusted absorbance of the cells treated with Tb-complex in comparison to the control cells.[183]

$$viablity_{MTT}\,[\%] = \frac{(A_{570} - A_{690})_{Tb-complex}}{(A_{570} - A_{690})_{control}}$$

Results are expressed as mean ± SD (*n* = 3).

Cellular association by ICP-MS. The cellular association of [Tb-**4.1**] – [Tb-**4.10**] was investigated by seeding in triplicate L6 myoblasts (225 μL) at 4.5 x 10^4 cells mL^{-1} in a 48 well plate (~10,000 cells mL^{-1}). Cells were allowed to recover for 48 h and had grown to

80% confluence at which time a concentrated solution of Tb-complex in PBS (25 µL) was added to achieve a final concentration of 50 µM in the cellular media. Cells grown in Tb-complex free media (addition of only PBS) were included as a negative control. Following 4 h of incubation, the media was removed, and the wells were washed twice with room temperature by adding PBS and rocking the culture plate back and forth several times. The addition of a lysis buffer (75 µL of 10 mM Tris, pH 7.5, 100 mM NaCl, 1 mM Na_2EDTA, and 1% Triton X- 100) followed by a 20 min incubation at 4 °C ruptured the cell membranes.[53] Aliquots (3 × 8 µL) from each well were removed for a BCA assay to determine the protein concentration. Samples (50 µL) were combined with concentrated nitric acid (50 µL) and heated to 95 °C for 18 h in flame sealed glass ampules prior to ICP-MS analysis. The Tb content (ppb) was determined by ICP-MS, and the cellular association of each Tb-complex (C_{Tb}), expressed as µMol Tb g protein^{-1}, was calculated according to the following equation:

$$C_{Tb} = \left(\frac{C_m}{M}\right)/(C_p)$$

Where C_m is the measured metal concentration (ppb) of the cell samples; M is the molecular mass of Tb; C_p is the protein concentration (mg/mL). Results are expressed as mean ± SD (*n* = 3).

Fluorescence microscopy. L6 myoblasts (passage 9 or 10) were seeded in a poly lysine coated 8-well glass-bottom plate and allowed to grow for 24 h to 50% confluence at 37 °C in 5% CO_2. Then Tb-complexes [Tb-**4.2**]$^-$ - [Tb-**4.8**] were added in PBS for a final concentration of 200 µM. Negative control wells containing cells grown in Tb-complex free media (addition of only PBS) were included. Following a 4 h incubation, the media was removed, and cells were washed three times with PBS at room temperature by rocking the culture plate back and forth gently. Cells were fixed with 4% formaldehyde in PBS at room temperature for 15 min. Additionally, live cell imaging of [Tb-**4.6**] was performed in DMEM phenol red-free media. Epifluorescence images of representative cells were acquired on an Olympus IX81 inverted microscope equipped with a 60x (N.A. 1.45) oil immersion objective. Excitation was supplied by an Exfo XCite 120 metal halide lamp source coupled to the microscope via a liquid light guide, images

were collected with a C9100-01 CCD camera, and HCImage software was utilized to control the microscope and camera and to process images. An excitation filter (325 - 375 nm), dichoric (460 nm), and emission filter (470 - 750 nm) were employed with an exposure times of 0.4 s for fixed cells and 0.1 s with live cells. Bright field images of cells were also collected to determine the position of cells (exposure time 0.04 s). The contrast of bright field images was adjusted to a contrast range of 0 - 100 (normal range 0 - 255) using HCImage software.

REFERENCES

1. Koskenkorva-Frank, T. S.; Weiss, G.; Koppenol, W. H.; Burckhardt, S., The complex interplay of iron metabolism, reactive oxygen species, and reactive nitrogen species: Insights into the potential of various iron therapies to induce oxidative and nitrosative stress. *Free Radic. Biol. Med.* **2013,** *65*, 1174-1194.
2. Bild, W.; Ciobica, A.; Padurariu, M.; Bild, V., The interdependence of the reactive species of oxygen, nitrogen, and carbon. *J. Physiol. Biochem.* **2013,** *69*, 147-154.
3. Winterbourn, C. C., Reconciling the chemistry and biology of reactive oxygen species. *Nat. Chem. Biol.* **2008,** *4*, 278-286.
4. Dickinson, B. C.; Chang, C. J., Chemistry and biology of reactive oxygen species in signaling or stress responses. *Nat. Chem. Biol.* **2011,** *7*, 504-511.
5. Valko, M.; Leibfritz, D.; Moncol, J.; Cronin, M. T. D.; Mazur, M.; Telser, J., Free radicals and antioxidants in normal physiological functions and human disease. *Int. J. Biochem. Cell Biol.* **2007,** *39*, 44-84.
6. Giorgio, M.; Trinei, M.; Migliaccio, E.; Pelicci, P. G., Hydrogen peroxide: a metabolic by-product or a common mediator of ageing signals? *Nat. Rev. Mol. Cell Biol.* **2007,** *8*, 722-728.
7. Hughes, M. What is oxidative stress. http://www.geneactivatornrf2.org/os/#.U0v_CaKa9bw (accessed 14 April 2014).
8. Ford, E.; Hughes, M. N.; Wardman, P., Kinetics of the reactions of nitrogen dioxide with glutathione, cysteine, and uric acid at physiological pH. *Free Radic. Biol. Med.* **2002,** *32*, 1314-1323.
9. Liu, G.; Li, Y.; Pagel, M. D., Design and characterization of a new irreversible responsive PARACEST MRI contrast agent that detects nitric oxide. *Magn. Reson. Med.* **2007,** *58*, 1249-1256.
10. Ashby, M. T.; Carlson, A. C.; Scott, M. J., Redox buffering of hypochlorous acid by thiocyanate in physiologic fluids. *J. Am. Chem. Soc.* **2004,** *126*, 15976-15977.
11. Carballal, S.; Bartesaghi, S.; Radi, R., Kinetic and mechanistic considerations to assess the biological fate of peroxynitrite. *Biochim. Biophys. Acta* **2014,** *1840*, 768-780.
12. Flors, C.; Fryer, M. J.; Waring, J.; Reeder, B.; Bechtold, U.; Mullineaux, P. M.; Nonell, S.; Wilson, M. T.; Baker, N. R., Imaging the production of singlet oxygen in vivo using a new fluorescent sensor, singlet oxygen sensor green *J. Exp. Bot.* **2006,** *57*, 1725-1734.
13. da Silva, E. F. F.; Pedersen, B. W.; Breitenbach, T.; Toftegaard, R.; Kuimova, M. K.; Arnaut, L. G.; Ogilby, P. R., Irradiation- and sensitizer-dependent changes in the lifetime of ntracellular singlet oxygen produced in a photosensitized process. *J. Phys. Chem. B* **2011,** *116*, 445-461.
14. Gungor, N.; Knaapen, A. M.; Munnia, A.; Peluso, M.; Haenen, G. R.; Chiu, R. K.; Godschalk, R. W.; van Schooten, F. J., Genotoxic effects of neutrophils and hypochlorous acid. *Mutagenesis* **2010,** *25*, 149-154.
15. Makrigiorgos, G. M.; Baranowska-Kortylewicz, J.; Bump, E.; Sahu, S. K.; Berman, R. M.; Kassis, A. I., A method for detection of hydroxyl radicals in the vicinity of biomolecules using radiation-induced fluorescence of coumarin. *Int. J. Radiat. Biol.* **1993,** *63*, 445-458.
16. Sueishi, Y.; Hori, M.; Ishikawa, M.; Matsu-Ura, K.; Kamogawa, E.; Honda, Y.; Kita, M.; Ohara, K., Scavenging rate constants of hydrophilic antioxidants against multiple reactive oxygen species. *J. Clin. Biochem. Nutr.* **2014,** *54*, 67-74.

17. Bonini, M. G.; Augusto, O., Carbon dioxide stimulates the production of thiyl, sulfinyl, and disulfide radical anion from thiol oxidation by peroxynitrite. *J. Biol. Chem.* **2001,** *276*, 9749-9754.
18. Winterbourn, C. C.; Metodiewa, D., Reactivity of biologically important thiol compounds with superoxide and hydrogen peroxide. *Free Radic. Biol. Med.* **1999,** *27*, 322-328.
19. Folkes, L. K.; Wardman, P., Kinetics of the reaction between nitric oxide and glutathione: Implications for thiol depletion in cells. *Free Radic. Biol. Med.* **2004,** *37*, 549-556.
20. Medinas, D. B.; Cerchiaro, G.; Trindade, D. F.; Augusto, O., The carbonate radical and related oxidants derived from bicarbonate buffer. *IUBMB Life* **2007,** *59*, 255-262.
21. Czapski, G.; Lymar, S. V.; Schwarz, H. A., Acidity of the carbonate radical. *J. Phys. Chem. A* **1999,** *103*, 3447-3450.
22. Bartberger, M. D.; Liu, W.; Ford, E.; Miranda, K. M.; Switzer, C.; Fukuto, J. M.; Farmer, P. J.; Wink, D. A.; Houk, K. N., The reduction potential of nitric oxide (NO) and its importance to NO biochemistry. *Proc. Natl. Acad. Sci. U. S. A.* **2002,** *99*, 10958-10963.
23. Winterbourn, C. C., The challenges of using fluorescent probes to detect and quantify specific reactive oxygen species in living cells. *Biochim Biophys Acta* **2014,** *1840*, 730-738.
24. Shafirovich, V.; Lymar, S. V., Nitroxyl and its anion in aqueous solutions: spin states, protic equilibria, and reactivities toward oxygen and nitric oxide. *Proc. Natl. Acad. Sci. U. S. A.* **2002,** *99*, 7340-7345.
25. Buettner, G. R., The pecking order of free radicals and antioxidants: Lipid peroxidation, alpha-tocopherol, and ascorbate. *Arch. Biochem. Biophys.* **1993,** *300*, 535-543.
26. Dutton, A. S.; Fukuto, J. M.; Houk, K. N., Theoretical reduction potentials for nitrogen oxides from CBS-QB3 energetics and (C)PCM solvation calculations. *Inorg. Chem.* **2005,** *44*, 4024-4028.
27. Harris, D. C., *Exploring Chemical Analysis*. Fourth ed.; 2009.
28. Jomova, K.; Valko, M., Advances in metal-induced oxidative stress and human disease. *Toxicol.* **2011,** *283*, 65-87.
29. Stone, J. R.; Yang, S., Hydrogen peroxide: a signaling messenger. *Antioxid. Redox Signal.* **2006,** *8*, 243-270.
30. Prousek, J., Fenton chemistry in biology and medicine. *Pure Appl. Chem.* **2007,** *79*, 2325-2338.
31. Bertini, I.; Gray, H. B.; Stiefel , E. I.; Valentine, J. S., *Biological Inorganic Chemistry: Structure and Reactivity*. University Science Books: Sausalito, CA, 2007.
32. Domaille, D. W.; Que, E. L.; Chang, C. J., Synthetic fluorescent sensors for studying the cell biology of metals. *Nat. Chem. Biol.* **2008,** *4*, 168-175.
33. Thibon, A.; Pierre, V. C., Principles of responsive lanthanide-based luminescent probes for cellular imaging. *Anal. Bioanal. Chem.* **2009,** *394*, 107-120.
34. Cacheris, W. P.; Quay, S. C.; Rocklage, S. M., The relationship between thermodynamics and the toxicity of gadolinium complexes. *Magn. Reson. Imaging* **1990,** *8*, 467-481.
35. Hermann, P.; Kotek, J.; Kubicek, V.; Lukes, I., Gadolinium(III) complexes as MRI contrast agents: Ligand design and properties of the complexes. *Dalton Trans.* **2008**, 3027-3047.
36. Xu, J.; Franklin, S. J.; Whisenhunt, D. W.; Raymond, K. N., Gadolinium complex of tris[(3-hydroxy-1-methyl- 2-oxo-1,2-didehydropyridine-4-carboxamido)ethyl]-amine: A new class of gadolinium magnetic resonance relaxation agents. *J. Am. Chem. Soc.* **1995,** *117*, 7245-7246.
37. Tweedle, M. F.; Hagan, J. J.; Kumar, K.; Mantha, S.; Chang, C. A., Reaction of gadolinium chelates with endogenously available ions. *Magn. Reson. Imaging* **1991,** *9*, 409-415.
38. Di Gregorio, E.; Gianolio, E.; Stefania, R.; Barutello, G.; Digilio, G.; Aime, S., On the fate of MRI Gd-based contrast agents in cells. Evidence for extensive degradation of linear complexes upon endosomal internalization. *Anal. Chem.* **2013,** *85*, 5627-5631.

39. Kielar, F.; Montgomery, C. P.; New, E. J.; Parker, D.; Poole, R. A.; Richardson, S. L.; Stenson, P. A., A mechanistic study of the dynamic quenching of the excited state of europium(iii) and terbium(iii) macrocyclic complexes by charge- or electron transfer. *Org. Biomol. Chem.* **2007,** *5*, 2975-2982.
40. Poole, R. A.; Montgomery, C. P.; New, E. J.; Congreve, A.; Parker, D.; Botta, M., Identification of emissive lanthanide complexes suitable for cellular imaging that resist quenching by endogenous anti-oxidants. *Org. Biomol. Chem.* **2007,** *5*, 2055-2062.
41. Kielar, F.; Law, G.-L.; New, E. J.; Parker, D., The nature of the sensitiser substituent determines quenching sensitivity and protein affinity and influences the design of emissive lanthanide complexes as optical probes for intracellular use. *Org. Biomol. Chem.* **2008,** *6*, 2256-2258.
42. Dickins, R. S.; Aime, S.; Batsanov, A. S.; Beeby, A.; Botta, M.; Bruce, J. I.; Howard, J. A. K.; Love, C. S.; Parker, D.; Peacock, R. D.; Puschmann, H., Structural, luminescence, and NMR studies of the reversible binding of acetate, lactate, citrate, and selected amino acids to chiral diaqua ytterbium, gadolinium, and europium complexes. *J. Am. Chem. Soc.* **2002,** *124*, 12697-12705.
43. Botta, M.; Aime, S.; Barge, A.; Bobba, G.; Dickins, R. S.; Parker, D.; Terreno, E., Ternary complexes between cationic Gd(III) chelates and anionic metabolites in aqueous solution: An NMR relaxometric study. *Chem. Eur. J.* **2003,** *9*, 2102-2109.
44. Bruce, J. I.; Dickins, R. S.; Govenlock, L. J.; Gunnlaugsson, T.; Lopinski, S.; Lowe, M. P.; Parker, D.; Peacock, R. D.; Perry, J. J. B.; Aime, S.; Botta, M., The selectivity of reversible oxy-anion binding in aqueous solution at a chiral europium and terbium center: Signaling of carbonate chelation by changes in the form and circular polarization of luminescence emission. *J. Am. Chem. Soc.* **2000,** *122*, 9674-9684.
45. Que, E. L.; Chang, C. J., A smart magnetic resonance contrast agent for selective copper sensing. *J. Am. Chem. Soc.* **2006,** *128*, 15942-15943.
46. Major, J. L.; Parigi, G.; Luchinat, C.; Meade, T. J., The synthesis and in vitro testing of a zinc-activated MRI contrast agent. *Proc. Natl. Acad. Sci. U. S. A.* **2007,** *104*, 13881-13886.
47. Hyman, L. M.; Franz, K. J., Probing oxidative stress: Small molecule fluorescent sensors of metal ions, reactive oxygen species, and thiols. *Coord. Chem. Rev.* **2012,** *256*, 2333-2356.
48. Puckett, C. A.; Ernst, R. J.; Barton, J. K., Exploring the cellular accumulation of metal complexes. *Dalton Trans.* **2010,** *39*, 1159-1170.
49. Puckett, C. A.; Barton, J. K., Methods to explore cellular uptake of ruthenium complexes. *J. Am. Chem. Soc.* **2007,** *129*, 46-47.
50. Weidmann, A. G.; Komor, A. C.; Barton, J. K., Biological effects of simple changes in functionality on rhodium metalloinsertors. *Phil. Trans. R. Soc. A* **2013,** *371*, 20120117-20120117.
51. Chauvin, A.-S.; Thomas, F.; Song, B.; Vandevyver, C. D. B.; Bunzli, J.-C. G., Synthesis and cell localization of self-assembled dinuclear lanthanide bioprobes. *Phil. Trans. R. Soc. A* **2013,** *371*, 20120295-20120295.
52. New, E. J.; Congreve, A.; Parker, D., Definition of the uptake mechanism and sub-cellular localisation profile of emissive lanthanide complexes as cellular optical probes. *Chem. Sci.* **2010,** *1*, 111-118.
53. New, E. J.; Parker, D., The mechanism of cell uptake for luminescent lanthanide optical probes: the role of macropinocytosis and the effect of enhanced membrane permeability on compartmentalisation. *Org. Biomol. Chem.* **2009,** *7*, 851-855.
54. Murray, B. S.; New, E. J.; Pal, R.; Parker, D., Critical evaluation of five emissive europium(iii) complexes as optical probes: Correlation of cytotoxicity, anion and protein affinity with complex structure, stability and intracellular localisation profile. *Org. Biomol. Chem.* **2008,** *6*, 2085-2094.

55. Park, G. Y.; Wilson, J. J.; Song, Y.; Lippard, S. J., Phenanthriplatin, a monofunctional DNA-binding platinum anticancer drug candidate with unusual potency and cellular activity profile. *Proc. Natl. Acad. Sci. U. S. A.* **2012,** *109*, 11987-11992.
56. Dosio, F.; Stella, B.; Ferrero, A.; Garino, C.; Zonari, D.; Arpicco, S.; Cattel, L.; Giordano, S.; Gobetto, R., Ruthenium polypyridyl squalene derivative: A novel self-assembling lipophilic probe for cellular imaging. *Int. J. Pharm.* **2013,** *440*, 221-228.
57. Darghal, N.; Garnier-Suillerot, A.; Bouchemal, N.; Gras, G.; Geraldes, C. F. G. C.; Salerno, M., Accumulation of Eu^{3+} chelates in cells expressing or not P-glycoprotein: Implications for blood-brain barrier crossing. *J. Inorg. Biochem.* **2010,** *104*, 47-54.
58. Koide, Y.; Kawaguchi, M.; Urano, Y.; Hanaoka, K.; Komatsu, T.; Abo, M.; Teraia, T.; Nagano, T., A reversible near-infrared fluorescence probe for reactive oxygen species based on Te-rhodamine. *Chem. Commun.* **2012,** *48*, 3091-3093.
59. Miller, E. W.; Bian, S. X.; Chang, C. J., A fluorescent sensor for imaging reversible redox cycles in living cells. *J. Am. Chem. Soc.* **2007,** *129*, 3458-3459.
60. Liu, F.; Wu, T.; Cao, J.; Zhang, H.; Hu, M.; Sun, S.; Song, F.; Fan, J.; Wang, J.; Peng, X., A novel fluorescent sensor for detection of highly reactive oxygen species, and for imaging such endogenous hROS in the mitochondria of living cells. *Analyst* **2013,** *138*, 775-778.
61. Manjare, S. T.; Kim, S.; Do Heo, W.; Churchill, D. G., Selective and sensitive superoxide detection with a new diselenide-based molecular probe in living breast cancer cells. *Org. Lett.* **2014,** *16*, 410-412.
62. Lou, Z.; Li, P.; Pan, Q.; Han, K., A reversible fluorescent probe for detecting hypochloric acid in living cells and animals: utilizing a novel strategy for effectively modulating the fluorescence of selenide and selenoxide. *Chem. Commun.* **2013,** *49*, 2445-2447.
63. Wang, B.; Li, P.; Yu, F.; Song, P.; Sun, X.; Yang, S.; Lou, Z.; Han, K., A reversible fluorescence probe based on Se-BODIPY for the redox cycle between HClO oxidative stress and H2S repair in living cells. *Chem. Commun.* **2013,** *49*, 1014-1016.
64. Yu, F.; Li, P.; Li, G.; Zhao, G.; Chu, T.; Han, K., A near-IR reversible fluorescent probe modulated by selenium for monitoring peroxynitrite and imaging in living cells. *J. Am. Chem. Soc.* **2011,** *133*, 11030-11033.
65. Hilderbrand, S. A.; Lim, M. H.; Lippard, S. J., Dirhodium tetracarboxylate scaffolds as reversible fluorescence-based nitric oxide sensors. *J. Am. Chem. Soc.* **2004,** *126*, 4972-4978.
66. Koide, Y.; Urano, Y.; Kenmoku, S.; Kojima, H.; Nagano, T., Design and synthesis of fluorescent probes for selective detection of highly reactive oxygen species in mitochondria of living cells. *J. Am. Chem. Soc.* **2007,** *129*, 10324-10325.
67. Dickinson, B. C.; Lin, V. S.; Chang, C. J., Preparation and use of MitoPY1 for imaging hydrogen peroxide in mitochondria of live cells. *Nat. Protoc.* **2013,** *8*, 1249-1259.
68. Li, P.; Zhang, W.; Li, K.; Liu, X.; Xiao, H.; Zhang, W.; Tang, B., Mitochondria-targeted reaction-based two-photon fluorescent probe for imaging of superoxide anion in live cells and *in vivo*. *Anal. Chem.* **2013,** *85*, 9877-9881.
69. Yu, H.; Zhang, X.; Xiao, Y.; Zou, W.; Wang, L.; Jin, L., Targetable fluorescent probe for monitoring exogenous and endogenous NO in mitochondria of living cells. *Anal. Chem.* **2013,** *85*, 7076-7084.
70. Song, D.; Lim, J. M.; Cho, S.; Park, S.-J.; Cho, J.; Kang, D.; Rhee, S. G.; You, Y.; Nam, W., A fluorescence turn-on H2O2 probe exhibits lysosome-localized fluorescence signals. *Chem. Commun.* **2012,** *48*, 5449-5451.
71. Tang, B.; Zhang, N.; Chen, Z.; Xu, K.; Zhuo, L.; An, L.; Yang, G., Probing hydroxyl radicals and their imaging in living cells by ue of FAM–DNA–Au nanoparticles. *Chem. Eur. J.* **2008,** *14*, 522-528.
72. Ganea, G. M.; Kolic, P. E.; El-Zahab, B.; Warner, I. M., Ratiometric coumarin-neutral red (CONER) nanoprobe for detection of hydroxyl radicals. *Anal. Chem.* **2011,** *83*, 2576-2581.

73. Zhuang, M.; Ding, C.; Zhu, A.; Tian, Y., Ratiometric fluorescence probe for monitoring hydroxyl radical in live cells based on gold nanoclusters. *Anal. Chem.* **2014,** *86*, 1829-1836.
74. Kobayashi, H.; Ogawa, M.; Alford, R.; Choyke, P. L.; Urano, Y., New strategies for fluorescent probe design in medical diagnostic imaging. *Chem. Rev.* **2009,** *110*, 2620-2640.
75. Lenz, P., Fluorescence measurement in thick tissue layers by linear or nonlinear long-wavelength excitation. *Appl. Opt.* **1999,** *38*, 3662-3669.
76. Chen, X.; Tian, X.; Shin, I.; Yoon, J., Fluorescent and luminescent probes for detection of reactive oxygen and nitrogen species. *Chem. Soc. Rev.* **2011,** *40*, 4783-4804.
77. Kundu, K.; Knight, S. F.; Willett, N.; Lee, S.; Taylor, W. R.; Murthy, N., Hydrocyanines: A class of fluorescent sensors that can image reactive oxygen species in cell culture, tissue, and *in vivo*. *Angew. Chem., Int. Ed. Engl.* **2009,** *48*, 299-303.
78. Oushiki, D.; Kojima, H.; Terai, T.; Arita, M.; Hanaoka, K.; Urano, Y.; Nagano, T., Development and application of a near-infrared fluorescence probe for oxidative stress based on differential reactivity of linked cyanine dyes. *J. Am. Chem. Soc.* **2010,** *132*, 2795-2801.
79. Yuan, L.; Lin, W.; Song, J., Ratiometric fluorescent detection of intracellular hydroxyl radicals based on a hybrid coumarin-cyanine platform. *Chem. Commun.* **2010,** *46*, 7930-7932.
80. Herrmann, H.; Hoffmann, D.; Schaefer, T.; Braeuer, P.; Tilgner, A., Tropospheric aqueous-phase free-radical chemistry: Radical sources, spectra, reaction kinetics and prediction tools. *Chem. Phys. Chem.* **2010,** *11*, 3796-3822.
81. Page, S. E.; Wilke, K. T.; Pierre, V. C., Sensitive and selective time-gated luminescence detection of hydroxyl radical in water. *Chem. Commun.* **2010,** *46*, 2423-2425.
82. Cui, G.; Ye, Z.; Chen, J.; Wang, G.; Yuan, J., Development of a novel terbium(III) chelate-based luminescent probe for highly sensitive time-resolved luminescence detection of hydroxyl radical. *Talanta* **2011,** *84*, 971-976.
83. Xiao, Y.; Ye, Z.; Wang, G.; Yuan, J., A ratiometric luminescence probe for highly reactive oxygen species based on lanthanide complexes. *Inorg. Chem.* **2012,** *51*, 2940-2946.
84. Galvao, J.; Davis, B.; Tilley, M.; Normando, E.; Duchen, M. R.; Cordeiro, M. F., Unexpected low-dose toxicity of the universal solvent DMSO. *FASEB J* **2014,** *28*, 1317-1330.
85. Maki, T.; Soh, N.; Fukaminato, T.; Nakajima, H.; Nakano, K.; Imato, T., Perylenebisimide-linked nitroxide for the detection of hydroxyl radicals. *Anal. Chim. Acta* **2009,** *639*, 78-82.
86. Pou, S.; Huang, Y. I.; Bhan, A.; Bhadti, V. S.; Hosmane, R. S.; Wu, S. Y.; Cao, G. L.; Rosen, G. M., A fluorophore-containing nitroxide as a probe to detect superoxide and hydroxylradical generated by stimulated neutrophils. *Anal. Biochem.* **1993,** *212*, 85-90.
87. Yang, X. F.; Guo, X. Q., Investigation of the anthracene-nitroxide hybrid molecule as a probe for hydroxyl radicals. *Analyst* **2001,** *126*, 1800-1804.
88. Yang, X. F.; Guo, X. Q., Study of nitroxide-linked naphthalene as a fluorescence probe for hydroxyl radicals. *Anal. Chim. Acta* **2001,** *434*, 169-177.
89. Bian, Z. Y.; Guo, X. Q.; Zhao, Y. B.; Du, J. O., Probing the hydroxyl radical-mediated reactivity of peroxynitrite by a spin-labeling fluorophore. *Anal. Sci.* **2005,** *21*, 553-559.
90. Yapici, N. B.; Jockusch, S.; Moscatelli, A.; Mandalapu, S. R.; Itagaki, Y.; Bates, D. K.; Wiseman, S.; Gibson, K. M.; Turro, N. J.; Bi, L. R., New rhodamine nitroxide based fluorescent probes for intracellular hydroxyl radical identification in living cells. *Org. Lett.* **2012,** *14*, 50-53.
91. Li, P.; Xie, T.; Duan, X.; Yu, F.; Wang, X.; Tang, B., A new highly selective and sensitive assay for fluorescence imaging of hydroxyl radical in living cells: Effectively avoiding the interference of peroxynitrite. *Chem. Eur. J.* **2010,** *16*, 1834-1840.

92. Hong, J.; Zhuang, Y.; Ji, X.; Guo, X., A long-lived luminescence and EPR bimodal lanthanide-based probe for free radicals. *Analyst* **2011,** *136*, 2464-2470.
93. Manevich, Y.; Held, K. D.; Biaglow, J. E., Coumarin-3-carboxylic acid as a detector for hydroxyl radicals generated chemically and by gamma radiation. *Radiat. Res.* **1997,** *148*, 580-591.
94. Makrigiorgos, G. M.; Folkard, M.; Huang, C.; Bump, E.; Baranowska-Kortylewicz, J.; Sahu, S. K.; Michael, B. D.; Kassis, A. I., Quantification of radiation-induced hydroxyl radicals within nucleohistones using a molecular fluorescent probe. *Radiat. Res.* **1994,** *138*, 177-185.
95. Makrigiorgos, G. M.; Bump, E.; Huang, C.; Baranowska-Kortylewicz, J.; Kassis, A. I., A fluorimetric method for the detection of copper-mediated hydroxyl free radicals in the immediate proximity of DNA. *Free Radic. Biol. Med.* **1995,** *18*, 669-678.
96. Perry, C. C.; Tang, V. J.; Konigsfeld, K. M.; Aguilera, J. A.; Milligan, J. R., Use of a coumarin-labeled hexa-arginine peptide as a fluorescent hydroxyl radical probe in a nanoparticulate plasmid DNA condensate. *J. Phys. Chem. B* **2011,** *115*, 9889-9897.
97. Soh, N.; Makihara, K.; Ariyoshi, T.; Seto, D.; Maki, T.; Nakajima, H.; Nakano, K.; Imato, T., Phospholipid-linked coumarin: a fluorescent probe for sensing hydroxyl radicals in lipid membranes. *Anal. Sci.* **2008,** *24*, 293-296.
98. Meng, L.; Wu, Y.; Yi, T., A ratiometric fluorescent probe for the detection of hydroxyl radicals in living cells. *Chem. Commun.* **2014**.
99. Liu, M.; Liu, S. M.; Peterson, S. L.; Miyake, M.; Liu, K. J., On the application of 4-hydroxybenzoic acid as a trapping agent to study hydroxyl radical generation during cerebral ischemia and reperfusion. *Mol. Cell. Biochem.* **2002,** *234*, 379-385.
100. Linxiang, L.; Abe, Y.; Nagasawa, Y.; Kudo, R.; Usui, N.; Imai, K.; Mashino, T.; Mochizuki, M.; Miyata, N., An HPLC assay of hydroxyl radicals by the hydroxylation reaction of terephthalic acid. *Biomed. Chromatogr.* **2004,** *18*, 470-474.
101. Newton, G. L.; Milligan, J. R., Fluorescence detection of hydroxyl radicals. *Radiat. Phys. Chem.* **2006,** *75*, 473-478.
102. Saran, M.; Summer, K. H., Assaying for hydroxyl radicals: Hydroxylated terephthalate is a superior fluorescence marker than hydroxylated benzoate. *Free Radic. Res.* **1999,** *31*, 429-436.
103. Page, S. E.; Arnold, W. A.; McNeill, K., Terephthalate as a probe for photochemically generated hydroxyl radical. *J. Environ. Monit.* **2010,** *12*, 1658-1665.
104. Barreto, J. C.; Smith, G. S.; Strobel, N. H. P.; McQuillin, P. A.; Miller, T. A., Terephthalic acid: A dosimeter for the detection of hydroxyl radicals *in vitro*. *Life Sci* **1994,** *56*, PL89-PL96.
105. Yan, E. B.; Unthank, J. K.; Castillo-Melendez, M.; Miller, S. L.; Langford, S. J.; Walker, D. W., Novel method for in vivo hydroxyl radical measurement by microdialysis in fetal sheep brain in utero. *J. Appl. Physiol.* **2005,** *98*, 2304-2310.
106. Mishin, V. M.; Thomas, P. E., Characterization of hydroxyl radical formation by microsomal enzymes using a water-soluble trap, terephthalate. *Biochem. Pharmacol.* **2004,** *68*, 747-752.
107. Qu, X. H.; Kirschenbaum, L. J.; Borish, E. T., Hydroxyterephthalate as a fluorescent probe for hydroxyl radicals: Application to hair melanin. *Photochem. Photobiol.* **2000,** *71*, 307-313.
108. Lippert, A. R.; Keshari, K. R.; Kurhanewicz, J.; Chang, C. J., A hydrogen peroxide-responsive hyperpolarized ^{13}C MRI contrast agent. *J. Am. Chem. Soc.* **2011,** *133*, 3776-3779.
109. Liu, M.; Ye, Z.; Wang, G.; Yuan, J., Development of a novel europium(III) complex-based luminescence probe for time-resolved luminescence imaging of the nitric oxide production in neuron cells. *Talanta* **2012,** *99*, 951-958.

110. Aime, S.; Calzoni, S.; Digilio, G.; Giraudo, S.; Fasano, M.; Maffeo, D., A novel F-19-NMR method for the investigation of the antioxidant capacity of biomolecules and biofluids. *Free Radic. Biol. Med.* **1999,** *27*, 356-363.
111. Bunzli, J. C. G.; Piguet, C., Taking advantage of luminescent lanthanide ions. *Chem. Soc. Rev.* **2005,** *34*, 1048-1077.
112. Thibon, A.; Pierre, V. C., A highly selective luminescent sensor for the time-gated detection of potassium. *J. Am. Chem. Soc.* **2009,** *131*, 434-435.
113. Hanaoka, K.; Kikuchi, K.; Kojima, H.; Urano, Y.; Nagano, T., Development of a zinc ion-selective luminescent lanthanide chemosensor for biological applications. *J. Am. Chem. Soc.* **2004,** *126*, 12470-12476.
114. Gunnlaugsson, T.; Harte, A. J.; Leonard, J. P.; Nieuwenhuyzen, M., The formation of luminescent supramolecular ternary complexes in water: Delayed luminescence sensing of aromatic carboxylates using coordinated unsaturated cationic heptadentate lanthanide ion complexes. *Supramol. Chem.* **2003,** *15*, 505-519.
115. Law, G.-L.; Pham, T. A.; Xu, J.; Raymond, K. N., A single sensitizer for the excitation of visible and NIR lanthanide emitters in water with high quantum yields. *Angew. Chem., Int. Ed.* **2012,** *51*, 2371-2374.
116. Kotova, O.; Comby, S.; Gunnlaugsson, T., Sensing of biologically relevant d-metal ions using a Eu(III)-cyclen based luminescent displacement assay in aqueous pH 7.4 buffered solution. *Chem. Commun.* **2011,** *47*, 6810-6812.
117. Horrocks, W. D.; Sudnick, D. R., Lanthanide ion luminescence probes of the structure of biological macromolecules. *Acc. Chem. Res.* **1981,** *14*, 384-392.
118. Samuel, A. P. S.; Moore, E. G.; Melchior, M.; Xu, J.; Raymond, K. N., Water-soluble 2-hydroxyisophthalamides for sensitization of lanthanide luminescence. *Inorg. Chem.* **2008,** *47*, 7535-7544.
119. Gunnlaugsson, T.; Harte, A. J.; Leonard, J. P.; Nieuwenhuyzen, M., Delayed lanthanide luminescence sensing of aromatic carboxylates using heptadentate triamide Tb(III) cyclen complexes: the recognition of salicylic acid in water. *Chem. Commun.* **2002**, 2134-2135.
120. Soh, N.; Makihara, K.; Sakoda, E.; Imato, T., A ratiometric fluorescent probe for imaging hydroxyl radicals in living cells. *Chem. Commun.* **2004**, 496-497.
121. Kim, Y.-S.; Yang, C.-T.; Wang, J.; Wang, L.; Li, Z.-B.; Chen, X.; Liu, S., Effects of targeting moiety, linker, bifunctional chelator, and molecular charge on biological properties of ^{64}Cu-labeled triphenylphosphonium cations. *J. Med. Chem.* **2008,** *51*, 2971-2984.
122. Zhu, J.; Wang, X.-Z.; Chen, Y.-Q.; Jiang, X.-K.; Chen, X.-Z.; Li, Z.-T., Hydrogen-bonding-induced planar, rigid, and zigzag oligoanthranilamides. Synthesis, characterization, and self-assembly of a metallocyclophane. *J. Org. Chem.* **2004,** *69*, 6221-6227.
123. Adams, H.; Hunter, C. A.; Lawson, K. R.; Perkins, J.; Spey, S. E.; Urch, C. J.; Sanderson, J. M., A supramolecular system for quantifying aromatic stacking interactions. *Chem. Eur. J.* **2001,** *7*, 4863-4877.
124. Pecoraro, V. L.; Weit, F. L.; Raymond, K. N., Ferric ion-specific sequestering agents. Synthesis, iron-exchange kinetics, and stability constants of *N*-substituted, sulfonated catechoylamide analogs of enterobactin. *J. Am. Chem. Soc.* **1981,** *103*, 5133-5140.
125. Weitz, E. A.; Pierre, V. C., A ratiometric probe for the selective time-gated luminescence detection of potassium in water. *Chem. Commun.* **2011,** *47*, 541-543.
126. Beeby, A.; M. Clarkson, I.; S. Dickins, R.; Faulkner, S.; Parker, D.; Royle, L.; S. de Sousa, A.; A. Gareth Williams, J.; Woods, M., Non-radiative deactivation of the excited states of europium, terbium and ytterbium complexes by proximate energy-matched OH, NH and CH oscillators: an improved luminescence method for establishing solution hydration states. *J. Chem. Soc., Perkin Trans. 2* **1999,** *0*, 493-504.

127. Ghosh, P.; Federwisch, G.; Kogej, M.; Schalley, C. A.; Haase, D.; Saak, W.; Lutzen, A.; Gschwind, R. M., Controlling the rate of shuttling motions in [2]rotaxanes by electrostatic interactions: a cation as solvent-tunable brake. *Org. Biomol. Chem.* **2005,** *3*, 2691-2700.
128. Ay, E.; Chaumeil, H.; Barsella, A., Syntheses of four new pyridinium phenolates with caged phenolate functionalities as chromophores for quadratic optics. *Tetrahedron* **2012,** *68*, 628-635.
129. Winston, G. W.; Harvey, W.; Berl, L.; Cederbaum, A. I., The generation of hydroxyl and alkoxyl radicals from the interaction of ferrous bipyridyl with peroxides. *Biochem. J.* **1983,** *216*, 415-421.
130. Hu, L.; Hockett, F. D.; Chen, J.; Zhang, L.; Caruthers, S. D.; Lanza, G. M.; Wickline, S. A., A generalized strategy for designing F-19/H-1 dual-frequency MRI coil for small animal imaging at 4.7 tesla. *J. Magn. Reson. Imaging* **2011,** *34*, 245-252.
131. Harvey, P.; Kuprov, I.; Parker, D., Lanthanide complexes as paramagnetic probes for ^{19}F magnetic resonance. *Eur. J. Inorg. Chem.* **2012**, 2015-2022.
132. Yu, J.-X.; Hallac, R. R.; Chiguru, S.; Mason, R. P., New frontiers and developing applications in F-19 NMR. *Prog. Nucl. Magn. Reson. Spectrosc.* **2013,** *70*, 25-49.
133. Yu, J. X.; Kodibagkar, V. D.; Cui, W. N.; Mason, R. P., F-19: A versatile reporter for non-invasive physiology and pharmacology using magnetic resonance. *Curr. Med. Chem.* **2005,** *12*, 819-848.
134. Li, L. X.; Abe, Y.; Nagasawa, Y.; Kudo, R.; Usui, N.; Imai, K.; Mashino, T.; Mochizuki, M.; Miyata, N., An HPLC assay of hydroxyl radicals by the hydroxylation reaction of terephthalic acid. *Biomed. Chromatogr.* **2004,** *18*, 470-474.
135. Eberhardt, M. K.; Ramirez, G.; Ayala, E., Does the reaction of copper(I) with hydrogen peroxide give hydroxyl radicals? A study of aromatic hydroxylation. *J. Org. Chem.* **1989,** *54*, 5922-5926.
136. Jadan, A. P.; Moonen, M. J. H.; Boeren, S.; Golovleva, L. A.; Rietjens, I.; van Berkel, W. J. H., Biocatalytic potential of p-hydroxybenzoate hydroxylase from Rhodococcus rhodnii 135 and Rhodococcus opacus 557. *Adv. Synth. Catal.* **2004,** *346*, 367-375.
137. Molander, G. A.; Cavalcanti, L. N., Oxidation of organotrifluoroborates *via* oxone. *J. Org. Chem.* **2011,** *76*, 623-630.
138. Moonen, M. J. H.; Rietjens, I.; van Berkel, W. J. H., F-19 NMR study on the biological Baeyer-Villiger oxidation of acetophenones. *J. Ind. Microbiol. Biotechnol.* **2001,** *26*, 35-42.
139. Xu, R.; Hong, J.; Morse, C. L.; Pike, V. W., Synthesis, structure-affinity relationships, and radiolabeling of selective high-affinity 5-HT4 receptor ligands as prospective imaging probes for positron emission tomography. *J. Med. Chem.* **2010,** *53*, 7035-7047.
140. Aime, S.; Digilio, G.; Bruno, E.; Mainero, V.; Baroni, S.; Fasano, M., Modulation of the antioxidant activity of HO center dot scavengers by albumin binding: a F-19-NMR study. *Biochem. Biophys. Res. Commun.* **2003,** *307*, 962-966.
141. Chalmers, K. H.; De Luca, E.; Hogg, N. H. M.; Kenwright, A. M.; Kuprov, I.; Parker, D.; Botta, M.; Wilson, J. I.; Blamire, A. M., Design principles and theory of paramagnetic fluorine-labelled lanthanide complexes as probes for F-19 magnetic resonance: A proof-of-concept study. *Chem. Eur. J.* **2010,** *16*, 134-148.
142. Bertini, I.; Turano, P.; Vila, A. J., Nuclear magnetic resonance of paramagnetic metalloproteins *Chem. Rev.* **1993,** *93*, 2833-2932.
143. Bertini, I.; Capozzi, F.; Luchinat, C.; Nicastro, G.; Xia, Z. C., Water proton relazation for some lanthanide aqua ions in solution. *J. Phys. Chem.* **1993,** *97*, 6351-6354.
144. Peters, J. A.; Huskens, J.; Raber, D. J., Lanthanide induced shifts and relaxation rate enhancements. *Prog. Nucl. Magn. Reson. Spectrosc.* **1996,** *28*, 283-350.
145. Gysling, H.; Tsutsui, M., Organolanthanides and Organoactinides. In *Adv. Organomet. Chem.*, Stone, F. G. A.; Robert, W., Eds. Academic Press: 1971; Vol. Volume 9, pp 361-395.

146. Bleaney, B., Nuclear magnetic resonance shifts in solution due to lanthanide ions. *J. Magn. Resonance* **1972,** *8*, 91-100.
147. Bertini, I.; Luchinat, C.; Parigi, G., Magnetic susceptibility in paramagnetic NMR. *Prog. Nucl. Magn. Reson. Spectrosc.* **2002,** *40*, 249-273.
148. Alsaadi, B. M.; Rossotti, F. J. C.; Williams, R. J. P., Hydration of complexone complexes of lanthanide cations. *Dalton Trans.* **1980**, 2151-2154.
149. Allegrozzi, M.; Bertini, I.; Janik, M. B. L.; Lee, Y. M.; Lin, G. H.; Luchinat, C., Lanthanide-induced pseudocontact shifts for solution structure refinements of macromolecules in shells up to 40 angstrom from the metal ion. *J. Am. Chem. Soc.* **2000,** *122*, 4154-4161.
150. Chalmers, K. H.; Kenwright, A. M.; Parker, D.; Blamire, A. M., ^{19}F lanthanide complexes with increased sensitivity for 19F MRI: Optimization of the MR acquisition. *Magn. Reson. Med.* **2011,** *66*, 931-936.
151. Chalmers, K. H.; Botta, M.; Parker, D., Strategies to enhance signal intensity with paramagnetic fluorine-labelled lanthanide complexes as probes for F-19 magnetic resonance. *Dalton Trans.* **2011,** *40*, 904-913.
152. Weitz, E. A. M., M.; Peterson, K.L.; Pierre, V.C., Fe- and Ln-DOTAm-F12 are effective paramagnetic fluorine contrast agents for MRI in water and blood. *Manuscript in preparation*.
153. Dorai, K.; Kumar, A., Fluorine chemical shift tensors in substituted fluorobenzenes using cross correlations in NMR relaxation. *Chem. Phys. Lett.* **2001,** *335*, 176-182.
154. Deutsch, C. J.; Taylor, J. S., New class of ^{19}F pH indicators: Fluoroanilines *Biophys. J.* **1989,** *55*, 799-804.
155. Jiraroj, D.; Unob, F.; Hagege, A., Degradation of Pb-EDTA complex by a H_2O_2/UV process. *Water Res.* **2006,** *40*, 107-112.
156. Cullen, T. D.; Mezyk, S. P.; Martin, L. R.; Mincher, B. J., Elucidating the radical kinetics involved in the radiolytic destruction of lanthanide-complexed DTPA. *J. Radioanal. Nucl. Chem.* **2013,** *296*, 717-720.
157. Criscione, J. M.; Le, B. L.; Stern, E.; Brennan, M.; Rahner, C.; Papademetris, X.; Fahmy, T. M., Self-assembly of pH-responsive fluorinated dendrimer-based particulates for drug delivery and noninvasive imaging. *Biomaterials* **2009,** *30*, 3946-3955.
158. De Luca, E.; Harvey, P.; Chalmers, K.; Mishra, A.; Senanayake, P. K.; Wilson, J. I.; Botta, M.; Fekete, M.; Blamire, A.; Parker, D., Characterisation and evaluation of paramagnetic fluorine labelled glycol chitosan conjugates for 19F and 1H magnetic resonance imaging. *J. Biol. Inorg. Chem.* **2013**, 1-13.
159. Jiang, Z.-X.; Liu, X.; Jeong, E.-K.; Yu, Y. B., Symmetry-guided design and fluorous synthesis of a stable and rapidly excreted imaging tracer for ^{19}F MRI. *Angew. Chem., Int. Ed. Engl.* **2009,** *48*, 4755-4758.
160. Du, W.; Nystrom, A. M.; Zhang, L.; Powell, K. T.; Li, Y.; Cheng, C.; Wickline, S. A.; Wooley, K. L., Amphiphilic hyperbranched fluoropolymers as nanoscopic ^{19}F magnetic resonance imaging agent assemblies. *Biomacromolecules* **2008,** *9*, 2826-2833.
161. Thurecht, K. J.; Blakey, I.; Peng, H.; Squires, O.; Hsu, S.; Alexander, C.; Whittaker, A. K., Functional hyperbranched polymers: Toward targeted *in vivo* ^{19}F magnetic resonance imaging using designed macromolecules. *J. Am. Chem. Soc.* **2010,** *132*, 5336-5337.
162. Ogawa, M.; Nitahara, S.; Aoki, H.; Ito, S.; Narazaki, M.; Matsuda, T., Synthesis and evaluation of water-soluble fluorinated dendritic block-copolymer nanoparticles as a F-19-MRI contrast agent. *Macromol. Chem. Phys.* **2010,** *211*, 1602-1609.
163. Peng, H.; Blakey, I.; Dargaville, B.; Rasoul, F.; Rose, S.; Whittaker, A. K., Synthesis and evaluation of partly fluorinated block copolymers as MRI imaging agents. *Biomacromol.* **2009,** *10*, 374-381.

164. Ogawa, M.; Nitahara, S.; Aoki, H.; Ito, S.; Narazaki, M.; Matsuda, T., Fluorinated polymer nanoparticles as a novel F-19 MRI contrast agent prepared by dendrimer-initiated living radical polymerization. *Macromol. Chem. Phys.* **2010,** *211*, 1369-1376.
165. Zhu, Q.; Qiu, F.; Zhu, B.; Zhu, X., Hyperbranched polymers for bioimaging. *RSC Adv.* **2013,** *3*, 2071-2083.
166. Yu, Y. B., Fluorinated dendrimers as imaging agents for F-19 MRI. *Nanomed. Nanobiotech.* **2013,** *5*, 646-661.
167. Frisch, M. J. T., G. W.; Schlegel, H. B.; Scuseria, G. E.; Robb, M. A.; Cheeseman, J. R.; Scalmani, G.; Barone, V.; Mennucci, B.; Petersson, G. A.; Nakatsuji, H.; Caricato, M.; Li, X.; Hratchian, H. P.; Izmaylov, A. F.; Bloino, J.; Zheng, G.; Sonnenberg, J. L.; Hada, M.; Ehara, M.; Toyota, K.; Fukuda, R.; Hasegawa, J.; Ishida, M.; Nakajima, T.; Honda, Y.; Kitao, O.; Nakai, H.; Vreven, T.; Montgomery, J. A., Jr.; Peralta, J. E.; Ogliaro, F.; Bearpark, M.; Heyd, J. J.; Brothers, E.; Kudin, K. N.; Staroverov, V. N.; Kobayashi, R.; Normand, J.; Raghavachari, K.; Rendell, A.; Burant, J. C.; Iyengar, S. S.; Tomasi, J.; Cossi, M.; Rega, N.; Millam, N. J.; Klene, M.; Knox, J. E.; Cross, J. B.; Bakken, V.; Adamo, C.; Jaramillo, J.; Gomperts, R.; Stratmann, R. E.; Yazyev, O.; Austin, A. J.; Cammi, R.; Pomelli, C.; Ochterski, J. W.; Martin, R. L.; Morokuma, K.; Zakrzewski, V. G.; Voth, G. A.; Salvador, P.; Dannenberg, J. J.; Dapprich, S.; Daniels, A. D.; Farkas, Ö.; Foresman, J. B.; Ortiz, J. V.; Cioslowski, J.; Fox, D. J. , *Gaussian 09, Revision D.01*. Gaussian, Inc.: Wallingford CT, 2009.
168. Dolg, M.; Stoll, H.; Preuss, H., A combination of quasirelativistic pseudopotential and ligand field calculations for lanthanoid compounds. *Theor. Chim. Acta* **1993,** *85*, 441-450.
169. Dolg, M.; Stoll, H.; Savin, A.; Preuss, H., Energy-adjusted pseudopotentials for the rare earth elements. *Theor. Chim. Acta* **1989,** *75*, 173-194.
170. Platas-Iglesias, C., The solution dtructure and dynamics of MRI probes based on lanthanide(III) DOTA as investigated by DFT and NMR spectroscopy. *Eur. J. Inorg. Chem.* **2012,** *2012*, 2023-2033.
171. Coogan, M. P.; Fernandez-Moreira, V., Progress with, and prospects for, metal complexes in cell imaging. *Chem. Commun.* **2014,** *50*, 384-399.
172. Kobayashi, H.; Longmire, M. R.; Ogawa, M.; Choyke, P. L., Rational chemical design of the next generation of molecular imaging probes based on physics and biology: mixing modalities, colors and signals. *Chem. Soc. Rev.* **2011,** *40*, 4626-4648.
173. Lo, K. K.-W.; Choi, A. W.-T.; Law, W. H.-T., Applications of luminescent inorganic and organometallic transition metal complexes as biomolecular and cellular probes. *Dalton Trans.* **2012,** *41*, 6021-6047.
174. Baggaley, E.; Weinstein, J. A.; Williams, J. A. G., Lighting the way to see inside the live cell with luminescent transition metal complexes. *Coord. Chem. Rev.* **2012,** *256*, 1762-1785.
175. Lippert, A. R.; Gschneidtner, T.; Chang, C. J., Lanthanide-based luminescent probes for selective time-gated detection of hydrogen peroxide in water and in living cells. *Chem. Commun.* **2010,** *46*, 7510-7512.
176. Peterson, K. L.; Margherio, M. J.; Doan, P.; Wilke, K. T.; Pierre, V. C., Basis for sensitive and selective time-delayed luminescence detection of hydroxyl radical by lanthanide complexes. *Inorg. Chem.* **2013,** *52*, 9390-9398.
177. Comby, S.; Tuck, S. A.; Truman, L. K.; Kotova, O.; Gunnlaugsson, T., New trick for an old ligand! The sensing of Zn(II) using a lanthanide based ternary Yb(III)-cyclen-8-hydroxyquinoline system as a dual emissive probe for displacement assay. *Inorg. Chem.* **2012,** *51*, 10158-10168.
178. Moore, J. D.; Lord, R. L.; Cisneros, G. A.; Allen, M. J., Concentration-independent pH detection with a luminescent dimetallic Eu(III)-based probe. *J. Am. Chem. Soc.* **2012,** *134*, 17372-17375.

179. McMahon, B. K.; Pal, R.; Parker, D., A bright and responsive europium probe for determination of pH change within the endoplasmic reticulum of living cells. *Chem. Commun.* **2013,** *49*, 5363-5365.
180. Weitz, E. A.; Chang, J. Y.; Rosenfield, A. H.; Pierre, V. C., A selective luminescent probe for the direct time-gated detection of adenosine triphosphate. *J. Am. Chem. Soc.* **2012,** *134*, 16099-16102.
181. Major, J. L.; Meade, T. J., Bioresponsive, cell-penetrating, and multimeric MR contrast agents. *Acc. Chem. Res.* **2009,** *42*, 893-903.
182. Vithanarachchi, S. M.; Allen, M. J., Strategies for target-specific contrast agents for magnetic resonance imaging. *Curr. Mol. Imag.* **2012,** *1*, 12-25.
183. Song, B.; Vandevyver, C. D.; Chauvin, A. S.; Bunzli, J. C., Time-resolved luminescence microscopy of bimetallic lanthanide helicates in living cells. *Org. Biomol. Chem.* **2008,** *6*, 4125-4133.
184. Parker, D., Critical design factors for optical imaging with metal coordination complexes. *Aust. J. Chem.* **2011,** *64*, 239-243.
185. New, E. J.; Parker, D.; Smith, D. G.; Walton, J. W., Development of responsive lanthanide probes for cellular applications. *Curr. Opin. Chem. Biol.* **2010,** *14*, 238-246.
186. Weitz, E. A.; Chang, J. Y.; Rosenfield, A. H.; Morrow, E. A.; Pierre, V. C., The basis for the molecular recognition and the selective time-gated luminescence detection of ATP and GTP by a lanthanide complex. *Chem. Sci.* **2013,** *4*, 4052-4060.
187. Smolensky, E. D.; Peterson, K. L.; Weitz, E. A.; Lewandowski, C.; Pierre, V. C., Magnetoluminescent light switches--dual modality in DNA detection. *J. Am. Chem. Soc.* **2013,** *135*, 8966-8972.
188. Woods, M.; Kiefer, G. E.; Bott, S.; Castillo-Muzquiz, A.; Eshelbrenner, C.; Michaudet, L.; McMillan, K.; Mudigunda, S. D. K.; Ogrin, D.; Tircsó, G.; Zhang, S.; Zhao, P.; Sherry, A. D., Synthesis, relaxometric and photophysical properties of a new pH-responsive MRI contrast agent: The effect of other ligating groups on dissociation of a *p*-nitrophenolic pendant arm. *J. Am. Chem. Soc.* **2004,** *126*, 9248-9256.
189. Jeon, J. W.; Son, S. J.; Yoo, C. E.; Hong, I. S.; Song, J. B.; Suh, J., Protein-cleaving catalyst selective for protein substrate. *Org. Lett.* **2002,** *4*, 4155-4158.
190. Moreau, J.; Guillon, E.; Pierrard, J. C.; Rimbault, J.; Port, M.; Aplincourt, M., Complexing mechanism of the lanthanide cations Eu^{3+}, Gd^{3+}, and Tb^{3+} with 1,4,7,10-tetrakis(carboxymethyl)-1,4,7,10-tetraazacyclododecane (dota)-characterization of three successive complexing phases: Study of the thermodynamic and structural properties of the complexes by potentiometry, luminescence spectroscopy, and EXAFS. *Chemistry (Weinheim an der Bergstrasse, Germany)* **2004,** *10*, 5218-5232.
191. Lattuada, L.; Barge, A.; Cravotto, G.; Giovenzana, G. B.; Tei, L., The synthesis and application of polyamino polycarboxylic bifunctional chelating agents. *Chem. Soc. Rev.* **2011,** *40*, 3019-3049.
192. Lakowicz, J. R., *Principles of Fluorescence Spectroscopy*. 3rd ed ed.; Springer: Singapore, 2006.
193. Parker, D.; Senanayake, P. K.; Williams, J. A. G., Luminescent sensors for pH, pO_2, halide and hydroxide ions using phenanthridine as a photosensitiser in macrocyclic europium and terbium complexes. *J. Chem. Soc., Perkin Trans. 2* **1998**, 2129-2139.
194. Li, C.; Liu, Y.; Wu, Y.; Sun, Y.; Li, F., The cellular uptake and localization of non-emissive iridium(III) complexes as cellular reaction-based luminescence probes. *Biomaterials* **2013,** *34*, 1223-1234.
195. Resch-Genger, U.; Grabolle, M.; Cavaliere-Jaricot, S.; Nitschke, R.; Nann, T., Quantum dots versus organic dyes as fluorescent labels. *Nat. Methods* **2008,** *5*, 763-775.
196. Fernandez-Moreira, V.; Thorp-Greenwood, F. L.; Coogan, M. P., Application of d^6 transition metal complexes in fluorescence cell imaging. *Chem. Commun.* **2010,** *46*, 186-202.

197. Puckett, C. A.; Barton, J. K., Mechanism of cellular uptake of a ruthenium polypyridyl complex. *Biochem.* **2008,** *47*, 11711-11716.
198. Lo, K. K.-W.; Lee, P.-K.; Lau, J. S.-Y., Synthesis, characterization, and properties of luminescent organoiridium(III) polypyridine complexes appended with an alkyl chain and their interactions with lipid bilayers, surfactants, and living cells. *Organometallics* **2008,** *27*, 2998-3006.
199. Walton, J. W.; Bourdolle, A.; Butler, S. J.; Soulie, M.; Delbianco, M.; McMahon, B. K.; Pal, R.; Puschmann, H.; Zwier, J. M.; Lamarque, L.; Maury, O.; Andraud, C.; Parker, D., Very bright europium complexes that stain cellular mitochondria. *Chem. Commun.* **2013,** *49*, 1600-1602.
200. Lee, P.-K.; Law, W. H.-T.; Liu, H.-W.; Lo, K. K.-W., Luminescent cyclometalated iridium(III) polypyridine di-2-picolylamine complexes: synthesis, photophysics, electrochemistry, cation binding, cellular internalization, and cytotoxic activity. *Inorg. Chem.* **2011,** *50*, 8570-8579.
201. Zhao, Q.; Huang, C.; Li, F., Phosphorescent heavy-metal complexes for bioimaging. *Chem. Soc. Rev.* **2011,** *40*, 2508-2524.
202. Belitsky, J. M.; Leslie, S. J.; Arora, P. S.; Beerman, T. A.; Dervan, P. B., Cellular uptake of *N*-methylpyrrole/*N*-methylimidazole polyamide-dye conjugates. *Bioorg. Med. Chem.* **2002,** *10*, 3313-3318.
203. Stewart, K. M.; Horton, K. L.; Kelley, S. O., Cell-penetrating peptides as delivery vehicles for biology and medicine. *Org. Biomol. Chem.* **2008,** *6*, 2242-2255.
204. Gianolio, E.; Stefania, R.; Di Gregorio, E.; Aime, S., MRI paramagnetic probes for cellular labeling. *Eur. J. Inorg. Chem.* **2012**, 1934-1944.
205. Allen, M. J.; MacRenaris, K. W.; Venkatasubramanian, P. N.; Meade, T. J., Cellular delivery of MRI contrast agents. *Chem. Biol.* **2004,** *11*, 301-307.
206. Allen, M. J.; Meade, T. J., Synthesis and visualization of a membrane-permeable MRI contrast agent. *J. Biol. Inorg. Chem.* **2003,** *8*, 746-750.
207. Endres, P. J.; MacRenaris, K. W.; Vogt, S.; Allen, M. J.; Meade, T. J., Quantitative imaging of cell-permeable magnetic resonance contrast agents using x-ray fluorescence. *Mol. Imag.* **2006,** *5*, 485-497.
208. Futaki, S.; Goto, S.; Sugiura, Y., Membrane permeability commonly shared among arginine-rich peptides. *J. Mol. Recognit.* **2003,** *16*, 260-264.
209. Que, E. L.; New, E. J.; Chang, C. J., A cell-permeable gadolinium contrast agent for magnetic resonance imaging of copper in a Menkes disease model. *Chem. Sci.* **2012,** *3*, 1829-1834.
210. Bhorade, R.; Weissleder, R.; Nakakoshi, T.; Moore, A.; Tung, C. H., Macrocyclic chelators with paramagnetic cations are internalized into mammalian cells via a HIV-tat derived membrane translocation peptide. *Bioconjugate Chem.* **2000,** *11*, 301-305.
211. Mohandessi, S.; Rajendran, M.; Magda, D.; Miller, L. W., Cell-penetrating peptides as delivery vehicles for a protein-targeted terbium complex. *Chem. Eur. J.* **2012,** *18*, 10825-10829.
212. Blackmore, L.; Moriarty, R.; Dolan, C.; Adamson, K.; Forster, R. J.; Devocelle, M.; Keyes, T. E., Peptide directed transmembrane transport and nuclear localization of Ru(II) polypyridyl complexes in mammalian cells. *Chem. Commun.* **2013,** *49*, 2658-2660.
213. Puckett, C. A.; Barton, J. K., Targeting a ruthenium complex to the nucleus with short peptides. *Bioorg. Med. Chem.* **2010,** *18*, 3564-3569.
214. Keliris, A.; Ziegler, T.; Mishra, R.; Pohmann, R.; Sauer, M. G.; Ugurbil, K.; Engelmann, J., Synthesis and characterization of a cell-permeable bimodal contrast agent targeting beta-galactosidase. *Bioorg. Med. Chem.* **2011,** *19*, 2529-2540.
215. Wolf, M.; Hull, W. E.; Mier, W.; Heiland, S.; Bauder-Wuest, U.; Kinscherf, R.; Haberkorn, U.; Eisenhut, M., Polyamine-substituted gadolinium chelates: A new class of intracellular

contrast agents for magnetic resonance imaging of tumors. *J. Med. Chem.* **2007,** *50*, 139-148.

216. Lee, J.; Burclette, J. E.; MacRenaris, K. W.; Mustafi, D.; Woodruff, T. K.; Meade, T. J., Rational design, synthesis, and biological evaluation of progesterone-modified MRI contrast agents. *Chem. Biol.* **2007,** *14*, 824-834.
217. Corot, C.; Robert, P.; Lancelot, E.; Prigent, P.; Ballet, S.; Guilbert, I.; Raynaud, J.-S.; Raynal, I.; Port, M., Tumor imaging using P866, a high-relaxivity gadolinium chelate designed for folate receptor targeting. *Magn. Reson. Med.* **2008,** *60*, 1337-1346.
218. Goswami, L. N.; Ma, L.; Cai, Q.; Sarma, S. J.; Jalisatgi, S. S.; Hawthorne, M. F., cRGD peptide-conjugated icosahedral closo-B122- core carrying multiple Gd^{3+}-DOTA chelates for αvβ3 integrin-targeted tumor imaging (MRI). *Inorg. Chem.* **2013,** *52*, 1701-1709.
219. Andre, J. P.; Geraldes, C.; Martins, J. A.; Merbach, A. E.; Prata, M. I. M.; Santos, A. C.; de Lima, J. J. P.; Toth, E., Lanthanide(III) complexes of DOTA-glycoconjugates: A potential new class of lectin-mediated medical imaging agents. *Chem. Eur. J.* **2004,** *10*, 5804-5816.
220. Crich, S. G.; Cabella, C.; Barge, A.; Belfiore, S.; Ghirelli, C.; Lattuada, L.; Lanzardo, S.; Mortillaro, A.; Tei, L.; Visigalli, M.; Forni, G.; Aime, S., *In vitro* and *in vivo* magnetic resonance detection of tumor cells by targeting glutamine transporters with Gd-based probes. *J. Med. Chem.* **2006,** *49*, 4926-4936.
221. Digilio, G.; Menchise, V.; Gianolio, E.; Catanzaro, V.; Carrera, C.; Napolitano, R.; Fedeli, F.; Aime, S., Exofacial protein thiols as a route for the internalization of Gd(III)-based complexes for magnetic resonance imaging cell labeling. *J. Med. Chem.* **2010,** *53*, 4877-4890.
222. Puckett, C. A.; Barton, J. K., Fluorescein redirects a ruthenium-octaarginine conjugate to the nucleus. *J. Am. Chem. Soc.* **2009,** *131*, 8738-8739.